UNIVERSITÉ DE LORRAINE | BIBLIOTHÈQUES UNIVERSITAIRES

AVERTISSEMENT

Ce document est le fruit d'un long travail approuvé par le jury de soutenance et mis à disposition de l'ensemble de la communauté universitaire élargie.

Il est soumis à la propriété intellectuelle de l'auteur. Ceci implique une obligation de citation et de référencement lors de l'utilisation de ce document.

D'autre part, toute contrefaçon, plagiat, reproduction illicite encourt une poursuite pénale.

Contact bibliothèque : ddoc-theses-contact@univ-lorraine.fr
(Cette adresse ne permet pas de contacter les auteurs)

LIENS

Code de la Propriété Intellectuelle. articles L 122. 4
Code de la Propriété Intellectuelle. articles L 335.2- L 335.10
http://www.cfcopies.com/V2/leg/leg_droi.php
http://www.culture.gouv.fr/culture/infos-pratiques/droits/protection.htm

Online health monitoring of photovoltaic panels by converter-based impedance spectroscopy

Thèse de doctorat de l'Université de Lorraine

Ecole doctorale IAEM Lorraine
Spécialité de doctorat: Génie Electrique
Unités de recherche: Laboratoire Matériaux, Optique, Photonique et Systèmes (LMOPS)
Université de Lorraine & CentraleSupélec, Metz, France.
Site de Thionville-Yutz. Yutz. France.

Thèse présentée et soutenue à Metz, le 12/06/2024

Xin Wang

Composition du Jury :

Anne Migan Dubois Pr, GeePs, Université Paris-Saclay, Paris, France	Présidente
Demba Diallo Pr, GeePs, Université Paris-Saclay, Paris, France	Rapporteur
Corinne Alonso Pr, LAAS, Université Paul Sabatier, Toulouse, France	Rapporteure
Daniel Hissel Pr, Institut FEMTO-ST, Université de Franche-Comté, Belfort, France	Examinateur
Claude Delpha Pr, GeePs, Université Paris-Saclay, Paris, France	Examinateur
Javier Solano Researcher, EIFER, Karlsruhe, Germany	Invité
Michel Aillerie Pr, LMOPS, Université de Lorraine, Metz, France	Directeur de thèse
Zhixue Zheng Ass-Pr, LMOPS, Université de Lorraine, IUT Yutz-Thionville, France	Co-directrice de thèse

Acknowledgement

The three years of my Ph.D. journey have flown by quickly, leaving me with countless deep memories. In this place, there are many people and experiences for which I am profoundly grateful.

First of all, I want to express my sincerest gratitude to my two supervisors, Michel AILLERIE and Zhixue ZHENG. Over the past three years, you have been not only my supervisors but also my friends. As supervisors, you provided invaluable assistance with my research, and as friends, you helped me quickly integrate into lab life. Without you, I would not have been able to successfully complete my doctoral research. It has been a great pleasure and an enjoyable experience to work with them.

I still remember three and a half years ago when I received the news that I was going to France to pursue my Ph.D. I had both anticipation and anxiety about the lab where I would spend several years. As an introverted person, I was somewhat resistant to entering an unfamiliar environment. While rushing to the place I would stay after getting off the plane, I watched the Eiffel Tower grow larger and then slowly shrink, and it hit me that I was truly far from home. The courage I had mustered before boarding the plane dissipated in an instant, replaced by unease about whether I could adapt. By the time I reached the residence, it was already eleven o'clock at night. The moment I got out of the car, all my fears began to awaken, dispersing into every corner of the night. I was at a loss. Suddenly, I heard a voice calling me, which brought me back to reality. Two people appeared, their genuine smiles like bright lights in the night, dispelling my fear of the unfamiliar. That night was the first time I met my supervisor, Michel, and my colleague, Sadaqat. At the same time, I also received a message from my co-supervisor, Zhixue, asking if I had arrived safely and informing me that she would come from another city to meet me in the next morning. In that moment, I glimpsed what my three years in this lab would be like – how fortunate I am to join such a team!!!

Our platform started from scratch, and during this period we encountered many problems. Zhixue gave me enough patience and help me a lot. I remembered that for a long time, she stayed by my side almost every day, debugging the platform together. It was precisely because of her constant encouragement that I was able to overcome each obstacle. If Michel is like a heater in my PhD life, supporting energy and warming me in

the lab, then Zhixue is a guiding light, illuminating my path in academic research. Of course, this metaphor is somewhat simplistic. Both of them are indispensable directors in my PhD life and academic career.

Besides, special thanks to Prof. Marie-Cécile Péra and Prof. Daniel Hissel. They helped me a lot during the project implementation and provided useful suggestions for the research. Prof. Alexandre De Bernardinis and Dr. Jean-Paul Swaicki provided me a lot of suggestions about converter, which is an essential part of my thesis. Thank you for their contributions.

I also met many interesting people, made many new friends, and got to know my old friends more deeply. Yue Chai is my first Chinese friend in France. We've been through a lot together. Over three years of interaction, we've become friends who trust each other deeply. Sadaqat Ali and Christelle Habis are my colleagues and friends in the lab. We have a chat group named "Hard Workers," but our relationship feels more like family. How fortunate I am to have been part of many significant moments in their lives. Sandhya and Dani helped me a lot and exposed me to many interesting things at IUT (being stung by a bee truly hurts, but their concern is genuinely heartwarming...). We come from different countries, but we've become very good friends.

Another two important people are Qihao Guo and Zejie Li. We've been friends since university. We are fortunate to be working on our PhDs during the same period, and we discuss the present and the future, growing together. I am very grateful for their help, and I am lucky to have met them and become friends.

Furthermore, thanks should go to other friends and colleagues in LMOPS, especially Luis Antonio Garcia Gutierrez, Bachirou Bongon and D'heib Vall Kheir. We have spent a long time together. This journey was interesting because of you.

Thanks to the financial support of ANR-19-CE05-0008-01 and the Chinese Scholarship Council (CSC).

Last but not least, I should express my gratitude to my family, especially my parents. Their support and love make me courageous.

With these final words, I bring my PhD life to a close. However, learning and exploration never stop, a new chapter in life is about to begin. Stay tuned...

Abstract

To meet the world's growing energy needs and with a view to sustainable development, the use of solar energy is leading a significant increase in the installation of photovoltaic (PV) panels, enabling the production of clean and renewable electricity. However, the PV panels are susceptible to faults due to the environmental treats, human factors or prolonged operating periods. These faults can result in power losses, low efficiency, system instability, and in some cases, pose a risk of security, such as fire hazards. Health monitoring can mitigate these issues and improve the overall operating reliability and efficiency of PV panels.

Among existing health monitoring tools for PV panels, impedance spectroscopy (IS) provides a powerful, non-destructive way to acquire PV panels' internal impedance over a wide frequency range. Compared with specific workstation-based IS, converter-based IS performed as an added function of the connected power converter, provides an attractive mean to achieve online measurements. It can help reduce overall system costs and facilitate online applications, as no additional equipment is required. However, the control strategy of the power converter needs to be specifically designed. Firstly, since the injection of the perturbation signal is achieved by controlling the switching signals, the bandwidth of the converter will limit the maximum frequency of the perturbation signal. Obtaining a complete IS spectrum (with a maximum frequency up to 100 kHz) with sufficient accuracy can thus be challenging. Secondly, to ensure a quasi-maximum output power of PV panels even during IS implementation, a cooperative control scheme between maximum power point tracking (MPPT) and IS modes should be considered.

The major objectives of this research are twofold: (1) to propose a systematic design guideline for control strategies of converter-based IS implementation; (2) to establish an appropriate AC equivalent circuit model (AC-ECM) for PV panels and extract valuable health indicators for online health monitoring of PV panels.

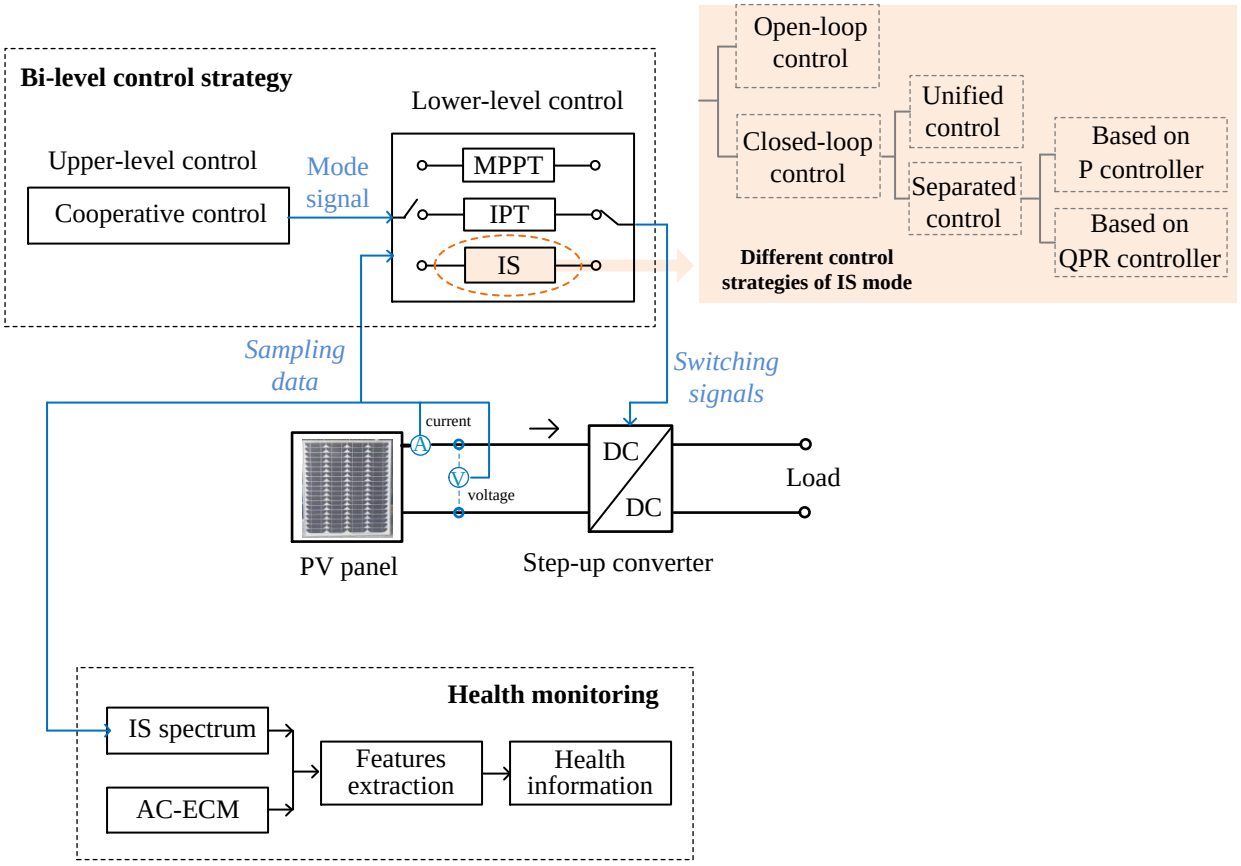
In one aspect, a bi-level control strategy of the power converter including an upper-level and a lower-level control is proposed, as shown in the graphical abstract below. The upper-level control achieves the cooperative control of different operating modes, including MPPT, injection point tracking (IPT) and IS modes. The lower-level control includes the separate control of each mode. Particularly, for the IS mode, both open-loop control

and closed-loop control have been systematically studied and compared. Under open-loop control, an analysis of the intrinsic resonance of the converter and the frequency limitation of the perturbation signal is performed. Furthermore, an adaptive configuration method for the amplitude of the AC duty cycle is proposed to eliminate the influence of the resonance and enhance the validity and the accuracy of IS measurement. Under closed-loop control, based on three commonly used compensation controllers in linear system control, two control methods, named unified control and separated control, are designed and compared. In the unified control, a single proportional-integral (PI) controller controls the DC and AC components together to meet the control objectives. Meanwhile, in the separated control, a segmented lower pass filter (LPF) with a variable cut-off frequency is designed to effectively separate the DC component of the PV panel current from the AC perturbation signal. A proportional (P) and a quasi-proportional resonant (QPR) are further applied separately to control the AC component.

In the other aspect, based on the acquired IS measurements, a simplified AC-ECM of the PV panel is proposed by considering both the internal relaxation processes of the PV panel and the frequency limitation of the converter. This AC-ECM offers a fitting approach for the incomplete spectrum obtained through converter-based IS. Additionally, four health features are extracted and defined for monitoring the health states of the PV panel under various operating conditions. Finally, an experimental platform which consists of a PV panel, a SiC module based DC/DC converter, an output load, a real-time control system (dSPACE SCALEXIO box), and a corresponding high-precision sampling circuit has been developed for online IS implementation in the laboratory from A to Z. An experimental study has been conducted to verify that under the proposed control strategies, reliable and accurate IS measurements can be achieved. Under various operating conditions, the effectiveness of the online IS monitoring method based on the extracted features of the PV panel is verified as well.

Key words: Photovoltaic (PV) panels; AC equivalent circuit model (AC-ECM); Control strategies; Converter-based impedance spectroscopy (IS); Health monitoring.

Graphical abstract



Résumé

Pour répondre aux besoins énergétiques croissants à travers le monde et dans un objectif de développement durable, l'utilisation de l'énergie solaire entraine une augmentation significative de l'installation de panneaux photovoltaïques (PV) permettant une production d'électricité propre et renouvelable. Cependant, les panneaux PV sont susceptibles de présenter des défauts dus aux menaces environnementales, aux facteurs humains ou à des périodes de fonctionnement prolongées. Ces défauts peuvent entraîner des pertes de puissance, une faible efficacité, une instabilité du système et, dans certains cas, présenter un risque de sécurité, comme des risques d'incendie. La surveillance de l'état de santé peut atténuer ces problèmes et améliorer la fiabilité globale et l'efficacité de fonctionnement des panneaux PV.

Parmi les outils de surveillance de l'état de santé existants pour les panneaux PV, la spectroscopie d'impédance (IS) offre un moyen puissant et non destructif d'acquérir l'impédance interne des panneaux PV sur une large plage de fréquences. Comparé à l'IS basée sur des postes de travail spécifiques, l'IS basée sur le convertisseur, réalisée en tant que fonction supplémentaire du convertisseur de puissance connecté, constitue un moyen attractif d'obtenir des mesures en ligne. Cela peut aider à réduire les coûts globaux du système et à faciliter les applications en ligne, car aucun équipement supplémentaire n'est nécessaire. Cependant, la stratégie de contrôle du convertisseur doit être spécifiquement conçue. Tout d'abord, étant donné que l'injection du signal de perturbation est réalisée en contrôlant les signaux de commutation, la largeur de bande du convertisseur limitera la fréquence maximale du signal de perturbation. Obtenir un spectre IS complet (avec une fréquence maximale allant jusqu'à 100 kHz) avec une précision suffisante peut donc être un défi. Deuxièmement, pour garantir une puissance de sortie quasi maximale des panneaux PV même pendant la mise en œuvre de l'IS, un schéma de contrôle coopératif entre le suivi du point de puissance maximale (MPPT) et le mode IS doit être envisagé.

Les principaux objectifs de cette recherche sont doubles : (1) proposer un guide de conception systématique pour les stratégies de contrôle de la mise en œuvre de l'IS basée sur le convertisseur ; (2) établir un modèle de circuit équivalent en courant alternatif (AC-ECM) approprié pour les panneaux PV et extraire des indicateurs

de l'état de santé pour la surveillance en ligne des panneaux PV.

Dans un aspect, une stratégie de contrôle à deux niveaux du convertisseur de puissance comprenant un contrôle de niveau supérieur et un contrôle de niveau inférieur est proposée, comme illustré dans le résumé graphique ci-dessous. Le contrôle de niveau supérieur réalise le contrôle coopératif des différents modes de fonctionnement, notamment les modes MPPT, de suivi du point d'injection (IPT) et IS. Le contrôle de niveau inférieur comprend le contrôle séparé de chaque mode. En particulier, pour le mode IS, les contrôles en boucle ouverte et en boucle fermée ont été étudiés et comparés systématiquement. Sous le contrôle en boucle ouverte, une analyse de la résonance intrinsèque du convertisseur et de la limitation de fréquence du signal de perturbation est effectuée. De plus, une méthode de configuration adaptative pour l'amplitude du rapport cyclique en courant alternatif est proposée pour éliminer l'influence de la résonance et améliorer la validité et la précision de la mesure IS. Sous le contrôle en boucle fermée, basé sur trois contrôleurs de compensation couramment utilisés en contrôle linéaire de systèmes, deux méthodes de contrôle, appelées contrôle unifié et contrôle séparé, sont conçues et comparées. Dans le contrôle unifié, un seul contrôleur proportionnel-intégral (PI) régule les composantes CC et CA ensemble pour atteindre les objectifs de contrôle. Dans le contrôle séparé, un filtre passe-bas segmenté (LPF) avec une fréquence de coupure variable est conçu pour séparer efficacement la composante CC du courant PV des signaux de perturbation CA. Un contrôleur proportionnel (P) et un contrôleur quasi-proportionnel résonant (QPR) sont ensuite appliqués séparément pour contrôler la composante CA.

Dans l'autre aspect, basée sur les mesures IS acquises, un AC-ECM simplifié du panneau PV est proposé en tenant compte à la fois des processus de relaxation internes du panneau PV et de la limitation de fréquence du convertisseur. Cet AC-ECM offre une approche d'ajustement pour le spectre incomplet obtenu par le biais de l'IS basée sur le convertisseur. De plus, quatre caractéristiques de l'état de santé sont extraites et définies pour surveiller les états de santé du panneau PV dans diverses conditions de fonctionnement. Enfin, une plateforme expérimentale composée d'un panneau PV, d'un convertisseur CC/CC basé sur un module SiC, une charge, d'un système de contrôle en temps réel (boîtier dSPACE SCALEXIO), et d'un circuit d'échantillonnage de haute précision correspondant a été développée pour la mise en œuvre en ligne de l'IS en laboratoire de A à Z. Une étude expérimentale a été menée pour vérifier que sous les stratégies de contrôle proposées, des mesures IS fiables et précises peuvent être obtenues. Dans diverses conditions de fonctionnement, l'efficacité de la méthode de surveillance IS en ligne basée sur les caractéristiques extraites du panneau PV est également vérifiée.

Mots clés : Panneaux photovoltaïques (PV) ; Modèle de circuit équivalent en courant alternatif (AC-ECM) ; Stratégies de contrôle ; Spectroscopie d'impédance (IS) basée sur le convertisseur ; Surveillance de l'état de santé.

Contents

Acknowledgement **i**

Abstract **iii**

Résumé **vii**

List of figures **xx**

List of tables **xxi**

List of abbreviations **xxi**

List of publications **xxvii**

Introduction générale **1**

Défi de ce sujet 2

Contenu principal de cette thèse 4

Apports majeurs de cette thèse 10

Perspectives Français 11

1 Health monitoring of PV panels: state-of-the-art **13**

1.1 General introduction of PV panels . . . 14
1.1.1 Background . . . 14
1.1.2 Fundamentals of PV panels . . . 15
1.2 Fault characterization tools for PV panels . . . 20
1.2.1 Typical faults in PV panels . . . 20
1.2.2 Characterization tools for PV panels . . . 25
1.3 Implementation ways of impedance spectroscopy . . . 30
1.3.1 IS fundamentals . . . 30
1.3.2 Workstation-based IS . . . 31
1.3.3 Converter-based IS . . . 32
1.3.4 Challenges . . . 33
1.4 Objectives of this work . . . 35
1.5 Conclusions . . . 37

2 Fundamentals of converter-based IS for PV panels 39

2.1 Introduction . . . 39
2.2 Fundamentals . . . 40
2.2.1 Operating regions of the PV panel . . . 40
2.2.2 Three operating modes of the PV panel . . . 42
2.2.3 Analysis of IS measurements . . . 43
2.3 Cooperative control strategy . . . 45
2.3.1 Control blocks . . . 45
2.3.2 Simulation platform . . . 46
2.3.3 Simulation results . . . 48

2.4 Conclusions 50

3 Equivalent circuit models of silicon PV panels 53

3.1 Introduction 53

3.2 Physical model 59

3.3 DC equivalent circuit model 61

3.4 AC equivalent circuit model 63

3.4.1 AC equivalent circuit model of silicon PV cells 63

3.4.2 AC equivalent circuit model of silicon PV panels 67

3.5 Conclusions 70

4 Open-loop control strategy for converter-based IS 71

4.1 Introduction 71

4.2 System description 72

4.2.1 Topology description 72

4.2.2 Average state-space model 73

4.3 Influence of various parameters 77

4.3.1 Parameter selection 77

4.3.2 Resonant information and frequency limitation 80

4.3.3 Simulation verification 85

4.4 Advanced open-loop control strategy 92

4.4.1 Control strategy 92

4.4.2 Experimental verification 94

4.5 Discussions 97

4.6 Conclusions . . . 97

5 Closed-loop control strategies for converter-based IS 99

5.1 Introduction . . . 99

5.2 Control objectives of closed-loop control strategies . . . 101

5.2.1 Control objectives . . . 101

5.2.2 Characteristics of the three controllers . . . 102

5.3 Unified control strategy . . . 104

5.4 Separated control strategy . . . 107

5.4.1 LPF design . . . 107

5.4.2 PI controller design for DC component control . . . 108

5.4.3 P and QPR controller design for AC component control . . . 110

5.5 Experimental verification of closed-loop control . . . 113

5.6 Discussions . . . 116

5.7 Conclusions . . . 117

6 Health monitoring by converter-based IS 119

6.1 Introduction . . . 119

6.1.1 Description of the experimental platform . . . 119

6.1.2 Control of irradiance and temperature . . . 121

6.2 Cooperative control of MPPT and IS modes . . . 122

6.3 Health monitoring . . . 123

6.3.1 Data processing . . . 124

6.3.2 Different injection points . . . 126

6.3.3 Different temperatures 128
6.3.4 Different irradiance levels 131
6.3.5 Partial shading 134
6.4 Conclusions 137

Conclusions and Perspectives **139**

List of Figures

1 Génération d'énergie de différentes sources: (a) 2020; (b) 2030 (adapté de [1]). 1

2 Courbes IV sous différents pourcentages d'ombrage partiel. 2

3 Contenu principal de cette thèse. 4

4 Plateforme de simulation. 6

5 Résultats de simulation sous la stratégie de contrôle coopératif. 7

6 AC-ECM des panneaux PV. 7

7 Forme d'onde expérimentale de tension et de courant sous contrôle en boucle ouverte : amplitude constante du signal de perturbation dans la condition O-II. 8

8 Stratégies de contrôle en boucle fermée pour le mode IS. 9

9 Spectres IS dans les tracés de Nyquist à différents points d'injection. 10

10 Quatre caractéristiques en condition de fonctionnement O-III. 10

1.1 Power generation of different sources (adapted from [1]) (a) Gross electricity generation of 2020; (b)Gross electricity generation of 2050. 14

1.2 Topology of grid-connected PV panels. 15

1.3 Topology of a simplified DC microgrid with PV panels. 16

1.4 Classification of PV cell technologies (adapted from [2]). 17

1.5 Typical structure of monofacial silicon PV panel [3]. 18

1.6 DC equivalent circuit models (a) Single-diode DC-ECM; (b) Two-diode DC-ECM. 18

1.7 IV and PV curves under different irradiance levels and temperatures. 19
1.8 Flowchart of P&O MPPT method [4]. 20
1.9 IV curves under different partial shading percentages. 28
1.10 AC signal injection in different regions: (a) (quasi-)linear region (b) nonlinear region. 31
1.11 Workstation-based IS [5]. 32
1.12 Converter-based IS with an extra excitation circuit. 33
1.13 Converter-based IS based on the existing converter. 34
2.1 Three operating regions of the PV panel. 41
2.2 Operating point in different modes (a) MPPT mode; (b) IPT mode; (c) IS mode. 43
2.3 Perturbation and response signals at frequency f_p (a) two signals in time domain; (b) phase vectors in complex plane, adapted form [6]. 44
2.4 Analyzing method of the IS information (a) IS spectrum; (b) Corresponding AC-ECM. 45
2.5 Control scheme of a PV panel with different operating modes. 45
2.6 Control flow of the cooperative control. 46
2.7 Simulation platform. 47
2.8 Output characteristics of the PV panel (a) IV curve; (b) PV curve. 49
2.9 FFT analysis results of response signal at 1 Hz. 49
2.10 Simulation results under cooperative control strategy. 50
3.1 Basic electrical elements. 54
3.2 Single-time-constant-based AC-ECM (adapted from [7]). 55
3.3 Double-time-constant-based AC-ECM (adapted from [8, 9]). 57
3.4 Three-time-constant-based AC-ECM (adapted from [8, 9]). 58
3.5 Schematic diagram of a PV cell structure. 59

3.6 Relaxation processes in silicon PV cells (adapted from [10]). 60

3.7 Two-diode DC-ECM of PV cells/panels. 61

3.8 Currents of two diodes of DC-ECM. 63

3.9 AC-ECM of PV cells (adapted from [11]). 64

3.10 IS spectrum of PV cells under different V_{PV}: Nyquist plots. 66

3.11 Equivalent structure of a PV panel with bypass diodes. 67

3.12 AC-ECM of PV panels. 68

4.1 Topology of the conventional boost converter. 72

4.2 State circuits of the boost converter: (a) when the switch T is on, (b) when the switch T is off. 73

4.3 Magnitude plot of $G_{i_{PV}-d}(s)$ with and without parasitic parameters. 77

4.4 Asymptotic diagram of gain of $G_{i_{PV}-i_L}(s)$ and $G_{i_{L}-d}(s)$ (a) magnitude of $G_{i_{PV}-i_L}(s)$; (b) magnitude of $G_{i_{L}-d}(s)$. 81

4.5 Magnitude plots of $G_{i_{PV}-d}(s)$ under constant R_L. 86

4.6 Magnitude plots of $G_{i_{PV}-d}(s)$ under constant D. 86

4.7 Magnitude plots of $G_{i_{PV}-d}(s)$ under constant I_{PV}. 87

4.8 Magnitude plots of $G_{i_{PV}-d}(s)$ under different L. 88

4.9 Simulation results of $|G_{i_{PV}-d}(s)|$ under different C_1. 89

4.10 Magnitude plots of $G_{i_{PV}-d}(s)$ under different C_{dc}. 89

4.11 Magnitude plots of $G_{i_{PV}-d}(s)$ under different r_{PV}. 90

4.12 Magnitude plots of $G_{i_{PV}-d}(s)$ under different r_L. 90

4.13 Magnitude plots of $G_{i_{PV}-d}(s)$ under different r_{dc}. 91

4.14 Magnitude plots of $G_{i_{PV}-d}(s)$ under different r_{C1}. 91

4.15 Comparison of the traditional and advanced open-loop strategies: (a) amplitude of the AC duty cycle; (b) amplitude of the perturbation current signal. 93

4.16 Voltage and current experimental waveform under open-loop control: constant amplitude of the perturbation signal under condition O-II. 95

4.17 Voltage and current experimental waveform under open-loop control: adapted amplitude of the perturbation signal under condition O-II. 95

4.18 DC components of I_{PV} under open-loop control strategy under condition O-II. 95

4.19 Amplitude of perturbation signal under open-loop control strategy under condition O-II. . . . 96

4.20 IS spectrum under different control methods under condition O-II. 97

5.1 Closed-loop current control without compensation. 101

5.2 Magnitude plot of the closed-loop transfer function without compensation. 101

5.3 Asymptotic Bode plots of the three controllers (upper: magnitude plots; lower: phase plots): (a) P controller; (b) PI controller; (c) QPR controller. 103

5.4 Control block of the unified control strategy. 104

5.5 Magnitude of system under the unified control strategy. 106

5.6 Control block of the separated control strategy. 107

5.7 Asymptotic magnitude plot of the LPF (example of $\omega_{p-l} = 2\pi \cdot 10$ rad/s, $\omega_{p-h} = 2\pi \cdot 90$ rad/s). 108

5.8 Control block of the separated control strategy – DC component control. 109

5.9 Asymptotic magnitude plot of DC component control with a PI controller. 109

5.10 Magnitude plot of the system under the separated control strategy – DC component. 110

5.11 Control block of the separated control strategy – AC component control. 110

5.12 Asymptotic magnitude plot of a QPR controller based compensation part of AC component control. 112

5.13 Magnitude plots of the system under the separated control strategy – AC component: (a) based on the P controller; (b) based on the QPR controller. 113

5.14 Experimental waveforms under different controllers during IS implementation. 115

5.15 Impedance information under different controllers: (a) Bode plots (b) Nyquist plots. 115

5.16 IS spectra under different control strategies: open-loop and closed-loop control. 116

6.1 Experimental platform for online IS implementation. 120

6.2 Schematic diagram of the illumination supply for the PV panel in our laboratory. 121

6.3 Experimental waveforms of IV (red) and PV curves (blue) under operating condition O-I. . . . 122

6.4 Experimental waveforms of the cooperative control among MPPT, IPT and IS modes under operating condition O-I: (a) output voltage and current (b) output power. 123

6.5 IS spectrum under operating condition O-III: Bode plot. 124

6.6 IS spectrum under operating condition O-III: Nyquist plot. 125

6.7 Kramers-Kronig (K-K) test result. 126

6.8 IV curve under operating condition O-III. 127

6.9 Equivalent parameters under operating condition O-III. 127

6.10 IS spectra in Nyquist plots under operating condition O-III. 127

6.11 Four features under operating condition O-III: (a) Feature 1; (b) Feature 2; (c) Feature 3: (d) Feature 4. 128

6.12 IV curves under operating condition O-IV. 129

6.13 Equivalent parameters under operating condition O-IV. 130

6.14 IS spectra in Nyquist plots under operating condition O-IV. 130

6.15 V_{PV} under operating condition O-IV. 130

6.16 Four features under operating condition O-IV: (a) Feature 1; (b) Feature 2; (c) Feature 3: (d) Feature 4. 131

6.17 IV curves under operating condition O-V. 132

6.18 Equivalent parameters under operating condition O-V. 132

6.19 IS spectra in Nyquist plots under operating condition O-V. 133

6.20 Four features under operating condition O-V: (a) Feature 1; (b) Feature 2; (c) Feature 3: (d) Feature 4. 133

6.21 IV curves under operating condition O-VI. 134

6.22 Equivalent parameters under operating condition O-VI. 135

6.23 IS spectrum in Nyquist plots under operating condition O-VI. 135

6.24 FFT analysis of the perturbation and response signals under P_5: (a) output voltage at 1 Hz; (b) output voltage at 1 kHz. 136

6.25 IS spectrum in Nyquist plots in the nonlinear region. 136

6.26 Four features under operating condition O-VI: (a) Feature 1; (b) Feature 2; (c) Feature 3: (d) Feature 4. 137

List of Tables

1.1 Parameters of the simulated PV panel. 19

1.2 Characteristics of typical faults. 24

1.3 Typical characteristics of different imaging tools. 27

1.4 Comparisons of three typical online tools. 29

1.5 Summarization of IS implementation ways. 35

4.1 Parameter values of the system as fixed in the study 80

4.2 Summarization of the influence of parameters 84

5.1 Comparison of the two control strategies. 113

5.2 Tracking performance of the three controllers. 114

5.3 Comparison of open-loop and closed-loop control strategies. 117

6.1 Key parameters of the SiC power module. 120

6.2 Six irradiance levels set in the experiment. 121

List of abbreviations

(V_l, V_h)	Voltage range for short disturbance in MPPT (V)
α	Phase shift of CPE
Δd_l	Large-step disturbance in MPPT
Δd_s	Short-step disturbance in MPPT
ΔI_{PV-max}	Maximum changing range of output current
ΔV_{PV-max}	Maximum changing range of output voltage
$\phi(f_p)$	Phase shift between voltage and current signals
τ	Time constant
A	Proportionality factor of CPE
C_p	Parallel capacitor
C_1	Support capacitor
f_p	Frequency of perturbation signal
G	Irradiance level ($\mathrm{W/m^2}$)
I_d	Diode current of one-diode DC-ECM of PV panel (A)
I_{ac}	Amplitude of perturbation current signal
I_{d1}	Diode current (diffusion) of two-diode DC-ECM of PV panel (A)
I_{d2}	Diode current (recombination) of two-diode DC-ECM of PV panel (A)

I_{MPP}	Current at MPP of PV panel (A)
I_{ph}	Photocurrent of PV panel (A)
I_{PV-pre}	Output current of PV panel during the last perturbing period in MPPT (A)
I_{PV}	Output current of PV panel (A)
I_{s1}, I_{s2}	Reverse saturation currents of the diffusion and recombination processes (A)
I_{sc}	Short-circuit current of PV panel (A)
I_{sh}	Current flowing shunt resistor (A)
$Im(f_p)$	Imaginary part of $Z(f_p)$
k	Boltzmann constant ($k = 1.38 \times 10^{-23}\mathrm{J/K}$)
n_1, n_2	Ideality factors of the diffusion and recombination diodes, respectively
P_{PV-pre}	Output power of PV panel during the last perturbing period in MPPT (W)
Pl_0	Minimal power loss under detection threshold
Pl_E	Exponential-shaped degradation of power over time
Pl_H	Hybrid degradation over time
Pl_L	Linear-shaped degradation of power over time
Pl_S	Saturated degradation over time
q	Elementary charge of an electron ($q = 1.6 \times 10^{-19}\mathrm{C}$))
R_p	Parallel resistor
R_s	Series resistor
R_{series}	Series resistor (Ω)
R_{sh}	Shunt resistor (Ω)
$Re(f_p)$	Real part of $Z(f_p)$
S_1	Approximate safe fault

S_2	Medium danger fault
S_3	Danger fault
$S_{I_{d1}}$, $S_{I_{d2}}$	Slope of I_{d1}-V_{PV} and I_{d2}-V_{PV} curves
T	Temperature ($^{\circ}$C)
T_t	Temperature of the operating PV cells/panels in Kelvin (K)
V_t	Thermal voltage
V_{ac}	Amplitude of response voltage signal
V_{MPP}	Voltage at MPP of PV panel (V)
V_{oc}	Open-circuit voltage of PV panel (V)
V_{PV-pre}	Output voltage of PV panel during the last perturbing period in MPPT (V)
V_{PV}	Output voltage of PV panel (V)
$Z(f_p)$	Impedance at f_p
Z_C	Impedance of capacitor
Z_L	Impedance of inductor
Z_R	Impedance of resistor
Z_{CPE}	Impedance of CPE
CdTe	Cadmium telluride
CIGSe	Copper-indium-gallium-diselenide
CPE	Constant phase element
DLIT	Dark lock-in thermography
ECM	Equivalent circuit model
EL imaging	Electroluminescence imaging
ERV	Estimating randomness in the voltage signal

FRA	Frequency response analyzer
FSA	Frequency spectrum analysis
IPT	Injection point tracking
IR imaging	Infrared thermal imaging
IS	Impedance spectroscopy
LID	Light induced degradation
LIT	Lock-in thermography
MGs	Microgrids
MPP	Maximum power point of PV panel
MPPT	Maximum power point tracking
P&O method	Perturb and observe method
PID	Potential induced degradatio
PL imaging	Photoluminescence imaging
PLA	Power losses analysis
PV	Photovoltaic
QNR	Quasi-neutral region
SCR	Space-charge region
SSTDR	Spread spectrum time-domain reflectometry
UAVs	Unmanned aerial vehicles
UVFL imaging	Ultraviolet fluorescence imaging

List of publications

International journals

1. **Xin Wang**, Zhixue Zheng, Michel Aillerie, Jean-Paul Sawicki, Alexandre De Bernardinis, Marie-Cecile Péra, Daniel Hissel, "Control Strategies of Converter-Based Online Impedance Spectroscopy for Photovoltaic Panels", IEEE Transactions on Industry Applications, 2024 (Accepted).

2. **Xin Wang**, Zhixue Zheng, Michel Aillerie, Marie-Cecile Péra, Daniel Hissel, "Online Health Monitoring of Silicon PV Panels by Converter-Based Impedance Spectroscopy", IEEE Transactions on Industrial Electronics, 2024 (in submission).

3. **Xin Wang**, Zhixue Zheng, Michel Aillerie, Marie-Cecile Péra, Daniel Hissel, "Converter-based Online Impedance Spectroscopy Monitoring of Photovoltaic Panels Using an Open-loop Control Strategy", IEEE Transactions on Energy Conversion, 2024 (in submission).

International conferences

1. **Xin Wang**, Zhixue Zheng, Michel Aillerie, Alexandre De Bernardinis, Jean-Paul Sawicki, Marie-Cécile Péra, Daniel Hissel, "Cooperative Control of Online Spectroscopy Impedance Monitoring Method and Maximum Power Point Tracking Method for Photovoltaic Panels", IEEE EPE'22 ECCE Europe, 5th -8th September 2022, Hannover, Germany (Oral presentation).

2. **Xin Wang**, Zhixue Zheng, Michel Aillerie, Alexandre De Bernardinis, Marie-Cécile Péra, Daniel Hissel, "Online Impedance Spectroscopy Characterization of PV Panels by Studying Resonant Behavior of Boost Converter", IEEE ITEC 2023, 21st-23rd June 2023, Detroit, USA (Oral presentation).

National conferences

1. **Xin Wang**, Zhixue Zheng, Michel Aillerie, "Online health monitoring of photovoltaic panels by converter-based impedance spectroscopy", Journées nationales 2024 GT Micro-réseaux, 25st-26th April 2024, Ajaccio, France (Oral presentation).

2. **Xin Wang**, Zhixue Zheng, Michel Aillerie, "Development of health management strategies for improving the efficiency and durability of DC microgrid", Journées des doctorants (JDD), 1st-2nd June 2021-2023 (three times), Metz, France (Oral presentations).

Invited seminars

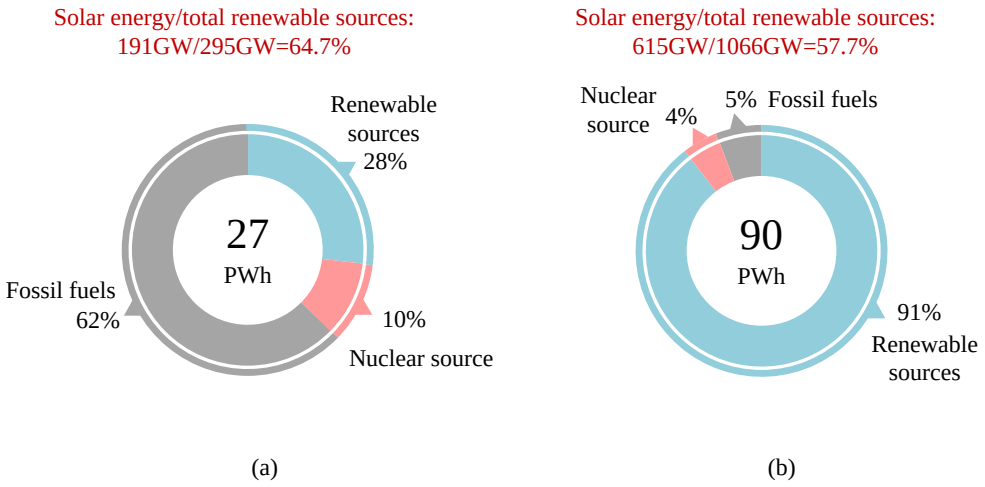
1. Chirstelle Habis, Carine Zaraket, Sadaqat Ali, **Xin Wang**, Javier Solena, Zhixue Zheng, Michel Aillerie, "Some current developments of electronics relative to renewable energies", invited lecture of University of West Attica (UWA), 4th March 2022, Egaleo, Greece ($\approx$ 50 participants, students (L3-M1) and colleagues of Departement Energy- Electronics of l'UWA).

2. **Xin Wang**, Zhixue Zheng, Michel Aillerie, "Fault diagnosis of photovoltaic panels installed in microgrid", invited seminar by the LMOPS research group photonics of CentraleSupélec, 13rd February 2023, Metz, France ($\approx$ 30 participants).

Introduction générale

Contexte et motivation

Les préoccupations environnementales et la réduction des réserves de combustibles fossiles ont donné lieu à une important modification du paysage énergétique mondial avec une forte augmentation de l'utilisation de sources renouvelables, du développement de réseaux distribués, comprenant des générateurs, des systèmes de stockage d'énergie et de nouveaux types de charges, tels que les véhicules électriques. L'énergie solaire, en tant que source d'énergie renouvelable importante, suscite un intérêt croissant depuis quelques années, tant dans le milieu universitaire que dans l'industrie, en raison de son caractère non polluant, de sa disponibilité sur toute la surface terrestre et des possibilités de conversion en électricite offertes grâce à l'effet photovoltaïque (PV) et aux progrès dans le rendement de conversion des nouveaux panneaux. Comme indiqué dans la Figure 1, la proportion d'énergie renouvelable, de 2020 à 2050, augmentera progressivement pour dépasser à termes 90%, dont l'énergie solaire représentera plus de 50%.



(a) (b)

Figure 1: Génération d'énergie de différentes sources: (a) 2020; (b) 2030 (adapté de [1]).

Ainsi, avec l'augmentation de la capacité installée des panneaux PV, la qualification de leur fiabilité et de leur efficacité de fonctionnement sont essentielles. La puissance de sortie d'un panneau PV est influencée par les conditions de fonctionnement, y compris la tension de sortie, les facteurs environnementaux et les facteurs de défaillance. Par exemple, la courbe IV d'un panneau PV sous un ombrage partiel, l'une des conditions de fonctionnement les plus fréquemment rencontrées dans la dégradation de l'efficacité d'un panneau, est illustrée dans la Figure 2, montrant que les défauts influencent significativement la puissance de sortie du panneau PV. De plus, les défauts PV peuvent entraîner des dangers pour la sécurité. Par conséquent, des stratégies de surveillance de l'état de santé sont nécessaires pour maintenir la fiabilité et la stabilité du panneau PV.

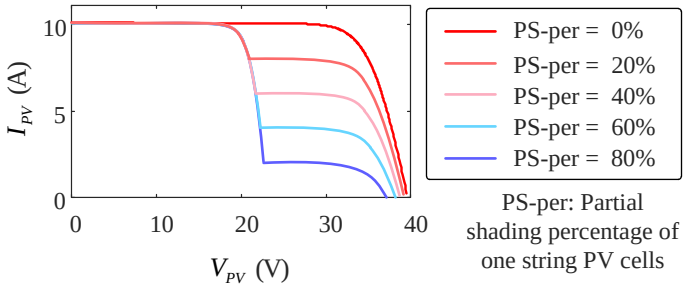


Figure 2: Courbes IV sous différents pourcentages d'ombrage partiel.

Il existe différents outils, on-line ou off-line, de surveillance de l'état de santé des panneaux PV. Parmi ceux là une relativement nouvelle technique, la spectroscopie d'impédance (IS) semble offrir un moyen puissant et non destructif d'acquérir l'impédance interne des panneaux PV sur une large plage de fréquences. En particulier, l'IS assurée par le convertisseur peut réaliser une injection en ligne du signal de perturbation grâce à une fonction ajoutée du convertisseur de puissance connecté. Cela peut aider à réduire les coûts globaux du système et faciliter les applications en ligne, car aucun équipement supplémentaire n'est requis. Cependant, cet outil est rarement mis en œuvre dans les panneaux PV du fait de la complexité d'optimiser la puissance fournie et le fonctionnement du panneau ainsi que la surveillance temps réel de ce même panneau. Pour combler cette lacune de recherche, cette thèse se concentre sur la stratégie de contrôle de l'IS appliquée aux panneaux PV, assurée par le convertisseur, et analyse et discute les données expérimentales mesurées.

Les principaux défis à relever de cette recherche

Lorsque l'IS est mise en œuvre sur des panneaux PV, plusieurs défis à résoudre se posent par manque d'information ou de systèmes existants concernant:

- **Les limitations existantes de l'IS assurée par le convertisseur utilisé dans un système PV**
  Selon la littérature, les conditions de validité de l'IS doivent respecter la linéarité, la causalité, la stabilité et la finitude. Néanmoins, le courant et la tension de sortie du panneau PV présentent des caractéristiques non linéaires. Par conséquent, une région quasi-linéaire doit être sélectionnée comme région d'injection du signal de perturbation. De plus, la bande passante et la résonance du convertisseur de puissance connecté auront un impact sur l'exactitude des résultats mesurés et limiteront la fréquence maximale du signal de perturbation. Par conséquent, une analyse systématique des orientations et des limitations de l'IS assurée par le convertisseur est nécessaire pour de futures recherches.

- **Le modèle de circuit équivalent AC approprié**
  Comme mentionné précédemment, la bande passante du convertisseur limitera la fréquence maximale du signal de perturbation. Obtenir un spectre IS complet (avec une fréquence maximale allant jusqu'à 100 kHz) avec une précision suffisante peut donc être difficile. De plus, les modèles de circuit équivalent AC existants (AC-ECMs) sont au niveau de la cellule. En réalité, pour réduire les impacts des points chauds et des ombrages partiels, des diodes de dérivation sont connectées aux cellules PV dans un seul panneau. Par conséquent, un AC-ECM prenant en compte l'effet de la diode de dérivation et capable de réagir aux changements des conditions de fonctionnement avec une fréquence étroite est nécessaire. En même temps, définir les caractéristiques de l'état de santé et analyser les informations correspondantes basées sur un spectre IS incomplet sont indispensables.

- **Les stratégies de contrôle**
  Pour mettre en œuvre l'IS assurée par le convertisseur, deux aspects doivent être pris en compte: (1) en général, le panneau PV fonctionne avec le suivi du point de puissance maximale (MPP), qui est situé dans une région non linéaire et n'est pas satisfait en tant que linéarité pour la validité de EST; (2) la plupart des défauts dans le panneau PV se produisent sur une courte période de temps, ce qui nécessite une plage de fréquences plus large du signal de perturbation, et la fréquence maximale du signal de perturbation doit être d'au moins 1 kHz. Ainsi, la stratégie de contrôle du convertisseur de puissance doit être spécifiquement conçue pour garantir que le contrôle coopératif entre le suivi du point de puissance maximale (MPPT) et le mode IS soit pris en compte, ainsi qu'une injection stable de signal de perturbation à large bande en mode IS.

Contenu principal de ce travail de thèse

Cette thèse réalise la surveillance de l'état de santé des panneaux PV basée sur la mesure de l'IS directement assurée par le convertisseur.

Les objectifs principaux de cette recherche seront doubles : (1) proposer un guide de conception systématique pour les stratégies de contrôle de la mise en œuvre de l'IS par convertisseur ; (2) établir un modèle de circuit équivalent AC (AC-ECM) approprié pour les panneaux PV et extraire des indicateurs de santé indispensables pour la surveillance en ligne de l'état de santé des panneaux PV. Dans un premier aspect, une stratégie de contrôle bi-niveau du convertisseur de puissance comprenant un contrôle de niveau supérieur et un contrôle de niveau inférieur est proposée. Cette stratégie est présentée dans la Figure 3 qui illustre également les différents travaux réalisés dans ce travail de thèse.

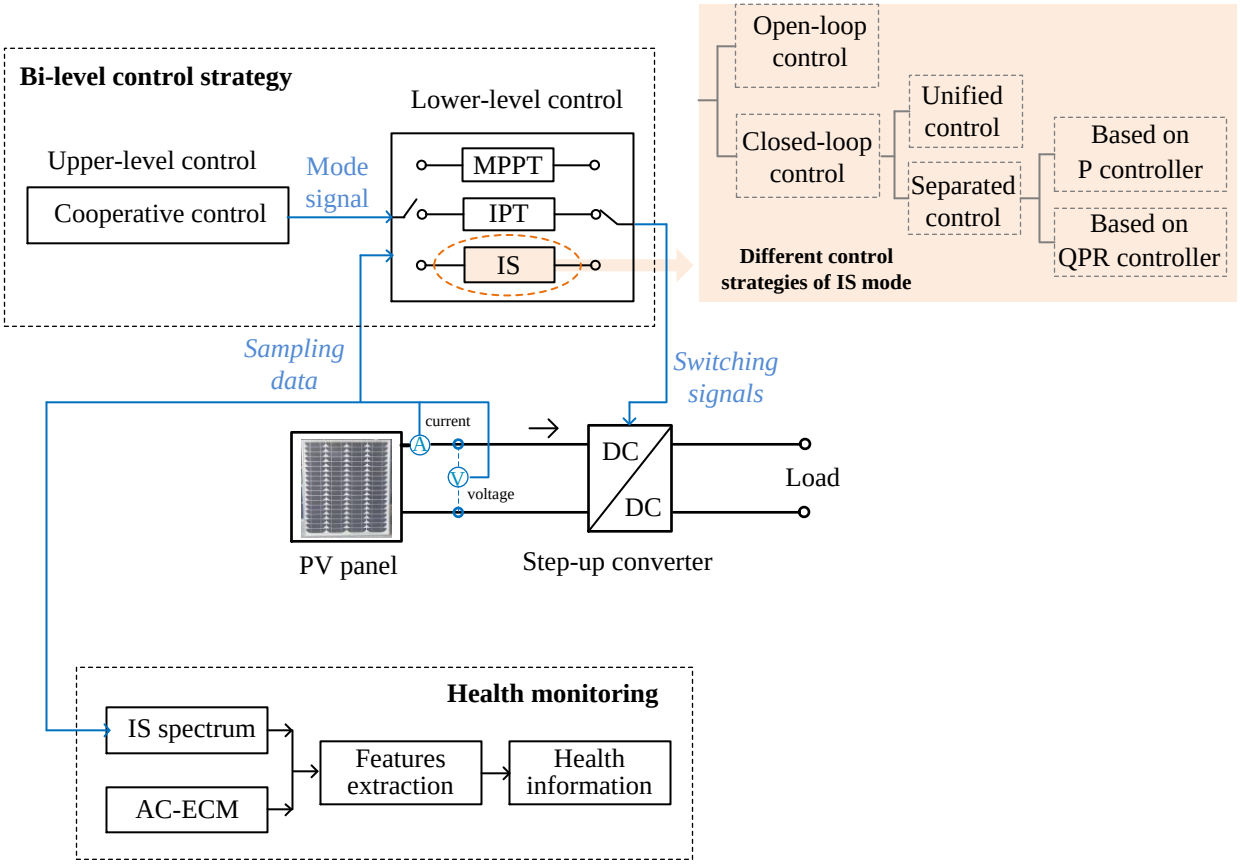


Figure 3: Contenu principal de cette thèse.

Le niveau inférieur permet le contrôle des trois principales phases de fonctionnement du panneau (MPPT, IPT, IS) qui seront décrite dans la suite de ce document et le niveau superieur assure un contrôle coopératif de

ces trois phases.

Dans le second aspect, basé sur les mesures de l'IS acquises expérimentalement sur un banc de caractérisation PV entièrement développé pendant cette thèse, un AC-ECM simplifié du panneau PV est proposé en tenant compte à la fois des processus de relaxation internes du panneau PV et de la limitation de fréquence du convertisseur. Pour être plus précis, cette thèse comprend les six chapitres principaux suivants:

- **Chapitrer I :** Dans ce chapitre, un état de l'art complet des panneaux PV est présenté. Les défauts typiques, y compris leurs causes, leurs impacts et leurs caractéristiques de défauts en termes d'échelle de temps, de niveau de sécurité et de perte de puissance, sont résumés. Les outils de caractérisation existants correspondants sont passés en revue et comparés entre eux. En particulier, comparativement aux outils hors ligne, les outils en ligne sont attrayants pour réduire les coûts et réaliser une surveillance de l'état de santé en temps réel.

- **Chapitre II :** Les fondamentaux de la mise en œuvre de l'IS sur les panneaux PV sont fournis Dans ce chapitre. Les principes de sélection du point d'injection sont expliqués et la stratégie de contrôle de niveau supérieur est alors proposée. Une plateforme de simulation est développée dans l'environnement MATLAB/Simulink, comme présenté dans la Figure 4.

  La stratégie de contrôle de niveau supérieur proposée est vérifiée pour permettre une transition stable entre le mode de suivi du point de puissance maximum, MPPT, le mode de suivi du point d'injection (IPT) et le mode lié à la spectroscopie d'impédance, IS. Cette stratégie est illustrée dans la Figure 5 présentant les résultats de simulation sous stratégie de contrôle coopératif (correspondant au niveau de contrôle supérieur) proposé.

- **Chapitre III:** En analysant le processus de relaxation des cellules PV et en tenant compte de la limitation de fréquence et de la structure du panneau PV, le modèle de circuit équivalent (ECM), en AC (AC-ECM) pour le niveau du panneau est développé dans ce chapitre sous une forme simplifiée. La Figure 6 présente l'AC-ECM.

  Ainsi, le modèle AC-ECM du panneau PV se compose de trois parties, comprenant une résistance en série et un sous-circuit constitué d'une résistance et d'un condensateur connectés en parallèle, comme indiqué dans la Figure 6 (b). La partie en série est combinée par la résistance équivalente du processus de transport, de l'influence de l'éclairage, de la diode de dérivation et de la connexion des lignes, comme illustré dans la Figure 6 (a). Le sous-circuit représente le processus de recombinaison du panneau PV. Sur la base de la simplification, le spectre IS incomplet peut être complété par la ligne en pointillés dans la Figure 6 (c). Enfin, quatre caractéristiques sont définies pour analyser l'état de santé du panneau PV,

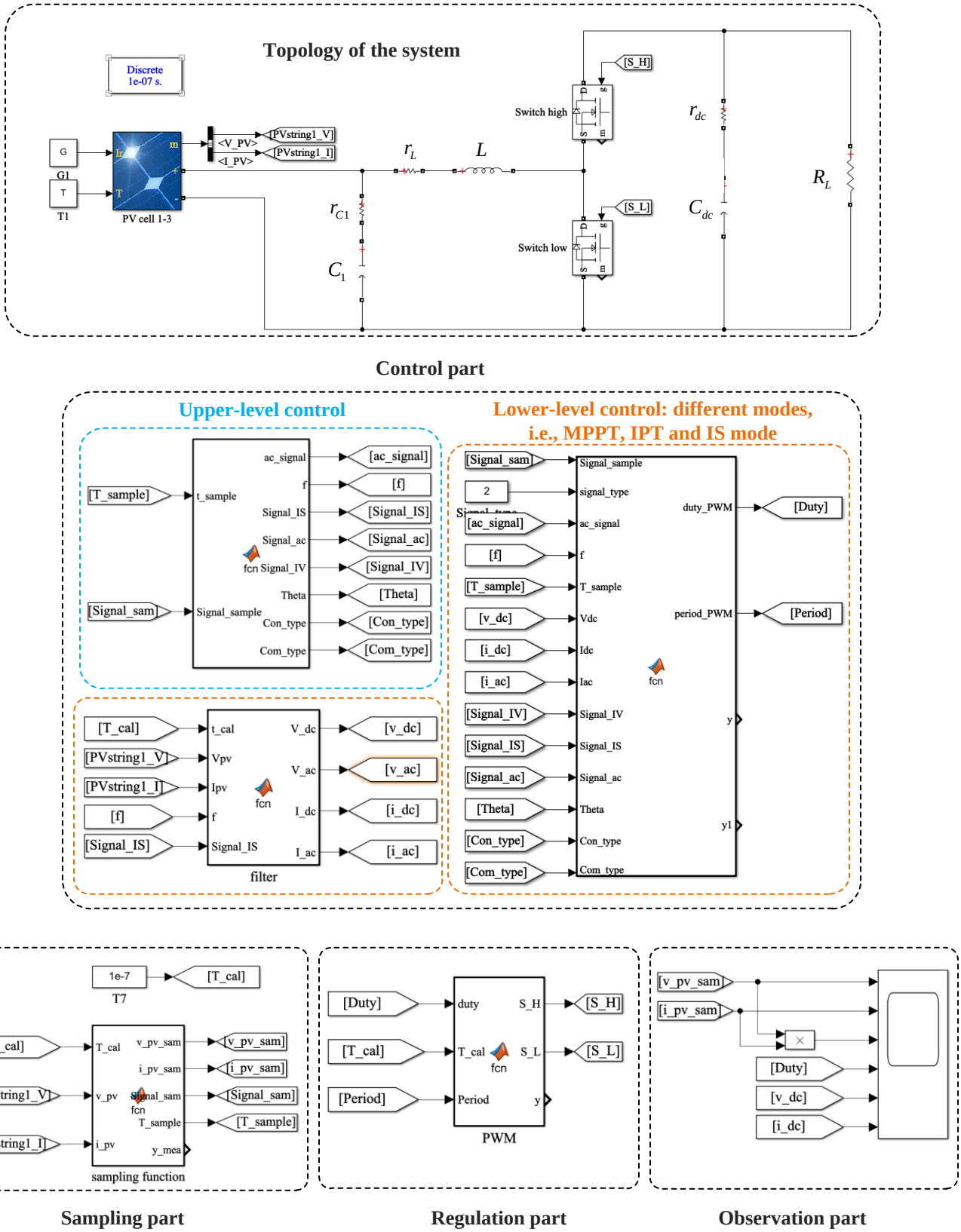


Figure 4: Plateforme de simulation.

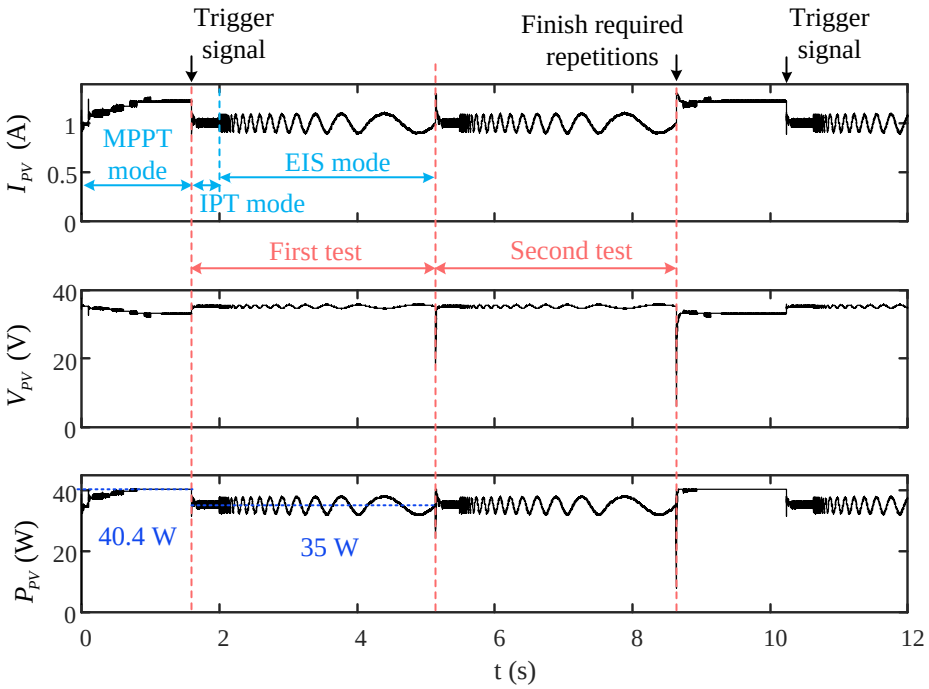


Figure 5: Résultats de simulation sous la stratégie de contrôle coopératif.

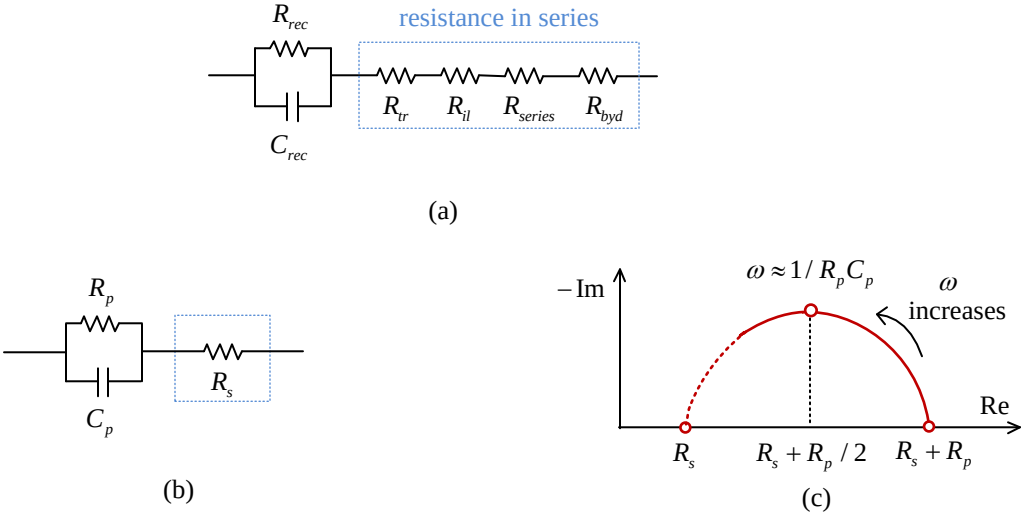


Figure 6: AC-ECM des panneaux PV.

comprenant la résistance totale, le logarithme naturel de la capacité et de la résistance, et la constante de temps de relaxation.

- **Chapitre IV :** Étant donné que lorsque l'interrupteur est éteint, l'inductance et le condensateur de bus DC se retrouvent connectés en série, le système présentera une fréquence de résonance lors de l'injection de signal de perturbation, ce qui entraînera un pic d'amplitude du signal de perturbation, comme le montre la Figure 7. De plus, l'amplitude diminuera avec l'augmentation de la fréquence. Ces deux facteurs affecteront la précision des résultats mesurés.

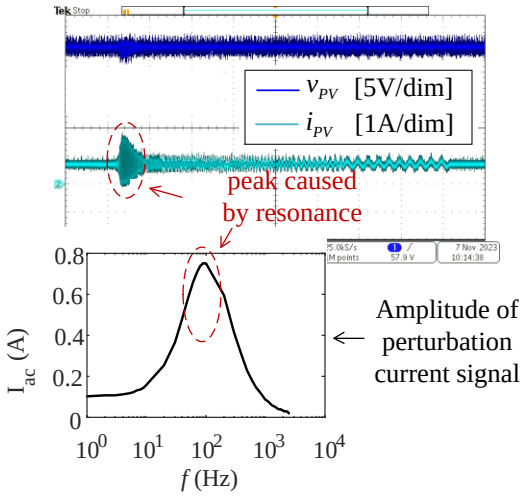
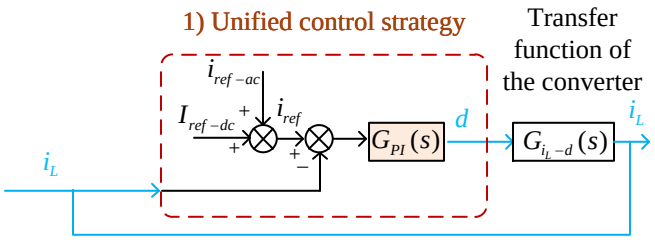


Figure 7: Forme d'onde expérimentale de tension et de courant sous contrôle en boucle ouverte : amplitude constante du signal de perturbation dans la condition O-II.

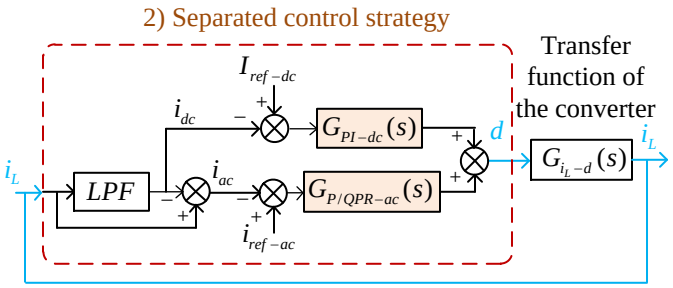
Les paramètres influençant la résonance et la limitation de fréquence du signal de perturbation sont analysés sur la base du modèle d'espace d'état moyen. De plus, une méthode de configuration adaptative pour l'amplitude du rapport cyclique AC est proposée pour éliminer l'influence de la résonance et améliorer la validité et la précision de la mesure de l'IS basée sur le contrôle en boucle ouverte.

- **Chapitre V :** En ce qui concerne les lacunes du contrôle en boucle ouverte, basé sur trois contrôleurs de compensation couramment utilisés dans le contrôle des systèmes linéaires, deux méthodes de contrôle, nommées contrôle unifié et contrôle séparé, sont conçues et comparées dans ce chapitre. Les blocs de contrôle sont représentés dans la Figure 8, où les lignes bleues représentent les signaux d'échantillonnage et de contrôle.

  Dans le contrôle unifié, un seul contrôleur proportionnel-intégral (PI) contrôle simultanément les composantes en courant continu et alternatif pour atteindre les objectifs de contrôle. Pendant ce temps, dans le contrôle séparé, un filtre passe-bas segmenté (LPF) avec une fréquence de coupure variable est conçu pour séparer efficacement la composante en courant continu du panneau PV du signal de perturbation



(a) Unified control strategy with a single PI controller



(b) Separated control strategy with a PI controller and a P/QPR controller

Figure 8: Stratégies de contrôle en boucle fermée pour le mode IS.

alternatif. Un contrôleur proportionnel (P) et un contrôleur résonant quasi-proportionnel (QPR) sont ensuite appliqués séparément pour contrôler la composante alternative. Les deux stratégies permettent d'atteindre un contrôle précis du point d'injection et du signal de perturbation.

- **Chapitre VI :** Au delà des aspects théoriques d'analyse et de modélisation, ce travail de thèse comprend une partie de développement expérimental importante permettant de valider les concepts et théories présentés dans les premiers chapitres de ce manuscrit. La plateforme expérimentale, son développement et les résultats expérimentaux obtenus et leurs analyses sont présentés dans ce chapitre VI. Pour vérifier les stratégies de contrôle susmentionnées, différentes conditions de fonctionnement sont configurées. Sur la base de la stratégie de contrôle bi-niveau proposée, comprenant le contrôle coopératif de niveau supérieur et la stratégie de contrôle unifié de niveau inférieur pour le mode IS, des expériences correspondantes sont menées pour vérifier l'efficacité de la surveillance de l'état de santé par l'IS basée sur le convertisseur. La Figure 9 indique le spectre IS à différents points d'injection dans la Région de tension quasi-linéaire de la caractéristique I-V. À mesure que la tension au point d'injection augmente, la courbe de Nyquist se déplace du coin supérieur droit vers le coin inférieur gauche. Quatre caractéristiques sont extraites sur la base du spectre IS ainsi obtenu. Les tendances de variation de ces caractéristiques peuvent refléter efficacement les variations des conditions de fonctionnement, comme illustré dans la Figure 10.

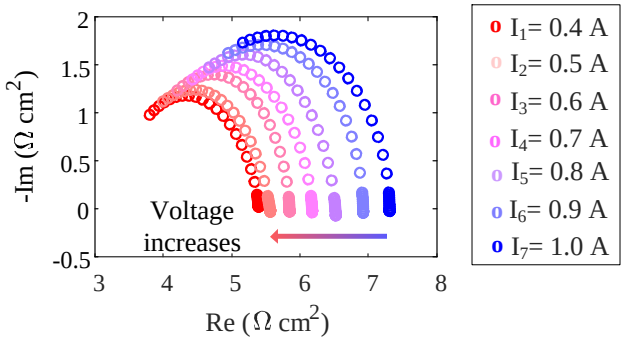


Figure 9: Spectres IS dans les tracés de Nyquist à différents points d'injection.

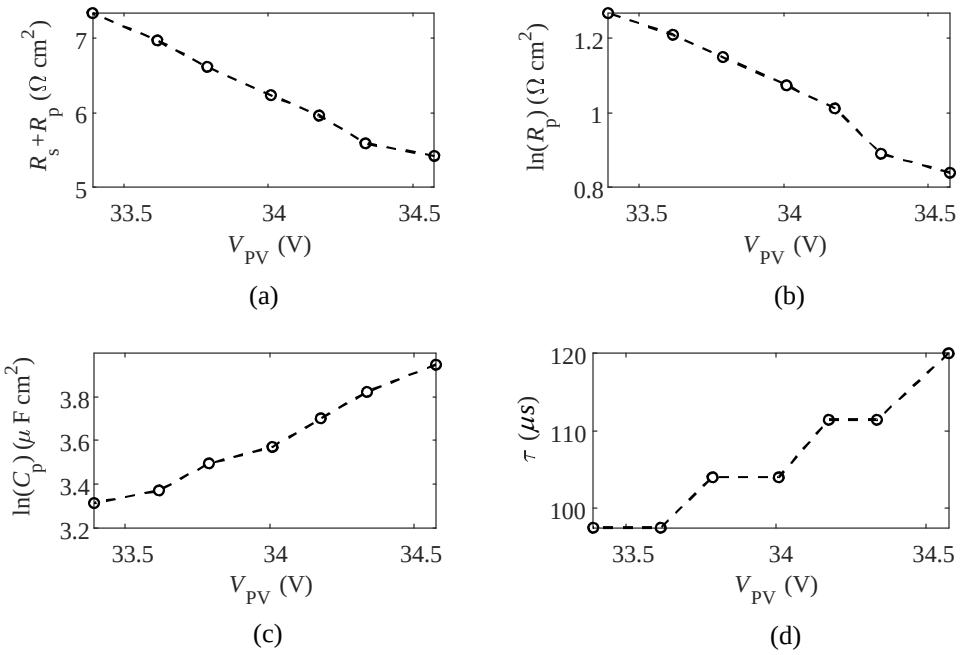


Figure 10: Quatre caractéristiques en condition de fonctionnement O-III.

Apports majeurs de cette thèse - Conclusions

Ce travail se concentre sur la mise en œuvre de la surveillance de l'état de santé basée sur des convertisseurs dans les panneaux PV. Un processus de recherche complet, depuis le développement du modèle de circuit équivalent AC, AC-ECM, la conception de la stratégie de contrôle, jusqu'à la simulation et la vérification expérimentale, est fourni. Les principales contributions de cette recherche sont doubles : (1) proposition d'un guide de conception systématique pour les stratégies de contrôle de la mise en œuvre de la surveillance de l'état de santé basée sur des convertisseurs ; (2) développement d'un AC-ECM approprié pour les panneaux PV et extraction de quatre indicateurs de santé précieux pour la surveillance en ligne de l'état de santé des

panneaux PV. Plus précisément, les contributions de cette thèse sont résumées dans les points suivants :

- Un modèle de circuit équivalent AC (AC-ECM) simplifié pour le panneau PV a été proposé et quatre caractéristiques sont définies pour décrire l'état de santé d'un panneau PV ;
- Les limitations et principes de la mesure IS basée sur le convertisseur sont analysés et résumés ;
- Une méthode de configuration adaptative de l'amplitude du rapport cyclique AC a été également proposée et validée expériementalement ;
- Deux stratégies de contrôle en boucle fermée basées sur trois contrôleurs de compensation couramment utilisés dans le contrôle de systèmes linéaires sont comparées et la conception des paramètres correspondants est présentée en détail ;
- Ce travail a été supporté par une validation expérimentale avec de nombreuses expériences qui ont vérifié la faisabilité, les performances mais également les limitations de l'IS assurée par le convertisseur dans la surveillance de l'état de santé des panneaux PV.

Perspectives

Comme nous l'avons vu, ce travail se concentre sur les fondements de la surveillance de l'état de santé des panneaux PV à l'aide de convertisseurs, notamment sur ses principes de fonctionnement, le modèle de contrôle alternatif simplifié des panneaux PV, les stratégies de contrôle et la définition des caractéristiques. De nombreuses voies de développement demeurent pour étudier toutes les caractéristiques spécifiques de cette technique appliquée aux énergies renouvelables et en particulier à la photovoltaïque, afin de conduire à des solutions industrielles et commerciales légèrement plus raffinées. Sur la base de ce travail actuel, quatre perspectives d'approfondissement sont dores et déjà envisagés :

- Surveillance de l'état de santé des panneaux PV défectueux :

  En termes de surveillance de l'état de santé, en dehors des conditions de fonctionnement et des ombrages partiels, les conditions défectueuses doivent être davantage prises en compte (voir le Chapitre 1). Les spectres IS dans des conditions de fonctionnement supplémentaires doivent être mesurés sur la base des méthodes proposées.

- Analyse des caractéristiques basée sur des algorithmes intelligents :

Les algorithmes intelligents, tels que l'apprentissage automatique, peuvent faciliter la détection des défauts en ligne et rendre les résultats de surveillance plus rapides et plus précis.

- Surveillance basée sur un convertisseur à rapport de tension élevé :

  Pour obtenir une tension de bus plus élevée, certains nouveaux convertisseurs DC/DC modulaires novateurs peuvent être appliqués dans les micro-réseaux (MGs). En général, leur fréquence de commutation équivalente est plus élevée que la fréquence de commutation du convertisseur boost conventionnel. Par conséquent, les limites du signal de perturbation seront différentes et un spectre IS avec une plage de fréquences plus large peut être obtenu.

- Influence du signal de perturbation sur la stabilisation de la tension du bus DC : L'injection de signaux de perturbation entraîne une certaine fluctuation de la tension du bus DC après le convertisseur de puissance. Sur la base de MATLAB/Simulink, il est observé que la fluctuation de tension du bus DC induite par le signal de perturbation dans la plage de fréquences sélectionnée dans notre travail peut être maintenue dans les spécifications techniques, c'est-à-dire $\leq 5\%$, par la mise en œuvre d'une stratégie de gestion de l'énergie (EMS) développée par S. Ali dans le même projet (ANR JCJC EREMITE-WP4). Sous le contrôle de l'EMS, la plupart des composantes à basse fréquence peuvent être absorbées par les autres systèmes de stockage d'énergie installés dans les MGs, tels que les batteries, les supercondensateurs, etc. L'analyse détaillée de l'influence de la perturbation sur la stabilité de la tension du bus DC est essentielle et sera analysée dans les travaux suivants.

- Interconnexion entre les résultats de la surveillance de l'état de santé et l'EMS des MGs : En plus de son application dans les panneaux PV, le système de surveillance de l'état de santé basé sur le convertisseur proposé peut également être mis en œuvre dans d'autres éléments des MGs, tels que les batteries et les supercondensateurs, pour effectuer une détection des défauts en temps réel de l'ensemble du système. Ce travail pourra être combiné avec les autres "work-packages" du projet ANR JCJC EREMITE.

Chapter 1

Health monitoring of PV panels: state-of-the-art

Concerns about the environmental impact of global warming due to fossil fuel have sparked immense interest in renewable and sustainable energy sources. Solar energy - in particular photovoltaic (PV) power which is pollution-free and causes no greenhouse gases after installation [12], is envisaged to be one of the key players in the future renewable energy mix. However, the faults will result in power losses, low efficiency and system instability, and in some cases, pose a risk of fire. Hence, the faults characterization is essential to ensure the safety of the system.

This chapter aims to provide a comprehensive state-of-the-art about health monitoring of PV panels. The fundamentals of PV panels are introduced in the Section 1.1. Section 1.2 introduces the typical faults of PV panels and corresponding characterization tools. Considering that converter-based impedance spectroscopy (IS) can be implemented online and reveal internal dynamic information, it will be introduced in Section 1.3. Based on the summary of existing methods, the objectives of our work are finally provided in Section 1.4 and this chapter ends with the conclusions in Section 1.5.

1.1 General introduction of PV panels

1.1.1 Background

Considering the decrease of fossil fuel and the global warming, the energy transition is crucial. Current energy structures are designed to support fossil fuels and must be redesigned to support renewable energy systems for addressing environmental challenges, ensuring long-term energy availability, and fostering sustainable development on a global scale. According to the report about world energy transitions outlook 2023 served by International Renewable Energy Agency (IRENA), the power generation of traditional energy sources (fossil fuels and nuclear source) and renewable sources is indicated in Figure 1.1 [1]. In comparison to 2020, it is projected that the power generation from renewable sources will account for more than 50% of the total power generation by 2050, aiming to achieve the goal of reducing global temperature by 1.5^{o}C or even 2^{o}C. Solar energy contributes more than 50% of the renewable energy generation, due to its pollution-free nature, wide distribution, year-round availability and the falling prices of PV panels [13, 14], which represents the major form of solar energy utilization. In recent years, the PV installed capacity has experienced rapid growth, with a manufacturing capacity for more than 1200 GW in the whole world in 2020 and a record of 56 GW of PV installations in Europe in 2023 [15].

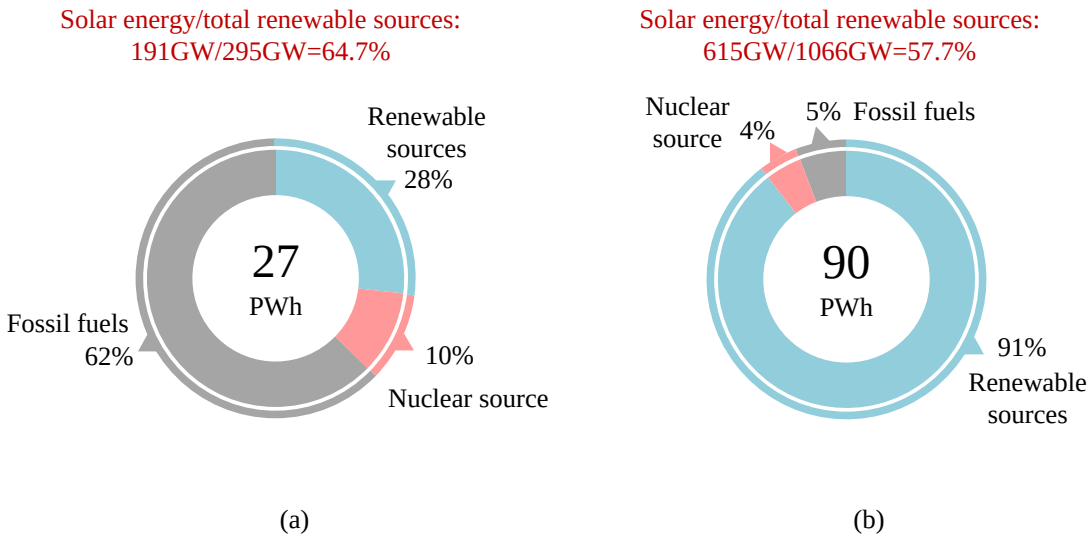


Figure 1.1: Power generation of different sources (adapted from [1])
(a) Gross electricity generation of 2020; (b)Gross electricity generation of 2050.

Regarding the installation of PV systems, there are two typical types of applications. The first one is grid-connected PV generation plants. As shown in Figure 1.2, PV panels are connected with the main grid

through converters and inverters. In this application, PV panels produce stable DC power through a converter connected to a control system. The inverter transforms the DC power into AC power, which is then linked to the main grid for power transmission. During the system operation, special attention must be paid to the reliability and efficiency of the system, power quality, implementation of protection and grid synchronization functions [16, 17].

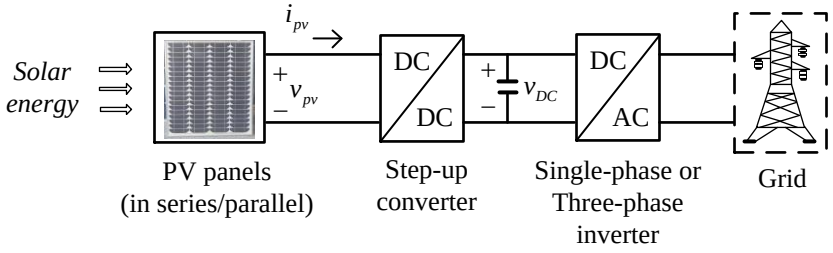


Figure 1.2: Topology of grid-connected PV panels.

The second one is based on microgrids (MGs), operating in conjunction with other renewable sources and energy storage systems to fulfill the energy supply needs for loads. As a single controllable system consisting of a cluster of loads and microsources, MGs allow power generation and provide energy to remote, isolated community without the need for costly and inefficient long-distance high-voltage transmission and distribution infrastructures [18, 19, 20]. Moreover, MGs make the use of solar energy more flexible, especially in some remote villages and isolated islands, and receive widespread attention [21]. In particular, this work conducts research on PV panels based on MGs.

As an illustration, a simplified single-bus DC MG is depicted in Figure 1.3. PV panels and wind turbines operate as power generation devices; supercapacitors and batteries are used to store excess energy, and also supply energy to loads when the power generator cannot support the loads' operation; a number of DC/DC converters realizes the control of operating points of all elements, power flow and the value of DC bus voltage. The main challenges of the system include balancing generation and demand, and maintaining a stable and safe operation of the system [22]. The operating states of PV panels can significantly affect the efficiency and stability of the whole system. Therefore, in the next section, the fundamentals of PV panels will be introduced.

1.1.2 Fundamentals of PV panels

PV panels generate electricity from light energy. From the first discovery of photoconductivity in 1839 and the first selenium PV cell in 1877 to today's perovskite PV cells, PV cell technology can be classified into three generations, as summarized in Figure 1.4 [2]. The first generation of PV cells are based on *p-n* junctions

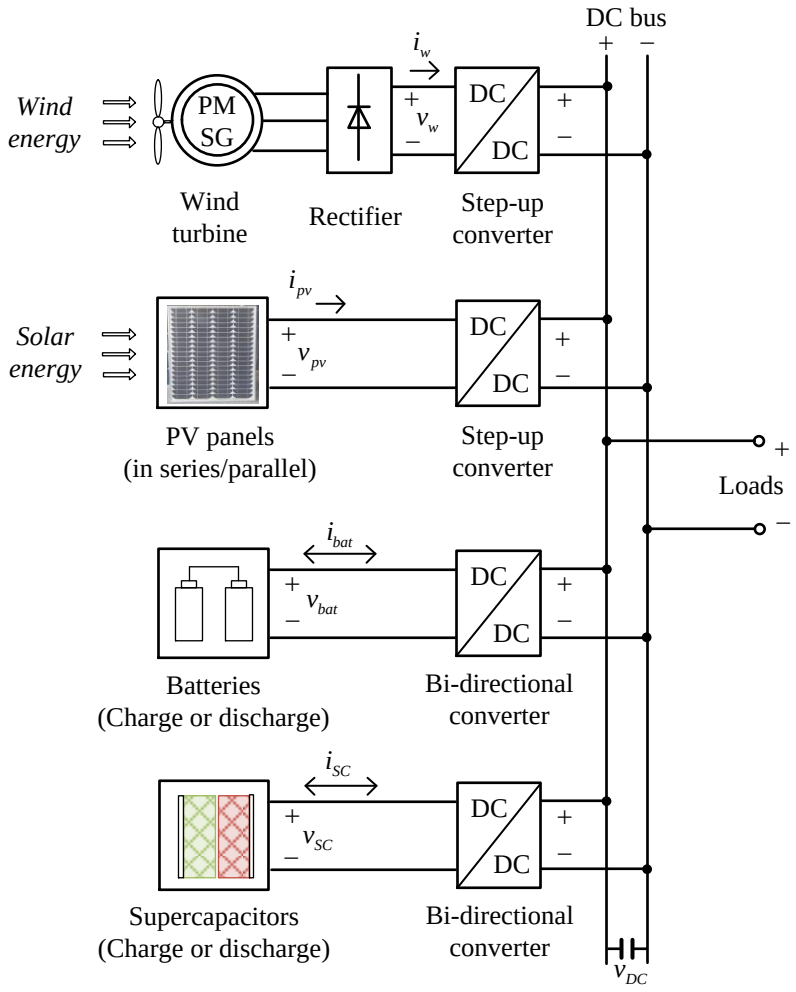


Figure 1.3: Topology of a simplified DC microgrid with PV panels.

consisting of silicon, whose efficiency can reach a maximum of 25.6%. Depending on whether impurities are added, silicon PV cells can be divided into mono-crystalline and poly-crystalline silicon cells. These cells are based on thick silicon slides and due to the high price of pure silicon, a new generation of PV cells was developed to reduce costs, while maintaining or even improving the PV properties, by employing thin film technologies. The cadmium telluride (CdTe) cells, copper-indium-gallium-diselenide (CIGSe) and amorphous silicon cells entered the commercialization stage over 20 years ago. However, the efficiencies of these PV cell families are less than 30%. Hence, a third generation of PV cells enters the researching field with a goal to obtain efficiencies in the range of 30% – 60%. This generation includes dye-sensitized cells [23], perovskite cells [24], and multi-junction cells [25, 26]. Currently, in 2024, the efficiency of multi-junction cells can reach 39.5% (three junction (non-concentrator)) and even 47.6% (four-junction or more (concentrator)) [27]. However, the technological and environmental costs of these third-generation cells, as well as the reliability

of certain cells, mean that they are still mainly dedicated to specific applications such as space ones, and have not yet been developed for mass production. As a result, the main commercial products are still dominated by the first and second generations, with the first generation, i.e., that based on silicon, occupying more than 50% in particular. Therefore, the researching work presented in this manuscript is based on silicon PV cells/panels.

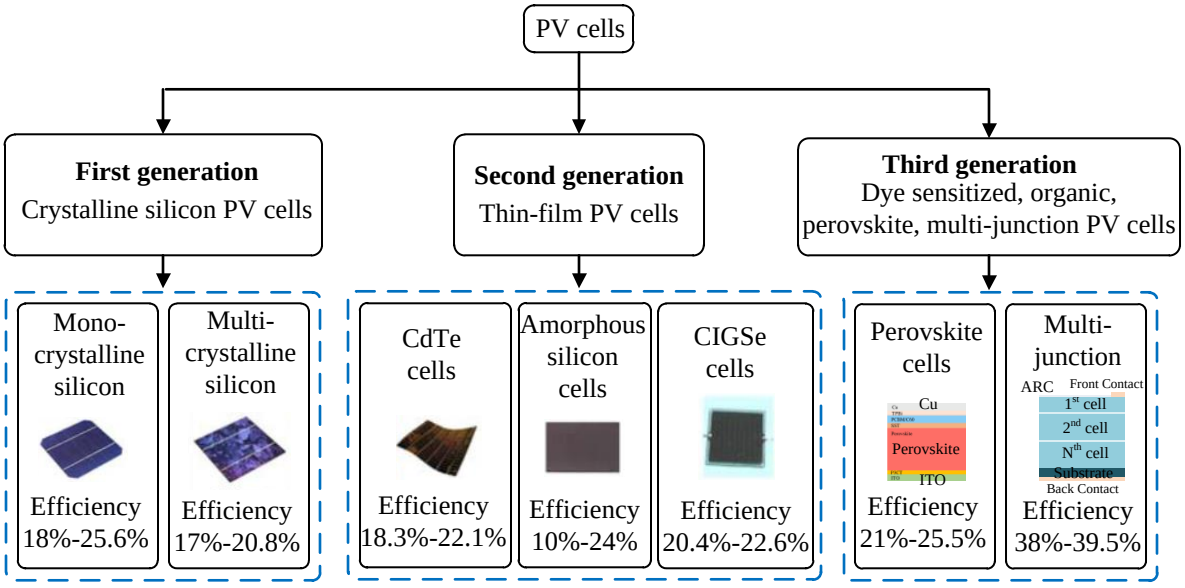


Figure 1.4: Classification of PV cell technologies (adapted from [2]).

A common structure of silicon PV panel is illustrated in Figure 1.5, including frame, front glass encapsulant layers, silicon PV cells, back sheet and junction box. In silicon PV cell layers, multiple PV cells are connected both in series and in parallel to achieve a panel with high voltage and current [28]. Typically, the junction box contains several bypass diodes in parallel with the PV cells to mitigate hot spot formation appearing due to defects, dirt or partial shading that may occur on the panel surface [29].

DC equivalent circuit model (ECM) is commonly used to describe the relationship between input environment factors (irradiance and temperature) and output signals (output voltage and current, i.e., V_{PV}, I_{PV}). The most common DC-ECMs include single-diode and two-diode models [30], as indicated in Figure 1.6.

In the single-diode DC-ECM, I_{ph} represents the photocurrent and its value is dependent on the flux of incident irradiation as well as the absorption capacity of the semiconductor material; the current flowing through the diode in parallel, i.e., I_d, represents the diffusion process (also called transition process); R_{series} and R_{sh} represent the series resistor caused by the material connection and the shunt resistor resulting from the leakage current. One additional parallel diode is connected in the two-diode DC-ECM as depicted in Figure 1.6 (b). The newly added diode is employed to describe the recombination process, providing a more reliable description of the internal parameters than the one-diode model. Corresponding equations for the two

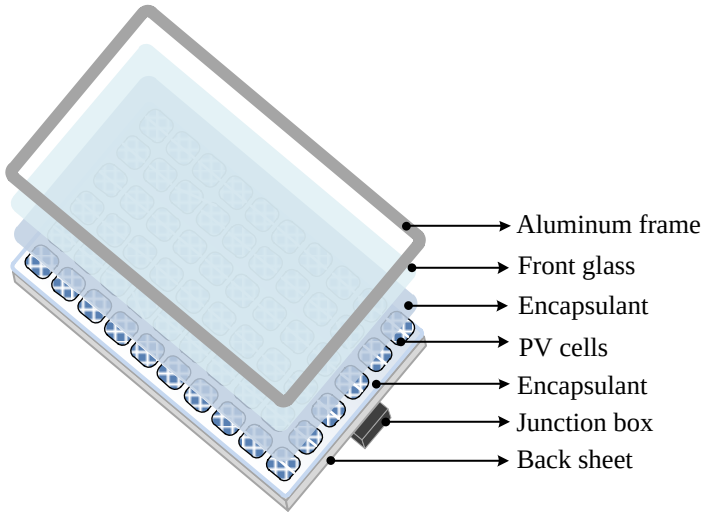


Figure 1.5: Typical structure of monofacial silicon PV panel [3].

diodes, i.e., I_{d1} and I_{d2}, will be analyzed in detail in Chapter 3.

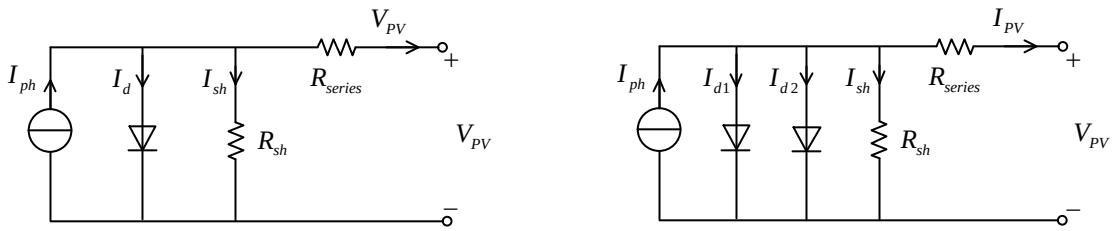


Figure 1.6: DC equivalent circuit models
(a) Single-diode DC-ECM; (b) Two-diode DC-ECM.

Based on the two-diode model simulated in MATLAB/Simulink for a PV panel available in LMOPS laboratory (310 W Recom-Sillia PV panel reference 60M310 composed of 60 monocrystalline silicon cells) with the parameters at standard conditions (air mass = 1.5, G = 1000 $\mathrm{W/m^2}$ and T = 25 $^o\mathrm{C}$) specified in Table 1.1, the impacts of environmental factors on the output signals are analyzed and demonstrated in Figures 1.7. By analyzing the IV and PV curves, it is observed that:

1- the open-circuit voltage, denoted as V_{oc}, is primarily affected by irradiance with a positive correlation;

2- the short-circuit current, i.e., I_{sc}, is mainly impacted by temperature with a negative correlation;

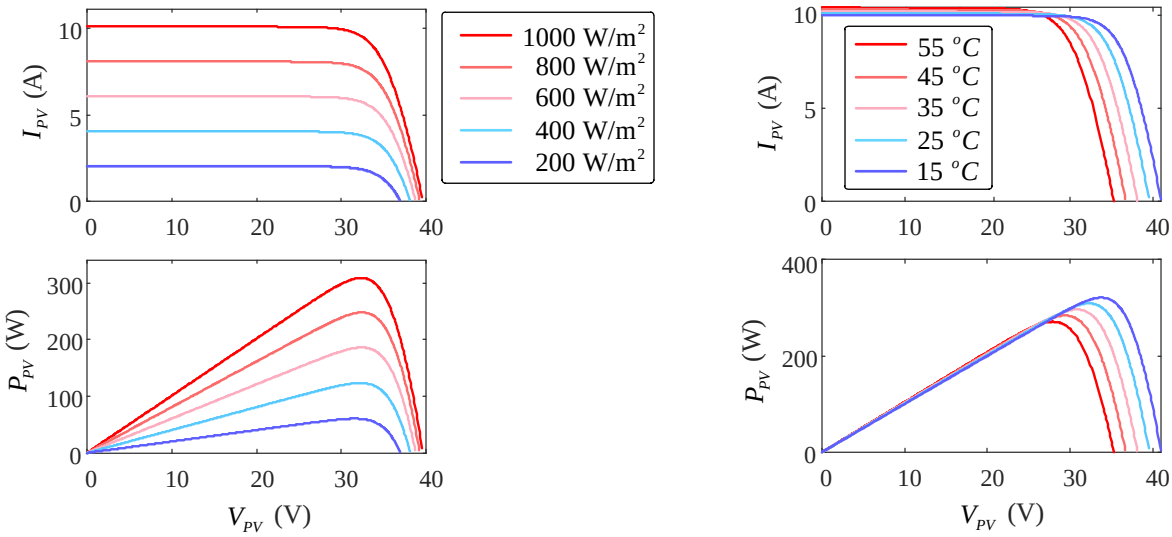
3- the output power, i.e., P_{PV}, is inversely proportional to the value of V_{PV}.

Moreover, Figures 1.7 also points out that the maximum output power is significantly influenced by environmental factors, increasing with irradiation and decreasing with temperature.

Table 1.1: Parameters of the simulated PV panel.

Physical meaning	Symbol	Value
Open-circuit voltage	V_{oc}	39.6 V
Short-circuit current	I_{sc}	9.95 A
Voltage at MPP	V_{MPP}	32.3 V
Current at MPP	I_{MPP}	9.56 A

In order to ensure the maximum efficiency of the PV panel and thus of the entire PV generator system, a maximum power point tracking (MPPT) method is necessary during PV panels' operation. Numerous MPPT methods have been proposed as those in [31, 4]. Due to its simple control, fast tracking speed and small steady-state power oscillation, perturb and observe (P&O) method with variable-step is widely employed in the PV system for an efficient finding of the MPP [4]. For these reasons, this method has been selected in our research. The corresponding control flow is illustrated in Figure 1.8, where V_{PV-pre}, I_{PV-pre} and P_{PV-pre} represent the output voltage, current and power during the last perturbing period, respectively. In the voltage range (V_l, V_h), a short-step disturbance, i.e., Δd_s, is used. Instead, a larger-step disturbance, i.e., Δd_l, is employed if V_{PV} is out of the defined range.



(a) IV and PV curves under different irradiances

(b) IV and PV curves under different temperatures

Figure 1.7: IV and PV curves under different irradiance levels and temperatures.

Applying MPPT method can improve the efficiency of PV panels during operation. However, in addition to efficiency, stability and reliability are also crucial aspects for a PV system. Faults caused by environmental factors and failures during operation do not only affect the efficiency of the system but also impact its

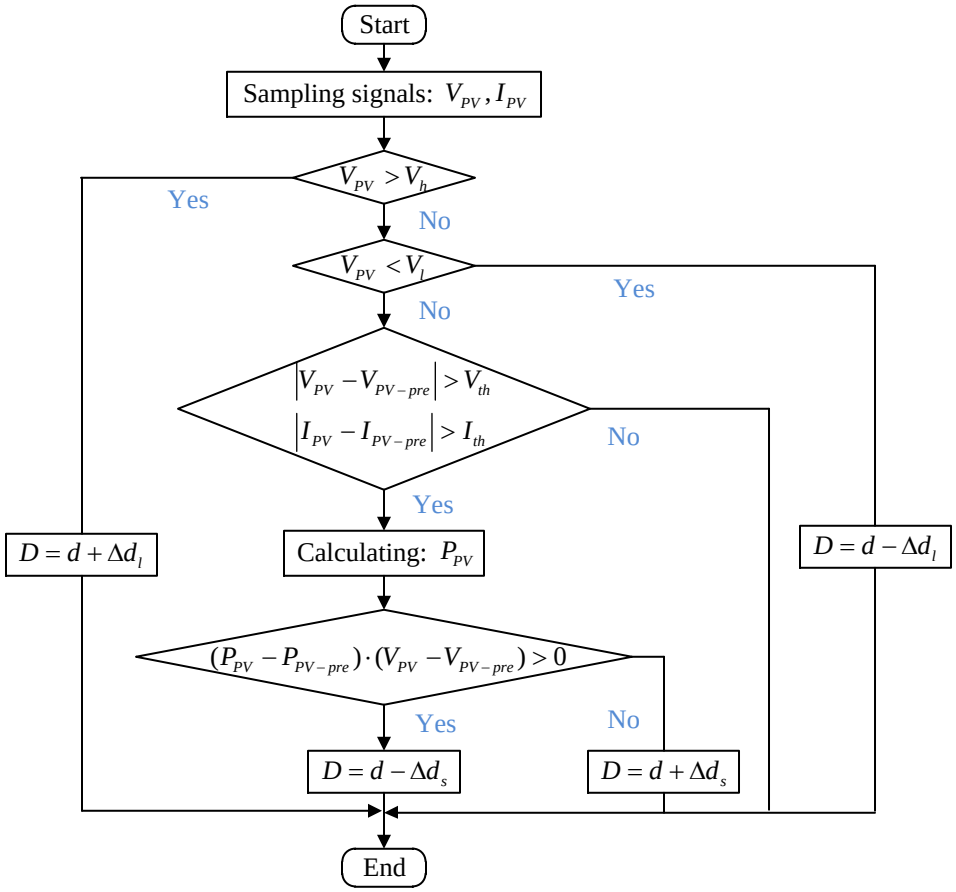


Figure 1.8: Flowchart of P&O MPPT method [4].

stability. Therefore, fault characterization and detection are vital in the operation of PV panels and typical characterization tools will be focused on in next section.

1.2 Fault characterization tools for PV panels

1.2.1 Typical faults in PV panels

During normal operation, the output power of PV panels is close to the theoretical power. However, in field conditions, a number of factors can cause a power reduction, including human factors from transport to installation, environmental factors such as partial shading, bird droppings, as well as the causal relationships between various factors [32]. For instance, partial shading may lead to a hot spot, and the detailed causal relationship between mismatch and degradation can be found in [33]. All the factors resulting in power losses

or safety risk are considered as ”fault” in this work. The faults can be classified in many ways, including based on duration and severity [34], based on symptoms, effects and consequences [35], based on the cause of the faults [36] and from a part to the whole of the system [37].

In this work, the primary focus is on the application of PV panels in MGs. With advancements in electronic device technology, it has become possible to convert the generated power of each PV panel independently through a single/modular converter, thereby enhancing the efficiency and reliability of PV panels implemented in MGs. Hence, following the classification method outlined in [37], this section will give detailed introductions of cell-level and panel-level faults. To evaluate and describe these faults, three criteria are selected and named as faults characteristics, including time characteristic, security level and power loss. Their definitions and classifications are as follows:

Time characteristic: The time characteristic of faults can be used to express the duration of the impact of a failure [34].

- Permanent: permanent fault represents persistent, continuous, or constant issue or defect in PV panels. A permanent fault remains present throughout the operation until it is identified and addressed.
- Intermittent: intermittent fault is a type of fault in PV panels that occurs sporadically or irregularly, whose impacts are reversible. They can be caused by a variety of factors, including temperature and irradiance level variations. Due to their unpredictable natures, intermittent faults often require careful monitoring to maintain the reliability and performance of a system.
- Incipient: incipient fault refers to the initial or early stage of a fault or abnormal condition appearing in the normal operation of PV panels. It is a fault that is just beginning to develop but has not yet fully manifested or escalated into a critical issue. This incipient faults may lead to the permanent faults.

Security level: Security contains three levels, ranging from S_1 to S_3, with the associated security risks escalating progressively [35][36][37].

- Approximate safe (S_1): faults at this level won't pose a clear threat to the safety of PV panels.
- Medium danger (S_2): faults at this level result in a medium possibility or potential threat to causing a fire, an electrical shock to working personnel or physical danger.
- Danger (S_3): faults at this level have a high possibility to causing a fire, an electrical shock to working personnel or physical danger.

Power loss: the power loss can be categorized into five trends based on how the power loss evolves from the initial power value to a time in the service life of a PV panel [37].

- Pl_0– minimal power loss under detection threshold;
- Pl_L – linear-shaped degradation of power over time;
- Pl_S – saturated degradation over time;
- Pl_H – hybrid degradation over time;
- Pl_E – exponential-shaped degradation of power over time.

Except for the time characteristic, a class of faults may exhibit more than one security level and type of power loss. The typical faults occurring in PV panels and their descriptions are described as following:

1. Cell cracks:
   Definition: Cell cracks cause disconnection between PV cells, appearing in the transportation from the factory to their place of installation, installation, and subsequently due to exposure to repeated climatic events. It results in a decrease in the output power of PV panels, insulation failure, and potential safety hazards [38].
   Faults characteristics: Permanent & S_1, S_2 & Pl_0, Pl_L, Pl_S.

2. Discoloration:
   Definition: Discoloration always represents the discoloration of the ethylene vinyl acetate (EVA) or other encapsulation materials [32]. The discoloration will reduce the light reaching the PV cells, which results in a drop in the output power of PV panels [39].
   Faults characteristics: Incipient & S_2 & Pl_S, Pl_H.

3. Snail track:
   Definition: A snail track is a grey/black discoloration of the silver paste of the front metallisation of screen printed solar cells. The discoloring typically occurs 3 months to 1 year after the installation of PV panels, with the speed depending on the season and the environmental conditions [32].
   Faults characteristics: Incipient & S_2 & Pl_L.

4. Delamination:
   Definition: Delamination is located between encapsulant and active cells caused by salt accumulation,

contamination, moisture penetration or external factors. It appears frequently in humid and hot conditions and will result in reflection and power losses [35].
Faults characteristics: Incipient & S_2 & Pl_S, Pl_H, Pl_E.

5. Breakages:
   Definition: Breakages include defects in frame, glass breakage and broken interconnection. Defects in frame are often due to a heavy snow load on PV panels installed in regions with heavy snowfall, but also can be due to a falling stone-type object or movement of the panel on its support. It leads to deformation of the module and detachment of the frame from the PV glass [40, 37]. Glass breakages are also possibly caused by poor packaging during transportation, installation or by hail and stone throwing, etc., while the broken interconnection is attributed to frequent changes in temperature [40]. All of them will result in large power losses.
   Faults characteristics: Permanent & S_2, S_3 & Pl_0, Pl_L, Pl_S.

6. Junction box faults:
   Definition: Junction box faults contain observed junction box failures and bypass diode faults. Observed junction box failures, including poor fixing, improperly sealed junction boxes, bad wiring, broken connections, etc., arise from a flawed manufacturing process, cable rework during installation, and connector rework, along with prolonged heat exposure. It can lead to moisture ingress, internal arcing, fire risk, and power loss [37, 32]. The bypass diode is an internal component of the junction box and it is then broken due to excessive current level and improper or insufficient heat sinking [41].
   Faults characteristics: Permanent & S_1, S_2 & Pl_0, Pl_S.

7. Electrical connection faults:
   Definition: Electrical connection faults incorporate short-circuit and open-circuit faults. This type faults occurs when short-circuit or disconnection problems appear in one PV cells string or more. With these faults, the maximum output power is decreased and a fire may be occurred [34].
   Faults characteristics: Permanent & S_2, S_3 & Pl_S.

8. Partial shading:
   Definition: Partial shading encompasses snowing covering, soiling, shading, and other conditions with uneven lighting caused by external factors. Snowing covering depends on the installation location; soiling is caused by the dust, bird dropping and other particles covering the surface of PV panels; shading and partial shading are usually caused by clouds, trees, building, chimney, overhead power lines, etc.. Under these conditions, the incident irradiance on the surface of PV panels irregularly decreases, leading to degraded operation, or even with the appearance of local MPPs inducing a decrease

in the output power [33, 42, 43].
Faults characteristics: Intermittent & S_2 & Pl_S.

9. Hot spots:
   Definition: Hot spots arise when a single-cell, or group of cells operates at reverse-bias, resulting in abnormal elevated temperature levels. This can decrease the generated power of PV panels and even cause a fire [44, 45].
   Faults characteristics: Intermittent & S_2 & Pl_S.

10. Degradation:
    Definition: Degradation is precipitated by corrosion and electron-migration in interconnects and contact layers or other faults, including potential induced degradation (PID), light induced degradation (LID) and abnormal degradation [33, 35, 46].
    Faults characteristics: Permanent & S_1, S_2 & Pl_L, Pl_S.

According to the above analysis, the characteristics of typical faults are summarized in Table 1.2. The faults can make a significant influence on the system security and power losses, which should be detected in time. Most of faults are incipient or permanent, and they require regular detection and repair. Electrical connection faults may cause the highest level of safety issues, should be resolved promptly once discovered. Hot spots and partial shading display a intermittent characteristics, and real-time monitoring are necessary to detect them and to improve the operating efficiency of PV panels. Considering that partial shading has a possibility to result in most faults concluded in [32], it is selected as an example faulty condition to verify the validity and efficiency of the proposed online health monitoring method in our work.

Table 1.2: Characteristics of typical faults.

Typical faults	Time characteristic	Security level	Power loss
Cell cracks	Permanent	S_1, S_2	Pl_0, Pl_L, Pl_S
Discoloration	Incipient	S_2	Pl_S, Pl_H
Snail track	Incipient	S_2	Pl_L
Delamination	Incipient	S_2	Pl_S, Pl_H, Pl_E
Breakages	Permanent	S_2, S_3	Pl_0, Pl_L, Pl_S
Junction box faults	Permanent	S_1, S_2	Pl_0, Pl_S
Electrical connection faults	Permanent	S_2, S_3	Pl_S
Partial shading	Intermittent	S_2	Pl_S
Hot spot	Intermittent	S_2	Pl_S
Degradation	Permanent	S_1, S_2	Pl_L, Pl_S

1.2.2 Characterization tools for PV panels

All the faults mentioned in the previous section will cause some changes in PV panels, including internal and external changes. The external changes are always visible, such as the breakages and discoloration, while the internal changes cannot be directly observed, generally including the internal temperature, electrical features and relaxation processes. Therefore, specific equipment or methods are needed to capture the changes and make them visible. The health information of PV panels can be monitored through analyzing these changes. Based on whether the PV panels supply power to loads/DC-bus during measurement, these tools are classified as offline and online tools. When a tool can be implemented both offline and online, it is categorized as a more common option. For example, IV curves of PV panels can be measured based on the IV plotter (offline) or by hardware solutions integrated in PV converters (online). Considering the efficiency, relative information on eventual faults is predominantly obtained online. Therefore, IV curves will be classified as an online tool in our study.

Offline tools

The offline tools, which can provide health information of PV panels, include lock-in thermography (LIT), ultraviolet fluorescence imaging (UVFL imaging), photoluminescence imaging (PL imaging) and electroluminescence imaging (EL imaging). They require disconnection with the other components of MGs during measurements. Among these tools, LIT is a variation of the infrared method, the rest are types of luminescence. All of their applications require darkness or open-circuit conditions. PV panels cannot supply energy to loads under both operating conditions. Hence, these four tools are considered as offline tools.

- **Lock-in thermography (LIT)**
  LIT is used to detect and quantify all kinds of shunts to qualify PV cells. A pulsed bias in dark condition (dark lock-in thermography – DLIT) or pulsed light irradiation under open-circuit conditions (illuminated lock-in thermography under open-circuit condition – V_{oc}-ILIT) is applied to PV cells. To complete the detection process, an infrared camera is utilized to capture the local temperature modulations caused by various shunt currents, aiding in the diagnostic differentiation of various procedures. Small defects of PV cells can be detected by using this method [47].

- **Ultraviolet fluorescence imaging (UVFL imaging)**
  UVFL imaging of ethylene vinyl acetate (EVA) in PV cells can be used to analyze the discoloration of PV panels [48]. The ethylene vinyl acetate (EVA) layer which serves as an encapsulant in PV panels,

as shown in Figure 1.5, is used by UVFL imaging thanks to its fluorescence properties. This EVA layer absorbs ultraviolet light and re-emits it in the visible range, making it possible to analyze the discoloration of PV panels. Even in dark outdoor setting, this tool can detect the number and location of cell cracks in PV panels. However, since this method relies on EVA, cracks on the border of the cells cannot be detected [32].

- **Photoluminescence imaging (PL imaging)**
  PL imaging uses light, typically in the form of lasers or other high-energy light sources, to induce the generation of emission light. Highly sensitive cameras are necessary to create visual representations of the PL properties of the entire surface from the emission light. The PL signal intensity is generally represented by gray levels, where a brighter shade of gray indicates a higher intensity PL value and signifies the presence of faults in PV panels [49].

- **Electroluminescence imaging (EL imaging)**
  EL imaging realizes the release of photons and the generation of light based on the application of an electric field. When an external DC current is fed into a PV panel, the recombination of carriers and holes results in emission light, which will be captured and recorded as an image [50]. The light intensity increases with the local voltage, so areas with poor contact appear dark in EL test results [51]. However, this tool requires tested PV panels to be disconnected from the whole system.

All these imaging tools make it possible to obtain more or less partial, or even general, information on the health states of PV panels, without significantly influencing their normal characteristics. Combined with corresponding image processing, machine learning or deep learning methods, the type and location of faults can be diagnosed [53, 54]. Typical characteristics of imaging tools are summarized in Table 1.3, including two online tools which will be introduced below. As additional but generally costly imaging devices are required, their applications in MGs could be limited.

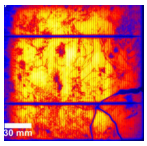
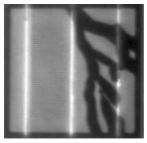
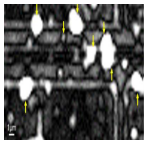
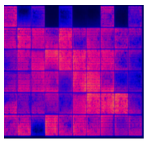
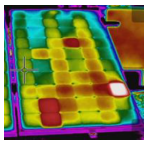
Online tools

Online tools do not need to disconnect PV panels from MGs, meaning the PV panels continuously output power during measurements. Commonly used online tools are specified in the following:

1. Images

   - **Infrared thermal imaging (IR imaging)**
     IR imaging is based on the concept of localized heat generation because of the joule heating effect

Table 1.3: Typical characteristics of different imaging tools.

Characteristics	Name & Example	Operating condition request	Equipment	Detectable faults
Offline tools	ITL [47] 	Dark condition / Open circuit	Pulsed voltage or light Infrared camera	Cell cracks
	UVFL [48] 	Dark condition	UV light Highly sensitive camera	Cell cracks, Discoloration
	PL [49] 	Dark condition	High-energy light Highly sensitive camera	Cell cracks, Degradation, Interconnection broken
	EL [51] 	Open circuit	DC current source Infrared-sensitive camera	Cell cracks, Degradation, Interconnection broken, etc.
Online tools	IR [52] 	Normal condition	Infrared camera	Faults causing abnormal heating hot spot, Partial shading, etc.
	Visual [52] 	Normal condition	Trained staff / conventional imaging devices	Discoloration, Dlamination, Snail track, Partial shading, Breakages, etc.

caused by shunted cells, poor contacts, short circuits, etc.. It provides rapid, real-time characteristics of PV panels with non-destructive measurements. During thermal imaging, temperature gradient is formed in the two-dimensional distribution images. In the case of a healthy PV panel, the resulting temperature distribution is observed to be homogeneous. On the other hand, defects in the PV panel resulting in a significant impact will appear as bright spots [40, 53]. IR imaging cameras can also be embedded on UAVs to improve the measurement speed [52].

- **Visual inspection**

  Visual inspection is carried out by trained staff or conventional imaging devices. It is always conducted regularly and under standardized conditions and follows IEC-61215 standards [40]. Unmanned aerial vehicles (UAVs) provide an efficient way to obtain a large number of images to analyze the state of PV panels, which is more suitable for large PV installations [52].

2. Electrical signal measurements

- **IV curves**

  IV curves contain the information: V_{oc}, I_{sc}, V_{MPP}, I_{MPP} and the slope of the curve. Current mismatches lead to a decrease in the generated power, causing distortions in the characteristics of IV curves of PV panels [55, 56]. Current faults are associated with partial shading, hot spots, cracks, and so on [57, 58, 38]. As depicted in Figure 1.9, under different partial shading percentages, IV curves present steps at different current levels. Intelligent algorithms can be used to analyze the IV curves and detect the faults, such as machine learning methods [59]. IV curves are usually obtained with an IV plotter or by hardware solutions directly integrated in PV converters. Both of them need to scan the entire voltage range (from open circuit to short circuit), which will affect the operating efficiency of PV panels.

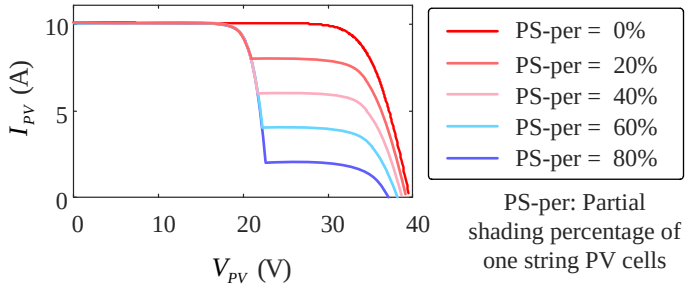


Figure 1.9: IV curves under different partial shading percentages.

- **Power losses analysis (PLA)**

  PLA identifies faults of PV panels based on the deviations between the monitored and the theoretical output powers. The simulated output power based on a prediction model during operation is compared with the measured value, taking into consideration the variations of temperature and irradiation. This method, therefore, does not require knowledge of the complete IV curves. Nevertheless, the accuracy of the monitoring results is highly dependent on the prediction model [60], and only a limited number of fault types can be detectable.

- **Impedance spectroscopy (IS)**

  IS provides information on the internal impedance of the PV panels, associated with the elec-

tronic relaxation processes. It can be used to differentiate between types of internal defects in PV panels that cannot be distinguished on the basis of macroscopic IV characteristics alone. To implement the IS on the PV panel, perturbation current/voltage signals with a broadband frequency are injected at a steady-state operating point. In this process, a DC-bias voltage is selected, as the impedance of the PV panel depends on this DC-bias voltage [61]. The impedance is then determined from the panel's electrical response to an injected AC perturbation signal. The impedance curve, also denoted as IS spectrum, in frequency domain can reflect the health states of the PV panel. By identification with the health features extracted based on AC-ECM of PV panels, the origin of the faults can be identified. The corresponding principles will be presented in detail in the following section and in Chapter 2. However, to date, this tool has rarely been used in MGs to monitor the PV panels' health states.

Other electrical tools, such as spread spectrum time-domain reflectometry (SSTDR), estimating randomness in the voltage signal (ERV), frequency spectrum analysis (FSA) of the voltage or current waveform, are used to detect the array-level faults, and are not described in our work.

Table 1.4: Comparisons of three typical online tools.

Name	Measurements	Pros	Cons
IV curves	V_{dc}, I_{dc}, covering the whole voltage range (0 V – V_{oc})	Simple control method; advanced follow-up analysis algorithm	Poor operating efficiency
PLA	P_{PV}, environmental factors: temperature and irradiance	High efficiency; no requirement of specific equipment	Requirement of an accurate model; limited faults types detected
IS	V_{dc}, I_{dc}, v_{ac}, i_{ac} at injection point	High efficiency; react internal impedance information	Lack of detailed principles and analysis methods implemented on PV panels

The pros and cons of three tools based on electrical signal measurements are summarized in Table 1.4. All of them can obtain online health information of PV panels without additional equipment. As mentioned above, PLA can detect limited faults types. Compared with PLA, the remaining two tools demonstrate superior performance in detecting a broader range of fault types. IV curves already boast mature algorithms that can achieve accurate monitoring of faults. However, as introduced, this method necessitates measurement of the complete IV curve, leading to greater PV power loss during the scanning process. On the other hand, IS offers a potential monitoring approach to achieve quasi-maximum output power of PV panels while detecting faults, thus without a significant decrease of the efficiency of the monitored PV panels or system. Nevertheless, this method is currently mainly utilized at the cell-level or only at laboratory stage, highlighting a current

research gap in its practical applications. Therefore, this manuscript mainly focuses on the IS method, from fundamentals to application with PV panels in real-time production. The next section will give the detailed introduction of existing IS methods, including types and challenges implemented in PV panels.

1.3 Implementation ways of impedance spectroscopy

1.3.1 IS fundamentals

IS is a powerful method of characterizing many of the electrical properties of materials and their interfaces with electronically conducting electrodes. IS is based on the perturbation of the target system in equilibrium or in steady state, via the application on a DC bias of AC signals over a wide frequency range and the monitoring of response signals of the system toward the applied perturbation. The general form of the electrical impedance of a tested system can be expressed as:

$$Z(f_p) = \frac{V_{ac}(f_p)}{I_{ac}(f_p)} e^{j\Theta(f_p)} \tag{1.1}$$

where f_p is the frequency of the perturbation signal, $V_{ac}(f_p)$ and $I_{ac}(f_p)$ are the amplitudes of the AC components of the voltage and current at frequency f_p, respectively; $\Theta(f_p)$ represents the phase of the impedance at frequency f_p, which is the phase shift between the voltage and current signals:

$$\Theta(f_p) = \Theta_v(f_p) - \Theta_i(f_p) \tag{1.2}$$

where $\Theta_v(f_p)$ and $\Theta_i(f_p)$ represent the phases of the voltage and current signals, respectively.

Theoretically, to ensure the validity of IS measurement, the operating condition should satisfy linearity, stability, causality and finiteness [62, 63]. In the current work, IS is specially applied to the characterization of the health states of PV panels and herein, the linearity and stability criteria are firstly emphasized.

- **Linearity**: In the nonlinear region, current changes are not proportional to voltage changes, i.e., $\Delta V \neq \Delta I \cdot Z$, since the signals do not satisfy superposition and scaling. As indicated in Figure 1.10, the response shows asymmetrical characteristic in the nonlinear region. Hence, to guarantee linearity, the system should operate in a linear/quasi-linear region. In practice, the amplitude of the perturbation signal should be low enough to ensure that the response signals behave linearily and have to be larger than the system's inherent noises to guarantee a good signal-to-noise ratio (SNR). A suggested range

for the amplitude of the perturbation signal is 5% – 15% of the DC component [64].

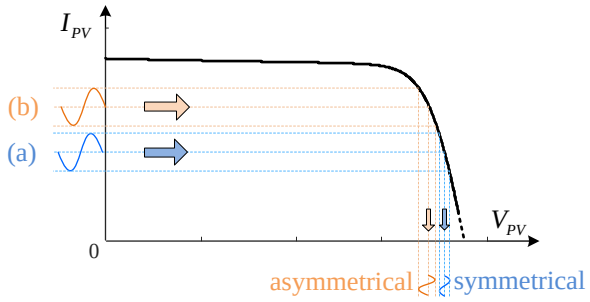


Figure 1.10: AC signal injection in different regions:
(a) (quasi-)linear region (b) nonlinear region.

- **Stability**: Measuring an IS spectrum takes time, especially in the low-frequency plage. To validate the spectrum, the tested system works in the same steady-state before and after the perturbation. To achieve a steady-state environment, the operating conditions of PV panels cannot be changed during the IS implementation, such as irradiance and temperature. And some actions must be taken before starting each measurement (e.g., keeping system operating for a period at the measurement point [65]). Meanwhile, the IS must also be stationary, which can be verified by repeating the measurements and checking their consistency [63].

Maintenance of the measurement environment and excitation perturbation signals can be achieved by specific devices or integrated into PV converters [66, 67]. According to the implementation ways, IS can be classified as workstation-based IS (also named impedance-bridge based IS) and converter-based IS.

1.3.2 Workstation-based IS

Workstation-based IS is the most common way for IS implementation. The workstation-based IS measurement systems are named ”spectrometer” and typically consist of a potentiostat (sometimes called electrochemical interface) together with a frequency response analyzer (FRA) or a spectrum analyzer, or even a combination of both [68]. The potentiostat provides buffered connections to the tested system under investigation together with circuitry for controlled smooth perturbations of the voltage or current signal generation, high-speed data acquisition and the measurement of the DC properties of the tested system. The FRA is used to analyze the obtained responses and is connected to the tested system through the potentiostat. Hence, the bandwidth of the potentiostat is a very important parameter of the workstation to be considered for obtaining sensitive and accurate analysis, possible at high frequencies.

A computer application software is required to provide control of the instrumentation, data storage, display of graphical results and for running the detailed analysis function (including access to equivalent circuit fitting and data analysis programs). A simplified experimental setup is illustrated in Figure 1.11 [5]

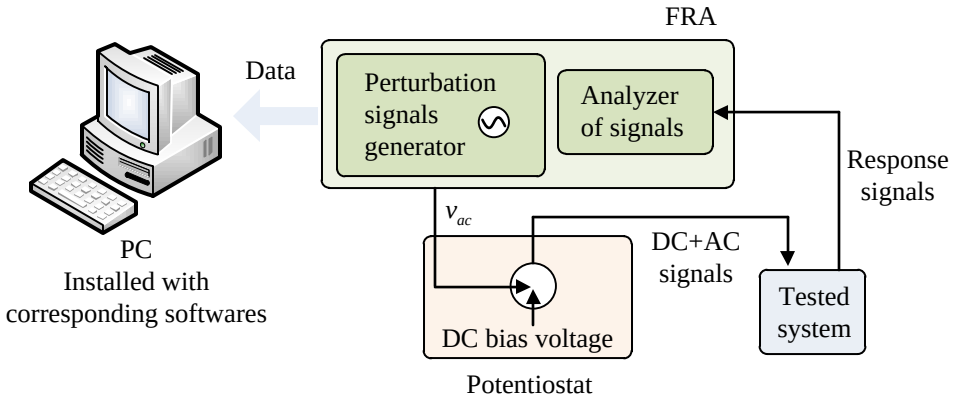


Figure 1.11: Workstation-based IS [5].

Numerous types of spectrometers with good performance can be found in the market, which can achieve measurements from μHz to MHz with a high accuracy. Nevertheless, most of them are designed with a low DC bias voltage and allow small currents to flow, such as CS310 ($\pm$10V and $\pm$2A)[69], which make them only suitable for cell-level tests. If applied in the panel-level, a power amplifier is required. In addition, given the large number of PV panels that typically make up a MG, an equivalent number of spectrometers is required to ensure efficient and accurate health monitoring of the entire MG. This implementation way is expensive ($\geq$20 k€) and is thus preferred for cell-level and lab characterizations [70].

1.3.3 Converter-based IS

Converter-based IS achieves the perturbation signal injection and stable operating condition by modifying the control strategy of the existing DC/DC converter or optimizer. This method allows the IS measurements to be applied while the PV panel is connected to the grid. There are two ways to implement this method and the simplified structures are shown in Figure 1.12 and Figure 1.13.

Figure 1.12 depicts the method of separating the device for injecting perturbation signals and guaranteeing the stable operating condition. The converter connected with the DC bus/loads are used to control the PV panel operating at a stable condition. An additional excitation device composed of a signal generator and a power amplifier are designed to supply the perturbation signals [67]. Due to the separation of these two parts, the frequency of perturbation signals is not influenced by the bandwidth of the connected power converter and

thus a broadband IS spectrum can be obtained. The corresponding control methods are quite simple, as each converter only needs to implement the control of single DC or AC signals. However, additional circuits need to be designed which will increase the complexity and cost of the system.

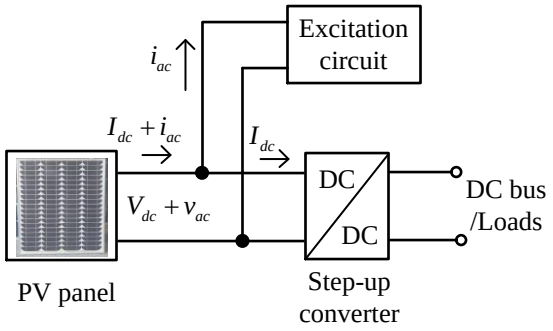


Figure 1.12: Converter-based IS with an extra excitation circuit.

Because of the aforementioned drawbacks of converter-based IS with an additional excitation circuit, a new topology has emerged, integrating the two control objectives into a single converter as shown in Figure 1.13. Since no extra equipment is required, it is popular with researchers and is applied in fuel cells, batteries and recently PV panels [66, 71, 72]. To satisfy the requests of IS implementation, the control of DC and AC signals are achieved by one converter, which results in a complex control strategy. An AC duty signal is directly added to the DC duty signal in [66, 71, 73, 74, 75]. It can simply excite the perturbation on the tested system. However, maintaining a constant DC duty cycle is difficult to ensure the voltage or current at the injection point under various operating conditions, which can impact the analysis of results. A closed-loop compensator is applied in [76] to ensure the characteristics of the injection point, while the perturbation duty cycle signals with a constant amplitude are directly superimposed. Meanwhile, the resonance caused by the series connection of inductor and capacitor of the converter must be considered during IS implementation [77], which may bring the PV panel to a nonlinear operating region. Qahouq $et\ al.$ [78] and Shen $et\ al.$ [79] have provided a solution by controlling both AC and DC signals in a closed loop. The control strategies become more complex in this setup. And the frequency of perturbation signals is not only limited by the bandwidth of the converter, but is also affected by the crossover frequency of the control system for this type converter-based IS.

1.3.4 Challenges

The aforementioned methods for IS implementation are summarized in Table 1.5, in terms of the frequency range, dedicated applications, control complexity and risks, and cost. It indicates that converter-based

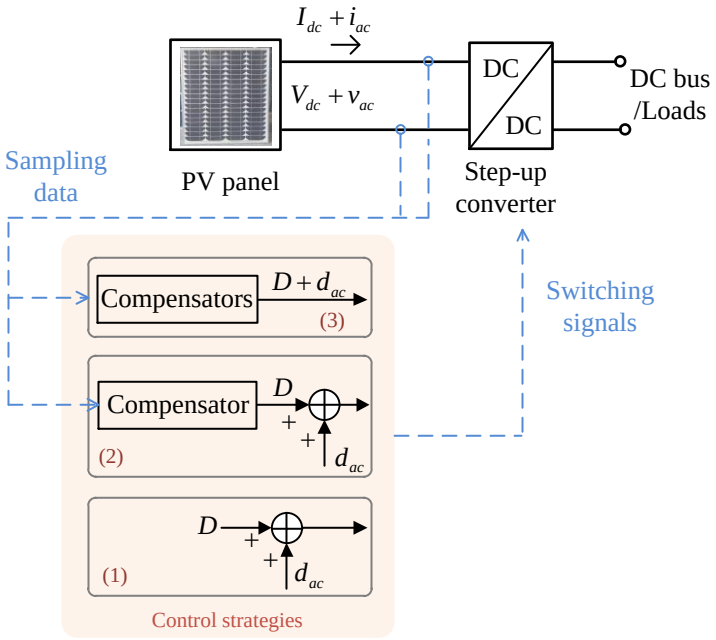


Figure 1.13: Converter-based IS based on the existing converter.

IS without an extra excitation circuit does not need additional equipment, has lower price, and is more suitable for the MGs with multiple PV panels. Three control strategies exist without additional excitation circuitry as indicated in Figure 1.13. Of the three control strategies compared, open-loop control is the simplest strategy. However, the unstable injection point and perturbation signals can significantly impact the accuracy of the results. On the other hand, closed-loop strategies that control both DC and AC signals can ensure the stability of the injection point and perturbation signals. To summarize the responses to these challenges in terms of complexity and accuracy, referring to the strategy controlling both DC and AC signals, the closed-loop control is more effective, while the control strategies may be complex.

Additionally, if the relatively complete IS spectrum of PV panels is required, wider frequency range perturbation signals should be applied ($\geq$ 1 MHz [80]). With today's technology, it is impossible for converter-based IS to achieve such high frequencies at a low cost. Therefore, when implementing converter-based IS on PV panels for online health monitoring, some challenges need to be addressed:

- **Appropriate control strategies**
  The control strategies for PV panels should include both upper-level and lower-level control strategies. The upper-level control strategy is responsible for the cooperative operation of different modes, such as MPPT mode, IS mode, etc.. The lower-level control strategy represents the control of each mode. Special attention should be paid to the fact that in IS mode, the control strategy should guarantee a

Table 1.5: Summarization of IS implementation ways.

Name			Frequency	Applications	Control complexity	Risk	Cost
Workstation-based IS			From μHz to MHz	Preferred for cell-level or lab characterization	–	–	High
Converter -based IS	With an extra excitation circuit		≤ 10 kHz	Panel-level	Simple	–	Medium high
	Without an extra excitation circuit	Open-loop	≤ 10 kHz	Panel-level	Simple	Nonlinearity, poor SNR	Low
		Closed-loop (only control DC signal)	≤ 10 kHz	Panel-level	Medium complex	Nonlinearity, poor SNR	Low
		Closed-loop (control both DC and AC signals)	≤ 10 kHz	Panel-level	Complex	–	Low

certain power output of PV panels. At the same time, it should achieve the widest possible frequency range while ensuring the validity of IS measurements.

- **Reasonable analysis methods**
  Considering the switching frequency of devices and the requirements of current ripple of converters applied in MGs, converter-based IS can only obtain an incomplete IS spectrum (reaching up to kHz). To obtain accurate information about PV panels under variable operating conditions and faults, the relationship between internal relaxation processes and the IS spectrum should be analyzed in a rational manner.

1.4 Objectives of this work

To address the challenges of implementing converter-based IS on PV panels mentioned in the last section, the major objectives of this thesis are as follows:

1. **Design and comparison of control strategies for converter-based IS implementation**
   - Operating principles – Operating region and frequency limitation
     The validity and accuracy of the results are related to the location of the injection point. By analyzing the characteristics of PV panel, a selection guide for the injection point can be provided.

Moreover, the frequency of perturbation signals is limited by the bandwidth of the converter itself. Thus, on the basis of the converter characteristics, frequency limitations are analyzed and a comprehensive analysis of the system parameters is performed, providing indications for the converter and controller design.

- Upper-level control strategy – Cooperative control strategy
  In general, a PV panel operates in different modes. According to the requirements of the MPP tracker and IS implementations, three operating modes are needed to be defined in our work, i.e., maximum power point tracking mode (MPPT mode), injection point tracking mode (IPT mode) and impedance spectroscopy mode (IS mode). An upper-level control strategy enables the cooperative control of all these three modes.
- Lower-level control strategy – Advanced open-loop control strategy
  Traditional open-loop control strategy may suffer from nonlinearity and poor SNR. In order to meet the requirements for IS measurement, an advanced open-loop control strategy is proposed in this work. When designing the control strategy, the resonance and frequency limitations are taken into consideration. A good interpretability of the method could greatly facilitate the operator to evaluate and to react using the expertise knowledge. This method can guarantee that a sufficiently wide frequency range and quasi-constant amplitude perturbation signals are injected into the PV panel.
- Lower-level control strategy – Closed-loop control strategies
  Based on the characteristics of linear controllers, two types of closed-loop control strategies are designed. Corresponding design details are provided step by step. These strategies can be complementary to the open-loop control strategy and be applied to different work scenarios to enhance the online implementability of IS measurement. Simulations and experiments will also carried out for the validation of the developed strategies.

2. **Online health monitoring of PV panels based on IS measurements**

- AC equivalent circuit model (AC-ECM)
  AC-ECM can help to evaluate the health states of PV panels based on IS spectrum. An AC-ECM of PV panel will be proposed, taking into account of the injection point and the presence of bypass diodes in the panel.
- Interpretation of incomplete IS spectrum
  Based on the simplified AC-ECM, a fitting method will be provided to complete the IS spectrum. And the physical meaning of fitted IS spectrum is also presented. Additionally, the parameters of AC-ECM can be calculated based on the fitted IS spectrum.

- Health features
  Health features are the intuitive expressions of health states of PV panel under different conditions. By analysing the equivalent parameters of the AC-ECM, four health features are defined and extracted. Experiment are organized to verify the correction and effectiveness of the proposed AC-ECM, complete IS spectrum and defined health features in monitoring the health of PV panels.

1.5 Conclusions

In this chapter, the fundamentals of PV panels are introduced, with a focus on silicon PV panels due to their commercialization rate. Corresponding typical faults occurred in panel level are summarized. A state-of-the-art overview of the typical characterization tools for PV panels was then presented, mainly discussed through two categories: offline and online tools. Depending on the signals obtained, these characterization tools can also be classified into two types: imaging tools and electrical signal measurement tools. Each kind of associated characterization method has its strengths and weaknesses. For instance, imaging tools allow for simple and fast examination, but the requirement for additional equipment limits their application in MGs. On the other hand, electrical signal measurement tools exhibit an online characteristics, while corresponding algorithms can be complex. Taking into account the application in MGs, the state of the art in this field of research, numerous improvements in the technological and electronic, theoretical and applied fields are possible for the detection of faults and therefore for the health management of PV panels constituting MGs (Health Management Strategy, HMS). In particular, this thesis focuses on the implementation of the IS and associated control strategies applied to PV panels. IS applied to PV panels is directly integrated into the DC/DC converter, yielding to the converter-based IS. Additionally, the methods specifically studied in this work are based on the development of information systems linked to the simulated and experimental properties of the power converter.

Chapter 2

Fundamentals of converter-based IS for PV panels

2.1 Introduction

IS provides a powerful, non-destructive way to acquire PV panels' internal impedance over a wide frequency range, which can be used to monitor their health states. Compared with workstation-based IS, converter-based IS performed as an added function of the connected DC/DC converters supplies an attractive mean to achieve online IS measurements. It can help reduce overall system costs and facilitates online applications, especially in DC MGs, since this method does not require additional equipment. As introduced in Chapter 1, to ensure the validity of IS implementation, PV panels should operate at a linear/quasi-linear operating region and under stable conditions. However, the output voltage and current of a PV panel show nonlinear characteristics, as indicated by the IV curve in Figure 1.7. As in [81], an IV curve can be divided into three operating regions, including two quasi-linear regions (one quasi-linear current region and one quasi-linear voltage region) and one nonlinear power region close to the maximum power point (MPP). However, the boundaries between these regions are not well defined and can depend on the classification criterion used.

In general, PV panels are controlled by MPPT methods to ensure the output power efficiency [82]. The corresponding operating point, i.e., MPP, is located in the nonlinear power region. When PV panels exhibit soft nonlinearity in proximity to the MPP, MPP can be considered as an injection point for perturbation signal injection. For instance, in [83], an adaptive amplitude-modulated pseudo-random binary sequence excitation method was proposed to improve the accuracy of IS measurements, which was applied at the MPP. However,

in most cases, the MPP is usually not used as the injection point, as it seems to violate the linearity criterion required for IS measurements, as emphasized in section 1.3. Hence, the operating point of PV panels should be changed when transitioning from MPPT mode to IS mode.

This chapter focuses on the cooperative control of MPPT and IS modes. Based on the requirements of the perturbation signals, a classification criterion for operating regions is defined. The selection of the injection region and point for IS implementation is provided in Section 2.2. Considering the requirements of IS measurements, an intermediate mode is defined and the cooperative control strategy of three operating modes is proposed. Meanwhile, the approach of obtaining the IS spectrum based on the perturbation and response signals, along with the corresponding analysis method is provided. Finally, the cooperative control strategy is verified through simulations in MATLAB/Simulink.

2.2 Fundamentals

2.2.1 Operating regions of the PV panel

In linear systems, the output at any frequency is directly proportional to the input at that frequency. Nonlinear systems can generate harmonics and intermodulation products, which are additional frequency components not present in the input signal. According to the performance of PV panels, there is no absolute linear region on the IV curve. Therefore, quasi-linear regions are defined, in our work, based on the percentage of the fundamental component of the response signal at the injecting frequency.

In order to ensure accuracy and linearity, it is generally suggested that the amplitude of the perturbation signal be within the range of 5% to 15% of the DC component [64]. Apart from the amplitude, the fundamental component of the response signal to the perturbation signal at low frequencies (e.g., 1 Hz) reaches or exceeds 85% to guarantee the accuracy. When all the points satisfy the two requirements, corresponding region can be considered as a quasi-linear region. Based on the defined criterion, as illustrated in Figure 2.1, the IV curve can be divided into the three regions, above mentioned and now detailed:

- **Region I:** this region is indicated as the quasi-linear current region, where the PV panel exhibits characteristics akin to a current source.
- **Region II:** this region belongs to nonlinear power region. MPP will be located in this region. However, the response signal exhibits significant asymmetry when injected with a sinusoidal perturbation signal, making it difficult to accurately extract the fundamental signal.

- **Region III:** this region is denoted as the quasi-linear voltage region, where the PV panel operates as a voltage source.

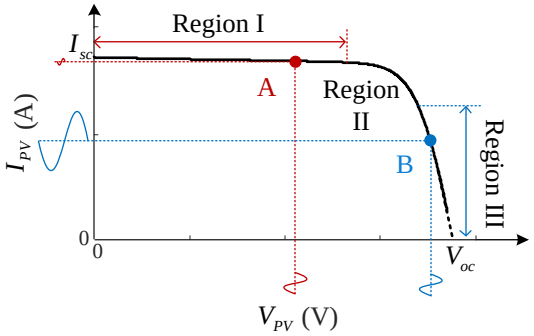


Figure 2.1: Three operating regions of the PV panel.

In theory, either of the quasi-linear regions can be selected to inject the perturbation signal. To ensure the accuracy of measured results, both perturbation signals and response signals should have a sufficient signal-to-noise ration (SNR), which necessitates signals with high amplitudes or accurate sampling devices. According to the characteristics of the PV panel available in LMOPS laboratory (as a reminder, 310 W Recom-Sillia PV panel) under standard conditions, as illustrated in Table 1.1, the maximum changing ranges of the output voltage and current in Region I and III, respectively, can reach:

$$\begin{cases} \Delta V_{PV-max} = 32.3V; \Delta I_{PV-max} = 0.39A; & \text{(in Region I)} \\ \Delta V_{PV-max} = 6.3V; \Delta I_{PV-max} = 9.56A. & \text{(in Region III)} \end{cases} \tag{2.1}$$

Based on (2.1), in Region I, the variable range of output current amplitude is too narrow to accurately extract fundamental perturbation/response signals. By taking A as the injection point, we can observe that the variation range of the PV current is very narrow. It will then be difficult to obtain a variation of the current with sufficient amplitude to distinguish whether the signal corresponds to the response of a disturbance signal from the IS procedure or to a variation of the normal response of the panel. On the other hand, by taking B as the injection point, we can observe that due to the relatively large variation ranges of the voltage and current in Region III, it is possible to inject the perturbation signal of the IS procedure in the form of current or voltage and then clearly identify the corresponding response of the panel. Therefore, Region III is selected as the injection region in our work.

In Region III, the variable range of current is relatively wider compared to voltage. Moreover, the voltage range is more susceptible to environmental factors, such as T, which poses challenges for potential perturbation. Thus, a current perturbation makes it easier to guarantee that the injection point and the perturbation

signal will be located in this region. Meanwhile, a wider frequency range can be obtained by directly controlling the current as it will be analyzed in Chapter 4. Thus, the AC current perturbation signal (hereafter, the perturbation signal represents the AC current perturbation signal) is superimposed on the DC current of the PV panel.

Regarding the selection of the injection point in Region III, in addition to the quasi-linearity of the perturbation response, output power efficiency is another aspect that needs special consideration. Considering the PV curve as shown in Figure 1.7, the closer the injection point is to the MPP, the higher the output power of the PV panel will be available during IS measurements. Therefore, the point closest to the MPP in Region III that can satisfy the amplitude of perturbation signal to reach 5-15% of the DC component will be selected as the injection point of the perturbation signal.

2.2.2 Three operating modes of the PV panel

The stability condition for the validity of IS measurements requires that the system operates in the same stable state before and after the perturbation. This comprises two aspects during IS implementation: stable external operating conditions, maintained by keeping environmental factors unchanged (e.g., irradiance levels and temperatures), and stable internal operating conditions, necessitating a constant output DC current/voltage of the PV panel (in this work, constant DC current is selected) with a steady-state operating state achieved before starting measurements. Concerning this last operating condition, when the PV panel transitions from MPPT mode to IS mode, it will experience a dynamic process due to the change of the operating point, from Region II to Region III. To ensure the stability, the PV panel should operate at the selected injection point for a period before starting IS measurements. Therefore, an intermediate mode, which is named injection point tracking mode (IPT mode) is added between MPPT and IS modes to confirm that the PV panel stably operates at the injection point before the injection of the perturbation signal.

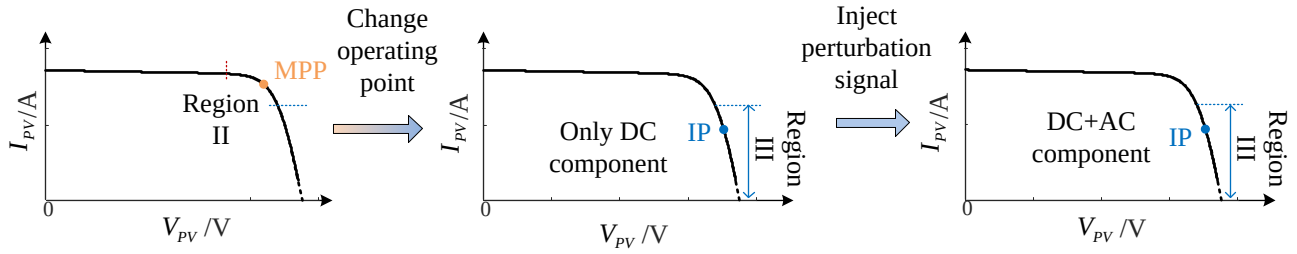
Finally, we see that the PV panel controlled with a health management system by converter-based IS has at least three operating modes:

- **Maximum Power Point Tracking (MPPT) mode**: Output power of the PV panel reaches the maximum value; the operating point, i.e., MPP, is located in Region II, as indicated in Figure 2.2 (a); output voltage and current are optimized to get the maximum power considering their DC components, dynamic perturbations around the MPP only originate from the tracking procedure.
- **Injection Point Tracking (IPT) mode**: Output power of the PV panel will reduce down to the power available in the following IS mode. Nevertheless, it can be guaranteed to a quasi-maximum value by

selecting an appropriate injection point (IP) located in Region III close to the MPP, as shown in Figure 2.2 (b). Output voltage and current only contain their DC components.

- **Impedance Spectroscopy (IS) mode**: The operating point is stabilized at the injection point as illustrated in Figure 2.2 (c). Therefore, output power of the PV panel is approximately equal to that in IPT mode. Perturbation signals will be injected in the system. Thus, output and current will include a DC-bias component modulated with an AC one.

Accurate switching among these different operating modes, associated with a precise control over all these modes can ensure the efficiency and stability of the system, ultimately enhancing the accuracy of IS measurement results.



(a) MPPT mode (b) IPT mode (c) IS mode

Figure 2.2: Operating point in different modes
(a) MPPT mode; (b) IPT mode; (c) IS mode.

2.2.3 Analysis of IS measurements

Once the stability and linearity of IS measurements are satisfied, i.e., when the IS mode is achieved, the impedance of the PV panel can be calculated based on (1.1) in Chapter 1. The perturbation signal and response signal at frequency f_p in time domain can be expressed in Figure 2.3 (a). The red and blue lines represent the AC components of voltage and current signals at f_p, respectively. The phase shift between the two signals is expressed as $\phi(f_p)$. The forms of the phase vectors of all the signals and corresponding impedance in complex coordinates are depicted in Figure 2.3 (b). The impedance at f_p is classically expressed as:

$$Z(f_p) = Re(f_p) + j \cdot Im(f_p) \tag{2.2}$$

where $Re(f_p)$ and $Im(f_p)$ represent the real part and imaginary part of the impedance, respectively. Their value are calculated by:

$$\begin{aligned} Re(f_p) &= \frac{V_{ac}}{I_{ac}} \cdot cos(\phi(f_p)) \\ Im(f_p) &= \frac{V_{ac}}{I_{ac}} \cdot sin(\phi(f_p)) \end{aligned} \tag{2.3}$$

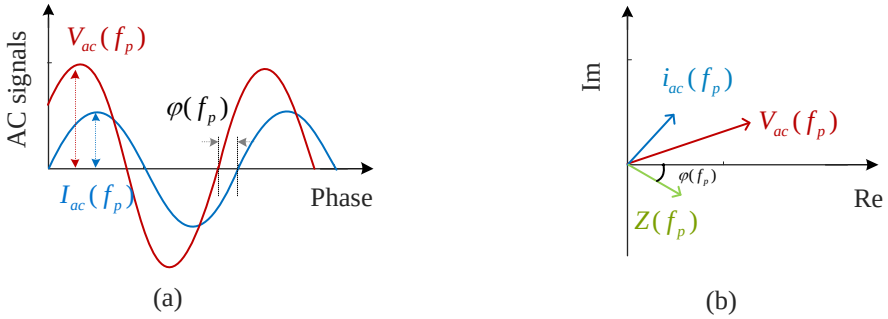


Figure 2.3: Perturbation and response signals at frequency f_p
(a) two signals in time domain; (b) phase vectors in complex plane, adapted form [6].

Based on the injection of a perturbation signal with a wide-band frequency range, a series of impedance points can be obtained to constitute the IS spectrum. In general, the IS spectrum remains incomplete due to the limited frequency range of the perturbation signal($\leq$ 10 kHz), and needs to be completed according to the operating conditions, with further details discussed in Chapter 3. Then, combined with the AC equivalent circuit model (AC-ECM), the corresponding health features can be extracted to describe the health states of the PV panel.

A typical IS spectrum of PV panel in Nyquist plot with a single time constant is illustrated in Figure 2.4 (a). In this figure, the green solid line represents the information based on the tested results, green dashed line is the fitting part. It corresponds to an AC-ECM shown in Figure 2.4 (b), which consists of a resistance R_p in parallel with a capacitor C_p, which is shifted from the origin by a series resistance R_s. The frequency of the top point of the Nyquist plot is satisfied as: $f_0 = 1/(2\pi R_p C_p)$ [66]. Theoretically, once the impedance at f_0 is obtained, the value of R_s can be determined by curve fitting methods even without a complete spectrum [84]. Detailed information, such as the physical meaning of each parameter and the corresponding values, will be presented and analyzed in Chapter 3.

In summary, the key to the implementation of converter-based IS is the accurate control of different modes. The consideration of an appropriate AC-ECM is crucial to analyze the health states of the PV panel based on the measured IS information. The next section will focus on the cooperative control strategy of different modes.

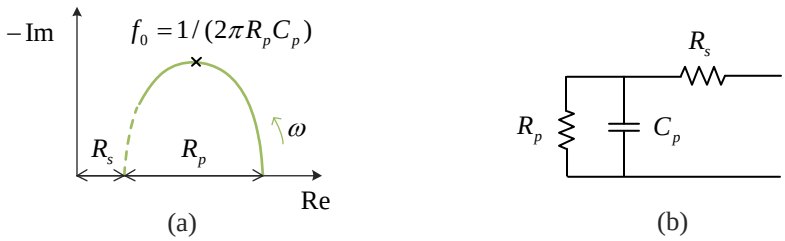


Figure 2.4: Analyzing method of the IS information
(a) IS spectrum; (b) Corresponding AC-ECM.

2.3 Cooperative control strategy

2.3.1 Control blocks

The control scheme of the PV panel applied in MGs is shown in Figure 2.5. The blue lines in the figure represent the signal flow, including sampling data and switching signals. The voltage and current signals are sampled by corresponding sensors and sent to the control part. An appropriate control strategy, named as a bi-level control strategy, provides switching signals to the connected DC/DC converter. This bi-level control strategy can be divided into upper-level and lower-level control. The upper-level control manages all the operating modes, also named as cooperative control. The lower-level control handles the control of different operating modes. In this work, the various step P&O MPPT method is selected for MPPT mode, whose flowchart is shown in Figure 1.8. Two types of lower-level control strategies for IPT and IS modes are proposed in Chapter 4 and Chapter 5.

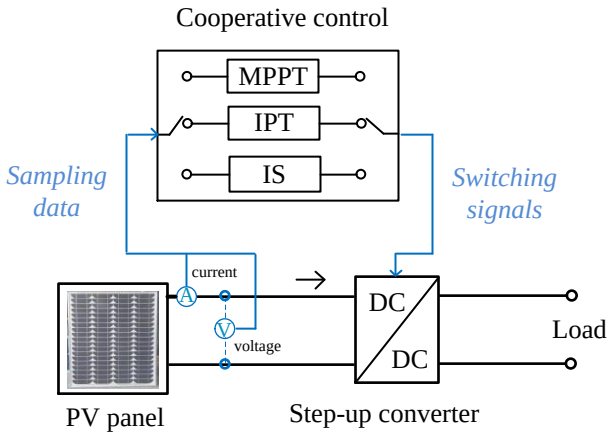


Figure 2.5: Control scheme of a PV panel with different operating modes.

The control flowchart of the cooperative control strategy is depicted in Figure 2.6. According to the

operating period or whether the maximum output power is abnormally reduced, a trigger signal for starting health monitoring is set. When there is no trigger signal, the PV panel operates in MPPT mode. When the trigger signal is started, the PV panel switches to the IPT mode to ensure that it reaches a stable state after the injection point is changed from the MPP to IP. The PV panel then outputs the target DC current of IP. Once the PV panel works in IS mode, it starts injecting perturbation signals with a wide-band frequency. In order to further ensure the stability of the IS measurements, multiple measurements should be repeated under the same operating conditions and their consistency will be checked. The sign to end health monitoring (IPT and IS modes) is determined by judging whether the number of repetitions has been reached. After health monitoring ends, the PV panels will revert to MPPT mode and await the trigger for the next health monitoring cycle, unless the end signal is received to cease control.

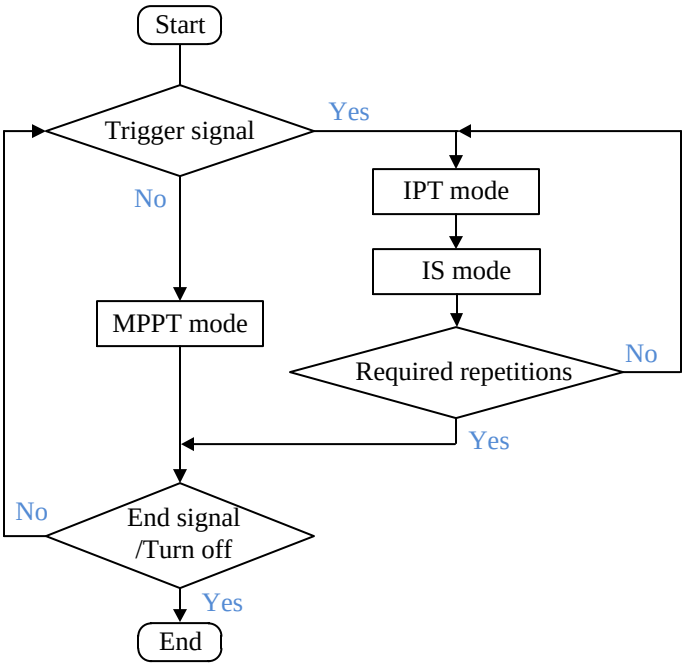


Figure 2.6: Control flow of the cooperative control.

2.3.2 Simulation platform

To verify the proposed control strategy, a simulation platform is established in MATLAB/Simulink, as indicated in Figure 2.7. The parameters of all elements are the same as those of the experimental platform in Chapter 6. Considering the simulation is executed in discrete mode, a capacitor, i.e., C_1, is parallel with PV panel to ensure a continuous voltage output. A conventional boost converter based on a half-bridge is selected to achieve the step-up of the output voltage of PV panel. The value of the inductor and DC bus

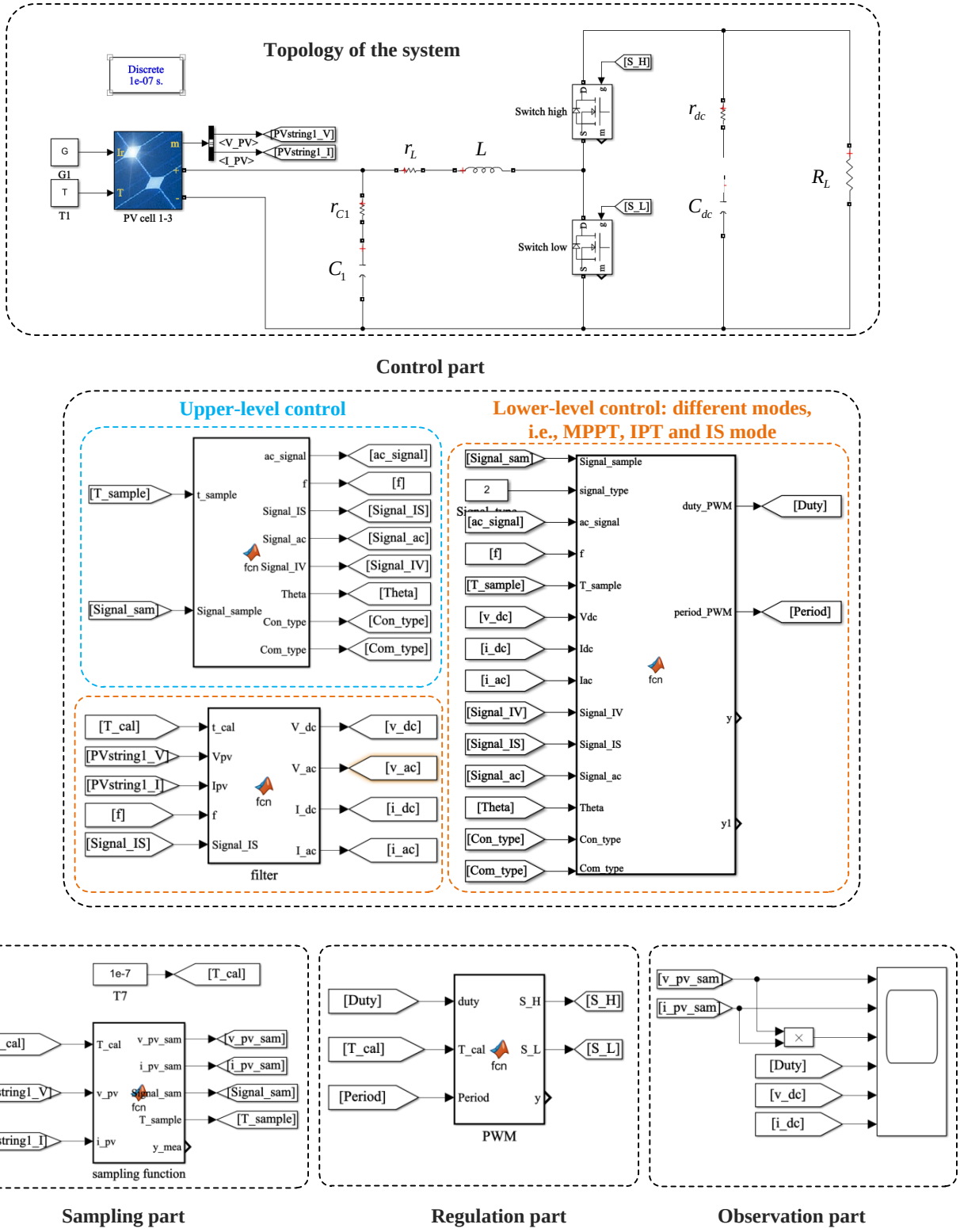


Figure 2.7: Simulation platform.

capacitor are set as: $L = 2.5\ m\mathrm{H}, C_{dc} = 260\ \mu\mathrm{F}$. Both the sampling frequency and switching frequency are equal to $80\ k\mathrm{Hz}$, i.e., $f_{sam} = 80\ k\mathrm{Hz}$ and $f_{sw} = 80\ k\mathrm{Hz}$. The environmental factors, i.e., irradiance levels and temperature, are denoted as G and T in the simulation, whose values can be set in the workspace, e.g., $G = 250\ \mathrm{W/m^2}, T = 323.15\ \mathrm{K}$. The resistance is operated as the load, e.g., $R_L = 163\Omega$.

All the control strategies are written in discrete format based on *m-function*. To save the simulation time, there are some differences from the experiment: the MPPT mode will last for 1.6 s, after which the trigger signal for starting health monitoring will be given; the number of receptions of IPT and IS modes is set to 2; the perturbation signal at each frequency only runs for one cycle considering the simulation time limitation. The frequency range of perturbation signal is equal to [1 Hz 2 kHz] based on the experimental conditions and the characteristics of the PV panel in the laboratory.

It must be noted that the model of the PV panel in MATLAB/Simulink is an equivalent circuit based on a single-diode DC ECM as illustrated in Figure 1.6 (a), which can effectively reflect the DC voltage and current characteristics under different operating conditions, depicted as the IV and PV curves. However, it cannot accurately mirror the AC impedance characteristics of the real PV panels. Therefore, in our work, the simulation is only used to verify the effectiveness of the control strategy's functions, but the corresponding perturbation and response signals are not used to analyze the IS information.

2.3.3 Simulation results

Based on the simulation platform, the IV and PV curves are simulated and shown in Figure 2.8. The maximum output power under the set operating conditions can reach 41 W, and the corresponding output voltage and current are equal to 33.1 V and 1.22 A, respectively. According to the classification criterion of the quasi-linear region and the consideration of the selection of the injection point, the current of IP is equal to 1 A. The FFT analysis results of the response signal (AC component of voltage signals) at 1 Hz is depicted in Figure 2.9, where the percentage of the fundamental component is equal to 85.9%. The output power at IP is equal to 35 W. Compared to the MPPT mode, the output power at IP is larger than 85% of the MPP, which ensures a quasi-maximum output power in IS mode.

The cooperative control results are demonstrated in Figure 2.10. The simulation results show that when there is a trigger signal, the PV panel is first controlled in the IPT mode and quickly stabilizes at the IP. Then a perturbation signal is injected, indicating that the PV panel is performed in IS mode. During the measurement, the DC component of the output current of the PV panel remains at a constant value, i.e., 1 A, ensuring a stable IP. Stable control of the system is realized during repeated IPT and IS modes. After completing the required

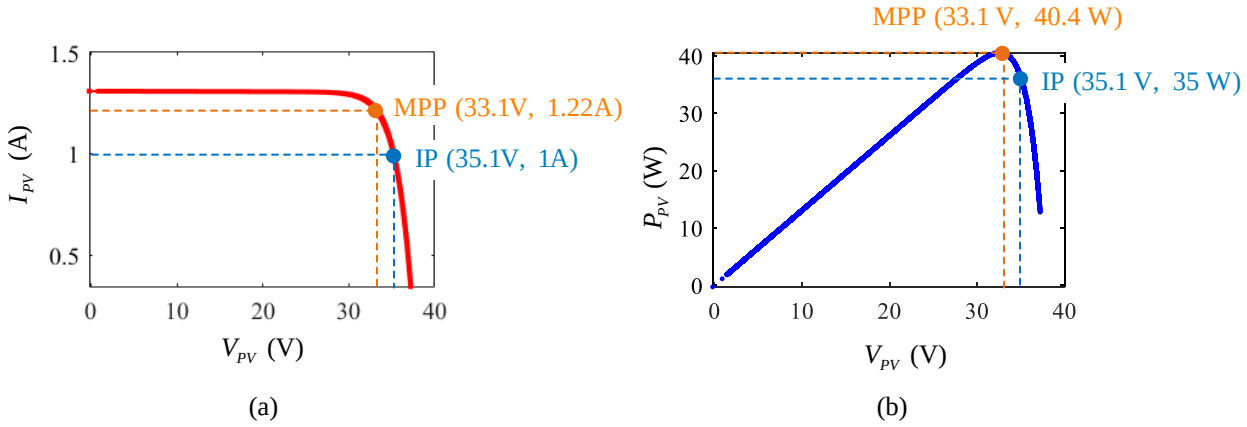


Figure 2.8: Output characteristics of the PV panel
(a) IV curve; (b) PV curve.

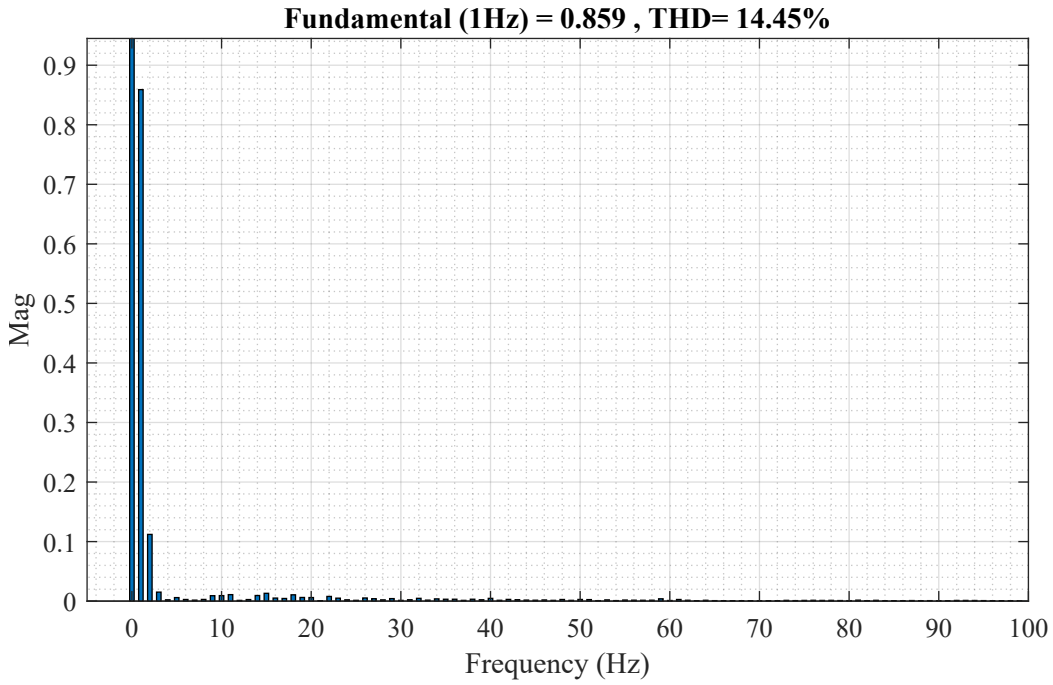


Figure 2.9: FFT analysis results of response signal at 1 Hz.

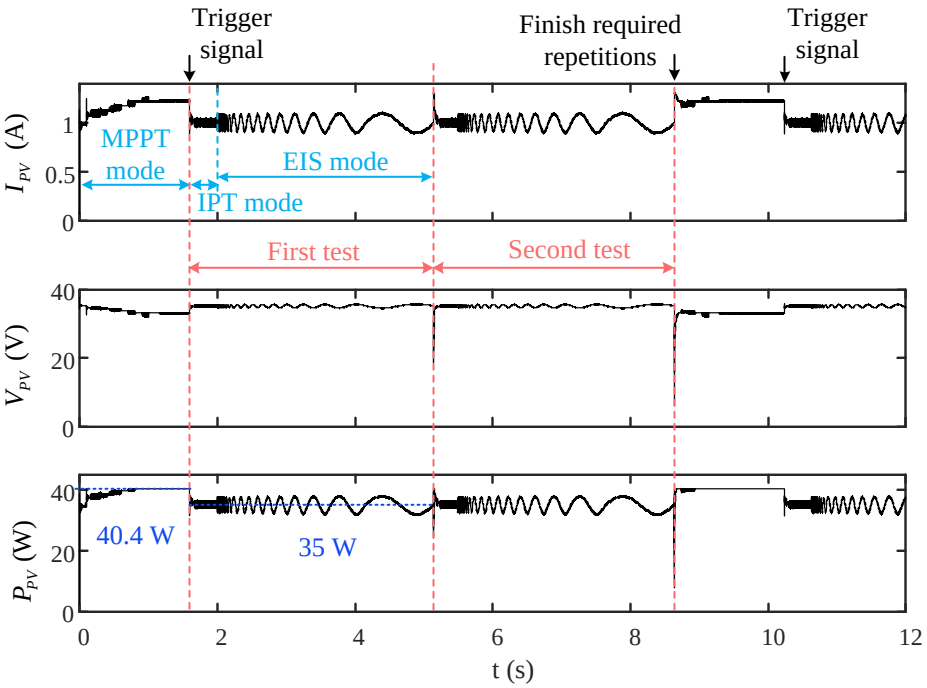


Figure 2.10: Simulation results under cooperative control strategy.

repetitions, the PV panel operates in MPPT mode again and rapidly stabilizes to the MPP until it receives next trigger signal.

The simulation results validate that the control program well executes the flowchart shown in Figure 2.6, achieving the cooperative control between different modes and the online injection of perturbation signals. The detailed control strategy and the parameter setting of IPT and IS modes will be introduced in Chapter 4 and Chapter 5.

2.4 Conclusions

In this chapter, the fundamentals of converter-based IS for PV panels are introduced. In order to guarantee the stability and linearity during IS implementation, the selection criteria for the injection region and point are provided based on the analysis of the characteristics of PV panels. Meanwhile, an intermediate mode is defined to ensure the stability before and after perturbation signal injection. The analysis method of the IS spectrum is further presented, which indicates that an appropriate AC-ECM is crucial to interpret the IS measurements and the health states of PV panels.

A bi-level control strategy consisting of upper-level and lower-level control is proposed. The upper-level

control strategy is focused on in this chapter to achieve the cooperative control between different modes. It is verified by simulation in MATLAB/Simulink. The simulation results show that the converter-based IS can achieve relatively higher output power (higher than 85%) when operating at the IP selected based on the defined criteria in this chapter. In the next chapter, the AC-ECMs of silicon PV panel will be focused on. Meanwhile, more detailed connections between the IS spectrum, AC-ECM and operating conditions will be revealed.

Chapter 3

Equivalent circuit models of silicon PV panels

3.1 Introduction

Converter-based IS provides an approach to obtain the IS spectra online. The analysis of IS spectra needs to be combined with corresponding algorithms to extract health features, such as machine learning methods and so on. In this process, the AC equivalent circuit model of silicon PV panels, i.e., AC-ECM, is an indispensable part. It equates the internal relaxation processes of the PV cells/panels to corresponding electrical elements, and the values of these elements can be used to quantify the health states under different conditions.

The AC-ECMs consist of basic electrical elements connected in parallel and series. Their electrical symbols are illustrated in the Figure 3.1, including resistor, R, inductor, L, capacitor, C and constant phase element, CPE. CPE is a non-intuitive circuit element that was introduced by X. Yuan $et\ al.$ [62, 68] in the course of investigations into responses from real systems. The impedance of all the elements at angular frequency ω can be calculated by:

$$\begin{cases} \text{Resistor}: & Z_R(\omega) = R; \\ \text{Inductor}: & Z_L(\omega) = j\omega L; \\ \text{Capacitor}: & Z_C(\omega) = 1/(j\omega C); \\ \text{CPE}: & Z_{CPE}(\omega) = A^{-1}(j\omega)^{-\alpha}; \end{cases} \tag{3.1}$$

where A and α represent the factor of proportionality having numerical values, and the CPE exponent that characterizes the phase shift, respectively. The value of α is located in [-1 1]. For integral values of α ($\alpha = 1,\ 0,\ -1$), the CPE represents C, R and L, respectively. The total impedance of AC-ECM can be expressed by the value of corresponding elements based on (3.1) and Kirchhoff's Laws.

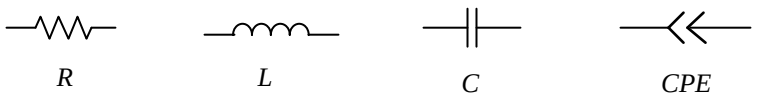


Figure 3.1: Basic electrical elements.

Several AC-ECMs of PV cells/panels are proposed to describe their internal characteristics, efficiency and degradation, etc. In the AC-ECMs, a sub-circuit consisting of a combination of parallel resistor and capacitor or CPE is associated with a time constant, i.e., $\tau = RC$ or $\tau = RCPE$, representing one relaxation process. Based on the number of time constants, the typical AC-ECMs of silicon PV cells/panels can be categorized into three types: single-time-constant-based, double-time-constant-based and three-time-constant-based AC-ECMs, as described below.

1. Single-time-constant-based AC-ECM

Single-time-constant-based AC-ECM is the simplest one, as shown in Figure 3.2 (a), including one series resistor and inductor, and one parallel resistor and capacitor denoted as R_{s1}, L_{s1}, R_{p1} and C_{p1}, respectively. In general, the series inductor represent the impedance characteristic at high frequencies, and therefore is ignored in most literature due to the frequency limitation of impedance analyzers. In our work, to ensure the integrity, the inductor is indicated in the schematic diagram. Of course, the two AC-ECMs with and without series inductor are regarded as the same type. The same considerations apply to both double-time-constant-based and three-time-constant-based AC-ECMs.

From [7], we illustrate the AC-ECM in Figure 3.2 (b). In this model, C_{p1} is replaced by CPE used to fit and analyze the IS spectrum of PV cells obtained under dark conditions across a wide frequency range, from 1 Hz to 100 kHz. R.A. Guejia-Burbano $et\ al.$ [85] used the same AC-ECM to analyze the impedance of PV panels operating at MPP in the outdoor conditions with a frequency range from 10 Hz to 50 kHz. The analyzing results in both literature show the value of the phase shift is very closed to 1, meaning that the CPE can be approximated as a capacitor. Therefore, IS spectrum of PV cells can be accurately fit by the AC-ECM in Figure 3.2 (a).

The impedance of PV panels under normal conditions and suffering from Potential induced degradatio (PID) were compared experimentally in [86] using a HP 4284A Precision LCR meter. The frequency range employed was 20 Hz - 100 kHz. Its results show that PID will cause a substantial increase in the value of R_{p1}

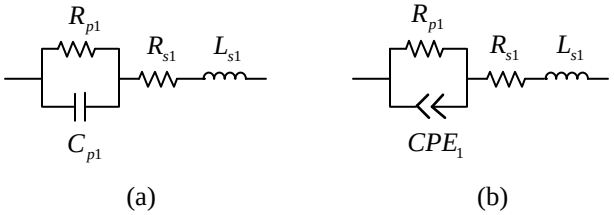


Figure 3.2: Single-time-constant-based AC-ECM (adapted from [7]).

and a decrease in the value of C_{p1}. In [87], following the analysis of IS spectrum measured at MPP under the constant irradiance level, it was found that the value of R_{s1} is nearly unchanged and is not influenced by the failure of the semiconductor, such as PID. It can be treated as a characteristic to determine whether electrical connection faults have occurred.

The physical meaning of each element in AC-ECM is provided in Refs. [88, 89, 90, 91] by analyzing corresponding DC-ECM. R_{s1} and L_{s1} represent the wire and lead resistance and inductance, respectively. Their values are impacted by the physical length, area, and shape of the leads and usually keep constant. On the other hand, the values of R_{p1} and C_{p1} vary with the temperatures and irradiance levels [92, 93]. In [88], D. Chenvidhya $et\ al.$ analyzed the influence of forward DC-bias voltage on the impedance of PV cells in dark conditions. In Refs [29, 89, 90, 94], authors combined in C_{p1} three capacitors in parallel: junction, diffusion, and breakdown capacitor. The partial shading and hot spot can be detected based on the value changing of $R_{s1} + R_{p1}$ and C_{p1}. The single-diode DC-ECM is enhanced in [95] based on the analysis of various layouts of PV cells. Simultaneously, the meanings of junction and diffusion capacitor are elucidated.

However, in [96] S. Kumar $et\ al.$ studied the PV cells impedance information of different light intensities and wavelengths and found that the value of R_{s1} displays an obvious decreasing trend with the increase in light intensity. However, at different wavelengths, it was not a single trend. With the 850 nm wavelength being the boundary, R_{s1} shows a trend of initially increasing and then decreasing. Meanwhile, the impedance of PV cells under illumination is measured under different forward DC-bias voltages in [97]. It was verified that a second time constant appears within a certain voltage range. However, the corresponding reasons and physical meanings for the second time constant are not analytically explained.

Therefore, it can be summarized that the irradiance level and the forward DC-bias voltage at the injection point will significantly affect the accuracy of the monitoring result analysis based on single-time-constant-based AC-ECM, especially in operational conditions, i.e., for the PV panels installed outdoors.

2. Double-time-constant-based AC-ECM

Considering the limitations of single-time-constant-based AC-ECM, the double-time-constant-based AC-

ECM is proposed as shown in Figure 3.3, including two sub-circuits, i.e., $C_{p2}||R_{p2}$ and $C_{p3}||R_{p3}$ or $\mathrm{CPE}_2||R_{p3}$ in Figure 3.3 (a) and (b). In Refs. [8], D. J. Crain $et\ al.$ changed the form of the sub-circuit to describe the high-frequency and low-frequency parts more clearly. But the final IS spectrum of the three types of sub-circuits behaves in almost the same way and represent two relaxation processes. These two relaxation processes have been explained from different perspectives.

In Refs. [9, 98], authors represent in two sub-circuits the equivalent impedance of the $p-n$ junction and low-high junction, respectively. In [99] I. Mora-Sero $et\ al.$ analyzes the recombination rate in silicon PV cells based on impedance information, where the capacitive and resistive effects of two sub-circuits arise from the electrons and holes capture, respectively. On the other hand, in [11], A. Panigrahi $et\ al.$ described the relaxation processes as transport dynamics of the disordered junction and carrier recombination dynamics.

Based on Fermi level analysis, a detailed electro-analytical framework for the direct determination of a broad range of performance-indicator parameters of silicon solar cells was reported in [9, 98]. Meanwhile, they pointed out that the series element, i.e., R_{s2}, contains a strictly ohmic component and non-ohmic resistance associated with the irradiance level. The corresponding influence of temperature, irradiance level and forward DC-bias voltage on other parameters of AC-ECMs were analyzed in Refs. [9, 98, 11]. The locations of all the equivalent electrical elements in the layout of PV cells were provided in Refs. [95, 100]. By analyzing the recombination processes in both the space-charge region (SCR) and quasi-neutral region (QNR), the reason for the occurrence of an obvious second time constant within a certain voltage range becomes clear. It was pointed out that as the forward DC-bias voltage of PV cells increases, the width of the SCR decreases, thereby altering the relative size of the two regions, leading to the emergence of the second time constant.

Based on the double-time-constant-based AC-ECMs, some fault detection and carrier lifetime analysis were made in Refs. [101, 102, 103, 104] with the frequency range primarily distributed across a wide band, e.g. 100 Hz - 150 kHz. However, the detailed information of IS implemented in PV cells/panels was not provided. The influence of the amplitude of the perturbation signal on the accuracy of measured results was analyzed in [105], where the MPP was selected as the injection point. The measurement results show that due to the nonlinear characteristics of the PV panel at the MPP, different amplitudes of the perturbation signal have a significant impact on the measurement results, even if the amplitude of perturbation signal accounts for less than 3/550 of the DC component at MPP. This poses a big challenge to the accuracy of the sampling device, as stated in Chapter 2.

In [106], T. Tanahashi $et\ al.$ used IS to study the degraded location and characteristics of PV panels. The voltage at the injection point is equal to the open-circuit voltage. According to above explanation, in theory, the PV cell/panel should exhibit a single time constant. However, due to the degradation with acidic corrosion,

an additional impedance appears. The value of this impedance is unaffected by the forward-bias voltage, and can be therefore used to help identify the occurrence of degradation on the back surface.

A summary of existing single-time-constant-based and double-time-constant-based AC-ECMs was provided in [107]. Most studies focused on the cell level and considered the influence of forward DC-bias voltage. However, the impact of illumination was ignored, which would result in an additional relaxation process. Therefore, double-time-constant-based AC-ECMs are more suitable for dark conditions or the low irradiance-level conditions.

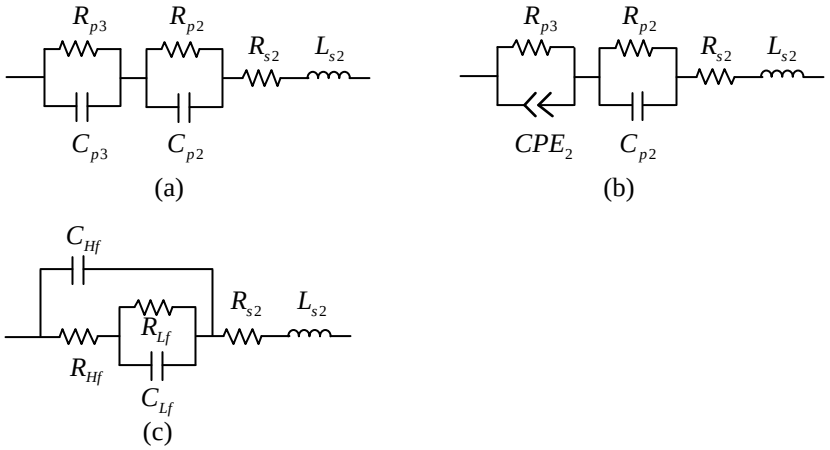


Figure 3.3: Double-time-constant-based AC-ECM (adapted from [8, 9]).

3. Three-time-constant-based AC-ECM

Based on the double-time-constant-based AC-ECM shown in Figure 3.3 (b), three-time-constant-based AC-ECM for PV cells under illuminations was proposed in [11], and illustrated in Figure 3.4 (a), where an additional sub-circuit $R||C$ was included to account for the dynamics caused by illumination. Detailed changing trends of all parameters with the changes of operating conditions were provided as well. Similar to the considerations in double-time-constant-based AC-ECM shown in Figure 3.3 (c), an AC-ECM indicated in Figure 3.4 (b) was proposed to enhance the description clarity of low-frequency and high-frequency parts in [8]. However, the calculation of corresponding relaxation time constants becomes complicated. It should be noted that the frequency of perturbation signals should exceed 10^6 Hz to obtain the complete IS spectrum covering three time constants.

In addition to the above three types, several AC-ECMs have been proposed to analyze the internal structures of third generation PV cells. An ECM was proposed in [108] to analyze the characteristics of organic PV cells at the nanostructured level. A. Omar *et al*. [109] studied the electron transport properties of titanium dioxide dye-sensitized PV cells based on different dyes. The AC-ECMs about metal halide perovskites PV

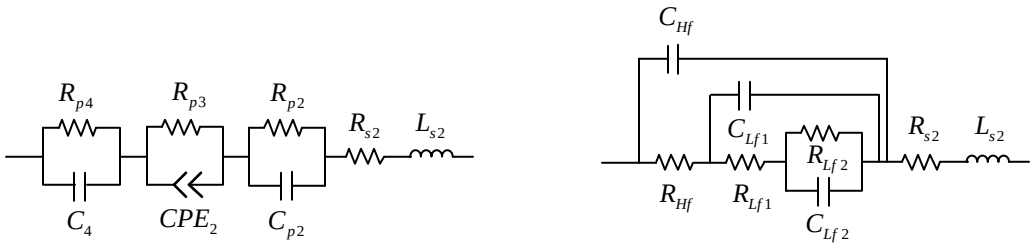


Figure 3.4: Three-time-constant-based AC-ECM (adapted from [8, 9]).

cells under different conditions were summarized in [110].

This work mainly focuses on converter-based IS for silicon PV cells/panels, which currently holds the largest percentage in the commercial market. Based on above analysis, a three-time-constant-based AC-ECM is a better choice for accurately describing the impedance performance of PV cells. Nevertheless, when existing AC-ECMs are employed in converter-based IS analysis, several limitations exist, which can be summarized in following aspects:

- **Application limitation**
  Most of the existing AC-ECMs have been tested based on PV cells or small PV panels. However, large PV panels integrate bypass diodes to mitigate the impact of partial shading and enhance the operating efficiency [28]. These bypass diodes are not considered in the existing AC-ECMs.

- **Testing condition limitation**
  In laboratory testing conditions, which are typically conducted in indoor environments, PV cells are usually tested in dark or open-circuit conditions. Consequently, no generated power exists under both conditions. However, with a converter-based IS implementation, the PV panel will exhibit a continuous power output to ensure the operating efficiency. This results in a deviation of the internal relaxation process from that without power output.

- **Frequency limitation**
  To obtain a relatively complete IS spectrum, the frequency range of the perturbation signal should be wide enough. For example, the current IS workstations for cell-level tests have reached MHz. Such a wide frequency range brings several challenges, including wide-band frequency devices (i.e., switches and sampling sensors), and control strategies. Although wide bandwidth devices are developing well, they still pose a high cost for small to medium power scale residential MGs.

To overcome all the above-mentioned limitations, an AC-ECM suitable for large PV panels in MGs is re-

quired. With this in mind, this chapter focuses on the design of the AC-ECM for silicon PV panels considering the presence of bypass diodes. Section 3.2 provides a detailed explanation of the internal relaxation process of PV cells. The two-diode DC-ECM is introduced in Section 3.3. In Section 3.4, based on the AC-ECM of PV cells, a simplified AC-ECM of PV panels with consideration the bypass diode is proposed, which is more suitable for the health monitoring based on converter-based IS. Corresponding features to describe the relaxation processes are extracted and analyzed. Finally, the conclusions are given in Section 3.5.

3.2 Physical model

As introduced in Chapter 1, silicon PV cells/panels account for 90% of the commercial productions. Silicon PV cells/panels rely on a $p-n$ junction to achieve the conversion from solar energy to electricity. Typically, the $p-n$ junction is made in a wafer of $p-$type silicon, which is thick $(300-500\ \mu m)$ to absorb as much light as possible and lightly doped ($\sim 10^{16}\ cm^{-3}$) to improve diffusion lengths. $n-$type silicon is used as the emitter with heavy doping ($\sim 10^{19}\ cm^{-3}$) to reduce sheet series resistance. It must be noticed that $n-$type silicon should be thin enough to allow as much light as possible to pass through to the base, but thick enough to keep series resistance reasonably low [111].

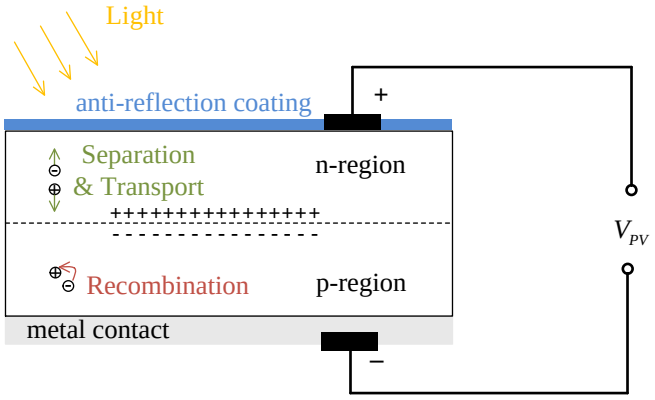


Figure 3.5: Schematic diagram of a PV cell structure.

A schematic diagram of a PV cell is shown in Figure 3.5. The light shining on the PV cell is divided into three parts: reflection, transmission and absorption. The absorption part excites the electrons in the $p-n$ junction, providing them with enough energy to undergo energy level transitions, resulting in the formation of free electrons and holes, known as carriers. When the positive and negative electrodes are connected by loads or a forward DC-bias voltage source, the carriers move in a direction, generating an output current, denoted as I_{PV}, and the corresponding output voltage is denoted as V_{PV}.

In this process, there are four main relaxation processes inside the PV cell and the corresponding typical time scales and frequency ranges are indicated in Figure 3.6 adapted from [10]. Based on the speed of the time scales, these relaxation processes are expresses as following:

- Femtosecond-level time scale: The relaxation process in this time scale is caused by electronic transitions and can typically be studied with transient optical spectroscopy.
- Nanoseconds-level time scale: The relaxation process in this time scale can be used to describe the molecular or lattice polarization, as well as dipolar rearrangement, which may be observed with dielectric spectroscopy.
- Microseconds-level time scale: The relaxation processes appear in Microseconds level or slower can be investigated with electrical spectroscopy and results from both electronic and ionic conduction. It is illustrated as conductivity and electron transfer in Figure 3.6.

Electronic and ionic conduction are associated with carrier diffusion and recombination processes in PV cells, as illustrated in Figure 3.5. This relationship can be possibly examined using IS spectrum analysis, which is one type of electrical spectroscopy. Conductivity is determined by the total equivalent resistance of PV cells and is closely related to the output characteristics of electrical signals, namely I_{PV} and V_{PV}. Therefore, in the following investigation of DC characteristics and AC impedance information, these two aspects are the focus.

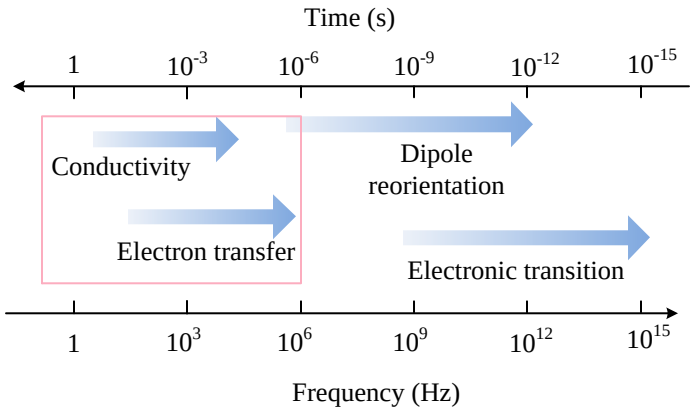


Figure 3.6: Relaxation processes in silicon PV cells (adapted from [10]).

3.3 DC equivalent circuit model

To describe the DC characteristics of PV cells/panels, several DC-ECMs have been proposed in the literature. The diffusion and recombination processes can be represented by two diodes in a typical two-diode DC-ECM [112], as depicted in Figure 3.7, where I_{ph} represents the photocurrent determined by the irradiance level; I_{d1} and I_{d2} are the currents flowing the two diodes and represent the diffusion and recombination processes, respectively; the leakage current, i.e., I_{sh}, flows through the shunt resistor denoted as R_{sh}; R_{series} represents the series resistor.

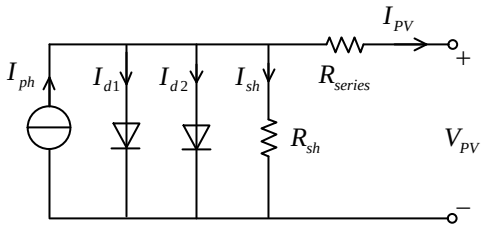


Figure 3.7: Two-diode DC-ECM of PV cells/panels.

With illumination, the output current, denoted as I_{PV}, can be expressed as:

$$I_{PV} = I_{ph} - I_{d1} - I_{d2} - I_{sh} \tag{3.2}$$

The relationships between the I_{d1} and I_{d2} and the output voltage V_{PV}, are described by:

$$\begin{cases} I_{d1} = I_{s1}\left(exp\left(\dfrac{V_{PV} + R_{series}I_{PV}}{n_1 V_t}\right) - 1\right) \\ I_{d2} = I_{s2}\left(exp\left(\dfrac{V_{PV} + R_{series}I_{PV}}{n_2 V_t}\right) - 1\right) \\ I_{sh} = \dfrac{V_{PV} + R_{series}I_{PV}}{R_{sh}} \end{cases} \tag{3.3}$$

with:

$$V_t = \frac{kT_t}{q} \tag{3.4}$$

where:

- I_{s1} and I_{s2}: the reverse saturation currents of the diffusion and recombination processes, respectively;
- n_1 and n_2: the ideality factors of the diffusion and recombination diodes, respectively;
- V_t: the thermal voltage;
- T_t: the temperature of the operating PV cells/panels in Kelvin (K);
- k: the Boltzmann constant ($k = 1.38 \times 10^{-23}\mathrm{J/K}$);
- q: the elementary charge of an electron ($q = 1.6 \times 10^{-19}\mathrm{C}$);

Based on (3.2), (3.3) and (3.4), the relationship between I_{PV} and V_{PV} can be obtained:

$$\begin{aligned} I_{PV} =& I_{ph} - I_{s1}\left(exp\left(\frac{V_{PV} + R_{series}I_{PV}}{n_1 V_t}\right) - 1\right) \\ & - I_{s2}\left(exp\left(\frac{V_{PV} + R_{series}I_{PV}}{n_2 V_t}\right) - 1\right) - \frac{V_{PV} + R_{series}I_{PV}}{R_{sh}} \end{aligned} \tag{3.5}$$

(3.5) clearly points out that the relationship between the output current and voltage of PV cells/panels are nonlinear. Based on this relationship, the DC characteristics of PV cells/panels can be analyzed. And some faults can be detected. In this process, seven unknown parameters in the two-diode DC ECM are I_{ph}, I_{s1}, I_{s2}, n_1, n_2, R_{sh} and R_{series}. According to the analysis in [113, 114], the value of n_1 and n_2 are usually equal to 1 and 2, respectively. In general, the value of I_{ph}, I_{s1} and I_{s2} can be calculated based on the open-circuit voltage, i.e., V_{oc}, short-circuit current, i.e., I_{sc}, and the voltage and current at MPP, i.e., V_{MPP} and I_{MPP}. Detailed calculations can be found in [112], with an example provided. It shows that the value of I_{s2} is much significantly larger than I_{s1}, e.g., $I_{s1} = 7.9406 \times 10^{-11}$ A, $I_{s2} = 5.0762 \times 10^{-6}$ A for a mono-crystalline PV cell. This substantial difference causes the relationship in relative magnitudes between I_{d1} and I_{d2} to vary with the changes of V_{PV}, as indicated in Figure 3.8, based on the provided other parameters in [112].

Here, the conductivity of the PV panel is defined and interpreted as follows: it represents the total value of the equivalent resistance of the PV panel, mainly including two resistances caused by diffusion and recombination processes. As the total value of the equivalent resistance decreases, the conductivity increases, presenting as the increase of the internal current, i.e., $I_{d1} + I_{d2}$.

It can be observed in Figure 3.8 that, as the V_{PV} increases, the conductivity of PV cells/panels also increases. The alteration in the relative magnitudes of I_{d1} and I_{d2} signifies the shift in the dominant relaxation process, meaning that the hindrance to conductivity created by diffusion and recombination processes changes with the output voltage of the PV panel.

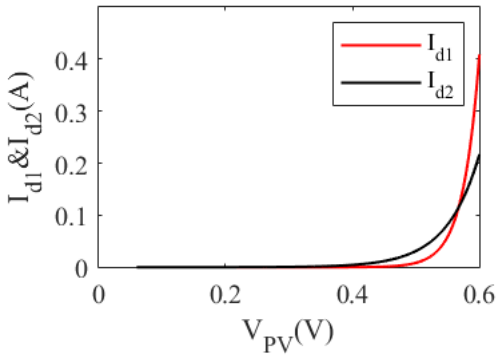


Figure 3.8: Currents of two diodes of DC-ECM.

In the low voltage region, especially in Region I as indicated in Figure 2.1, the conductivity of PV cells/panels is poor, and the diffusion process has a greater hindrance to conductivity. In the high voltage region, such as Region III as illustrated in Figure 2.1, the conductivity is greatly improved, and the main obstacle becomes the recombination process. However, because DC-ECM only consider DC components, it can only reflect changes in conductivity related to equivalent resistance. The time constant at which the internal relaxation process occurs is not available. To obtain more information, development and analysis of AC-ECMs are necessary.

3.4 AC equivalent circuit model

3.4.1 AC equivalent circuit model of silicon PV cells

According to the DC-ECM and considering the influence of illumination, an AC-ECM of PV cells is illustrated as Figure 3.9. Three sub-circuits represent the relaxation processes of diffusion(transport dynamics of carriers), recombination, and illumination influence, denoted as $R_{tr}||C_{tr}$, $R_{rec}||C_{rec}$, and $R_{il}||C_{il}$, respectively. R_{series} and L_{serie} represent the resistance and inductance caused by the connection and associated with the physical length, area, and shape of the leads, respectively.

In order to simplify the analysis, the following assumptions are made in this work when studying the AC-ECM of PV cells/panels:

1. The irradiance and temperature of PV cells/panels are uniform and constant during IS implementation.
2. The voltage across R_{series} is ignored considering the small value of R_{series}. In other words, the forward

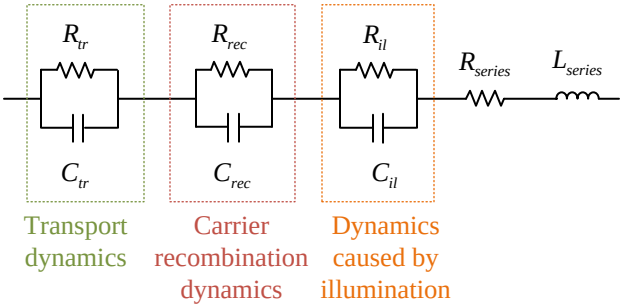


Figure 3.9: AC-ECM of PV cells (adapted from [11]).

DC-bias voltage of PV cells/panels is equal to V_{PV}.

3. The CPE is considered as a capacitor since the tested phase shift is very close to 1 in most literature.

Based on the above assumptions, the detailed information of the three sub-circuits can be summarized as follows:

- **Diffusion relaxation process** $R_{tr}||C_{tr}$
  The corresponding relaxation time constant, denoted as τ_{tr}, represents the transit time or the time of charge transport, i.e., the time taken by a charge carrier to transit across the PV cell. This value can be expressed as:

$$\tau_{tr} = R_{tr}C_{tr} \tag{3.6}$$

  The corresponding values of R_{tr} and C_{tr} are associated with V_{PV}, temperature and irradiance level. And the values of the three variables are satisfied as:

$$\begin{cases} ln(R_{tr}) \propto -\dfrac{V_{PV}}{m_{tr1}V_t} \\ ln(C_{tr}) \propto \dfrac{V_{PV}}{m_{tr2}V_t} \\ \tau_{tr} \propto exp\left(-\dfrac{V_{PV}}{m_{tr3}V_t}\right) \end{cases} \tag{3.7}$$

  where V_t is the thermal voltage, m_{tr1}, m_{tr2} and m_{tr3} are coefficients associated with the ideality factor n_1 [11].

- **Recombination relaxation process** $R_{rec}||C_{rec}$
  The time constant of this relaxation process, denoted as τ_{rec}, indicates the carrier recombination time of

PV cells. It can be calculated by:

$$\tau_{rec} = R_{rec}C_{rec} \tag{3.8}$$

The impact of operating conditions on three variables can be expressed as:

$$\begin{cases} ln(R_{rec}) \propto -\dfrac{V_{PV}}{m_{rec1}V_t} \\ ln(C_{rec}) \propto \dfrac{V_{PV}}{m_{rec2}V_t} \\ \tau_{rec} \propto exp\left(\dfrac{V_{PV}}{m_{rec3}V_t}\right) \end{cases} \tag{3.9}$$

where m_{rec1}, m_{rec2} and m_{rec3} are fitting coefficients. Since the slope of the linear fit in the $ln(C_{rec})$ vs V_{PV} plot could be an indicator of the cell's ideality factor [11], whose value is typically located in the interval [1, 2] and is affected by illumination [115]. Additionally, the high-quality passivation of the silicon surfaces results in very high C_{rec}.

- **Illumination relaxation process** $R_{il}||C_{il}$
  As introduced in [9], an additional diode affected by the illumination is added. Considering the small value of C_{il} and the low normal irradiance level, $R_{il}||C_{il}$ is regarded as a constant resistor in [9, 98]. In our work, it is treated as a variable resistor with respect to the irradiance level, considering the various irradiance level during experiment and the relatively samll capacitance, i.e., R_{il}.

Therefore, under certain illumination conditions, as the PV output voltage changes (from 0 V to V_{oc}), the impedance spectrum of the PV cell appears a single arc, an obvious double arc, and then a single arc due to the dominance of different relaxation processes, as shown in Figure 3.10. The intercepts with the real axis, together with the frequency of occurrence at the spectrum vertices are also indicated.

Figure 3.10 (a) shows that when approaching the short-circuit condition (i.e., $V_{PV} = 0$ V), only the diffusion process is considered dominant. In contrast, the frequencies of the illumination and recombination processes are too fast, and their impedances are relatively small and can be ignored. Based on the analysis in [11], the relaxation time constants of the two processes calculated by (3.6) and (3.8) become almost the same as V_{PV} increases. In this voltage range, both relaxation processes are clearly visible on the IS spectrum at the same time, as indicated in Figure 3.10 (b). As V_{PV} further increases, the relative relationship between the diffusion and recombination time constants changes. The values of R_{tr} and τ_{tr} will decrease rapidly. Especially when V_{PV} is closed to the open-circuit voltage (i.e., $V_{PV} = V_{oc}$), only one arc representing the

recombination process is prominently observed on the IS spectrum, as depicted in Figure 3.10 (c).

Through analysis, it is found that AC-ECM of PV cells can be simplified to varying degrees as V_{PV} changes. However, to obtain a more complete IS spectrum, the perturbation signal frequency needs to reach the megahertz range. Therefore, if the AC-ECM of PV cells is used directly to analyze the impedance of PV panels, it may pose challenges for the measuring device. In the next section, the AC-ECM of PV panels will be simplified based on that of PV cells.

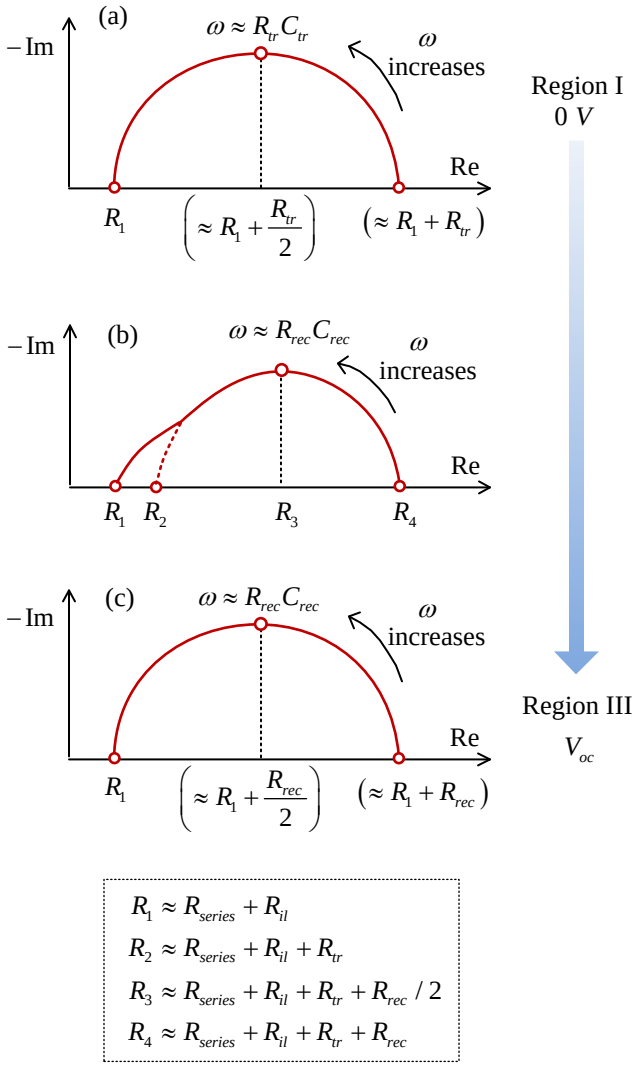


Figure 3.10: IS spectrum of PV cells under different V_{PV}: Nyquist plots.

3.4.2 AC equivalent circuit model of silicon PV panels

In general, to improve the operating efficiency of PV panels under partial shading or hot spot conditions, several bypass diodes are connected in parallel with the PV cell strings, which consist of multiple PV cells in series [28]. A simplified structure of a PV panel in our laboratory is depicted in Figure 3.11. The PV panel contains three bypass diodes. When the PV panel experiences partial shading or other faulty conditions, bypass diodes will beactivated, causing steps in the IV and PV curves, as illustrated in Figure 1.9. This activation will also affect the impedance performance of the PV panel. Therefore, the AC-ECM of the PV panel needs to be reconsidered and redesigned.

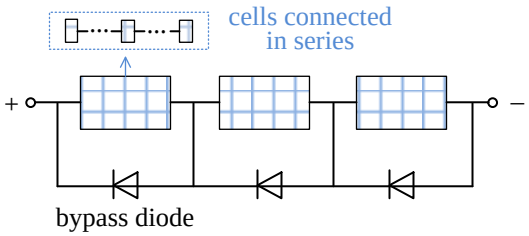


Figure 3.11: Equivalent structure of a PV panel with bypass diodes.

When the AC-ECM is associated with converter-based IS, three aspects need to be considered: the location of the injection point, the frequency limitation and the influence of bypass diodes.

Location of the injection point

As analyzed in Chapter 2, the injection point is located in Region III and selected as close to the MPP as possible to maintain the operating efficiency of the PV panel during IS measurement. Based on the analysis in the last section, the IS spectrum of PV cells is displayed as shown in Figure 3.10 (b). Both diffusion and recombination processes are clearly visible on the IS spectrum. The corresponding relaxation time constants are satisfied as:

$$\tau_{rec} > \tau_{tr} \tag{3.10}$$

However, to obtain the detailed values of the two relaxation time constants, the frequency of the perturbation signal should be larger than $100\ k\mathrm{Hz}$.

Frequency limitation

As mentioned, converter-based IS achieves the injection of the perturbation signal by controlling the switch signals. Hence, the bandwidth of the converter will limit the maximum frequency of the perturbation signal. In general, a perturbation frequency below $10\ k\mathrm{Hz}$ is appropriate for converter-based IS with current

technology of devices. However, this frequency limitation may make it difficult to obtain an IS spectrum covering both processes. Detailed information on the calculation of the converter bandwidth will be provided in Chapter 4.

Influence of bypass diodes

When a bypass diode is off, it can be ignored. When it is on, considering the frequency range of the perturbation signal in this work, it behaves like a resistor, denoted as R_{byd} [116, 117]. Its value is impacted by the flowing current, i.e., I_{byd}. As the slope of I_{byd} vs V_{PV}, defined as S_{byd}, increases, the value of R_{byd} decreases. The value of S_{byd} is determined by the partial shading size.

Combining these three aspects, a low frequency range is selected in our work, which can guarantee the acquisition of vertex information of the arc representing the recombination process. In this frequency range, $R_{tr}||C_{tr}$, $R_{li}||C_{li}$ are approximately equal to a resistor, i.e., R_{tr}, R_{il}, and L_{series} can be ignored. The AC-ECM of the PV panel for converter-based IS is shown in Figure 3.12 (a). It can be simplified as shown in Figure 3.12 (b), including a resistor and capacitor in parallel, i.e., $R_p||C_p$, and a resistor in series R_s. The impedance of the AC-ECM of the PV panel can be expressed as:

$$\begin{aligned} Z_{PV}(\omega) &= R_s + \frac{R_p}{1 + j\omega R_p C_p} \\ &= \left(R_s + \frac{R_p}{1 + (\omega R_p C_p)^2} \right) - j \frac{\omega R_p^2 C_p}{1 + (\omega R_p C_p)^2} \end{aligned} \tag{3.11}$$

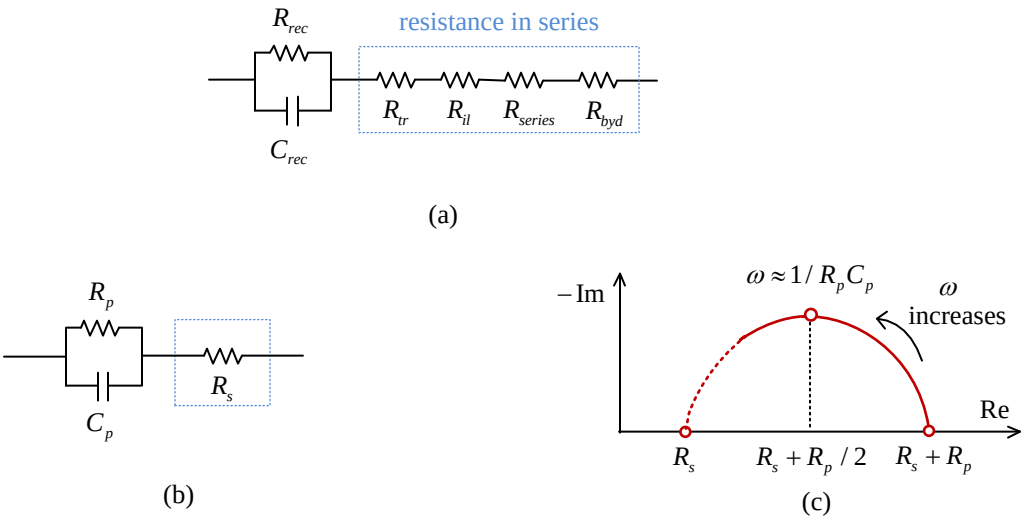


Figure 3.12: AC-ECM of PV panels.

Based on the the measurement results, and the fitting method as expressed in (3.11), the IS spectrum can

be completed, as indicated in Figure 3.12 (c), where the solid line represents the experimental part and the dashed line is the fitting part, respectively. From the IS spectrum, the following information can be obtained:

The values of the impedance Z_{PV} at the intersections of the IS spectrum with the real axis at high and low frequencies are equal to:

$$Z_{PV}(+\infty) = R_s \tag{3.12}$$

$$Z_{PV}(0) = R_s + R_p \tag{3.13}$$

The angular frequency of the IS spectrum vertex is equal to: $\omega_{top} = 1/R_pC_p$, and the corresponding impedance can be expressed as:

$$Z_{PV}(\omega_{top}) = \left(R_s + \frac{R_p}{2}\right) - j\frac{R_p}{2} \tag{3.14}$$

Based on (3.13) and (3.14), when the frequency of the perturbation signal covers the IS spectrum vertex, the values of R_s, R_p and C_p can be calculated. This can further reduce the required frequency range of the perturbation signal for IS implementation. By repeating the experiment multiple times, the value of ω_{top} of the PV panel in our lab satisfies: $\omega_{top} < 2\pi \times 2 \times 10^3$ rad/s (corresponding frequency 2 kHz).

According to the analysis of the AC-ECM of PV cells, the influence of irradiance level, temperature and output voltage on these parameters can be concluded:

R_p: $lnR_p \propto -\dfrac{qV_{PV}}{m_R kT}$;

C_p: $lnC_p \propto \dfrac{qV_{PV}}{m_C kT}$, ($m_C < m_R$ [8]);

R_s: This part includes four parts, R_{tr} decreases with the current representing the diffusion process; $R_{il} \propto$ irradiance level; R_{byd} is affected by the size of partial shading; R_{series} depends on the physical parameters of PV panels, such as the length, width connected lines, etc.

Therefore, four features can be used to describe the relaxation process during injection and verify the influence of temperature and output voltage on the parameters mentioned above:

- Feature 1: $R_s + R_p$ reflects the conductivity of the PV panel; the smaller the value of $R_s + R_p$, the better the internal conductivity.
- Features 2 and 3: ln(R_p) and ln(C_p) verify the influence of temperature and output voltage, which can provide theoretical support for the calculation of external environmental conditions based on parameters in the further work.

- Feature 4: $\tau = R_p C_p$ represents the relaxation time constant of the recombination process.

These four features are considered as health indicators, and will be extracted in the experiment to verify the effectiveness of the AC-ECM of PV panels proposed in this chapter.

3.5 Conclusions

Existing AC-ECMs of PV cells/panels are summarized and analyzed in this chapter. Based on the analysis of the physical model of PV cells, the internal relaxation processes in three time scales are classified. Due to the frequnecy limiation, only relaxation processes in microsecond- time scale can be analyzed based on the IS spectrum, including the diffusion and recombination of carriers, which are associated with the internal conductivity and electron transfer. In the two-diode DC-ECM, two processes are represented by two reverse diodes. Detailed information on the two diodes is provided in this chapter. The current flowing through the two diodes indicates that the current of the diffusion process dominates at high output voltages, while the current of the recombination process dominates at low output voltages.

The analysis of the AC-ECM shows consistency with the DC-ECM. Apart from the diffusion and recombination processes, an additional relaxation process caused by illumination is considered in the AC-ECM of PV cells. Corresponding parameters of the AC-ECM of PV cells are analyzed, which provides a fundation for monitoring the operating conditions. According to the operating principles of converter-based IS implementation and considering the bypass diodes in PV panels, a simplified AC-ECM of PV panels is proposed, and based on the AC-ECM, four health features are defined. Meanwhile, the influence of operating conditions on the parameters of the AC-ECM of PV panels is analyzed. In subsequent chapters, the health monitoring of PV panel by converter-based IS will be carried out to assess the health states of PV panels based on the proposed simplified model.

Chapter 4

Open-loop control strategy for converter-based IS

4.1 Introduction

As introduced in Chapter 1, to ensure the stability and linearity during IS implementation, control strategies are divided into two levels: the upper-level control strategy – cooperative control of MPPT, IPT and IS modes, which is proposed and verified by simulation in Chapter 2; and the lower-level control strategies – control strategies for MPPT, IPT and IS modes. Various step P&O method is selected in our work to achieve the MPPT, and the corresponding control block is provided in Figure 1.8. This chapter focuses on the control of IPT and IS modes.

Open-loop control is the simplest control strategy for a DC/DC converter. In existing open-loop control strategies for perturbation signal injection, an AC duty signal with a constant amplitude has been directly added to the DC duty signal, as indicated in Figure 1.13 (1) or added to the controlled DC duty signal as depicted in Figure 1.13 (2). Corresponding implementation details can be obtained in [66, 71, 73, 74, 75, 77, 83]. Due to the series connection in the converter of the inductor and the DC-bus capacitor when the switch is off, there is a risk of resonance during perturbation signal injection [77]. However, the resonant behavior of the connected DC/DC converters was either not identified or disregarded, potentially increasing the risk of entering the nonlinear region. Additionally, rare literature focuses on the limitation of the converter's bandwidth on the frequency of the perturbation signal.

Addressing these limitations, this chapter analyzes the resonance information of the converter and the

frequency limitation of the perturbation signal. Meanwhile, an adaptive configuration method for the amplitude of the AC duty cycle is proposed to improve the accuracy of IS measurements based on open-loop control. Finally, corresponding simulations and experiments are provided to verify the analysis.

4.2 System description

4.2.1 Topology description

As the simplest step-up converter, the conventional boost converter is widely used in PV field. The corresponding topology considering the parasitic parameters is illustrated in Figure 4.1. Considering that the output current of the PV panel is affected by its output voltage as expressed in (3.5), under the discrete control, a capacitor (C_1) in parallel with the PV panel is required to maintain the output voltage and power of the PV panel throughout one switching cycle [16]. And C_1 is denoted as the support capacitor in this work. The meaning of each parameter in Figure 4.1 is summarized as follows:

v_{PV} and i_{PV}, the output voltage and current of the PV panel S. r_{PV}, the parasitic resistor of the connecting line and the junction box from the PV panel to the voltage sampling port. C_1 and r_{C_1}, the support capacitor and the corresponding parasitic resistor with v_{C_1} and i_{C_1}, the related voltage and current. L and r_L, the filter inductor and the corresponding parasitic resistor with i_L, the related current. T and r_{on}, power switch and the equivalent resistor when it's on. V_d and r_d, the constant voltage source and a on-resistor modeling the diode. C_{dc} and r_{dc}, the DC-bus capacitor and the corresponding parasitic resistor with v_{dc} and i_{dc}, the related voltage and current. Finally, v_o and i_o, the output voltage and the current of the boost converter supplying a resistive load R_L.

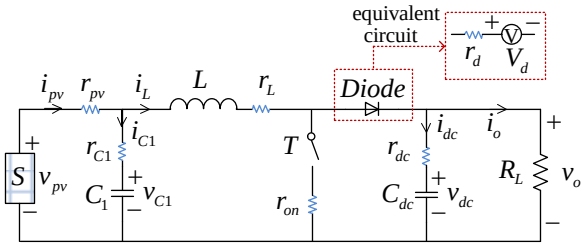


Figure 4.1: Topology of the conventional boost converter.

When the switch T is on, the state circuit is shown in Figure 4.2 (a), where L is in parallel with C_1; when the switch T is off, L is in series with C_{dc}, as indicated in Figure 4.2 (b). As also introduced in Chapter

2, the current signal is considered as the perturbation signal, while the voltage signal is the response signal. Therefore, attention should be paid to the resonance caused by the series connection of L and C_{dc}, which will result in a current peak as the perturbation frequency changes. The resonance can be analyzed based on the average state-space model of the converter provided below.

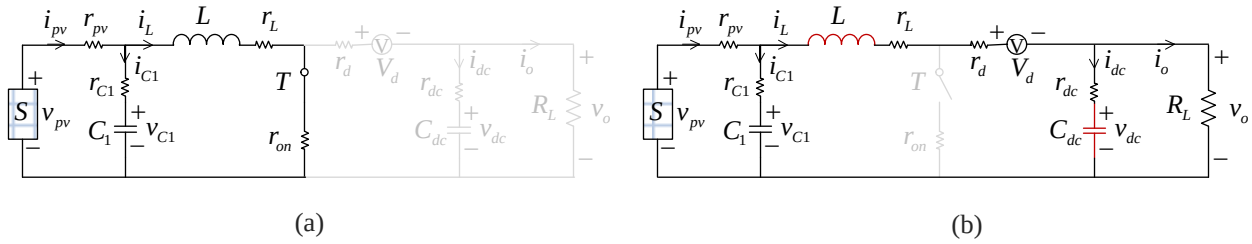


Figure 4.2: State circuits of the boost converter: (a) when the switch T is on, (b) when the switch T is off.

4.2.2 Average state-space model

The average state-space model is a well-known technique to obtain an average, linearized model of switching converters. To analyze the resonance of the conventional boost converter during the injection of perturbation signals, the state variables of the boost converter in Figure 4.1 can be expressed as:

when the switch T is on:

$$\begin{cases} L\dfrac{di_L(t)}{dt} = v_{PV}(t) - i_{PV}(t)\cdot r_{PV} - i_L(t)\cdot r_L - i_L(t)\cdot r_{on} \\ C_1\dfrac{dv_{C_1}(t)}{dt} = i_{C_1}(t) \\ C_{dc}\dfrac{dv_{dc}(t)}{dt} = i_{dc}(t) \end{cases} \tag{4.1}$$

when the switch T is off:

$$\begin{cases} L\dfrac{di_L(t)}{dt} = v_{PV}(t) - i_{PV}(t)\cdot r_{PV} - i_L(t)\cdot r_L - i_L(t)\cdot r_d - V_d - v_o(t) \\ C_1\dfrac{dv_{C_1}(t)}{dt} = i_{C_1}(t) \\ C_{dc}\dfrac{dv_{dc}(t)}{dt} = i_{dc}(t) \end{cases} \tag{4.2}$$

In order to derive the equations for all the state variables, Kirchhoff's voltage law (KVL), Kirchhoff's current law (KCL) and Ohm's law are applied as follows:

$$\begin{cases} v_{PV}(t) = i_{PV}(t)\cdot r_{PV} + v_{C_1}(t) + i_{C1}(t)\cdot r_{C_1} \\ i_{PV}(t) = i_L(t) + i_{C_1}(t) \\ v_o(t) = v_{dc}(t) + i_{dc}(t)\cdot r_{dc} \\ i_o(t) = \dfrac{v_o(t)}{R_L} \\ \begin{cases} i_{dc}(t) = -i_o(t) & \text{(Switch is on)} \\ i_{dc}(t) = -i_o(t) + i_L(t) & \text{(Switch is off)} \end{cases} \end{cases} \tag{4.3}$$

To derive the linearized model of the conventional boost converter around a steady-state duty cycle, i.e., D, a direct small-signal perturbation, i.e., $\hat{d}$, is considered. All variables are equal to a sum of a DC component and a small-signal perturbation, i.e., $d = D + \hat{d}$, $v_{PV} = V_{PV} + \hat{v}_{PV}$, $v_{C1} = V_{C1} + \hat{v}_{C1}$, $v_o = V_o + \hat{v}_o$, $i_{PV} = I_{PV} + \hat{i}_{PV}$, $i_{C1} = I_{C1} + \hat{i}_{C1}$, $i_L = I_L + \hat{i}_L$, $i_o = I_o + \hat{i}_o$.

Based on (4.1), (4.2), (4.3) and Laplace transform, the small-signal expressions of all state variables can

be expressed as:

$$\begin{cases} \hat{v}_o(s) = \dfrac{1}{(sC_{dc} + \dfrac{1}{R_L} + \dfrac{sC_{dc}r_{dc}}{R_L})} \cdot \Big(\hat{i}_L(s)(1-D)(sC_{dc}r_{dc}+1) - \hat{d}(s)I_L(sC_{dc}r_{dc}+1)\Big) \\ \hat{v}_{PV}(s) = sL\hat{i}_L(s) + \hat{i}_{PV}(s)r_{PV} + \hat{i}_L(s)(r_L + r_d) + D\hat{i}_L(s)(r_{on} - r_d) + \hat{d}(s)I_L(r_{on} - r_d) \\ \qquad\qquad - \hat{d}(s)V_d + (1-D)\hat{v}_o(s) - \hat{d}(s)V_o \\ \hat{i}_{PV}(s) = \dfrac{1}{(1 + sC_1r_{PV} + sC_1r_{C1})} \cdot \Big(sC_1\hat{v}_{PV}(s) + \hat{i}_L(s)(1 + sC_1r_{C1})\Big) \end{cases} \tag{4.4}$$

It should be noted that during the calculation, the differential products, i.e., $\hat{d}(s)\hat{i}_L(s)$ and $\hat{d}(s)\hat{v}_o(s)$ are ignored herein. Based on (4.4), the small-signal transfer function from the duty cycle to the output current of the PV panel, i.e., $G_{i_{PV}-d}(s)$, can be obtained:

$$\begin{aligned} G_{i_{PV}-d}(s) &= \frac{\hat{i}_{PV}(s)}{\hat{d}(s)}|_{\hat{v}_{PV}=0} \\ &= \frac{\hat{i}_{PV}(s)}{\hat{i}_L(s)} \cdot \frac{\hat{i}_L(s)}{\hat{d}(s)}|_{\hat{v}_{PV}=0} \end{aligned} \tag{4.5}$$

Two intermediate transfer functions are defined to simplify the analysis:

- $G_{i_{PV}-i_L}(s)$ represents the transfer function from the input current of the converter, i.e., i_L, to the output current of the PV panel, i.e., i_{PV}. It is expressed as:

$$\begin{aligned} G_{i_{PV}-i_L}(s) &= \frac{\hat{i}_{PV}(s)}{\hat{i}_L(s)}|_{\hat{v}_{PV}=0} \\ &= \frac{1 + \dfrac{s}{\omega_{z-i_{PV}}}}{1 + \dfrac{s}{\omega_{0-i_{PV}}}} \end{aligned} \tag{4.6}$$

  where $\omega_{z-i_{PV}} = 1/C_1r_{C_1}$ and $\omega_{0-i_{PV}} = 1/C_1(r_{C_1} + r_{PV})$, represent the frequency of the zero and the natural frequency of the transfer function $G_{i_{PV}-i_L}(s)$, respectively.

- $G_{i_L-d}(s)$ represents the transfer function from the small-signal duty cycle, i.e., $\hat{d}$, to the small-signal

input current of the converter, i.e., $\hat{i_L}$. Its expression is summarized as:

$$\begin{aligned} G_{i_L-d}(s) &= \frac{\hat{i}_L(s)}{\hat{d}(s)}|_{\hat{v}_{PV}=0} \\ &= K_{boost} \cdot \frac{1+\frac{s}{\omega_{z-i_L}}}{1+\frac{1}{Q}\cdot\frac{s}{\omega_{0-i_L}}+(\frac{s}{\omega_{0-i_L}})^2-\frac{sr_{PV}^2C_1\cdot(sC_{dc}(R_L+r_{dc})+1)}{1+sC_1(r_{C1}+r_{PV})}} \end{aligned} \tag{4.7}$$

where K_{boost} is the gain of the converter, when the frequency is going down to 0 $\mathrm{rad/s}$ (or expressed as 0 Hz); ω_{z-i_L} and ω_{0-i_L} represent the frequency of the zero and the natural frequency of the transfer function $G_{i_L-d}(s)$, respectively; Q represents the quality factor. Their values can be calculated by:

$$\begin{cases} K_{boost} = \dfrac{2V_o - V_{par}}{(1-D)^2R_L + r_{par}} \\ \omega_{z-i_L} = \dfrac{2V_o - V_{par}}{V_oC_{dc}(R_L+2r_{dc}) - V_{par}C_{dc}(R_L+r_{dc})} \\ \omega_{0-i_L} = \sqrt{\dfrac{(1-D)^2R_L + r_{par}}{LC_{dc}(R_L+r_{dc})}} \\ Q = \dfrac{\sqrt{(1-D)^2R_L+r_{par}}\cdot\sqrt{LC_{dc}(R_L+r_{dc})}}{(1-D)^2R_LC_{dc}r_{dc} + L + r_{par}C_{dc}(R_L+r_{dc})} \end{cases} \tag{4.8}$$

where $V_{par} = I_{PV}(r_{on} - r_d) - V_d$ and $r_{par} = r_{PV} + r_L + r_d + D(r_{on} - r_d)$, represent the average parasitic voltage and parasitic resistance in one switching cycle in our work.

Based on the rated/reference parameters in Table 4.1, the magnitude plot of $G_{i_{PV-d}}(s)$ based on Matlab is shown in Figure 4.3, including the ideal condition (where the values of all parasitic parameters are negligible or equal to 0), marked as the black line, and considering parasitic parameters, marked as the blue line. When the amplitude of the AC duty signal is constant, the magnitude plot shows a current peak, which may bring the PV panel into the nonlinear region, as indicated in Figure 1.10. The peak appears at the natural frequency, i.e., ω_{0-sys}, also known as the resonant frequency. The magnitude of $G_{i_{PV-d}}(s)$ at ω_{0-sys} is denoted as $\mathrm{Mag_{peak-sys}}$. $\omega_{max-sys}$ represents the maximum frequency of the perturbation signal that can satisfy the target amplitude, i.e., $15\%I_{PV}$, within the limitation range of the duty cycle. The values of $\mathrm{Mag}_{peak-sys}$ and ω_{0-sys} affect the linearity of the system, and the value of $\omega_{max-sys}$ limits the maximum frequency of the perturbation

signal during IS implementation. When comparing the simulation results of the two conditions, the values of $\mathrm{Mag}_{peak-sys}$, ω_{0-sys} and $\omega_{max-sys}$ are influenced by the parasitic parameters. Their influencing factors will be introduced in the next section.

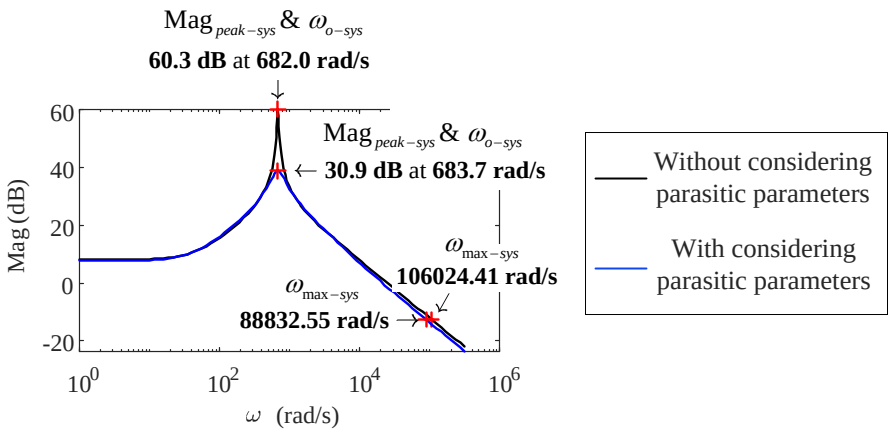


Figure 4.3: Magnitude plot of $G_{i_{PV-d}}(s)$ with and without parasitic parameters.

It should be noted that in our work, when describing the characteristics of the system, angular frequency (in rad/s) is used. Meanwhile, when describing the characteristics of a signal, frequency (in Hz) is used. The angular frequency is equal to frequency with the same footnote times 2π and this relationship will be implicitly used in the following analysis.

4.3 Influence of various parameters

To analyze the influence of each parameter on the frequency limitation of the perturbation signal and the peak value caused by resonance, the selection of each parameter will be made first. Based on the rated/reference value of each parameter and its varying range, the influence of each parameter on $\mathrm{Mag}_{peak-sys}$, ω_{0-sys} and $\omega_{max-sys}$ is analyzed, and simulations are performed to verify the changing trend.

4.3.1 Parameter selection

According to their physical meaning, the parameters can be classified into three types:

- **Operating parameters**: the values of operating parameters depend on the operating conditions, including V_{PV}, I_{PV}, D and R_L.

- **Element parameters**: the parameters of all the elements of the converter, containing L, C_1, C_{dc};
- **Parasitic parameters**: parasitic parameters include r_{PV}, r_{C1}, r_L, r_{on}, r_d, V_d and r_{dc};

It should be noted that, considering the coupling between element parameters and parasitic parameters, during the study process, the two parameters fluctuated around the rated/reference value respectively. Nevertheless, in the actual circuits, the parasitic parameters are usually coupled with corresponding element parameters, such as r_L with L. The selection guide can refer to the influence of each parameter, as analyzed below. In addition, considering that the output voltage of the PV panel in Region III changes within a very narrow range, V_{PV} is regarded as a constant value in the following analysis.

A. Setting of operating parameter values

In section 4.4, the operating condition O-II is utilized to verify the efficiency of the proposed open-loop control strategy. The operating condition O-II is set as:

▷ Irradiance level: 268 $\mathrm{W/m^2}$;

▷ Temperature: 323.15 K;

▷ DC component current at injection point, i.e., I_{PV}: 0.7 A.

Under this condition, the output voltage of the PV panel, i.e., V_{PV}, is approximately equal to 34 V. The corresponding value of DC duty cycle, i.e., D, is equal to 0.454. The value of the load, i.e., R_L, is set to 163 Ω.

B. Setting of element and parasitic parameter values

In this work, the voltage ripple of the DC bus is not the main focus since the DC bus voltage will be specifically regulated by the storage elements in the DC microgrid. Therefore, no additional capacitors are connected to DC bus except for the integrated capacitor of the half-bridge SiC power module (PEB 8024), which is enough to maintain a stable DC-bus voltage. The rated value of C_{dc} is thus equal to 260 μF. The corresponding parasitic resistance of the DC-bus capacitor is equal to 1.03 Ω, as provided in the user manual.

The setting principle of L

The relationship between the current ripple and the inductor of the conventional boost converter can be written as:

$$L = \frac{1}{\Delta i_L} \cdot (1 - D) \cdot T_{sw} \cdot (V_o - V_{PV}) \tag{4.9}$$

where T_{sw} represents the switching period and is set as $1/(8 \times 10^4)$ s, corresponding a switching frequency of 80 kHz. Taking into account the amplitude of the perturbation current signal, ranging from 5% to 15%, the

inductor value is set to 2.5 mH, ensuring that the peak of the current ripple remains smaller than 0.5 times the I_{ac} across the entire testing current range. According to the parameter manual displayed on the *RS* official website, the value of parasitic parameter, i.e., r_L, is equal to 0.013 Ω.

The setting principle of C_1

The support capacitor, i.e., C_1, is responsible to maintain the output voltage of the PV panel during one switching cycle. When the switch is turned on, C_1 operates in discharging state, and the voltage of C_1 can be expressed as:

$$v_{C_1}(t) = Ke^{-\alpha t}cos(\omega_{d-C_1}t + \Theta) \tag{4.10}$$

where the intermediate variables can be calculated by:

$$\begin{cases} K = \sqrt{K_1^2 + K_2^2} \\ \Theta = -arctg(K_2/K_1) \\ \alpha = r_{disc}/2L \\ \omega_{d-C_1} = \sqrt{1/LC_1 - \alpha^2} \end{cases}$$

$$\begin{cases} r_{disc} = r_{C1} + r_L + r_{on} \\ K_1 = V_{PV} \\ K_2 = \frac{1}{\omega_{d-C_1}}(\frac{I_{PV}}{C_1} + \alpha V_{PV}) \end{cases}$$

Based on Equation (4.10), the value of C_1 can be calculated: $C_1 \geq 114.6\ uF$. Finally, three parallel capacitor, each with a capacitance of 47 uF and a total capacitance of 141 uF, are selected in our platform. The corresponding value of their parasitic resistor, i.e., r_{C1}, is equal to 1.03 Ω.

The value of each parameter and the corresponding fluctuation range are summarized in Table 4.1. The rated/reference value of each parameters is the measured or provided value in their manual. The selection of the fluctuation range of each parameter considers the requirements of IS implementation and the actual operating condition of the converter. Since the value of r_d, V_d and r_{on} of different diodes and SiC switches are not significantly different, their variations are not analyzed and simulated in this work.

Table 4.1: Parameter values of the system as fixed in the study

Symbol		Rated/reference Value	Fluctuation range	Fluctuation value
Operating parameters	R_L	163 Ω	±20%	[130.4 Ω, 195.6 Ω]
	I_{PV}	0.7 A	±43%	[0.4 A, 1.0 A]
	D	0.45	±33%	[0.3, 0.8]
Element parameters	L	2.5 mH	±12%	[2.2 mH, 2.8 mH]
	C_1	141 μF	±20%	[112.8 μF, 169.2 μF]
	C_{dc}	260 μF	±20%	[208 μF, 312 μF]
Parasitic parameters	r_{PV}	0.3 Ω	[-67%, 233%]	[0.1 Ω, 1.0 Ω]
	r_L	0.013 Ω	[-38%, 115%]	[0.008 Ω, 0.028 Ω]
	r_{C1}	1.03 Ω	±20%	[0.82 Ω, 1.24 Ω]
	r_{dc}	1.03 Ω	±20%	[0.82 Ω, 1.24 Ω]
	r_d	0.07 Ω	–	–
	V_d	4.6 V	–	–
	r_{on}	0.08 Ω	–	–

4.3.2 Resonant information and frequency limitation

A. Simplified small-signal model

To analyze the influencing factors of ω_{0-sys}, $\mathrm{Mag}_{peak-sys}$ and $\omega_{max-sys}$, the magnitude of $G_{i_{PV}-i_L}$ and $G_{i_{L-d}}(s)$ are separately examined. Due to the relative small value of parasitic parameter r_{PV} of the connected line of the PV panel with the support capacitor and that the value of C_1 is in the order of uF, the term $sr_{PV}^2C_1$ in the denominator of Equation (4.7) can be ignored. Therefore, Equation (4.7) can be simplified as:

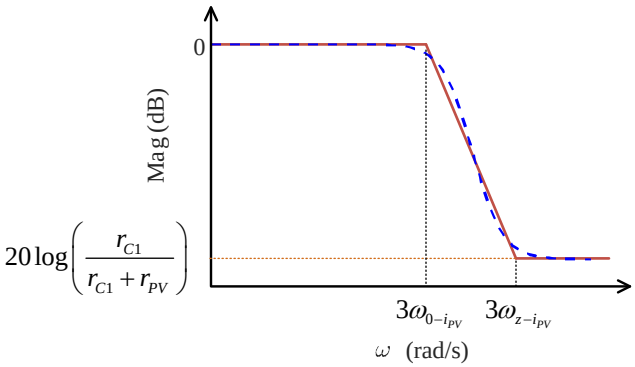
$$\begin{aligned} G_{i_L-d}(s) &= \frac{\hat{i}_L(s)}{\hat{d}(s)}|_{\hat{v}_{PV}=0} \\ &= K_{boost} \cdot \frac{1+\dfrac{s}{\omega_{z-i_L}}}{1+\dfrac{1}{Q}\cdot\dfrac{s}{\omega_{0-i_L}}+(\dfrac{s}{\omega_{0-i_L}})^2} \end{aligned} \tag{4.11}$$

Based on Equations (4.6) and (4.11), the asymptotic magnitude plots of $G_{i_{PV}-i_L}(s)$ and $G_{i_{L-d}}(s)$ are illustrated as the magenta lines in Figure 4.4 (a) and (b). The blue lines represent the simulation results based on the rated/reference values in Table 4.1. Figure 4.4 (a) shows that $G_{i_{PV}-i_L}(s)$ attenuates the signals

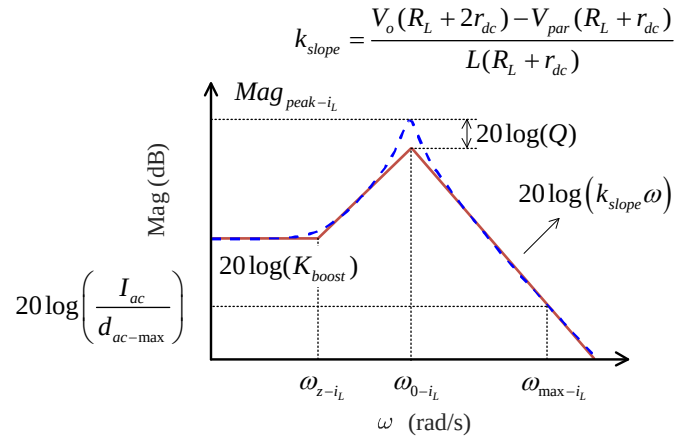
with frequencies higher than $3\omega_{z-i_{PV}}$ at a fixed ratio, i.e., $20\log(r_{C1}/(r_{C1}+r_{PV}))$, while hardly attenuates the signals with frequencies less than $3\omega_{0-i_{PV}}$. In Figure 4.4 (b), I_{ac} represents the target amplitude of the perturbation current signal, and d_{ac-max} represents the maximum amplitude of the AC duty signal, and their values are limited by:

$$I_{ac} = K_{per} \cdot I_{PV}$$
$$d_{ac-max} = \begin{cases} 1-D & (D > 0.5) \\ D & (D \leq 0.5) \end{cases} \tag{4.12}$$

where $K_{per} \in [5\%\ 15\%]$, representing the percentage between the amplitude of the perturbation signal and the DC component of the output current at the injection point.



(a)



(b)

Figure 4.4: Asymptotic diagram of gain of $G_{i_{PV}-i_L}(s)$ and $G_{i_{L-d}}(s)$
(a) magnitude of $G_{i_{PV}-i_L}(s)$; (b) magnitude of $G_{i_{L-d}}(s)$.

The value of K_{boost} determines the gain of the $G_{i_{L-d}}(s)$ with frequencies less than ω_{z-i_L}. The gain at

frequencies higher than ω_{0-i_L} is equivalent to a slope function of $1/\omega$, whose slope is denoted as k_{slope} as shown in Figure 4.4 (b). Another slope segment is located between ω_{z-i_L} and ω_{0-i_L}. The difference between the simulation and asymptotic results at ω_{0-i_L} is equal to Q. $\mathrm{Mag_{peak-i_L}}$ represents the magnitude of $G_{i_{L-d}}(s)$ at ω_{0-i_L}. The maximum frequency of the perturbation signal can reach ω_{max-i_L}, at which the gain of $G_{i_{L-d}}(s)$ can be calculated by $20\log(I_{ac}/d_{ac-max})$.

According to the rated/reference values in Table 4.1, the relationship between the different frequencies satisfies:

$$\omega_{0-i_L} < \omega_{0-i_{PV}} < \omega_{z-i_{PV}} < \omega_{max-i_L} \tag{4.13}$$

Therefore, the resonance will not be impacted by the $G_{i_{PV}-i_L}(s)$. The maximum frequency of the perturbation signal to reach the target amplitude is determined by both $G_{i_{PV}-i_L}(s)$ and $G_{i_{L-d}}(s)$. Corresponding analysis will be provided in the following subsections.

B. Resonant information

Based on Equation (4.13), the resonant frequency of the system is mainly determined by the value of ω_{0-i_L}, that is, $\omega_{0-sys} \approx \omega_{0-i_L}$. Moreover, as indicated in Equation (4.8), the influencing factors include:

▷ Operating parameters: R_L, I_{PV} and D;

▷ Element parameters: L and C_{dc};

▷ Parasitic parameters: r_{PV}, r_L and r_{dc}.

Considering the value of R_L, r_{par} and r_{dc}, the dominant influencing factors on the value of ω_{0-sys} include D, L and C_{dc}, and can be approximately expressed as:

$$\omega_{0-sys} \propto \frac{(1-D)}{\sqrt{LC_{dc}}} \tag{4.14}$$

The influence of each parasitic parameter can also be approximately written as:

$$\omega_{0-sys} \propto \begin{cases} \dfrac{1}{\sqrt{LC_{dc}}} \cdot \sqrt{\dfrac{r_{PV}}{R_L + r_{dc}}} & (\text{influence of } r_{PV}) \\ \dfrac{1}{\sqrt{LC_{dc}}} \cdot \sqrt{\dfrac{r_L}{R_L + r_{dc}}} & (\text{influence of } r_L) \\ \dfrac{(1-D)}{\sqrt{LC_{dc}}} \cdot \sqrt{\dfrac{R_L}{R_L + r_{dc}}} & (\text{influence of } r_{dc}) \end{cases} \tag{4.15}$$

(4.14) shows the ω_{0-sys} is inversely proportional to the root of the product of L and C_{dc} and inversely proportional to D. (4.15) exhibits that ω_{0-sys} will increase when r_{PV} and r_L increase and r_{dc} decreases. It is worth noting that the impacts of r_{PV}, r_L and r_{dc} on ω_{0-sys} are closely tied to the value of R_L. A higher R_L will reduce the relative variation.

By substituting 4.8, the magnitude of $G_{i_L-d}(s)$ at ω_{0-sys} can be calculated by:

$$\begin{aligned}\mathrm{Mag}_{\mathrm{peak-sys}} &\approx \frac{V_o(R_L+2r_{dc})-V_{par}(R_L+r_{dc})}{L(R_L+r_{dc})\omega_{0-i_L}}+Q \\ &= \frac{(V_o(R_L+2r_{dc})-V_{par}(R_L+r_{dc}))\sqrt{C_{dc}}}{\sqrt{L(R_L+r_{dc})((1-D)^2R_L+r_{par})}}+\frac{\sqrt{(1-D)^2R_L+r_{par}}\cdot\sqrt{LC_{dc}(R_L+r_{dc})}}{(1-D)^2R_LC_{dc}r_{dc}+L+r_{par}C_{dc}(R_L+r_{dc})}\end{aligned} \tag{4.16}$$

Considering that the values of the parasitic parameters are generally small, the dominant parameters in (4.16) include L, C_{dc}, D and R_L, and can be summarized as:

$$\mathrm{Mag}_{\mathrm{peak-sys}} \propto \frac{V_o}{(1-D)}\cdot\sqrt{\frac{C_{dc}}{L}}+(1-D)R_L\cdot\sqrt{\frac{C_{dc}}{L}} \tag{4.17}$$

It is obvious that the increase of C_{dc} and R_L or decrease of L results in the increase of $\mathrm{Mag}_{peak-sys}$. The impacts of D depends on the relative values of V_o and R_L. Comparing (4.16) and (4.17), it can be concluded that the existence of the parasitic parameters may lead to a reduction of $\mathrm{Mag}_{peak-sys}$.

C. Frequency limitation

As shown in (4.12), the requirements of I_{ac} and d_{ac-max} determine the limitation of the frequency of the perturbation signal. The value of the maximum frequency can be calculated by:

$$\omega_{max-sys} = \frac{r_{C1}}{(r_{C1}+r_{PV})}\cdot\frac{V_o(R_L+2r_{dc})-V_{par}(R_L+r_{dc})}{L(R_L+r_{dc})}\cdot\frac{d_{ac-max}}{I_{ac}} \tag{4.18}$$

Substituting (4.12) and $V_o = V_{PV}/(1-D)$ into (4.18), the influence of each parameter can be concluded in following:

- Influence of element parameters:

$$\omega_{max-sys} \propto 1/L \tag{4.19}$$

- Influence of parasitic parameters:

$$\omega_{max-sys} \propto \begin{cases} \dfrac{r_{C1}}{(r_{C1}+r_{PV})} & (\text{influence of} \quad r_{C1} \text{ and } r_{PV}) \\ \dfrac{r_{dc}}{R_L+r_{dc}} & (\text{influence of} \quad r_{dc}) \end{cases} \tag{4.20}$$

- Influence of operating parameters:

$$\omega_{max-sys} \propto \frac{d_{ac-max}V_{PV}}{(1-D)K_{per}I_{PV}} \tag{4.21}$$

Equations (4.19), (4.20) and (4.21) indicate that the increase in r_{C1} and r_{dc} will lead to an increase in $\omega_{max-sys}$; while the increase in L and r_{PV} will result in a decrease. Different with the influence of the resonant peak, $\omega_{max-sys}$ is inversely proportional to K_{per}. The influence of R_L, I_{PV} and D should take into account the coupling of these three parameters. Based on the analysis, the influence of all parameters on ω_{0-sys}, $\mathrm{Mag}_{\mathrm{peak-sys}}$ and $\omega_{max-sys}$ and corresponding based equations are summarized in Table 4.2.

Table 4.2: Summarization of the influence of parameters

Symbol		Resonant frequency (ω_{0-sys})	Peak value at resonant frequency ($\mathrm{Mag}_{\mathrm{peak-sys}}$)	Frequency limitation ($\omega_{max-sys}$)
Operating parameters	$R_L \uparrow (I_{PV}-)$	$\downarrow$ (4.26)	$\uparrow$ (4.27)	$R_L < 4V_{PV}/R_L I_{PV}$: $\uparrow$ $R_L > 4V_{PV}/R_L I_{PV}$: $-$ (4.28)
	$I_{PV} \uparrow (D-)$	$-$ (4.14)	$\uparrow$ (4.25)	$\downarrow$ (4.21)
	$D \uparrow (R_L-)$	$\downarrow$ (4.14)	$\uparrow$ (4.23)	$D < 0.5$: $\uparrow$ $D > 0.5$: $\downarrow$ (4.24)
Element parameters	$L \uparrow$	$\downarrow$ (4.14)	$\downarrow$ (4.17)	$\downarrow$ (4.19)
	$C_1 \uparrow$	$-$ (4.14)	$-$ (4.17)	$-$ (4.19)
	$C_{dc} \uparrow$	$\downarrow$ (4.14)	$\uparrow$ (4.17)	$-$ (4.19)
Parasitic parameters	$r_{PV} \uparrow$	$\uparrow$ (4.15)	$\downarrow$ (4.16)	$\downarrow$ (4.20)
	$r_L \uparrow$	$\uparrow$ (4.15)	$\downarrow$ (4.16)	$-$ (4.20)
	$r_{C1} \uparrow$	$-$ (4.15)	$-$ (4.16)	$\uparrow$ (4.20)
	$r_{dc} \uparrow$	$\downarrow$ (4.15)	$\downarrow$ (4.16)	$\uparrow$ (4.20)

$\uparrow$ represents the increase of the corresponding value of the parameter
$\downarrow$ represents the decrease of the corresponding value of the parameter
$-$ represents a constant value of the parameter

4.3.3 Simulation verification

Based on the value provided in Table 4.1, the simulation functions are organized in MATLAB to verify the conclusion in Table 4.2. Corresponding simulation results are analyzed in following.

I. Influence of operating parameters

As mentioned above, three operating parameters are coupled. Based on the power balance principle, three operating parameters are satisfied as:

$$(1-D)^2 R_L I_{PV} = V_{PV} \tag{4.22}$$

Therefore, a variation in one operating parameter will cause a change in at least one of the remaining operating parameters. In the simulation, the influence of operating parameters on ω_{0-sys}, $\mathrm{Mag}_{peak-sys}$ and $\omega_{max-sys}$ is verified by keeping one of them unchanged.

A. Influence of D

When the load R_L, remains constant, the duty cycle D, is controlled to vary from 0.3 to 0.8 as summarized in Table 4.1. In this condition, as D increases, the value of I_{PV} will decrease accordingly. (4.17) and (4.21) can consequently be expressed:

$$\mathrm{Mag}_{\mathrm{peak-sys}} \propto \sqrt{\frac{C_{dc}}{L}} \cdot \left(\frac{V_{PV}}{(1-D)^2} + (1-D)R_L \right) \tag{4.23}$$

$$\omega_{max-sys} \propto d_{ac-max}(1-D) \cdot \frac{R_L}{K_{per}} \tag{4.24}$$

The magnitude plots of $G_{i_{PV}-d}(s)$ under constant R_L and varying D are depicted in Figure 4.5. The simulation results show that an increase in D causes a decrease in ω_{0-sys}, but result in an increase in $\mathrm{Mag}_{peak-sys}$ as expressed in (4.23). As for $\omega_{max-sys}$, by substituting (4.12) in (4.24), if $D < 0.5$, it will exhibit an increasing trend with the increase of D; if $D > 0.5$, it will decrease with the increase of D. The simulation results are consistent with the theoretical analysis expressed in (4.14), (4.23) and (4.24).

B. Influence of I_{PV}

When the duty cycle D is kept constant, the output current of the PV panel I_{PV} is controlled to vary from 0.4 A to 1.0 A as summarized in Table 4.1. In this condition, the value of R_L will decrease as I_{PV} increases

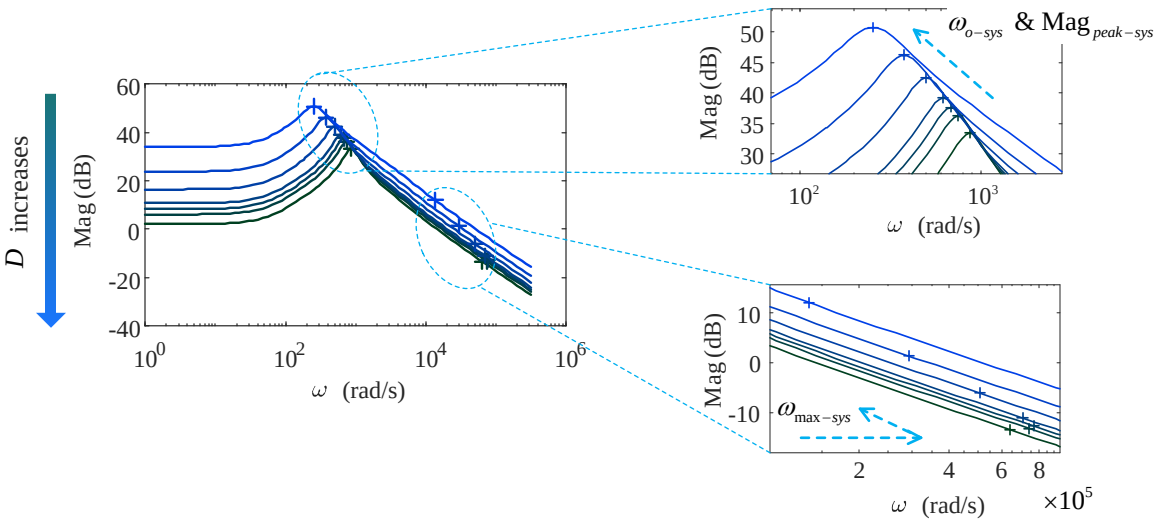


Figure 4.5: Magnitude plots of $G_{i_{PV}-d}(s)$ under constant R_L.

and (4.17) can consequently be expressed:

$$\mathrm{Mag}_{\mathrm{peak-sys}} \propto V_{PV} \cdot \sqrt{\frac{C_{dc}}{L}} \left(\frac{1}{(1-D)^2} + \frac{1}{(1-D)I_{PV}} \right) \tag{4.25}$$

(4.21) and (4.25) indicate that an increase in I_{PV} will cause a decrease in the maximum frequency of perturbation signal $\omega_{max-sys}$ and in the gain $\mathrm{Mag}_{\mathrm{peak-i_L}}$ of $|G_{i_{PV}-d}(s)|$ at resonant frequency. However and as shown by Equation (4.14), the resonant frequency ω_{0-sys} is almost not influenced by I_{PV}. The simulation results illustrated in Figure 4.6 verify the theoretical analysis.

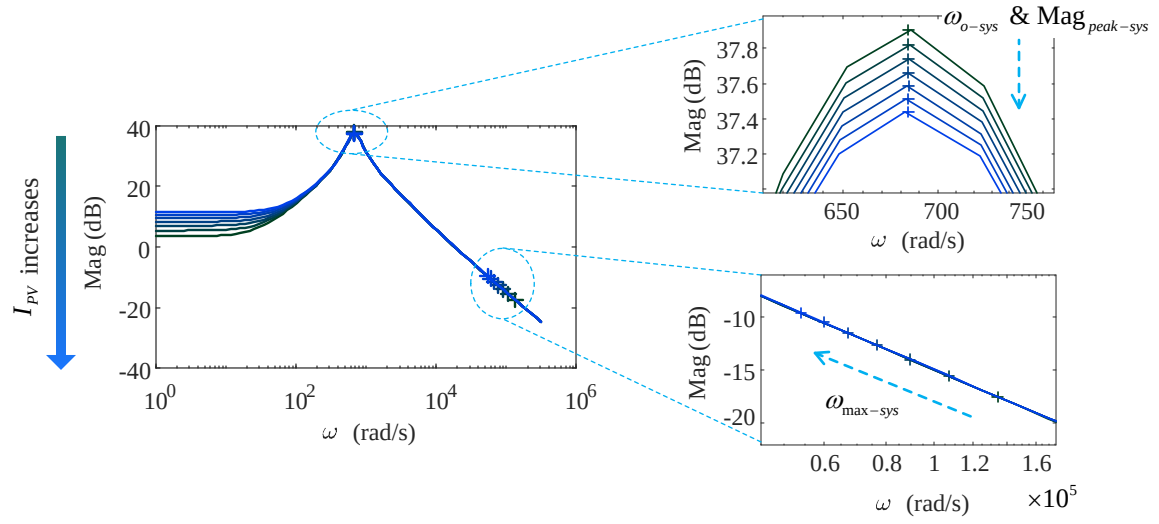


Figure 4.6: Magnitude plots of $G_{i_{PV}-d}(s)$ under constant D.

C. Influence of R_L

Figure 4.7 represents the magnitude plots of $G_{i_{PV}-d}(s)$ with a constant value of I_{PV} and a varying value of R_L. In this case, D will show an inverse changing trend with R_L. In this condition, the influence of R_L on ω_{0-sys}, $Mag_{peak-sys}$ and $\omega_{max-sys}$ can be expressed as:

$$\omega_{0-sys} \propto \sqrt{\frac{V_{PV}}{R_L I_{PV} L C_{dc}}} \tag{4.26}$$

$$\mathrm{Mag}_{\mathrm{peak-sys}} \propto \sqrt{\frac{C_{dc}}{L}} \cdot (R_L I_{PV} + \sqrt{\frac{V_{PV} R_L}{I_{PV}}}) \tag{4.27}$$

$$\omega_{max-sys} \propto \frac{d_{ac-max}\sqrt{R_L V_{PV}}}{K_{per}\sqrt{I_{PV}}} \tag{4.28}$$

where

$$d_{max} = \begin{cases} 1 - \sqrt{\dfrac{V_{PV}}{R_L I_{PV}}} & R_L < \dfrac{4V_{PV}}{R_L I_{PV}} \\ \sqrt{\dfrac{V_{PV}}{R_L I_{PV}}} & R_L > \dfrac{4V_{PV}}{R_L I_{PV}} \end{cases} \tag{4.29}$$

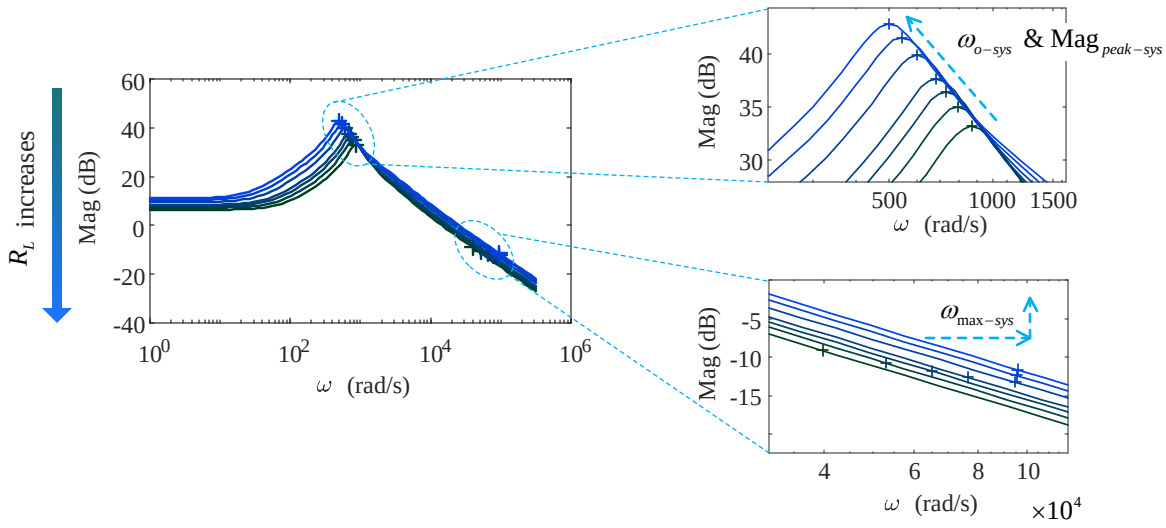


Figure 4.7: Magnitude plots of $G_{i_{PV}-d}(s)$ under constant I_{PV}.

(4.26), (4.27) and (4.28) show that as R_L increases, ω_{0-sys} decreases while $\mathrm{Mag}_{\mathrm{peak-sys}}$ increases. The changing trend of $\omega_{max-sys}$ depends on the value of R_L. When $R_L < 4V_{PV}/R_L I_{PV}$, $\omega_{max-sys}$ increases with

R_L; when $R_L > 4V_{PV}/R_L I_{PV}$, $\omega_{max-sys}$ will not be influenced by R_L. For our experimental platform, its boundary value is 194Ω. Simulation results in Figure 4.7 are consistent with the analysis.

II. Influence of element parameters

Based on the parameters in Table 4.1, the influences of element parameters on ω_{0-sys}, $\mathrm{Mag}_{peak-sys}$ and $\omega_{max-sys}$ are simulated in MATLAB. The corresponding results are shown in Figures 4.8, 4.9, and 4.10. Simulation results are consistent with the theoretical analysis. In particular, we can observe that the resonant frequency ω_{0-sys}, the gain at the resonant frequency $\mathrm{Mag}_{peak-sys}$, and the maximum frequency reached by the perturbation signal $\omega_{max-sys}$, will decrease with the increase of L, as indicated in Figure 4.8. The value of the support capacitance C_1, has almost no effect on ω_{0-sys}, $\mathrm{Mag}_{peak-sys}$ and $\omega_{max-sys}$, as illustrated in Figure 4.9.

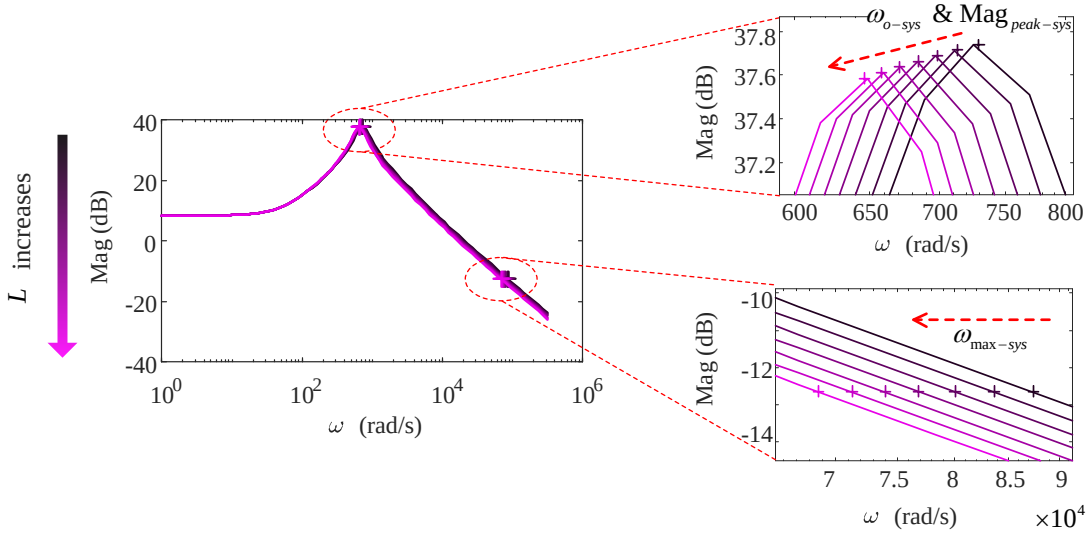


Figure 4.8: Magnitude plots of $G_{i_{PV}-d}(s)$ under different L.

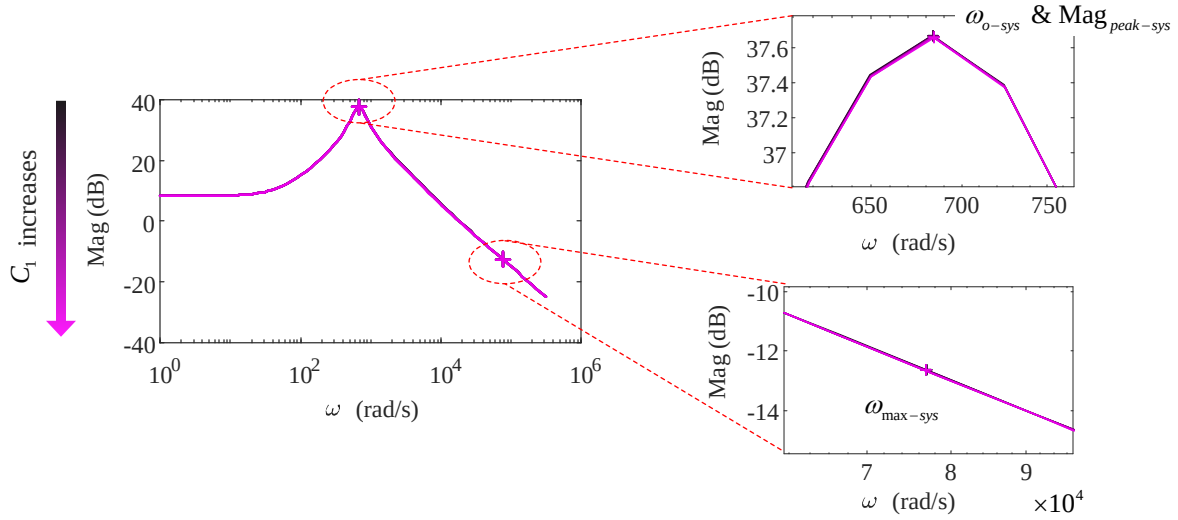


Figure 4.9: Simulation results of $|G_{i_{PV}-d}(s)|$ under different C_1.

Figure 4.10 illustrates that the value of the DC-bus capacitor C_{dc} significantly affects ω_{0-sys} and $\mathrm{Mag}_{peak-sys}$. As C_{dc} increases, ω_{0-sys} decreases, while $\mathrm{Mag}_{peak-sys}$ shows an increasing trend. The value of $\omega_{max-sys}$ is virtually unaffected by changes in C_{dc}.

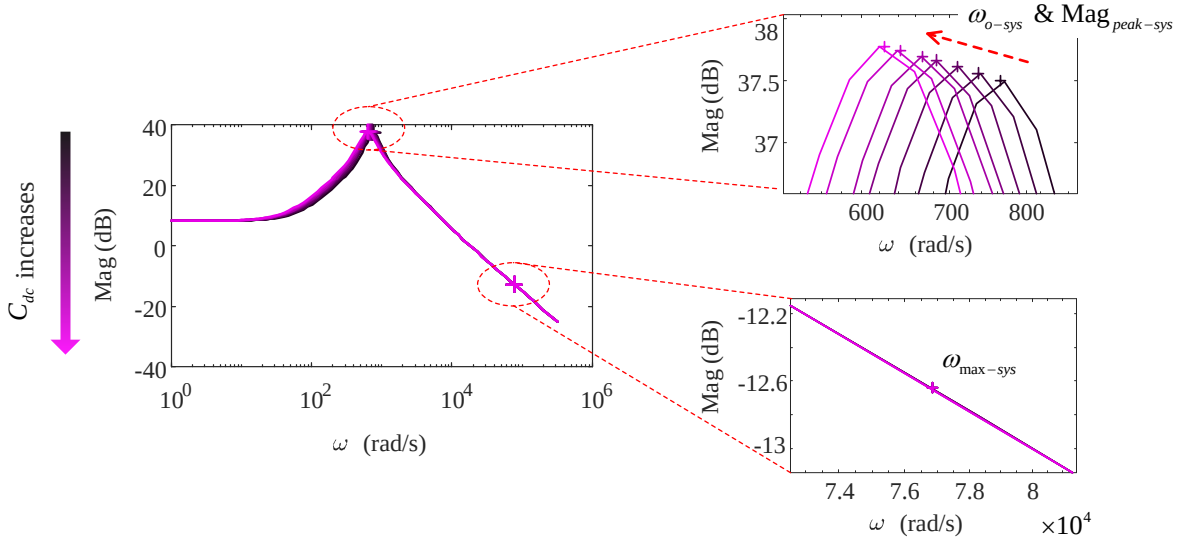


Figure 4.10: Magnitude plots of $G_{i_{PV}-d}(s)$ under different C_{dc}.

III. Influence of parasitic parameters

As analyzed above, the parasitic parameters, including r_{PV}, r_L and r_{dc}, mainly reduce the value of $\mathrm{Mag}_{peak-sys}$. Due to the big difference between their values and the value of the load R_L, the resonant frequency is slightly influenced by the parasitic parameters based on (4.15). The corresponding simulation results are illustrated in Figures 4.11, 4.12, and 4.13.

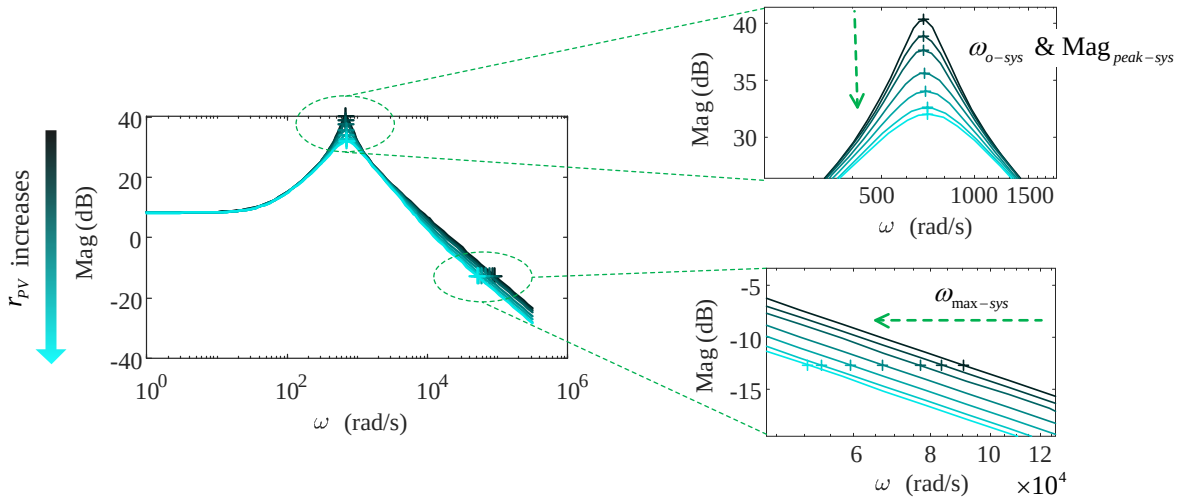


Figure 4.11: Magnitude plots of $G_{i_{PV}-d}(s)$ under different r_{PV}.

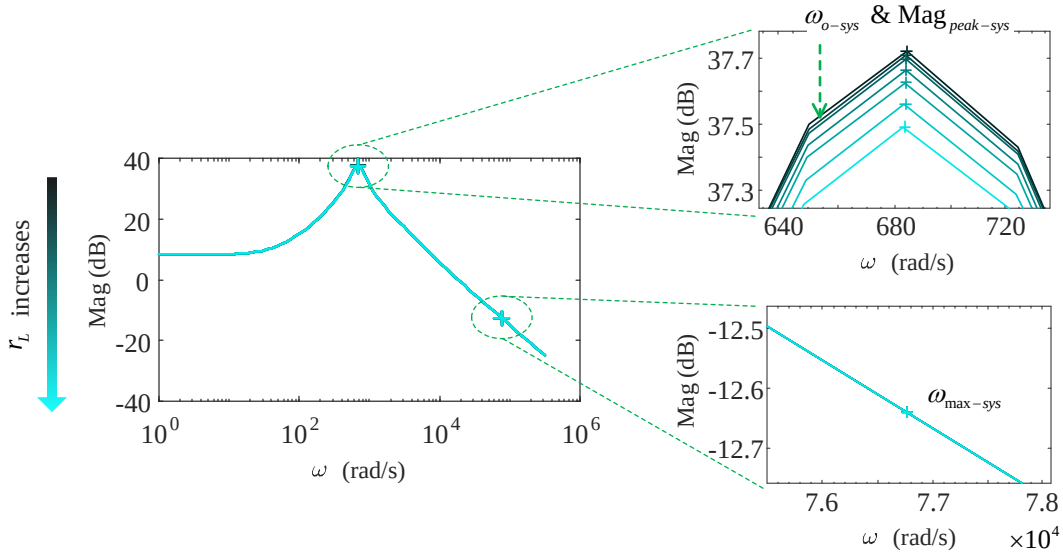


Figure 4.12: Magnitude plots of $G_{i_{PV}-d}(s)$ under different r_L.

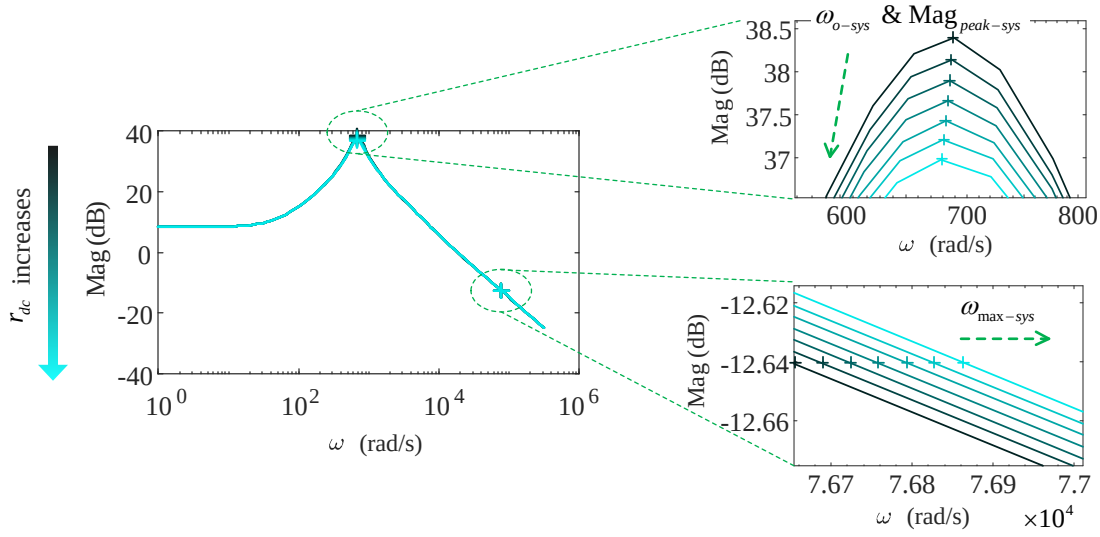


Figure 4.13: Magnitude plots of $G_{i_{PV}-d}(s)$ under different r_{dc}.

A larger value of r_{PV} causes a smaller value of $\omega_{max-sys}$, as indicated in Figure 4.11. The increasing values of r_{dc} and r_{C1} lead to an increase in $\omega_{max-sys}$, as shown in the simulation results in Figure 4.13 and Figure 4.14. However, Figure 4.12 verifies that the parasitic parameter r_L of L does not have an obvious effect on the maximum frequency of the perturbation signal $\omega_{max-sys}$.

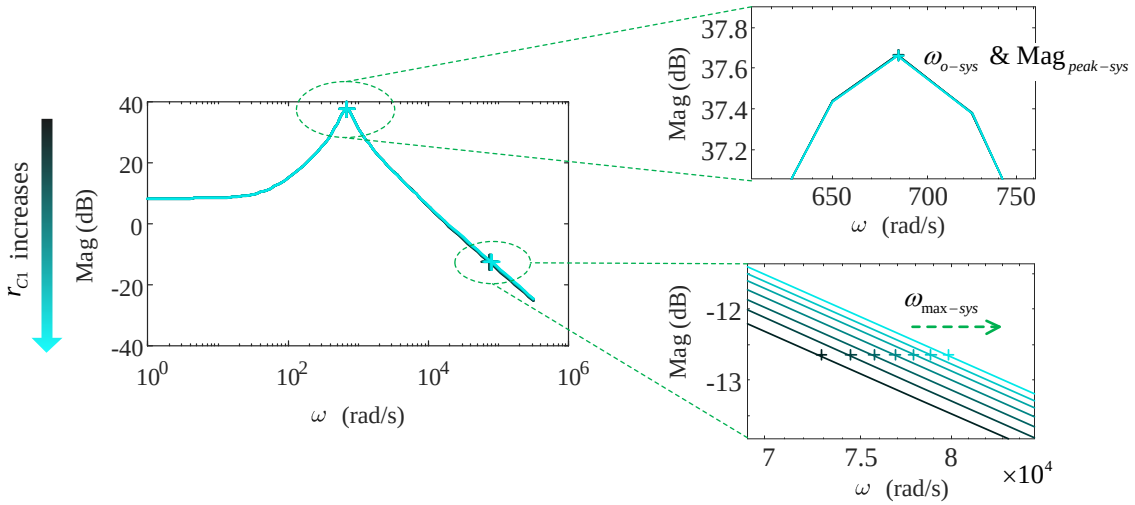


Figure 4.14: Magnitude plots of $G_{i_{PV}-d}(s)$ under different r_{C1}.

According to these simulation results, it can be concluded that as the value of D approaches 0.5, the value of $\omega_{sys-max}$ will be higher. Moreover, another significant impacting factor of $\omega_{sys-max}$ is L. To obtain a wider frequency range for the perturbation signal, the expected value of L should be as small as possible. Hence, in our platform, a small inductor with the required current ripple is selected. In addition, the resonant

frequency will easily fall within the frequency range of the perturbation signal. Large parasitic parameters can effectively reduce the influence of the resonant peak; however, this comes at the cost of increased power loss. Moreover, increasing the parasitic parameters cannot completely eliminate the influence of resonance due to their limited values, if the amplitude of the AC duty cycle signal remains constant. Therefore, to ensure the stability and linearity of the perturbation signal, the amplitude of the AC duty cycle should be adjusted. An adaptive configuration method of the AC duty cycle will be provided in the following section.

4.4 Advanced open-loop control strategy

4.4.1 Control strategy

We have introduced in Chapter 2 that between the MPPT and IS functionning modes of the PV panel, an intermediate mode IPT mode is added to guarantee the stability of the system. As defined , the PV panel should be controlled to operate at the injection point in IPT mode. Under the open-loop control, based on the power balance principle, the value of the DC duty cycle can be calculated by:

$$D = 1 - \sqrt{\frac{V_{PV}}{R_L I_{PV}}} \tag{4.30}$$

The value of V_{PV} and I_{PV} can be obtained from the IV curve; the value of R_L depends on the platform configuration. In this experiment, their values are set to: $V_{PV} = 34$ V, $I_{PV} = 0.7$ A and $R_L = 163\ \Omega$. The DC duty cycle can be calculated based on Equation (4.30), and its value is: $D = 0.454$.

According to the definition of $G_{i_{PV}-d}(s)$, the amplitude of the AC duty cycle can be calculated based on the magnitude of $G_{i_{PV}-d}(s)$ and the target amplitude of the perturbation signal, i.e., $K_{per}I_{PV}$. Considering the computational complexity of $|G_{i_{PV}-d}(s)|$, it is segmented into three frequency segments. By analyzing the gain of $G_{i_{PV}-i_L}(s)$ and $G_{i_L-d}(s)$ as shown in Figure 4.4, the frequency boundaries and the corresponding characteristics can be expressed as follows:

1. Frequency segment 1: $0 \leq \omega \leq \omega_{z-sys}$;
   The magnitude of $G_{i_{PV}-i_L}(s)$: $20\log(|G_{i_{PV}-i_L}(s)|) \approx 0$;
   The magnitude of $G_{i_L-d}(s)$: $20\log(|G_{i_{PV}-i_L}(s)|) \approx 20\log(K_{boost})$.

2. Frequency segment 2: $\omega_{z-sys} \leq \omega \leq \omega_{0-sys}$
   The magnitude of $G_{i_{PV}-i_L}(s)$: $20\log(|G_{i_{PV}-i_L}(s)|) \approx 0$;
   The magnitude of $G_{i_L-d}(s)$: $20\log(|G_{i_{PV}-i_L}(s)|) \approx 20\log(K_{boost} + k \cdot (\omega - \omega_{z-sys}))$.

3. Frequency segment 3: $\omega_{0-sys} \leq \omega \leq \omega_{max-sys}$
   The magnitude of $G_{i_{PV}-i_L}(s)$: $20\log(|G_{i_{PV}-i_L}(s)|) \approx 20\log(r_{C1}/(r_{C1} + r_{PV}))$;
   The magnitude of $G_{i_L-d}(s)$: $20\log(|G_{i_{PV}-i_L}(s)|) \approx 20\log(k_{slope}\omega)$.

where $k = (k_{slope}\omega_{0-sys} - K_{boost})/(\omega_{0-sys} - \omega_{z-sys})$.

Therefore, to obtain a stable perturbation signal based on the open-loop control strategy, the amplitude of the perturbation duty cycle is equal to:

$$\begin{aligned} 0 \leq \omega \leq \omega_{z-sys}: &\quad K_{per} I_{pv}/K_{boost} \\ \omega_{z-sys} \leq \omega \leq \omega_{0-sys}: &\quad K_{per} I_{pv}/(K_{boost} + k(\omega - \omega_{z-sys})) \\ \omega_{0-sys} \leq \omega \leq \omega_{max-sys}: &\quad K_{per} I_{pv}/(r_{C1} K_{per}\omega/(r_{C1} + r_{PV})) \end{aligned} \tag{4.31}$$

Under the selected rated/reference values of the parameters, the frequency boundary values are equal to: ω_{z-sys} = 50 rad/s, ω_{0-sys} = 683.7 rad/s, and $\omega_{max-sys}$ = 76858.41 rad/s. The target amplitude of the perturbation signal is set to 15% of I_{PV}. Based on the design described by (4.31), the calculated amplitudes of AC duty cycle signals from 1 Hz to 2 kHz are depicted in Figure 4.15 (a). The minimum value occurs around the resonant frequency. The corresponding amplitude of the perturbation current signal can be calculated and are shown in Figure 4.15 (b).

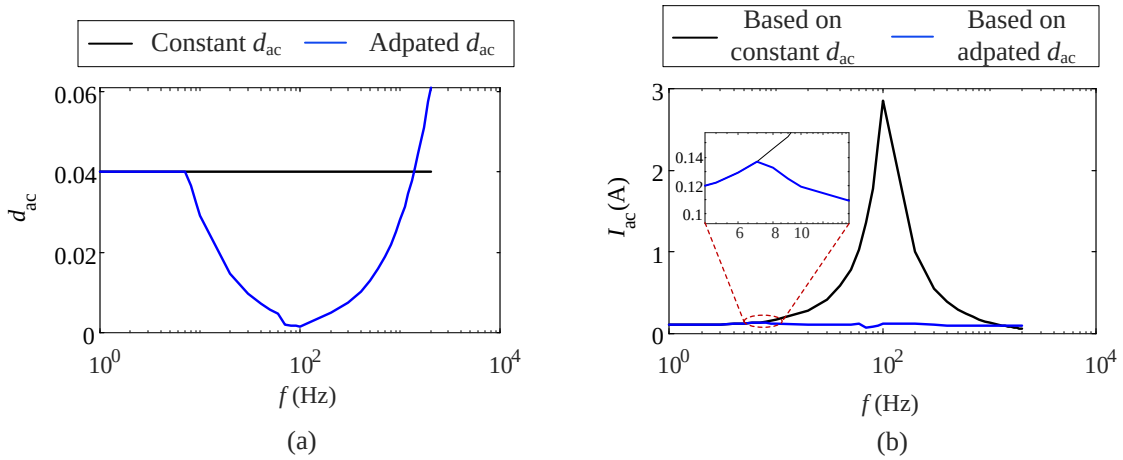


Figure 4.15: Comparison of the traditional and advanced open-loop strategies:
(a) amplitude of the AC duty cycle; (b) amplitude of the perturbation current signal.

Compared to the amplitude resulting from the constant d_{ac}, the adapted value can reduce the influence of resonance. However, there are still some frequencies where the amplitude of the perturbation current signal exceeds the target amplitude. This is illustrated in the enlarged portion in Figure 4.15 (b). If the PV panel enters the nonlinear region caused by the exceeded part, the calculated amplitude of the AC duty cycle needs to be further reduced by multiplying a proper proportional coefficient.The coefficient selection is based on analyzing the accuracy of the response signal, specifically the SNR or the percentage of fundamental component of the response signal at the frequency of the perturbation signal. The coefficient value decreases until the response signal achieves the desired accuracy, such as the percentage of fundamental component of the response signal $\geq 80\%$ in our work.

4.4.2 Experimental verification

To verify the effectiveness of the advanced open-loop control strategy, considering the variation range of the experimental AC signal, the experimental condition O-II is selected for open-loop verification. The operating condition O-II is set as:

▷ Irradiance level: 268 $\mathrm{W/m^2}$;

▷ Temperature: 323.15 K;

▷ DC component current at injection point, i.e., I_{PV}: 0.7 A.

When a constant amplitude of the AC duty cycle is added to realize the perturbation, there is a resonance caused by the series connection of the inductor and capacitor when switch is turned on, as shown in Figure 4.16. There is a significant peak of the output current signal during IS implementation. After analyzing, the amplitude of the corresponding perturbation current signal is obtained, which is depicted in the lower left corner of Figure 4.16. It can be observed that the peak (amplitude up to 0.7 A, exceeding 15% of the DC component current) occurs within the frequency range of [565 rad/s (90 Hz), 1256 rad/s (200 Hz)], aligning with the resonant frequency of the system. As a consequence of resonance, the operating point deviates from its linear characteristics. Furthermore, as the frequency increases, the amplitude of the perturbation current signal decreases to a level where obtaining accurate information about current and voltage becomes challenging, even if the frequency is less than the cutoff frequency of the converter.

When the amplitude of the perturbation signal is calculated and adapted based on the proposed method in last section, the influence of resonance can be effectively eliminated, as illustrated in Figure 4.17. The DC component of the output current is extracted and shown as the pink line in Figure 4.18. Compared with the reference value I_{ref}, the DC component value of output current I_{PV} is slightly bigger. The corresponding average control error is calculated and equal to 1.5%.

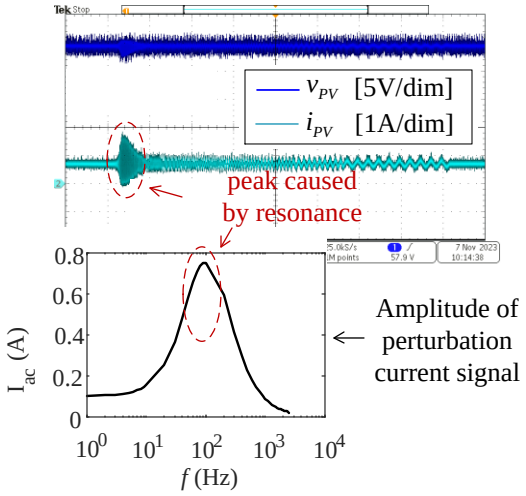


Figure 4.16: Voltage and current experimental waveform under open-loop control: constant amplitude of the perturbation signal under condition O-II.

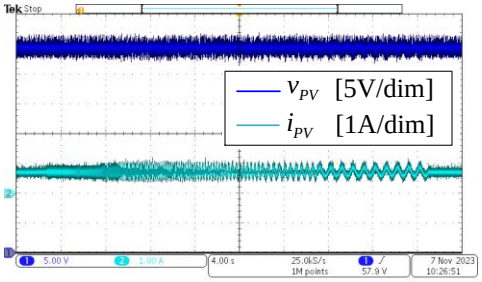


Figure 4.17: Voltage and current experimental waveform under open-loop control: adapted amplitude of the perturbation signal under condition O-II.

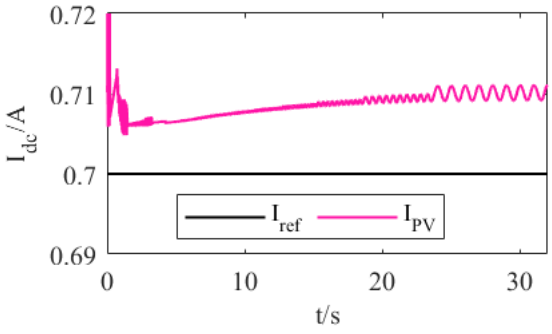


Figure 4.18: DC components of I_{PV} under open-loop control strategy under condition O-II.

The amplitude of the perturbation current signal is extracted and plotted in Figure 4.19. The blue line represents the average amplitude of the perturbation current signal under open-loop control based on equation (4.31). The blue shadow represents the confidence interval (95%) of the amplitude. Comparing the DC and AC components of the output current of the PV panel, the amplitude range of the perturbation signal are exhibited as the shaded mesh area in Figure 4.17, ranging from 11.4% I_{pv} to 20%I_{pv}, where the portion exceeding the target (15% I_{pv}) is depicted in red, while the portion below the target is shown in blue. It should be noted that 20%I_{pv} is the maximum value for the perturbation signal of our PV panel to ensure the linearity during IS implementation at this operating condition, after multi-experimental tests.

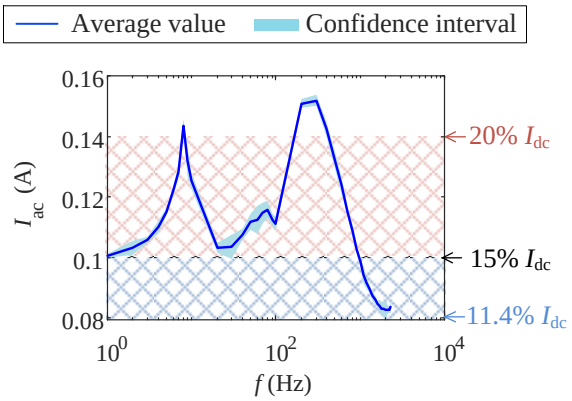


Figure 4.19: Amplitude of perturbation signal under open-loop control strategy under condition O-II.

The results indicate an effective suppression of the resonant peak. However, maintaining the amplitude of the perturbation signal stable within the target value across all frequencies remains challenging. In addition, the alterations in parasitic parameters during operation can result in the deviation on the calculated results and the location of the injection point. Considering the deviation between the data-sheet specifications and the actual parasitic parameters during operation, a compensation coefficient needs to be applied on the calculated perturbation duty cycle. Herein, a value of 0.8 is utilized to adjust the variation range of I_{ac} within 20% I_{dc}. It should be noted that this compensation coefficient should be adjusted during online experiment according to the actual operating operating condition and configuration of the system.

The IS spectra acquired under traditional and advanced open-loop control strategies are presented in the form of Nyquist curves in Figure 4.20. Under the open-loop control with a constant amplitude of the perturbation duty cycle, two abnormal areas, marked as area 1 and area 2, will impact the description accuracy of the performance of the PV panel based on IS information. Area 1 is caused by resonance, while Area 2 is formed due to the reduced accuracy of the sampling data when the amplitude of the perturbation current signal and response voltage signals are small. Under the advanced open-loop control strategy, the quality of the perturbation current signals will be improved and the Nyquist curves with high precision can be acquired.

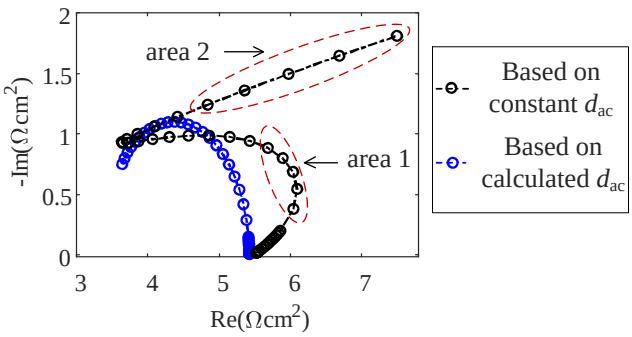


Figure 4.20: IS spectrum under different control methods under condition O-II.

4.5 Discussions

The advanced open-loop control strategy can reduce the risk of the PV panel to enter the nonlinear region caused by resonance and assure the measurement accuracy at high frequency. This allows the open-loop control strategy to be applied in health monitoring of the PV panel by converter-based IS. However, as analyzed in the last section, the calculation of the DC duty cycle relies on the power balance principle under ideal operating conditions. The existence of parasitic parameters results in a deviation of the location. And when the operating conditions is changed, such as irradiance levels, temperatures, etc., the output voltage and current of the PV panel will vary simultaneously. In these cases, the location of the injection will move, if the same DC duty cycle is used.

As for the calculation of the amplitude of the AC duty cycle, an adaptive configuration method is proposed herein to improve the feasibility of the open-loop control. Nevertheless, due to the parameter uncertainty, the obtained amplitudes of the perturbation signal across the entire frequency range vary widely, ranging from 11.4% I_{PV} to 20% I_{PV} in this work. An appropriate coefficient should be further designed and applied to adresse this issue. A similar challenge may arise in determining the location of the injection point – altering the operating conditions will impact the control accuracy.

4.6 Conclusions

An AC duty signal is directly added in the open-loop control. This method is the simplest one to implement. However, the converter will risk resonance due to the series connection of L and C_{dc} when the switch is off. The resonance will bring the PV panel to a nonlinear region, resulting in inaccuracies of IS measurement. The influencing factors of the resonant frequency and corresponding magnitude are analyzed. The parasitic

parameters will decrease the peak value of the gain.

Furthermore, the limitations on the maximum frequency for the perturbation signal are provided, at which the amplitude of the AC duty signal reaches its maximum value. To obtain a higher maximum frequency value, three adjustments can be made:

1. Shorten the connection between the PV panel and the support capacitor to reduce the value of r_{PV};
2. Select a small inductance. It should be noted that the current ripple should not impact the accuracy of IS measurement;
3. Modify the operating conditions to ensure that the value of the DC duty signal, i.e., D, is closed to 0.5.

The smaller the values of r_{PV}, L and the difference between D and 0.5, the higher the maximum frequency value can reach.

In order to guarantee the linearity and stability during IS implementation, an adaptive configuration method for the AC duty signal is proposed. The open-loop control strategy based on the calculated value can ensure that the amplitude of the perturbation signal is limited in a specific range. The simulation and experimental results verify that the advanced open-loop control can sufficiently eliminate the influence of resonance. However, the open-loop control strategy cannot ensure the precise location of the injection point and its accuracy is significantly influenced by the parasitic parameters and operating conditions. Therefore, as an alternative control strategy, closed-loop control will be addressed in the next chapter. Detailed information can be found in the following chapters.

Chapter 5

Closed-loop control strategies for converter-based IS

5.1 Introduction

As introduced in Chapter 4, it is difficult for the open-loop control strategy to maintain a stable current or voltage at the injection point when the operating condition is changed. Besides, the uncertainty of all parameters, i.e., operating parameters, element parameters and parasitic parameters, increases the difficulty of achieving accurate control results. Closed-loop control can provide a sufficient solution to these challenges.

The closed-loop control strategies for converters can be generally categorized into three categories: single-loop voltage control, single-loop current control and voltage-current dual-loop control. Single-loop voltage control directly regulates the perturbation voltage, and it may suffer from stability issues [118]. Meanwhile, dual-loop control typically combines an inner current loop with an outer voltage loop, and can greatly improve control stability. However, its control bandwidth is much limited due to the coupling design between the inner and outer loops. Typically, the crossover frequency of the outer loop should be at least five times smaller than that of inner loop.

In our work, the current signal is selected as the perturbation signal. Therefore, the single-loop current control is chosen for IS implementation in the PV panel, as it offers a higher bandwidth and better stability compared to the other two control methods.

Numerous closed-loop control methods have been presented in the literature for the IS implementation,

depending on the specific requirements of the target systems. Authors in [77] analyzed amplitude distortions in open-loop control of a boost converter, and designed a compensated current control method using a proportional-integral (PI) controller to obtain the internal impedances of two lithium-ion batteries. The achieved frequency range for the perturbation signal is [0.1 Hz, 1 kHz]. However, the PI controller herein was heuristically tuned. No design principle was outlined for the controller in order to meet a high tracking accuracy and a wide enough bandwidth for IS measurements. In [78], a closed-loop step-function perturbation of the output voltage of a bidirectional buck/boost converter was applied for online IS measurements of batteries. The perturbation frequencies of the step function used were from 10 Hz to 1 kHz. In this study, the compensator controller type was not specified. Moreover, a high sampling rate of at least 100 times larger than the highest perturbation frequency was required to ensure accurate representations of the AC voltage and current waveform. In [119], a controller design for fault diagnosis and load balancing of fuel cells based on IS measurements was introduced. The controller parameters were calculated based on the transfer function of a conventional boost converter, and the target frequency range was [0.1 Hz, 1 kHz]. However, the design criteria and limitations were not clearly stated. A combination of a PI controller with a resonant controller was proposed in [79], to achieve a higher frequency of the perturbation signal than the converter's crossover frequency for a fuel cell system. This method controlled the DC and AC components separately, with a particular focus on the resonant controller's design. However, the division of the DC and AC components was not emphasized, and only four impedances at 100 Hz, 500 Hz, 1 kHz and 2 kHz were measured.

Aiming at the researching gap, this chapter focuses on the design of closed-loop control strategies based on three commonly used compensation controllers in linear system control, i.e., proportional (P), PI and quasi-proportional resonant (QPR) controllers. According to the distinct characteristics of these three compensation controllers, two control strategies are designed and compared both in theory and experiment, including:

- Systematic design and comparison of two control strategies, i.e., unified control and separated control, for both the DC component and AC perturbation signal control. In the separated control strategy, a segmented low pass filter (LPF) with a variable cut-off frequency, which separates the DC and AC components, is proposed to ensure both the tracking accuracy and control speed of the control loops.
- Online experimental verification and comparison of the designed control strategies. In the experimental tests, a set of IS measurements are acquired online with high tracking accuracy and sufficient signal-to-noise ratio (SNR) in the frequency range of [1 Hz, 2 kHz]. Meanwhile, as an illustration, the operating states such as different irridiance levels, can be reflected effectively by the evolution of internal impedance.

5.2 Control objectives of closed-loop control strategies

5.2.1 Control objectives

The closed-loop current control block diagram without compensation is shown in Figure 5.1, where the blue lines represent the sampling current and the duty cycle, corresponding to the sampling data and the switching signals in Figure 2.2.

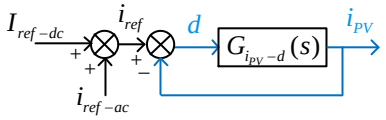


Figure 5.1: Closed-loop current control without compensation.

I_{ref_dc} and i_{ref_ac} represent the reference values of DC and AC components, respectively. The connection between the reference value and the output current of the PV panel, i.e., i_{PV}, is satisfied as:

$$i_{PV} = i_{ref} \left| \frac{G_{i_{PV}-d}(s)}{1 + G_{i_{PV}-d}(s)} \right| \tag{5.1}$$

Based on (5.1) and the rated/reference element and parasitic parameters summarized in Table 4.1, its corresponding uncompensated closed-loop gain is depicted in Figure 5.2. As for the operating parameters, in this chapter, the same operating conditions as in the simulation presented in Chapter 2, i.e., I_{PV} = 1 A, $V_{PV} \approx$ 33 V, are selected as an example to explain the parameters design.

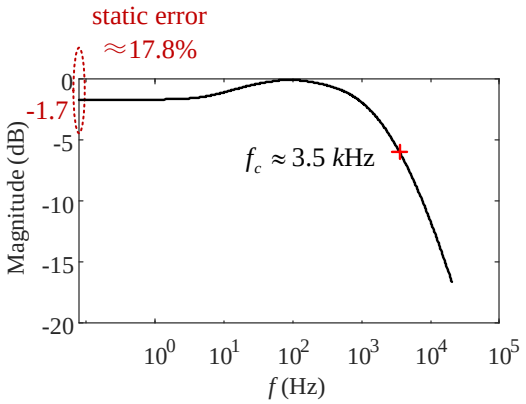


Figure 5.2: Magnitude plot of the closed-loop transfer function without compensation.

As can be observed in Figure 5.2, a static error exists at very low frequencies. And the corresponding

static error reaches 17.8%. It means that in an uncompensated control system, there is a deviation in the location of the injection point. When the frequency of the perturbation signal is higher than the crossover frequency, i.e., f_c, the amplitude of the actual current signal is significantly lower than the reference value, even at the target frequency of this work, i.e., 2 kHz, and the tracking error is bigger than 35.7%. As the injection point moves towards the open-circuit point, both the static error and the AC signal tracking error will increase.

In addition, the theoretical maximum frequency of the converter for the perturbation signal injection can reach $f_{max-sys} = \omega_{max-sys}/(2 * pi) = 10.3$ kHz, which is even larger than $f_c = 3.5$ kHz. (The value of $\omega_{max-sys}$ with the new operating parameters is calculated based on the method proposed in Chapter 4.) The value of f_c can limit the bandwidth of the perturbation current signal. Therefore, to achieve reliable broadband IS measurements in PV panels, a compensation controller is necessary and should meet the following requirements:

- High open-loop gain at 0 Hz. It should be as high as possible to ensure a stable injection point of the PV panel during IS implementation;
- Large crossover frequency. It should be sufficiently extended to ensure a wide bandwidth for the perturbation current signal;
- High tracking accuracy. The reference of the perturbation signal should be tracked with high accuracy to prevent the operating points from entering the nonlinear region during IS implementation;
- Stable control system. It is necessary to ensure that the system meets the stability criteria during IS implementation – the control system has sufficient phase margin ($> 30^o$) and gain margin (> 6 dB), or all the poles of the closed-loop transfer function lie in the left-half plane.

5.2.2 Characteristics of the three controllers

In order to meet the control objectives, it is essential to choose an appropriate controller for compensation. P, PI and proportional resonant (PR) controllers are three commonly used compensation controllers in linear system control [120]. Due to the presence of sampling errors, the PR controller is often replaced by the QPR controller in practical uses [121]. Hence, the QPR controller instead of the PR controller is analyzed in this study. The transfer functions of the three controllers can be expressed separately as follows:

P controller:

$$G_P(s) = K_p \tag{5.2}$$

PI controller:

$$G_{PI}(s) = K_{pi}(1 + \frac{\omega_{z-pi}}{s}) \tag{5.3}$$

QPR controller:

$$G_{QPR}(s) = K_{qpr} + \frac{K_r \omega_{c-qpr} s / \omega^2_{res-qpr}}{\frac{s^2}{\omega^2_{res-qpr}} + \frac{2s\omega_{c-qpr}}{\omega^2_{res-qpr}} + 1} \tag{5.4}$$

where K_p, K_{pi} and K_{qpr} represent the proportional factor of the P, PI and QPR controller, respectively; ω_{z-pi} is the angular frequency when the phase angle of PI controller is equal to -45^o; $\omega_{res-qpr}$ represents the angular resonant frequency of the QPR controller, ω_{c-qpr} and K_r denote the gain bandwidth and peak gain at its resonant point, respectively.

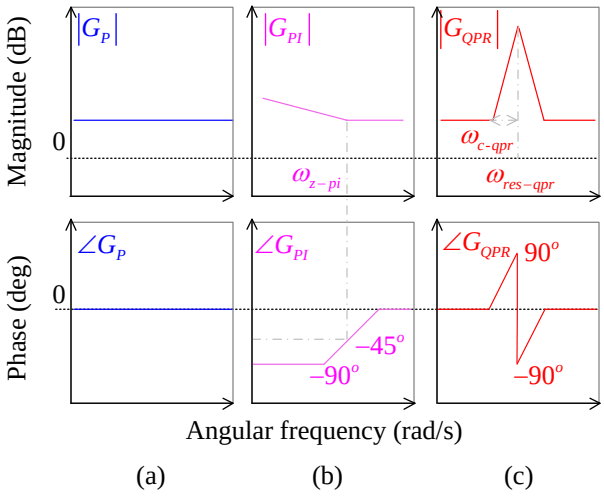


Figure 5.3: Asymptotic Bode plots of the three controllers (upper: magnitude plots; lower: phase plots): (a) P controller; (b) PI controller; (c) QPR controller.

Due to the pole at the origin and the zero at $f_{z-pi} = \omega_{z-pi}/2\pi$, the gain of the PI controller can theoretically reach an infinite value and the phase is smaller than 0^o, when the frequency is going down to 0 Hz. The QPR controller, on the other hand, adds one resonant part. Its two conjugate poles result in a significant gain at $f_{res-qpr} = \omega_{res-qpr}/2\pi$. The gain at other frequencies depends on the value of K_{qpr}. A suitable bandwidth of the QPR controller can be achieved by adjusting accordingly the value of ω_{c-qpr}.

In summary, the PI controller can track DC signals without static errors, but the phase margin of the system may be influenced. The P controller has the simplest structure, but exhibits an error in the location of the injection point, which affects the accuracy of IS measurement. The QPR controller can only track signals with a frequency of $f_{res-qpr}$ with high accuracy. To achieve the control objectives of converter-based IS, closed-loop control strategies relying on the three compensation controllers can be categorized into two

classes:

1. Unified control strategy, which utilizes a single controller to achieve all the aforementioned requirements. In this strategy, the DC component, i.e., the injection point, and the AC component, i.e., the perturbation signal, are controlled in a unified way;

2. Separated control strategy, which utilizes a combination of controllers in cases where a single controller cannot satisfy all the requirements. In this strategy, the DC and AC components are controlled separately.

The detailed information and the design of control parameters of the two control strategies will be provided in the next section.

5.3 Unified control strategy

As indicated in Figure 5.3 (b), the PI controller exhibits an infinite gain when the frequency is going down to 0 Hz and the system's crossover frequency can be sufficiently extended by adjusting the controller's parameters. It is possible to meet all the aforementioned requirements for IS implementation based on a single PI controller. Therefore, it is chosen for the unified control strategy, and corresponding control block is shown in Figure 5.4. It indicates that the DC and AC components are controlled by the same controller. Considering the characteristics of the two operating modes during IS implementation, i.e., IPT and IS modes, the same control method is applied. When the PV panel operates in IPT mode, the value of i_{ref-ac} is set as 0; when the PV panel operates in IS mode, the value of i_{ref-ac} represents the target value of the perturbation signal.

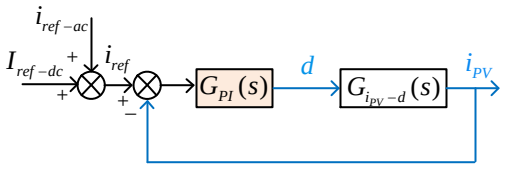


Figure 5.4: Control block of the unified control strategy.

The open-loop transfer function of the system with a single PI compensation controller, as indicated in Figure. 5.4, can be described as:

$$H_{PI}(s) = G_{PI}(s) \cdot G_{i_{PV}-d}(s) \tag{5.5}$$

At high frequencies (i.e., $\omega \gg \omega_{0-i_L}$), by substituting (4.6) and (4.11), the compensated gain can be approximated as:

$$\begin{aligned} |H_{PI}(s)| &= |G_{PI}(s)| \cdot |G_{i_{PV}-d-h}(s)| \\ &\approx |G_{PI}(s)| \cdot \frac{r_{PV}}{r_{PV}+r_{C1}} \cdot K_{boost} \cdot \frac{\omega_{0-i_L}^2}{\omega_{z-i_L} \cdot \omega_{inj}} \end{aligned} \tag{5.6}$$

where $|G_{i_{PV}-d-h}(s)|$ represents the gain of $G_{i_{PV}-d}(s)$ at high frequencies; ω_{inj} is the angular frequency of the perturbation signal.

The relationship between the output current of the PV panel (i.e., i_{PV}) and the reference current (i.e., i_{ref}) shown in Figure 5.4 is:

$$i_{PV} = i_{ref} \cdot \frac{|H_{PI}(s)|}{1+|H_{PI}(s)|} \tag{5.7}$$

Based on (5.7), to ensure that the current control loop is effectively compensated, the compensated gain, denoted as $|H_{PI}(s)|$, must meet: $|H_{PI}(s)| \geq 9$. As evidence, this condition that guarantees $i_{PV}/i_{ref} \geq 90\%$ allows to keep the tracking error of the perturbation signal smaller than 10%, and (5.6) can be further expressed as:

$$|G_{PI}(s)|_{\omega_{inj-max}} \cdot \frac{r_{PV}}{r_{PV}+r_{C1}} \cdot K_{boost} \cdot \frac{\omega_{0-i_L}^2}{\omega_{z-i_L} \cdot \omega_{inj-max}} \geq 9 \tag{5.8}$$

where $\omega_{inj-max}$ is the target maximum angler frequency of the perturbation signal.

To ensure a sufficient control bandwidth, the target crossover frequency, denoted as ω_{ct}, should be greater than the value of $\omega_{inj-max}$. According to the definition of the crossover frequency being the frequency at which the open-loop gain reaches the value 1, and with consideration of (5.6), the gain of the compensated current control loop at f_{ct} should satisfy:

$$|G_{PI}(s)|_{\omega_{ct}} \cdot \frac{r_{PV}}{r_{PV}+r_{C1}} \cdot K_{boost} \cdot \frac{\omega_{0-i_L}^2}{\omega_{z-i_L} \cdot \omega_{ct}} = 1 \tag{5.9}$$

Therefore, $\omega_{inj-max}$ should be $\leq (1/9) \cdot \omega_{ct}$ based on (5.8) and (5.9), while subject to the system constraints. Meanwhile, to mitigate the switching noises, the target crossover frequency, i.e., ω_{ct}, should be theoretically less than half of the switching frequency in angular form, denoted as ω_{sw}. The relationship between $\omega_{inj-max}$, ω_{ct} and ω_{sw} can thus be expressed as:

$$\omega_{inj-max} \leq min[\frac{1}{9}\omega_{ct}, \quad \omega_{max-sys}] < \frac{1}{2}\omega_{sw} \tag{5.10}$$

where $\omega_{sw} = 2\pi \cdot f_{sw}$.

In our experimental setup and due to hardware limitations, the switching frequency f_{sw} is set as 80 kHz. According to (5.10), ω_{ct} is set as between $[1/4,\ 1/5]$ of ω_{sw}, e.g., $2\pi \times 1.8 \times 10^4$ rad/s, to reduce sufficiently the switching noise in actual operation and $\omega_{inj-max}$ is thus set as $2\pi \times 2 \times 10^3$ rad/s. It is to be noted that this value is verified by several groups of experiments as enough to obtain the necessary impedance information for the simplified AC-ECM of the PV panel. Within these experimental conditions, the frequency range of the perturbation current signal is thus set within the range of [1 Hz, 2 kHz].

By adopting the rated/reference value of element parameters and parasitic parameters summarized in Table 4.1 and setting the target crossover frequency in the *pidtune* function in MATLAB, K_{pi} and ω_{z-pi} can be calculated as: $K_{pi} = 5.26$, $\omega_{z-pi} = 1.04 \times 10^4$, with a sufficient phase margin (i.e., 90^o) to guarantee the system's stability. The magnitude of the closed-loop transfer function under unified control with the calculated parameters is indicated in Figure 5.5.

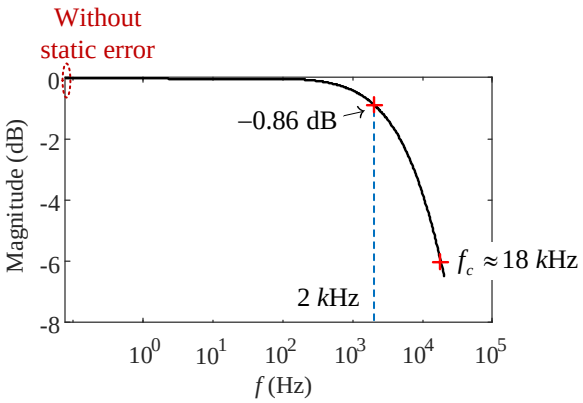


Figure 5.5: Magnitude of system under the unified control strategy.

With the unified control strategy, the static error is equal to 0, the magnitude at 2 kHz is equal to -0.85 dB, representing that the system will stably operate at the target injection point and the tracking efficiency of the amplitude of the perturbation signal is greater than 90%.

It should be noted that the parameters satisfying the requirements of stability and control targets are not just one set, but a range. Moreover, during practical applications, the controller parameters may need further tuning due to the influence of system parasitic parameters, potential noises and uncertainties. However, the theoretical values calculated herein can still serve as reference values. The same comment applies to the following controller parameters.

5.4 Separated control strategy

As analyzed in Section 5.2, the P controller amplifies the entire frequency range signal with the same proportional factor but cannot eliminate the static errors when the frequency decreases to 0 Hz. Meanwhile, the QPR controller can only achieve accurate control at its resonant frequency. Therefore, both controllers require an additional section to control the DC component to ensure the stability of the injection point. When applying the two controllers, a combined control is thus necessary, and two control loops for the DC and AC components control should be designed separately, which is thus named as separated control strategy herein.

In this strategy, as indicated in Figure. 5.6, a PI controller with a narrow control bandwidth can realize the DC component i_{dc} tracking without static errors, while P or QPR controllers is used to control the AC component i_{ac}. It should be noted that, to effectively separate the original current signal i_L into DC and AC components, a first-order LPF is added in the current feedback path and its parameters should be carefully designed to ensure both the tracking accuracy and the control speed of the control loops. When the reference signal of AC component i_{ref-ac} is set to 0, the PV panel will be controlled to operate at the targetinjection point IPT mode by the PI controller. The parameter design of separated control is divided into three parts: design of the LPF, design of the PI controller and design of the P/QPR controller.

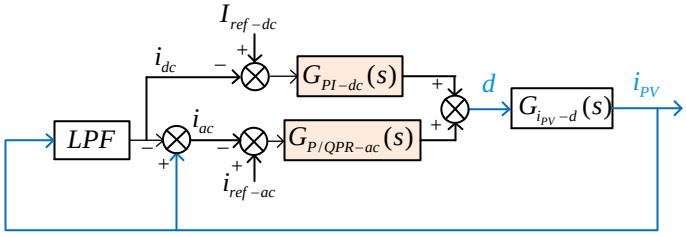


Figure 5.6: Control block of the separated control strategy.

5.4.1 LPF design

The transfer function of the LPF can be written as:

$$G_{LPF}(s) = \frac{1}{1 + s/\omega_{0-LPF}} \tag{5.11}$$

where ω_{0-LPF} is the cut-off frequency. The attenuation of the signal i_L at ω_{0-LPF} is -3 dB (approximately 70% times gain). The design principle of the LPF is to attenuate the AC component above ω_{0-LPF} as much as possible (with a sufficiently low ω_{0-LPF}), while ensuring the control speed (with a sufficiently high ω_{0-LPF},

as the settling time under unit step response is inversely proportional to ω_{0-LPF}). Under broadband frequency perturbations, maintaining a constant ω_{0-LPF} can hardly achieve both significant attenuation of the AC component and sufficient control bandwidth.

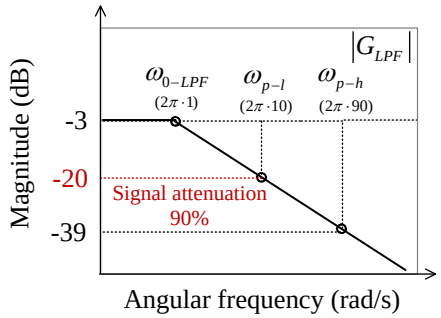


Figure 5.7: Asymptotic magnitude plot of the LPF (example of $\omega_{p-l} = 2\pi \cdot 10$ rad/s, $\omega_{p-h} = 2\pi \cdot 90$ rad/s).

For simplicity of online control, perturbation frequencies are divided into several ranges. Consequently, a segmented LPF with a variable cut-off frequency is designed according to the defined range. Each frequency range can be expressed as $[\omega_{p-l}, \omega_{p-h}]$, where $\omega_{p-l} = 2\pi \cdot 10^{(i-1)}$, $\omega_{p-h} = 2\pi \cdot 10^{i} - 2\pi \cdot 10^{(i-1)}$, with an angular frequency interval of $2\pi \cdot 10^{(i-1)}$ and $i = 1, 2, 3, \cdots$. In each range, the ω_{0-LPF} of the LPF is set as 10% of the lower frequency limit ω_{p-l} of the perturbation signal corresponding to a gain of -20 dB, i.e. 10% times gain or 90% signal attenuation as indicated in Figure. 5.7:

$$\omega_{0-LPF} = 0.1\omega_{p-l} \tag{5.12}$$

In this asymptotic magnitude plot of the LPF, the relationship between ω_{0-LPF}, ω_{p-l} and ω_{p-h} is indicated. When (5.12) is satisfied, the perturbation signal within the range $[\omega_{p-l}, \omega_{p-h}]$ will be significantly attenuated by at least 90%.

5.4.2 PI controller design for DC component control

To set appropriate PI controller parameters, the input of the AC component is considered as a disturbance and the corresponding control block diagram in Figure. 5.6 can be simplified as Figure. 5.8. In this case, the

transfer function of DC component open-loop current control can be written as:

$$\begin{aligned} H_{PI-dc}(s) &= G_{PI-dc}(s) \cdot G_{LPF}(s) \cdot G_{i_{PV}-d}(s) \\ &= K_{pi-dc} \cdot \frac{(1+\frac{\omega_{z-pi-dc}}{s})}{1+\frac{s}{\omega_{0-LPF}}} \cdot G_{i_{PV}-d}(s) \end{aligned} \tag{5.13}$$

where $G_{PI-dc}(s)$ represents the transfer function of the PI controller for DC component control.

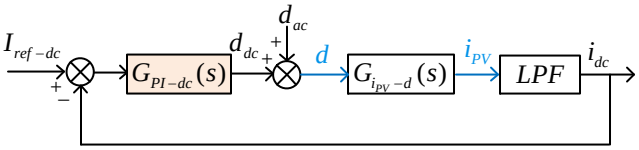


Figure 5.8: Control block of the separated control strategy – DC component control.

To further reduce the impact of residual perturbation signals on DC component control, the crossover frequency ω_{c-dc} of DC component control system should be smaller than the perturbation frequency. Meanwhile, to ensure the tracking accuracy of the DC component, the attenuation of the perturbation signal must be sufficient. It means ω_{c-dc} should be greater than the cutoff frequency of the LPF ω_{0-LPF}, as indicated in Figure. 5.9.

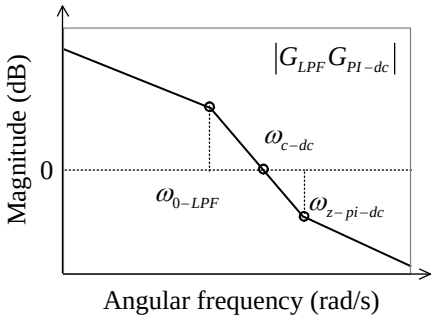


Figure 5.9: Asymptotic magnitude plot of DC component control with a PI controller.

Considering the selection of ω_{0-LPF} in the last subsection, ω_{c-dc} is expressed as:

$$\omega_{c-dc} = n \cdot \omega_{0-LPF} \tag{5.14}$$

where n represents the proportional relationship between ω_{c-dc} and ω_{0-LPF}, and belongs to [1, 9]. The maximum value of n implies a fast control speed for the system, but stabilization may be challenging. In our study, the value of n is selected as 5 during online experimental tests.

Based on (5.14), a group of appropriate parameters of the PI controller can be calculated by the *pidtune* function in MATLAB. For example, the PI controller parameters can be set as: $K_{pi-dc} = 0.307$, $\omega_{z-pi-dc} = 28.5$ to achieve the crossover frequency of 5 Hz, which can effectively filter out the residual perturbation signal within the range [10 Hz, 90 Hz] and also ensure the DC component tracking accuracy. With the set parameters, all the poles of the closed-loop transfer function shown in Figure 5.8 lie in the half-left plane which ensures the system stability.

Based on the designed parameters, the magnitude of the DC component of the system under separated control is illustrated in Figure 5.10. With the separated control strategy, the static error at the injection point is eliminated.

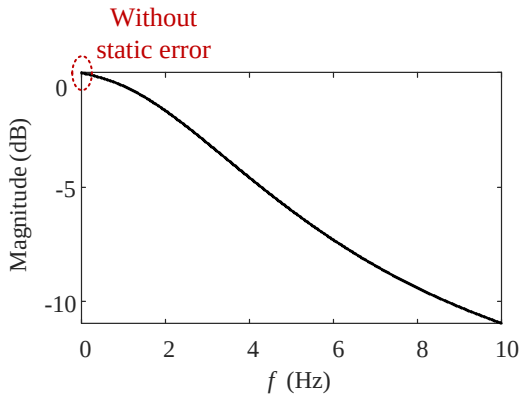


Figure 5.10: Magnitude plot of the system under the separated control strategy – DC component.

5.4.3 P and QPR controller design for AC component control

For the perturbation current signal control, the target is to achieve an open-loop gain as large as possible at the perturbation frequency. The DC component input is seen as a disturbance and the control block diagram can be simplified as Figure 5.11.

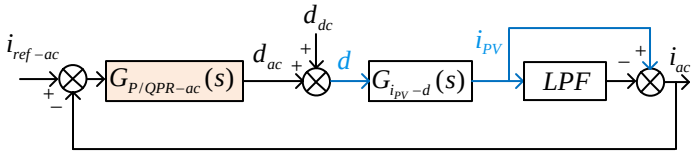


Figure 5.11: Control block of the separated control strategy – AC component control.

The transfer function of AC component open-loop control can be expressed as:

$$G_{ac}(s) = G_{P/QPR}(s) \cdot (1 - G_{LPF}(s)) \cdot G_{i_{PV}-d}(s) \tag{5.15}$$

As introduced, the P controller amplifies the entire frequency range signal with the same proportional factor with an adequate phase margin. If a P controller is selected, for (5.15), the crossover frequency of the control system only needs to be less than half of the switching frequency. To ensure that the current control loop is effectively compensated, the compensated gain, denoted as $|H_P(s)|$, must meet: $|H_P(s)| \geq 9$, following the same principle as that of the unified control strategy. This condition guarantees $i_{ac}/i_{ref-ac} \geq 90\%$, thus keeping the tracking error smaller than 10%, even at $\omega_{inj-max}$, and can be further expressed as:

$$|H_P(s)|_{\omega_{inj-max}} = |\frac{s}{s + \omega_{0-LPF}} \cdot K_p \cdot G_{i_{PV}-d}(s)|_{\omega_{inj-max}} \geq 9 \tag{5.16}$$

Under the same considerations as the unified control strategy, the target crossover frequency of the system should satisfy (5.10), if the P controller is selected in the separated control strategy. By applying the *pidtune* function in MATLAB, K_p is set as 5.26 for the entire frequency range [1 Hz, 2 kHz], with a sufficient phase margin equal to 90^o to ensure the system stability.

If a QPR controller is selected, (5.15) is equal to:

$$G_{ac}(s) = G_{Com-QPR}(s) \cdot G_{i_{PV}-d}(s) \tag{5.17}$$

where $G_{Com-QPR}(s)$ represents the compensation part, can be expressed as:

$$G_{Com-QPR}(s) = \frac{s}{s + \omega_{0-LPF}} \cdot G_{QPR}(s) \tag{5.18}$$

Its asymptotic magnitude plot is depicted in Figure 5.12.

According to (5.4), the gain of the QPR controller at the perturbation frequency ω_{inj} which is equal to $\omega_{res-qpr}$, is calculated as:

$$|G_{QPR}(s)|_{\omega_{inj}} = K_{qpr} + K_r/2 \tag{5.19}$$

In Figure 5.12, ω_2 affects the dynamic performance of the compensated system and its value is influenced by K_{qpr}. As K_{qpr} increases, ω_2 decreases, resulting in a better dynamic performance. Furthermore, the value of K_{qpr} determines the amplification factor of signals beyond just the perturbation signals. It means that

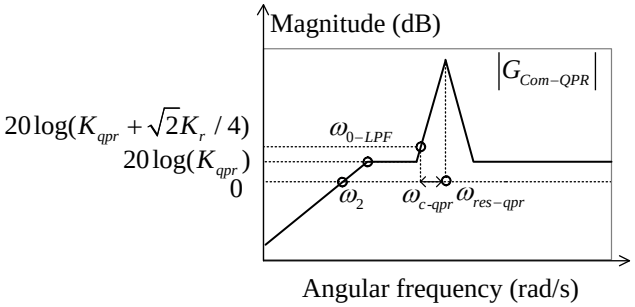


Figure 5.12: Asymptotic magnitude plot of a QPR controller based compensation part of AC component control.

a lower value of K_{qpr} will be beneficial to improve the SNR of the perturbation signals. ω_{c-qpr} represents the bandwidth of the QPR controller. A wider bandwidth can also increase the dynamic performance of the system, but will concurrently decrease the SNR of perturbation signals. However, in this application, IS implementation requires that the system operates at a steady-state operating point. The requirements for the dynamic performance are not very strict. Hence, a small K_{qpr} is normally sufficient, and it is set as 0.2 herein. For ω_{c-qpr}, a typical value is 5 rad/s. In practical applications, these two parameters can be appropriately increased according to the dynamic performance of the system.

Based on the same designing criterion as in (5.16), the gain expressed in (5.17) should satisfy:

$$|H_{QPR}(s)|_{\omega_{inj}} = |G_{Com-QPR}(s) \cdot G_{i_{PV}-d}(s)|_{\omega_{inj}} \geq 9 \tag{5.20}$$

Substituting (5.19) into (5.20) and the selected K_{qpr}, an appropriate range of K_r can be obtained. For example, in our experiment, $K_{qpr} = 0.2$, the corresponding range of K_r in the frequency range of [10 Hz ,90 Hz] is: $K_r \geq 2.5$. Based on the calculated parameters of P and QPR controllers, the tracking accuracy of the amplitude of the perturbation signal will be $\geq 90\%$, as depicted in Figure 5.13.

Based on the above theoretical analysis, both control strategies, i.e., unified control and separated control, can realize the required control objectives for converter-based IS implementation. A summary and comparison of the characteristics of the three controllers, in terms of number of control parameters, control bandwidth and controller type, are given in Table 5.1. The separated control strategy based on the QPR controller enables the widest control bandwidth for the perturbation signal while with the most number of control parameters equal to seven. The unified control strategy utilizing a single PI controller can achieve the same control bandwidth as the separated control strategy based on the P controller, while has a simpler design with only two control parameters. An experimental study is further conducted in the next section for online verification and comparison. The frequency range of the perturbation signal is uniformly set to [1 Hz, 2 kHz] for both

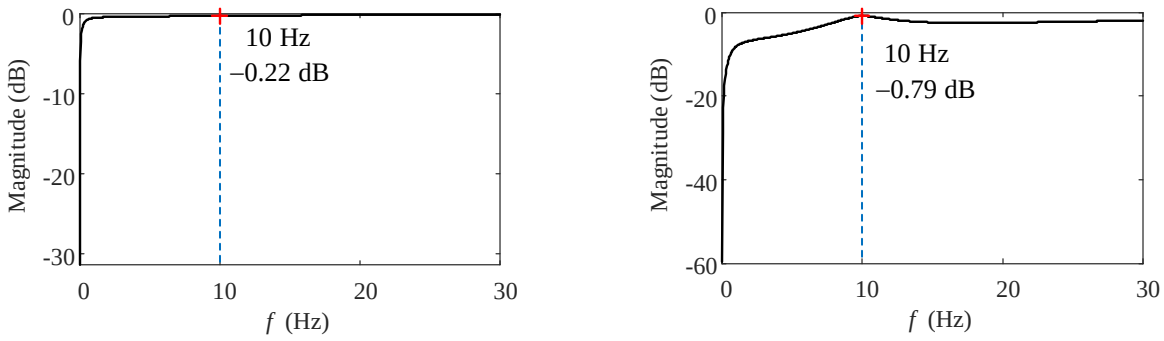


Figure 5.13: Magnitude plots of the system under the separated control strategy – AC component: (a) based on the P controller; (b) based on the QPR controller.

control strategies for fair comparison.

Table 5.1: Comparison of the two control strategies.

Control strategy	Number of control parameters	Control bandwidth	Controller type
Unified control	2 – K_{pi}, ω_{z-pi}	$\omega_{inj-max} \leq min[\frac{1}{9}\omega_{ct}, \omega_{inj-max-sys}]$	PI controller
Separated control	4 – K_p, K_{pi-dc}, $\omega_{z-pi-dc}$, ω_{0-LPF}	$\omega_{inj-max} \leq min[\frac{1}{9}\omega_{ct}, \omega_{inj-max-sys}]$	PI + P controllers
	7 – K_{qpr}, K_r, $\omega_{res-qpr}$, ω_{c-qpr}, K_{pi-dc}, $\omega_{z-pi-dc}$, ω_{0-LPF}	$\omega_{inj-max} < \omega_{sw}$	PI + QPR controllers

5.5 Experimental verification of closed-loop control

For lower-level control, this work pays more attention on the control of IPT and IS modes. Both open-loop and closed-loop control strategies are proposed and compared. Considering that the calculation of the injection point used in the open-loop control should be changed with the operating conditions, closed-loop control strategies are first verified in the experiment. The operating condition is set as condition O-I:

▷ Irradiance level: 250 $\mathrm{W/m^2}$;

▷ Stable temperature: 323.15 K;

▷ DC component at the injection point: 1.0 A.

To compare the performance of the two control strategies based on the three compensation controllers, a set of experiments is conducted based on the configured parameters given in Chapter 4. The experimental waveforms of the PV panel voltage and current during IS implementation based on the three controllers are

shown in Figure 5.14. To evaluate the tracking performance of perturbation signals, three comparison criteria are defined:

$$\begin{aligned} Acc_{dc} &= 1 - (I_{ref-dc} - I_{dc})/I_{ref-dc} \\ Acc_{Am} &= 1 - MAPE_{Am} = 1 - \frac{1}{n}\sum_{\omega=\omega_1}^{\omega_n} \frac{Am_{\omega_i} - \hat{Am}_{\omega_i}}{Am_{\omega_i}} \\ \mathrm{SNR}_{av} &= \frac{1}{n}\sum_{\omega=\omega_1}^{\omega_n} (\mathrm{SNR}_{\omega_i}) = \frac{1}{n}\sum_{\omega=\omega_1}^{\omega_n} (10log_{10}\frac{P_{signal_{\omega_i}}}{P_{noise_{\omega_i}}}) \end{aligned} \tag{5.21}$$

where Acc_{dc} represents the tracking accuracy of the DC component at the injection point, Acc_{Am} represents the average amplitude tracking accuracy, $MAPE_{Am}$ represents the mean absolute percent error between the reference amplitude and the actual amplitude of the perturbation signal for each perturbation frequency $(\omega_1, \omega_2, ..., \omega_n)$. SNR_{av} represents the average value of the SNR for each perturbation frequency SNR_{ω_i}, and SNR_{ω_i} is defined as the ratio in decibels of the summed squared magnitude of the perturbation signal $P_{signal_{\omega_i}}$ to that of the noise $P_{noise_{\omega_i}}$ at the perturbation frequency ω_i. The tracking performance of the perturbation current signal in the frequency range of [1 Hz, 2 kHz] are calculated and summarized in Table 5.2.

Table 5.2: Tracking performance of the three controllers.

Controller type	DC signal	AC signal	
	Acc_{dc}	Acc_{Am}	SNR_{av}
PI	99.5%	93.7%	6.9 dB
PI + P	98.8%	94.2%	7.7 dB
PI + QPR	99.2%	96.5%	5.2 dB

The DC component tracking accuracies of the three controllers exceed 98%, indicating that all of them can effectively control the operation of the PV panel at the target injection point. Meanwhile, the results demonstrate that all three controllers are capable of tracking the perturbation current signal with a high accuracy ($> 90\%$). The values of SNR exceed 4.77 dB, which indicates that the power of the perturbation signal is at least three times greater than that of the noise ($10log_{10}$ (3) $\approx$ 4.77 dB), allowing for reliable extraction of the perturbation signal. In terms of AC component tracking accuracy, the QPR controller exhibits superior accuracy equal to 96.5% as its control parameters are tuned in each divided frequency range. In terms of the SNR, the P controller has the biggest SNR equal to 7.7 dB. However, their control complexity is relatively higher than the single PI controller in terms of the number of control parameters.

According to the experimental results, the corresponding IS measurements of the PV panel based on the

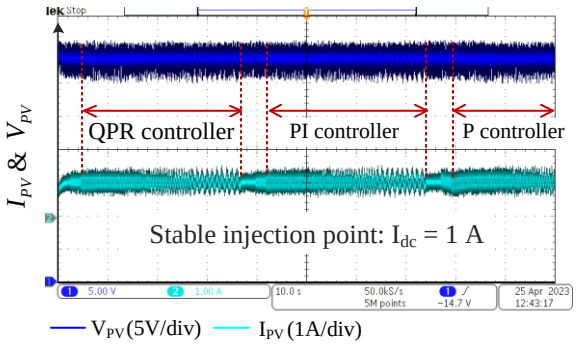


Figure 5.14: Experimental waveforms under different controllers during IS implementation.

three controllers are plotted in Figure 5.14. Detailed information of the curve fitting method can be found in Section 6.3.1. In the Bode plots, the asterisks represent the original values calculated from the experimental data, with grey, light blue and pink colors corresponding to the original IS measurements based on the P, PI and QPR controllers, respectively. The monochrome filled intervals are the corresponding confident intervals equal to 95%. Bode plots and Nyquist plots under different controllers are presented in Figures 5.15.

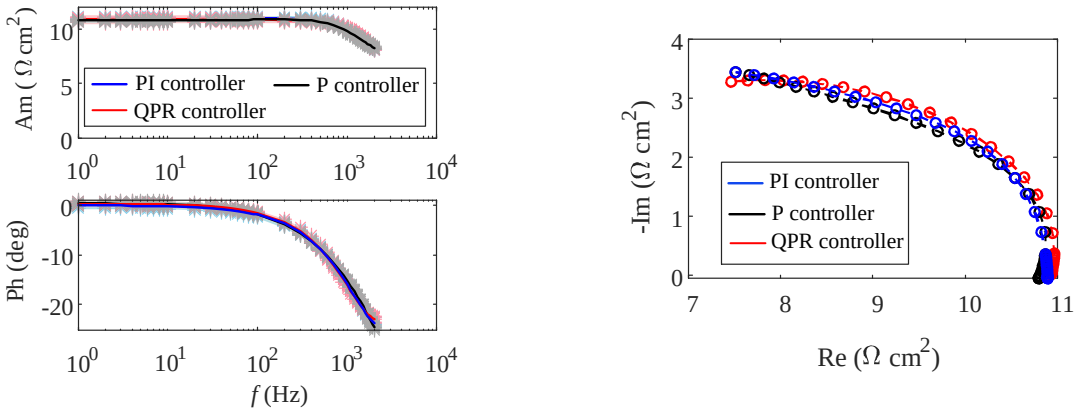


Figure 5.15: Impedance information under different controllers: (a) Bode plots (b) Nyquist plots.

The IS measurements calculated from the average value of amplitude and phase are shown as the solid line (blue, black and red separately) in Figure 5.15 (a). As shown in Figure 5.15 (b), a good consistency of IS measurements based on the three controllers can be observed. The root mean square error (RMSE) between the three IS curves depicted as the solid lines are less than 4.4%. It means that once the control parameters are appropriately set, all three controllers can achieve reliable and accurate IS measurements.

As previously summarized in Table 5.1, the unified control strategy based on a single PI controller has the least control parameters, while its tracking performance is comparable to that of the separated control strategy based on the P/QPR controller. Considering the simplicity of the controller design, the high tracking

accuracy ($> 90\%$) and sufficient SNR (> 4.77 dB), the PI controller based unified control strategy is further chosen for converter-based online IS implementation.

5.6 Discussions

According to the analysis and verification of simulation and experiment, it is obvious that both open-loop and closed-loop control strategies can achieve the control of IPT and IS modes. The experiment based on the unified control strategy is organized under the same operating conditions as the open-loop control strategy, i.e., O-II. The IS spectra under two control strategies are compared and demonstrated in Figure 5.16. It indicates that both open-loop and closed-loop control strategies can obtain reliable and accurate IS spectra with good consistency.

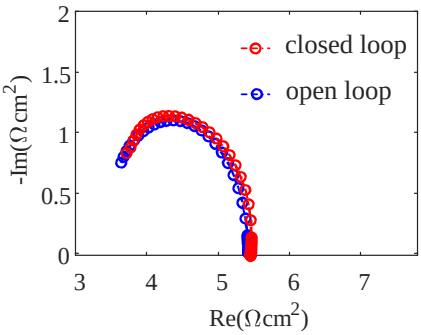


Figure 5.16: IS spectra under different control strategies: open-loop and closed-loop control.

The tracking performance of the open-loop control strategy can be calculated via (5.21):

$$\text{Open-loop control strategy: } Acc_{dc} = 98.57\%;\ Acc_{Am} = 88.47\%;\ \text{SNR}_{av} = 9.4 \text{ dB}.$$

Based on the above analysis, the characteristics of open-loop and closed-loop control strategies can be summarized as follows:

(1) Generally, the design of the open-loop control strategy is simpler, and the quality of the perturbation signal in terms of the SNR, is better. However, the location of the injection point can be easily influenced by the operating conditions.

(2) On the other hand, the closed-loop control strategy can achieve simultaneous accurate control of the location of the injection point and the perturbation signals under different operating conditions. Nevertheless, the maximum frequency of the perturbation signal will be limited by the bandwidth of the controller.

Table 5.3: Comparison of open-loop and closed-loop control strategies.

Comparison type		Open-loop strategy	Closed-loop strategy (Unified control strategy)
Control complexity		Directly calculate the duty cycle	Require specific design of controller
Injection point	Accuracy	98.57%	99.5%
	Dynamic	Significantly influenced by operating conditions	Automatically adjustable to variable operating conditions
Perturbation signal	Amplitude	88.47%	93.7%
	SNR	9.4 dB	6.9 dB
	Frequency limitation	Limited by the characteristics of the converter	Limited by the characteristics of both the converter and controller

(3) If the operating conditions do not change drastically or a wide-frequency range is required for IS implementation, the open-loop control strategy should be suitable; otherwise, the closed-loop control strategy will be more appropriate.

5.7 Conclusions

To overcome the limitation of the open-loop control strategy, mainly the influence of the operating condition on the stability of the location of the injection point, two closed-loop control strategies, named unified control and separated control, are proposed and designed in this chapter based on three commonly used controllers, i.e., P, PI and QPR controllers, in linear system control. In the unified control strategy, a single PI controller controls the DC and AC components together to meet the control objectives. Meanwhile, in the separated control strategy, when the P or QPR controller is used, a segmented LPF with a variable cut-off frequency is designed to separate firstly the DC and AC components. An additional PI controller is combined to control the PV panel at a steady-state operating point.

Based on the theoretical analysis, simulation and the experimental study, both control strategies can achieve the required control objectives for converter-based IS implementation in terms of tracking accuracy, control bandwidth and control stability. The separated control strategy based on the QPR controller enables the widest control bandwidth for the perturbation signal, while has the biggest number equal to seven of control parameters. The unified control strategy utilizing a single PI controller can achieve the same control bandwidth as the separated control strategy based on the P controller, while has a simpler design with only two control parameters. Considering the simplicity of the controller design, the high tracking accuracy (99.5%

for DC component and 93.7% for AC component) and sufficient SNR (6.9 dB), the PI controller based unified control strategy is considered suitable for converter-based online IS implementation. The transitions of the three operating modes, MPPT, IPT and IS modes, are validated by experiments based on the unified control strategy. In the next chapter, the online health monitoring of the PV panel based on the proposed methods in Chapter 3 and Chapter 5 will be verified.

Chapter 6

Health monitoring by converter-based IS

6.1 Introduction

In order to verify the theory and simulation, an experimental platform based on SiC module has been constructed in our laboratory. In this chapter, the platform will be introduced in detail. The health monitoring will be done in this chapter based on the simplified AC-ECM presented in Chapter 3 and the unified control strategy proposed in Chapter 5.

6.1.1 Description of the experimental platform

An experimental platform has been developed for online IS implementation in the laboratory from A to Z, which consists of a PV panel, a SiC module based DC/DC converter, an output load, a real-time control system, and a corresponding high-precision sampling circuit. The overall view of the experimental platform is shown in Figure 6.1. The PV panel (RECOM-SILLIA 60MXXX) is connected with the DC/DC converter. The parameters of the PV panel in the experimental and simulation tests are identical, as summarized in Table 1.1. The connected DC/DC converter is a conventional boost converter. It consists of a half-bridge SiC power module (PEB 8024) with an embedded DC bus capacitor and an external inductor. The key parameters of the SiC power module are summarized in Table 6.1. Other detailed information can be found in the official website of the product [122]. The value of the inductor is equal to 2.5 $m\mathrm{H}$ as determined by the setting principle described in Chapter 4 to ensure both the converter bandwidth and the input current ripple requirement. An adjustable resistor is selected as output load (R_L).

Table 6.1: Key parameters of the SiC power module.

Physical meaning	Symbol	Value
Embedded DC bus capacitor	C_{dc}	260 μF
Diode forward voltage	V_f	4.6 V
Maximum DC bus voltage	V_{dcmax}	850 V
Maximum continuous leg current	I_{legmax}	24 A
Maximum switching frequency	f_{swmax}	200 kHz

A real-time control system (dSPACE SCALEXIO box) is utilized in the platform as controller. It collects the sampling current and voltage signals and generates switching signals to the DC/DC converter. For IS implementation, the current sensor must have high accuracy and wide frequency bandwidth. A high-precision current transducer (IT 65-S ULTRASTAB) is selected in our experiment, whose frequency bandwidth equals to 600 kHz (± 1 dB). Corresponding DC power supplies are employed to supply necessary voltages for the switching drivers, fans and the current sensor. The control function is downloaded from the PC USB port. The corresponding current and voltage measurements are saved by the controller to a PC file and the experimental waveforms are meanwhile recorded by an oscilloscope (Tektronix MDO3024 Mixed Domain Oscilloscope).

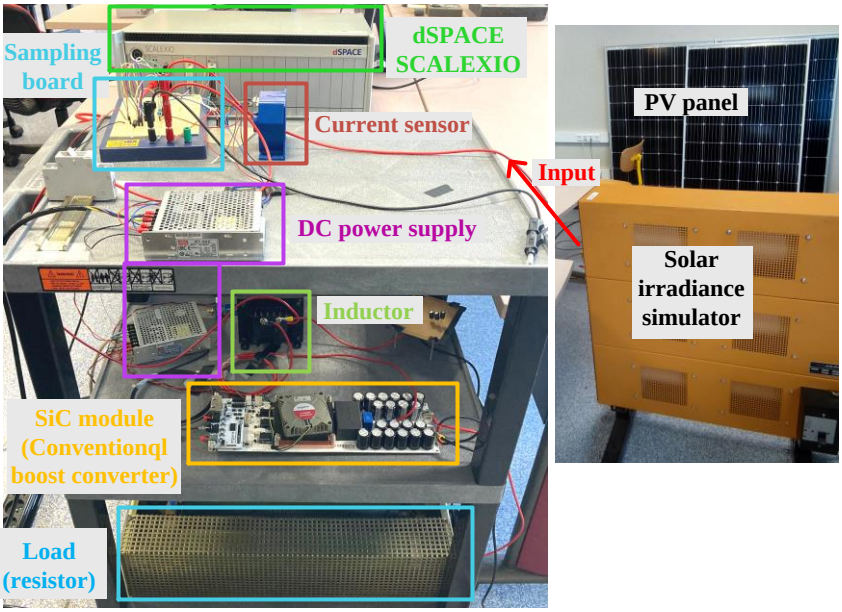


Figure 6.1: Experimental platform for online IS implementation.

6.1.2 Control of irradiance and temperature

As shown in Figure 6.1, a solar irradiance simulator (Deltalab) with six halogen light bulbs for an electrical power of 6 kW provides indoor illumination to achieve a controllable irradiance level during experiments. A schematic diagram of the locations of the solar irradiance simulator and the PV panel is indicated in Figure 6.2.

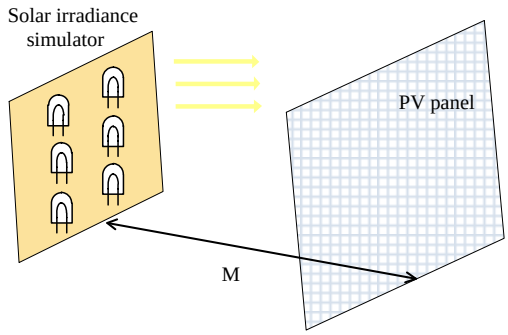


Figure 6.2: Schematic diagram of the illumination supply for the PV panel in our laboratory.

By changing the distance, i.e., M, the irradiance level can be adjusted. The irradiance level is measured by the Solar Power Meter – PYR1307. During the experiments, 6 irradiance levels were selected as shown in Table 6.2

Table 6.2: Six irradiance levels set in the experiment.

Irradiance	Value
G_1	218 $\mathrm{W/m^2}$
G_2	226 $\mathrm{W/m^2}$
G_3	250 $\mathrm{W/m^2}$
G_4	263 $\mathrm{W/m^2}$
G_5	268 $\mathrm{W/m^2}$
G_6	284 $\mathrm{W/m^2}$

In the early stages of operation, the temperature of the PV panel will exhibit an upward trend due to the illumination of solar irradiance simulator and the generation of PV power. It will stabilize after around half an hour of continuous operation. The temperature range is equal to [295.15 K, 323.15 K], measured by a handheld thermal imaging device (FLIR E8).

6.2 Cooperative control of MPPT and IS modes

As mentioned in Chapter 2, the control strategy of converter-based IS consists of two levels, the upper-level and lower-level control. The upper-level control achieves the cooperative control of the three operating modes under consideration, i.e., MPPT, IPT and IS modes. The lower-level control includes the separate control of each mode. As MPPT algorithms have been extensively studied in literature, the MPPT control is not the major focus in this work. A perturb & observe (P & O) algorithm with a variable perturbation step is applied herein for MPPT mode considering its efficiency and rapidity [4]. Corresponding control strategies of IPT and IS modes are introduced in Chapters 4 and 5. The cooperative control of the different modes hugely affect the efficiency and stabilization of the whole system. We remember here that, for this reason, the efficiency of the proposed cooperative control strategy was verified through simulation in Chapter 2. Under the same operating condition, i.e., O-I, the experiments are performed to verify the stable transition among the different modes.

For illustration,under the operating condition O-I both I-V and P-V curves are shown in Figure 6.4. As the PV output voltage varies, the MPP of the PV panel in the laboratory can reach 41 W, with the PV output current equal to 1.22 A at the MPP, as indicated by the green star in Figure 6.4. The open-circuit voltage and short-circuit current are approximately equal to 35.6 V and 1.3 A, respectively.

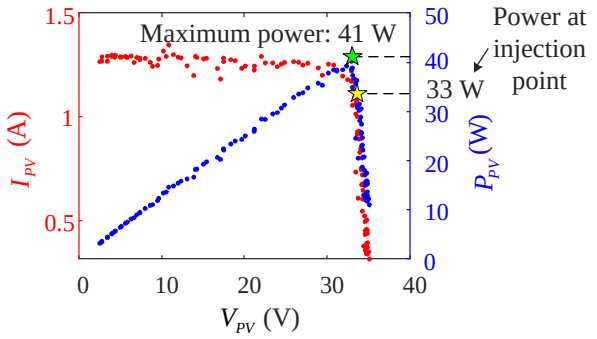


Figure 6.3: Experimental waveforms of IV (red) and PV curves (blue) under operating condition O-I.

When the current of the injection point is set to 1.0 A, the injection point can satisfy the validity conditions of IS implementation concluded in Chapter 2. At this point, the PV panel can maintain 80.5% of the maximum output power (equal to 33 W) during IS measurement as indicated by the yellow star, while ensuring the quasi-linear characteristic. As aforementioned, the amplitude of the perturbation signal is set as 0.15 A, i.e., 15% of the DC component current.

The corresponding experiments of the cooperative operation among three modes are performed and in-

dicated in Figure 6.4, with Figure 6.4 (a) the output voltage and current and Figure 6.4 (b) the output power of the PV panel. It can be observed that the PV panel operates initially in the MPPT mode. When there is a trigger for health monitoring, the PV panel transits to the IS mode through the IPT mode. The IPT mode takes around 3 seconds for stabilization. To ensure the validity and accuracy of IS measurements, multiple tests are repeated sequentially, with each including both IPT and IS modes, as illustrated in Figure 2.6.

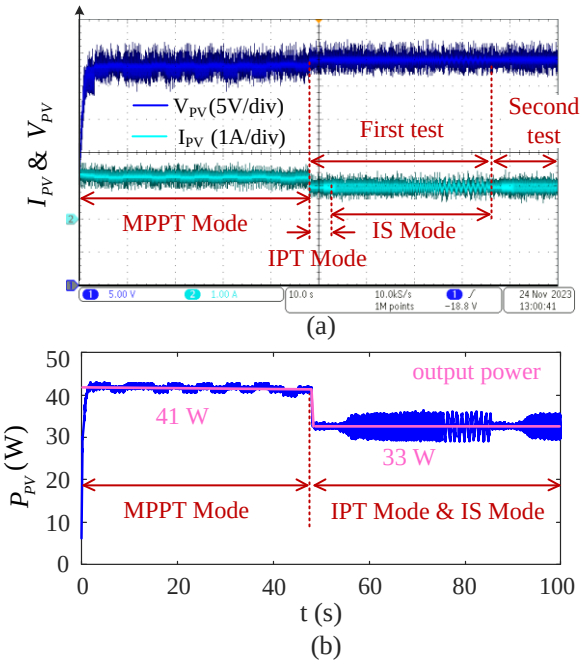


Figure 6.4: Experimental waveforms of the cooperative control among MPPT, IPT and IS modes under operating condition O-I: (a) output voltage and current (b) output power.

In MPPT mode, the output power of the PV panel is equal to 41 W, consistent with the value indicated on the IV curve. From MPPT to IS mode, the PV panel consistently produces power, and still maintains a quasi-maximum output power. This power percentage can be even higher for larger-power panels since the PV current shifts slightly downward into quasi-linear voltage source region while the PV output voltage is quasi-constant in this region.

6.3 Health monitoring

This section focuses on the validation of the effectiveness of the health monitoring based on the simplified AC-ECM in Chapter 2 and the control strategies proposed in Chapters 4 and 5. The design of experimental conditions includes changes in the injection point, irradiance level and temperature.

6.3.1 Data processing

Based on the control strategies, both perturbation and response signals are acquired and recorded. To analyze the health information, the corresponding fundamental information is extracted through FFT analysis in MATLAB, including the amplitude of AC components of current and voltage, and the phase shift between the current and voltage signals, denoted as I_{ac}, V_{ac} and ϕ. The normalized impedance amplitude, Am (Ω) can be calculated by:

$$Am = S \cdot \frac{N_{par}}{N_{ser}} \cdot \frac{V_{ac}}{I_{ac}} \tag{6.1}$$

where S means the effective area of each PV cell (cm^2); N_{par} and N_{ser} represent the number of PV cells connected in parallel and series inside the PV panel, respectively. For the PV panel considered during the experiments $S = 15.6 \times 15.6\ \mathrm{cm}^2$, $N_{par} = 1$ and $N_{ser} = 60$.

In order to ensure the validity criteria, IS measurements based on each controller are repeated at least five times. Taking operating condition O-III as an example (O-III: Iradiance level: G_5; Stable temperature: 323.15 K; DC component of output current at the injection point: 0.7 A), the corresponding IS spectra are calculated based on the experimental data as shown in Figure 6.5. Multiple sets of experimental data exhibit good consistency. A 95% confidence interval is applied, depicted by the shaded area in Figure 6.5. The corresponding average values are recorded with solid lines.

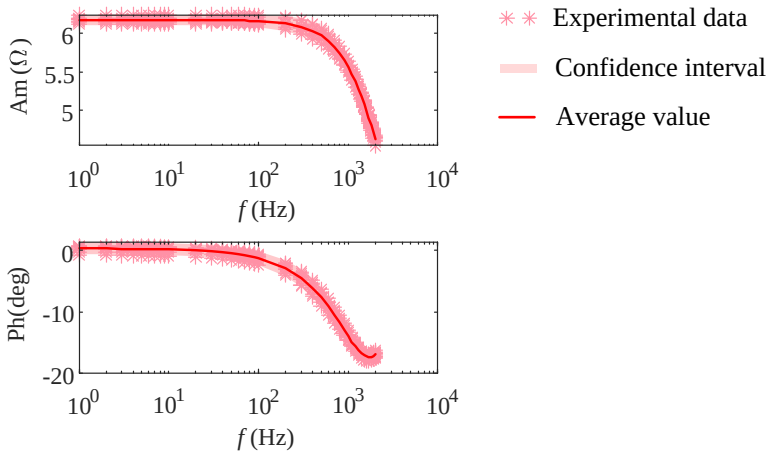


Figure 6.5: IS spectrum under operating condition O-III: Bode plot.

Considering the average values, the IS spectrum in the Nyquist plot is acquired, as shown by the circles in Figure 6.6. According to the theoretical value calculation method of the AC-ECM of the PV panel provided in (3.11) in Chapter 3 and experimental data, the parameters can be fitted. The fitting curve is indicated as the black line in Figure 6.6.

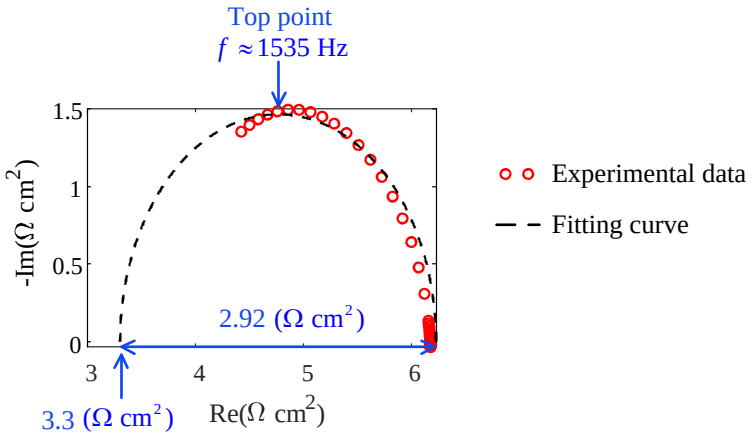


Figure 6.6: IS spectrum under operating condition O-III: Nyquist plot.

The fitting quality is assessed by the normalized root mean square error (NRMSE) in Equation (6.2), where X_{exp} represents the experimental data, and X_{model} represents the target parameters of AC-ECM, and n represents the number of the data of one group:

$$NRMSE = \frac{RSME}{(X_{exp,max} - X_{exp,min})}$$
$$RMSE = \sqrt{\frac{\sum_{i=1}^{n}(X_{exp} - X_{model})^2}{n}} \tag{6.2}$$

By setting the smallest value of NRMSE, the fitting results of the AC-ECM of the PV panel can be obtained as follows:

$$\begin{cases} R_s \approx 3.3\ \Omega\ \text{cm}^2 \\ R_p \approx 2.92\ \Omega\ \text{cm}^2 \\ C_p \approx 35.5\ \mu\text{F}\ \text{cm}^2 \end{cases} \tag{6.3}$$

The frequency of the perturbation signal at the top point is equal to 1535 Hz. The average fitting errors of the real and imaginary parts are equal to 6.77×10^{-11} and 0.0326, respectively. Meanwhile, the validity of IS measurements is also verified by passing the Kramers-Kronig (K-K) test based on an open source EIS analyzer [123]. The checked result is shown in Figure 6.7, where the residual of real part is so small that the value is shown as 0 in the software. In this test, all of the residuals (residuals of the real part $\Delta\text{Re}(\omega)$ and the imaginary part $\Delta\text{Im}(\omega)$) are less than 1%.

Finally, the equivalent parameters under different operating conditions are calculated based on the fitting

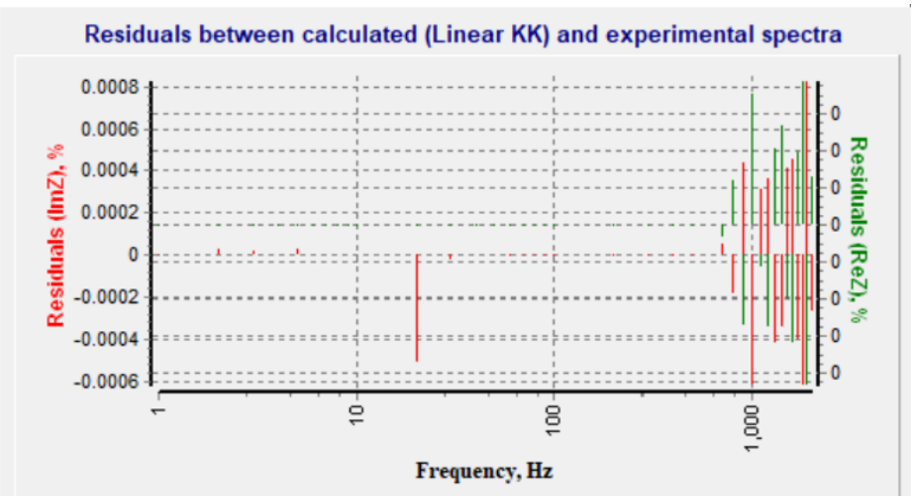


Figure 6.7: Kramers-Kronig (K-K) test result.

methods and corresponding health features are extracted in the following sections. The variations of Nyquist curves based on the average values under different operating conditions are compared, including injection point, irradiance level, temperature and partial shading.

6.3.2 Different injection points

To verify the influence of the injection point, several continuous injection points under the same environmental factors are selected by controlling the DC component of the injection point. The operating condition (i.e., O-III) is set as, :

▷ Irradiance level: G_5;

▷ Stable temperature: 323.15 K;

▷ DC component at the injection points: 1.0 A, 0.9 A, 0.8 A, 0.7 A, 0.6 A, 0.5 A and 0.4 A.

Corresponding locating range of these injection points is illustrated in Figure 6.8. From the IV curve, it can be obtained that the output voltage range is [33.39 V, 34.57 V].

After the data processing presented in the previous section, it is thus possible to calculate and finally present the values of the equivalent parameters in Figure 6.9, where the dashed lines with circles represent the average values and the shadows represent the confidence intervals. The corresponding Nyquist curves based on the average values are shown in Figure 6.10. It can be observed that both R_s and R_p decrease with the increase in the output voltage V_{PV}, while C_p increases with the rise in the output voltage. The Nyquist curves move from the upper right to the lower left as the output voltage increases, or the injection current decreases.

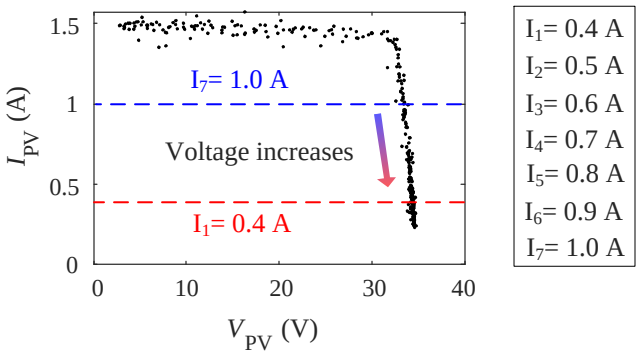


Figure 6.8: IV curve under operating condition O-III.

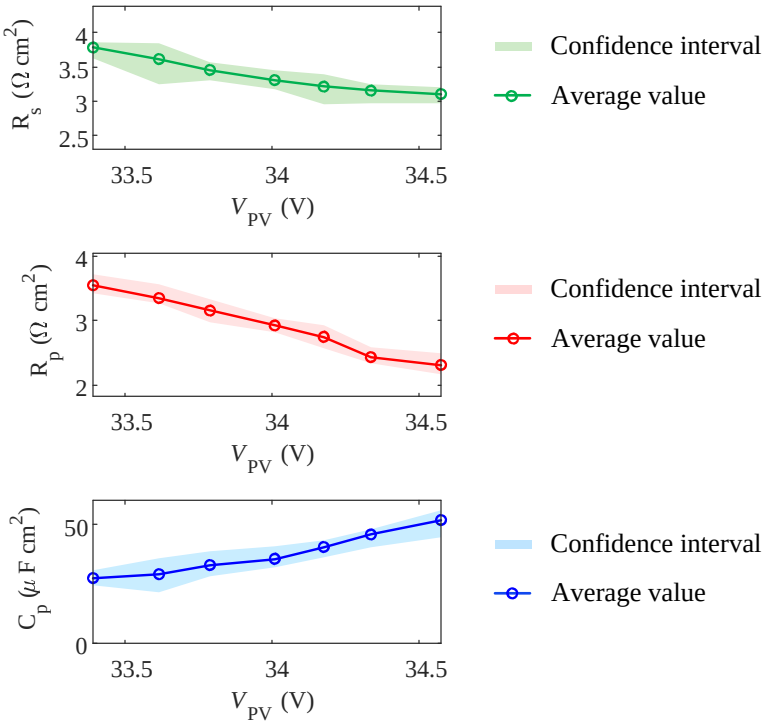


Figure 6.9: Equivalent parameters under operating condition O-III.

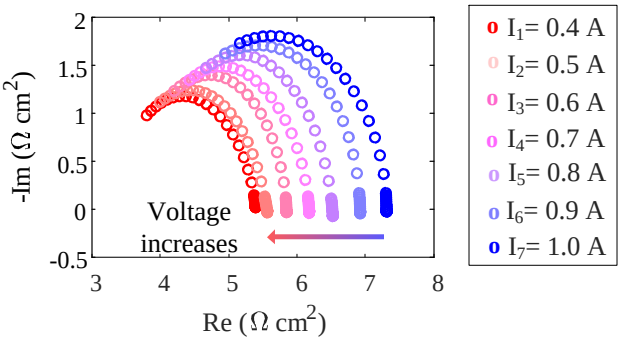


Figure 6.10: IS spectra in Nyquist plots under operating condition O-III.

Based on the average equivalent parameters, four features defined in Chapter 3, including $R_s + R_p$, $ln(R_p)$, $ln(C_p)$, and $\tau = R_pC_p$, are extracted and illustrated in Figure 6.11. When the irradiance level and temperature remain unchanged, as V_{PV} increases, the conductivity of the PV panel gradually increases, reflected by the decrease in $R_s + R_p$, as shown in Figure 6.11 (a). Figure 6.11 (b) and (c) indicate that $ln(R_p)$ and $ln(C_p)$ exhibit an approximately linear relationship with V_{PV}, showing an inversely proportional correlation and a directly proportional correlation, respectively. In Figure 6.11 (d), τ increases with the increase of V_{PV}, representing the relaxation time constant of the recombination process becomes longer, which is in line with the cell-level analysis results in literature.

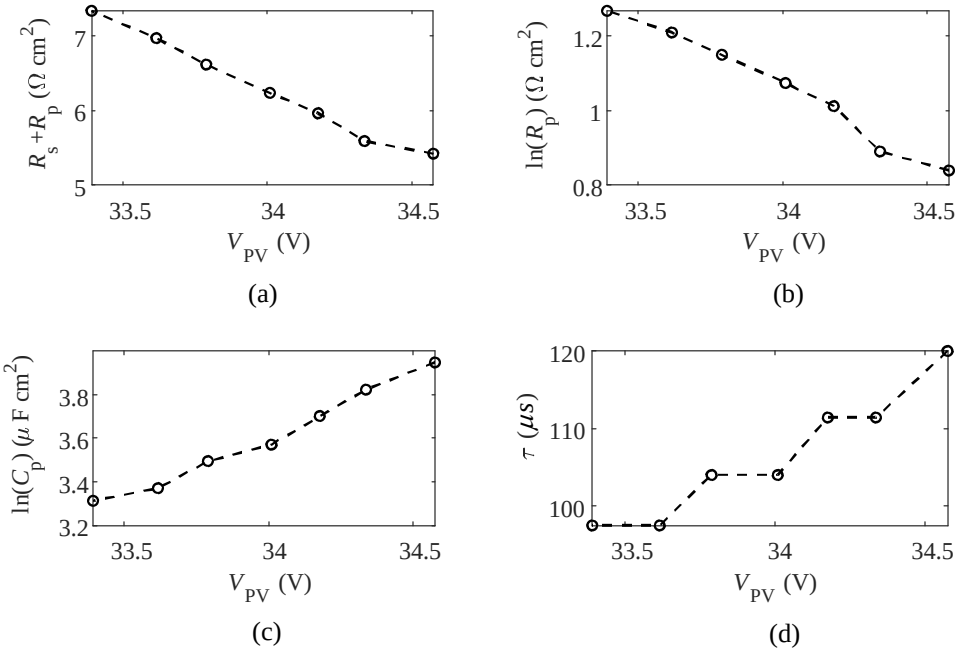


Figure 6.11: Four features under operating condition O-III:
(a) Feature 1; (b) Feature 2; (c) Feature 3: (d) Feature 4.

6.3.3 Different temperatures

Different from the control of the injection points, the temperature continues to rise until it reaches a stable value. Therefore, under a fixed irradiance level, the DC component of the injection point is set as 0.7 A, and continuous measurements are conducted on the PV panel. Every three IS measurements are performed, and the IV curve is scanned once. The IV curves are illustrated in Figure 6.12, under the operating condition named O-IV, which is set as:

▷ Irradiance level: G_5;

▷ Temperature: in the range 295.15 K to 323.15 K;

▷ DC component at the injection point: 0.7 A.

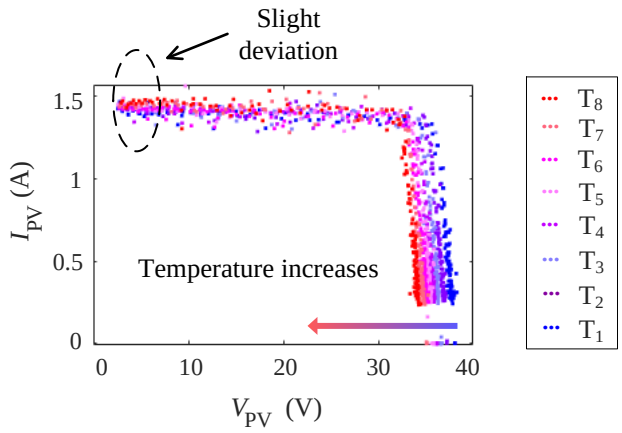


Figure 6.12: IV curves under operating condition O-IV.

It points out that the open-circuit voltage is significantly impacted by the temperature, while there is a slight deviation in the short-circuit current. Moreover, based on the experimental data, the equivalent parameters are extracted and depicted in Figure 6.13.

It shows that the equivalent parameters remain essentially unchanged at different temperatures, when the irradiance level and DC component at the injection point are controlled constant. Meanwhile, the Nyquist curves exhibit a high degree of coincidence, as illustrated in Figure 6.14.

The major underlying reason is that temperature has a slight effect on the photocurrent, i.e., I_{ph}, manifested as a slight deviation in the current in Region I. Therefore, when I_{PV} is controlled to be constant, i.e., 0.7 A, the currents of the equivalent diodes in the DC-ECM, i.e., I_{d1} and I_{d2}, remain nearly unchanged, which means that the conductivity of the PV panel is almost unchanged.

However, it can be clearly seen that the output voltage shows a decreasing trend as the temperature increases, as shown in Figure 6.15. Therefore, to clearily identify the changes of temperature, a normalization processing is performed on the Feature 2 and 3 quantities, and the results of four features under different temperatures are shown in Figure 6.16. The results show that due to the output voltage changes with the increase in temperature, the conductivity almost remains constant and recombination time shows the same trend. On the other hand, Feature 2 and 3 under unit voltage increases with the temerature.

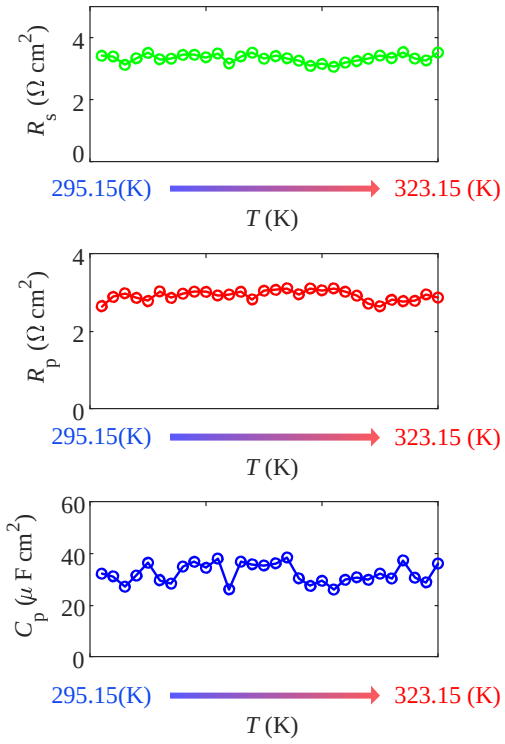


Figure 6.13: Equivalent parameters under operating condition O-IV.

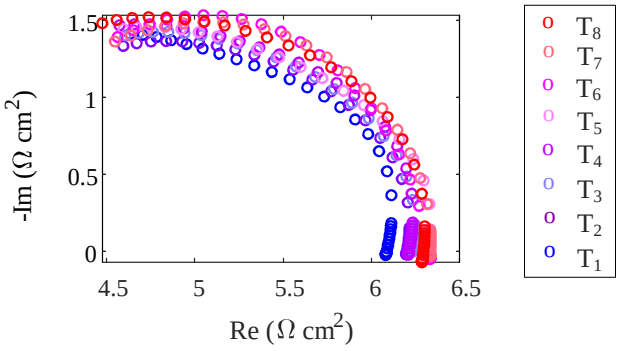


Figure 6.14: IS spectra in Nyquist plots under operating condition O-IV.

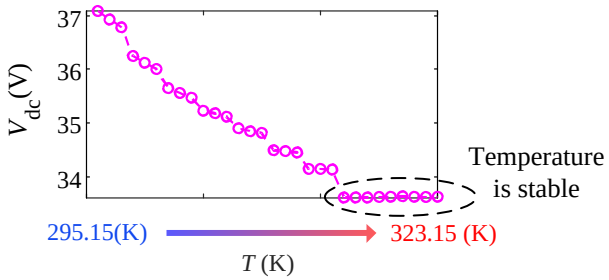


Figure 6.15: V_{PV} under operating condition O-IV.

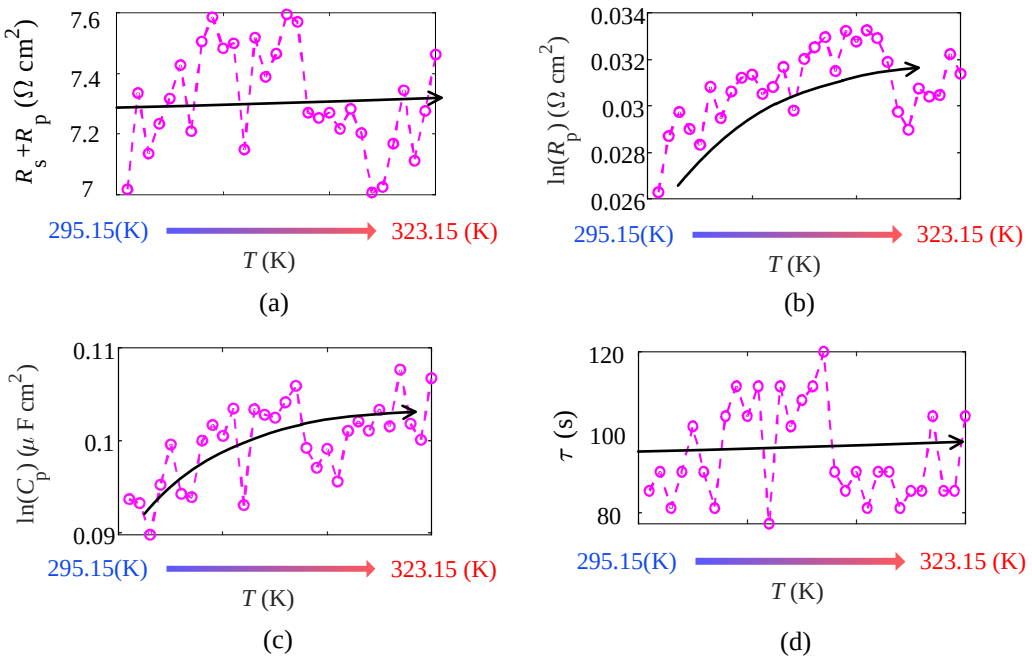


Figure 6.16: Four features under operating condition O-IV:
(a) Feature 1; (b) Feature 2; (c) Feature 3: (d) Feature 4.

6.3.4 Different irradiance levels

For analyzing the influence of the irradiance level, the operating condition is set and named as O-V:
▷ Irradiance level: from G_1 to G_6;
▷ Stable temperature: 323.15 K;
▷ DC component at the injection point: 0.7 A.

The IV curves under different irradiance levels are shown in Figure 6.17. It can be observed that the output voltage changes slightly with the irradiance levels at the same output current in Region III, representing that V_{PV} with the constant DC current shows little difference under various irradiance levels. The equivalent parameters are calculated based on the method introduced in Section 6.3.1 and illustrated in Figure 6.18.

Finally, the corresponding Nyquist curves for the six irradiance levels are shown in Figure 6.19.

The analyzed results show that R_s decreases with the increase of the irradiance level. The reasons can be classified into two aspects:

1. Under illumination, R_{il} will decrease with the increase of the irradiance level;

2. As the irradiance level increases, the photocurrent, denoted as I_{ph}, increases, causing an increase in I_{d1}

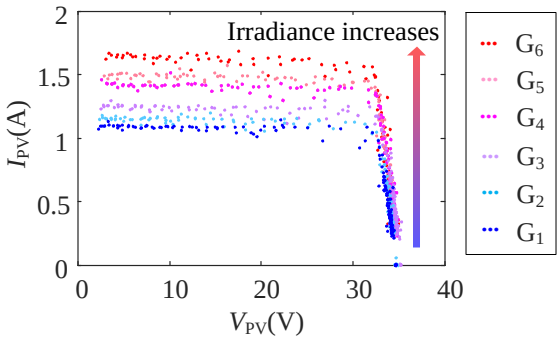


Figure 6.17: IV curves under operating condition O-V.

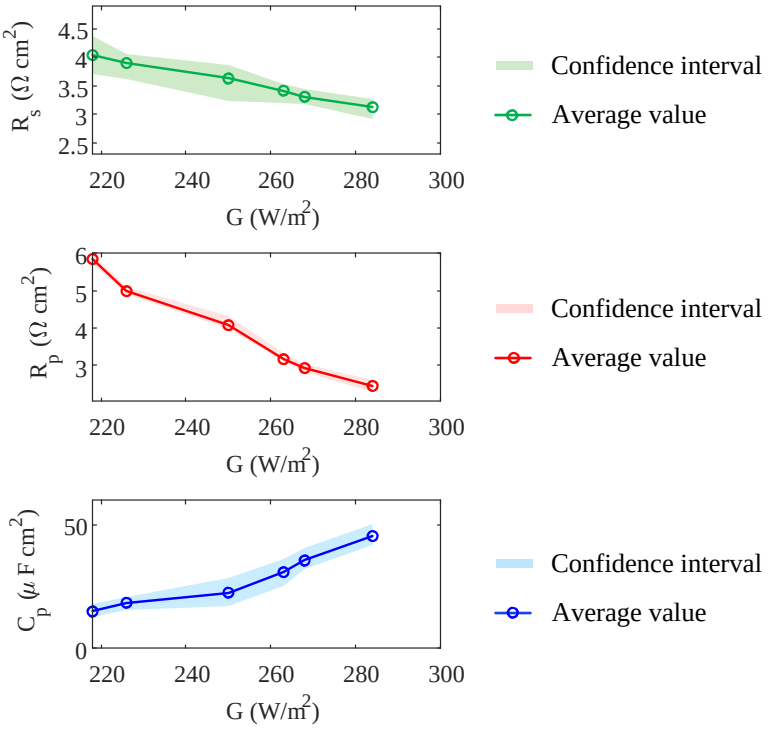


Figure 6.18: Equivalent parameters under operating condition O-V.

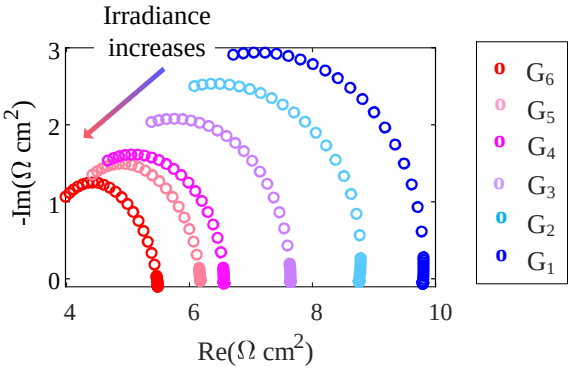


Figure 6.19: IS spectra in Nyquist plots under operating condition O-V.

and I_{d2}. The increase in I_{d1} causes a decrease in R_{tr}.

However, in the selected Region III, R_p compared to R_{tr} exhibits a larger relative change. Therefore, the decrease in R_p is more noticeable than in R_s. It indicates that, in region III, the recombination process dominates. The irradiance level changes are reflected in the Nyquist curve as it shrinks from the upper right to the lower left with an increasing irradiance level.

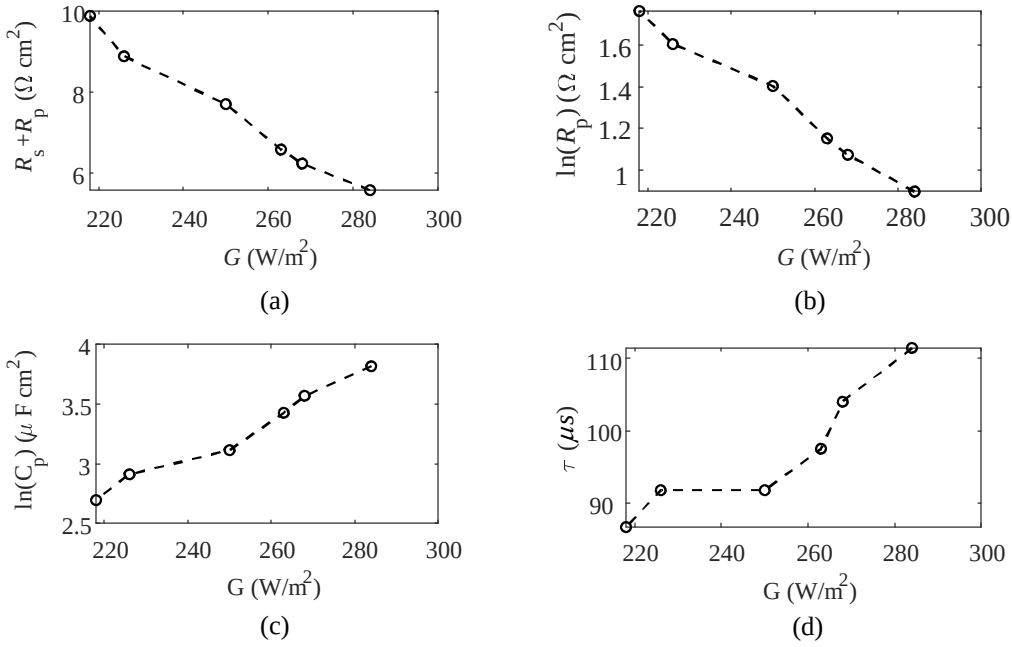


Figure 6.20: Four features under operating condition O-V:
(a) Feature 1; (b) Feature 2; (c) Feature 3: (d) Feature 4.

The four features are extracted and shown in Figure 6.20. In Figure 6.20 (a), $R_s + R_p$ decreases with the increase in irradiance level, indicating an increase in the conductivity of the PV panel. This result aligns with

the theoretical analysis, which indicates that the internal equivalent diode current increases as the irradiance level increases while I_{PV} remains constant. Both lnR_p and lnC_p show an approximate linearity with the irradiance level, which verifies the relationship between R_p, C_p and I_{d2}. Figure 6.20 (d) shows that the recombination time constant increases. The reason is that silicon cells absorb more energy under a high irradiance level, and thus, more electrons achieve energy level transitions and become free carriers, making the recombination process becomes more difficult.

6.3.5 Partial shading

Partial shading is a frequently encountered operating condition under normal, i.e. outside PV panel operating conditions. The PV panel utilized in this work has 60 PV cells, divided into 6 columns. To simulate the partial shading condition, the first column is shaded by an opaque plate at different percentages (from 0 $\%$ to 100 $\%$, denoted P_i, where $i = 1, 2, ..., 8$) and a group of IV curves are obtained, as shown in Figure 6.21. The corresponding operating condition (O-VI) is set as:

▷Irradiance level: G_6 with different percentage of partial shading;

▷Stable temperature: 323.15 K;

▷DC component at the injection point: 0.7 A.

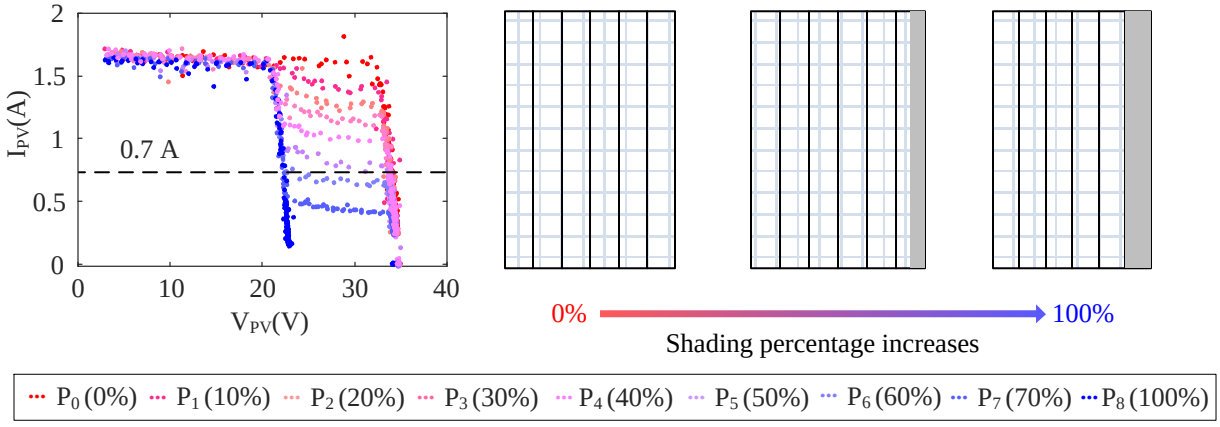


Figure 6.21: IV curves under operating condition O-VI.

Experimental results and the corresponding Nyquist curves are shown in Figures 6.22 and 6.23, respectively.

From the IV curves, the operating conditions under partial shading can be separated into 3 groups:

Group 1: this group includes the operating conditions $P_0 - P_4$. Under these conditions, the injecting points are located behind the steps cause by partial shading. In other words, the bypass diode is inactivated

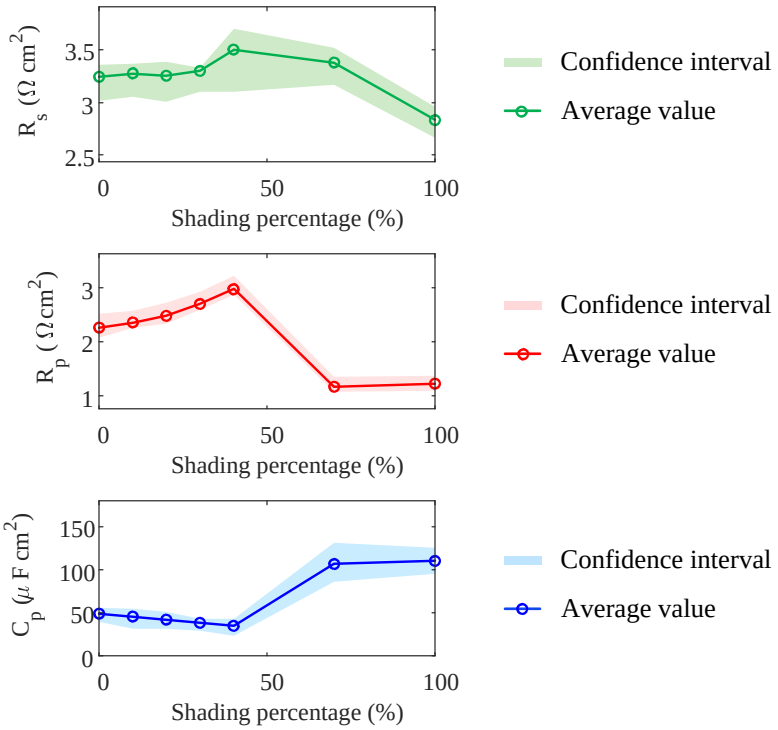


Figure 6.22: Equivalent parameters under operating condition O-VI.

during IS testing. Due to the partial shading, the photocurrent of shaded cells will decrease, leading their impedance information to exhibit as if the irradiance level decreases. meanwhile, the other cells without shading will perform normally. Considering the series connection among the PV cells, the total impedance will indicate: R_s and R_p increase, while C_p decreases with the increase of percentage of partial shading. The corresponding Nyquist curves will move toward the upper right.

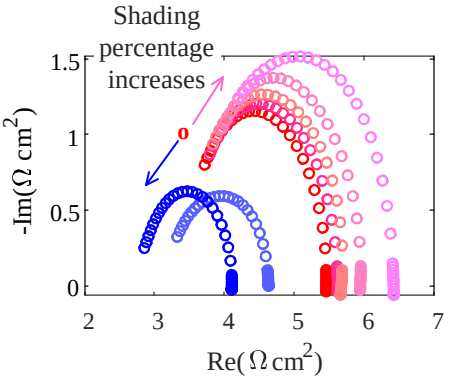


Figure 6.23: IS spectrum in Nyquist plots under operating condition O-VI.

Group 2: P_5 and P_6 belong to this group. As the shading percentage increases, the IV step moves downward, causing the injecting point to appear in a nonlinear or step region. The linearity of the response

voltage signal cannot be guaranteed in either region. Figure 6.24 (a) displays the FFT analysis of the response voltage under perturbation current signals at 1 Hz and 2 kHz under the operating condition P_5, respectively. The harmonics exhibiting amplitudes close to the fundamental frequency indicate that the voltage signal is non-sinusoidal in nature and the degree of voltage distortion is differs according to frequencies, resulting in the Nyquist curve to have more than one semi-arcs, as shown in Figure 6.25.

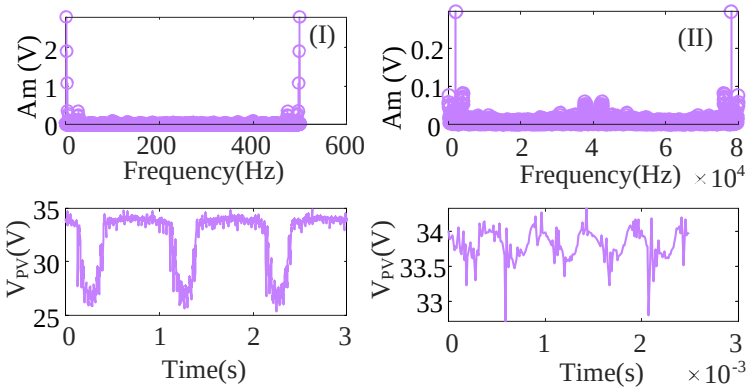


Figure 6.24: FFT analysis of the perturbation and response signals under P_5: (a) output voltage at 1 Hz; (b) output voltage at 1 kHz.

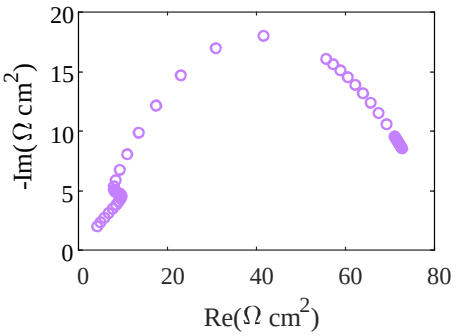


Figure 6.25: IS spectrum in Nyquist plots in the nonlinear region.

Group 3: When the injecting points are located in the front of step, the bypass diode will be activated during IS testing, such as P_7 and P_8. Since 20 cells are bypassed by the diode, the values of R_s and R_p will decrease significantly and C_p will increase, as shown in Figure 6.22. The corresponding Nyquist curve moves toward the lower left in turn, as illustrated in Figure 6.23. Compared with P_7, the value of R_s has a drop in P_8, which is mainly caused by the current flowing through the bypass diode. Because when the shading percentage increases, the current flowing through the bypass diode will increase and the value of R_{byd} will decrease [116, 117].

The four crucial health features are visualized and explained in Figure 6.26. When the bypass diode is

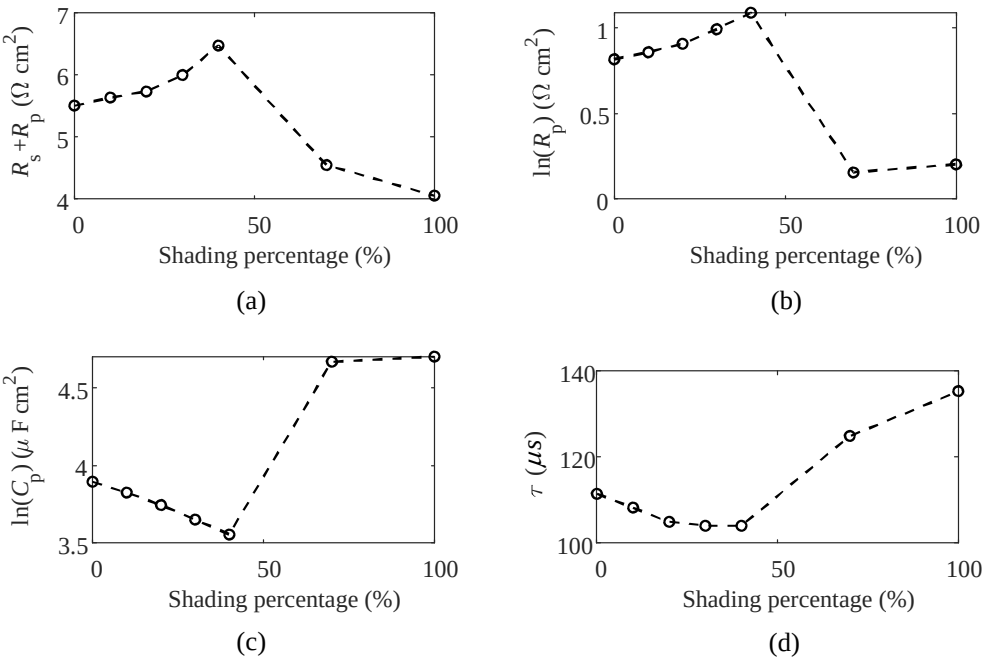


Figure 6.26: Four features under operating condition O-VI:
(a) Feature 1; (b) Feature 2; (c) Feature 3: (d) Feature 4.

switched off, the overall conductivity of the PV panel diminishes, as illustrated in Figure 6.26 (a), where the sum of R_s and R_p displays an upward trend. This signifies a hastened recombination process, leading to a reduction in the corresponding time constant, as evidenced in Figure 6.26 (d). Conversely, upon activating the bypass diode, all parameters undergo a sudden change. By bypassing the shaded regions, the conductivity of the PV panel increases, consequently elongating the recombination time constant.

6.4 Conclusions

Based on the proposed bi-level control strategy, i.e., upper-level and lower-level control, IS is successfully implemented in the PV system by controlling the connected power converter. As the operating conditions change, the IS spectra exhibit significant variations. Four features are consequently extracted to analyze the influence of operating conditions:

- Feature 1: $R_s + R_p$ reflects the conductivity of the PV panel; the lower the value of $R_s + R_p$, the higher the internal conductivity.
- Features 2 and 3: $ln(R_p)$ and $ln(C_p)$ verify the influence of temperature and output voltage, which can

provide theoretical support for deriving external environmental conditions based on parameters in the further work.

- Feature 4: $\tau = R_p C_p$ represents the relaxation time constant of the recombination process.

According to the analysis of the above four features, it can be concluded that in Region III, as the current at the injection point increases, the conductivity of the PV panel will weaken, and the relaxation time constant of the recombination process will decrease. The temperature affects the conductivity and recombination time constant under unit voltage. An increase in temperature will cause a decrease in the conductivity of the PV panel and an increase in the recombination time constant of recombination process. In addition, increasing the irradiance level leads to an increase in the conductivity and a decrease in the relaxation time constant. Under partial shading conditions, the conductivity and recombination process behave as the irradiance level decreases. However, as the partial shading size increases, the bypass diode will be activated, resulting in a jump in the variation of the features.

The features can efficiently reflect the changes in operating conditions. As possible perspectives for further work, IS measurements under more abnormal health states and natural degradation of the PV panel will be considered to provide more theoretical basis for online health monitoring.

Conclusions and Perspectives

Conclusions

This work focuses on the converter-based IS implemented in photovoltaic, PV, panels. A complete researching process from the AC equivalent circuit model, i.e., AC-ECM, development, control strategy design and to simulation and experimental verifications are provided. The major contributions of this research are twofold: (1) proposition of a systematic design guideline for control strategies of converter-based IS implementation; (2) development of an appropriate AC-ECM for PV panels and extraction of four valuable features for online health monitoring of PV panels.

In Chapter 1, a comprehensive state-of-the-art of PV panels is presented. The development trend of renewable energy sources and the role of solar energy explain the significance of the research on PV panels. The basic structures of silicon PV cells has the highest proportion in the market. The simulation of IV and PV curves indicate that the efficiency is obviously influenced by the operating condition and internal health states of PV panels. Typical faults, including their causes, impacts and fault characteristics in terms of timescale, security level and power loss, are summarized. Corresponding existing characterization tools are reviewed and compared. Compared to offline tools, online tools are attractive to reduce cost and realize real-time health monitoring. For converter-based IS, as it does not require additional equipment and can obtain the PV panel's internal dynamic information with the quasi-maximum output power during test, it is mainly focused on in our study.

In Chapter 2, a bi-level control strategy consisting of upper-level and lower-level control is proposed. The upper-level control is focused on to achieve the transition between MPPT and IS modes. The selection of the injection point is provided based on the analysis of the relationship between the output voltage and current of the PV panel. To ensure the stable transition between MPPT and IS modes, an intermediate mode, i.e., IPT mode, is defined. The flow chart of the cooperative control between the three modes is designed. Meanwhile, a simulation platform is developed in MATLAB/Simulink. The corresponding control methods are verified

based on this platform.

In Chapter 3, the relaxation process of PV cells are analyzed and classified into three groups based on their time scales. The relaxation processes in microseconds-level time scale can be detected by IS, and are expressed in the AC-ECMs. Existing AC-ECMs of PV cells are reviewed. According to the frequency limitation and the structure of the PV panel, the AC-ECM for panel-level is simplified. Considering the influence of bypass diodes and the location of the injection point, i.e., Region III, the AC-ECM of the PV panel consists of three parts, including one series resistor and a sub-circuit of a resistor and a capacitor connected in parallel. The series part is combined by the equivalent resistance of the transport process, the influence of illumination, the bypass diode and the connection of lines. The sub-circuit represents the recombination process of the PV panel. Finally, based on the simplified AC-ECM, four features are defined to analyze the health state of the PV panel, including the total resistance, the natural logarithm of capacitance and resistance, and the relaxation time constant.

In Chapter 4, the open-loop control strategy for IS implementation is focused on considering its simplicity. Firstly, the limitations and influencing factors for IS implementation are analyzed, including the resonant information of the conventional boost converter and the maximum frequency of the perturbation signal. Due to the resonant peak, there is a risk of entering in the nonlinear region during the small-signal perturbation. Secondly, the influences of different parameters including the operating parameters, the element parameters and the parasitic parameters are analyzed. It is found that the resonance can be reduced by selecting the elements with high parasitic parameters, but cannot be completely eliminated. In addition, the maximum frequency is mainly impacted by the operating conditions and the value of the inductor. Meanwhile, the distance between the PV panel and the support capacitor will cause a decrease of its value. To obtain a stable perturbation signal, an adaptive configuration method of the amplitude of the perturbation signal at different frequencies is proposed. The influence of the resonant peak is sufficiently decreased and the amplitude of the perturbation signal is located in an allowed range, which is further validated by the experiment.

In Chapter 5, to ensure the stability of the location of the injection point, two closed-loop control strategies are proposed and designed. Specifically, three commonly used controllers (P, PI and QPR) in linear system control are applied. According to the characteristics of the three controllers, the control strategies are divided into unified control and separated control. In unified control, DC and AC components are controlled together by a single PI controller. Meanwhile, in the separated control, DC and AC components are firslty separated by a segmented LPF with a variable cut-off frequency. Then the DC component is controlled by a PI controller with a narrow bandwidth, while AC signals are tracked by P/QPR controllers. The corresponding design guide of each parameter is provided. Finally, a comparison of the two control strategies is made in terms of control complexity, control bandwidth and stability. It shows that the unified control strategy has less

parameters to be designed and is suitable for the online implementation of IS.

In Chapter 6, an experimental platform has been developed in the laboratory, including a PV panel, a SiC module based DC/DC converter, an output load, a real-time control system, and a corresponding high-precision sampling circuit. To verify the aforementioned control strategies, different operating conditions are configured. Based on the proposed bi-level control strategy, including the upper-level cooperative control and the lower-level unified control strategy for IS mode, corresponding experiments are conducted to verify the effectiveness of the health monitoring by converter-based IS. Four features are extracted based on the obtained IS spectra. The changing trends of these features can effectively reflect the variations of the operating conditions, including the irradiance level, the temperature and partial shading. The proposed converter-based IS (including modeling, control strategies and extraction of features) is promising to be applied and further explored.

Perspectives

This work concentrates on the fundamentals of converter-based IS applied in PV systems, including its operating principles, the simplified AC-ECM of PV panels, the control strategies and the definition of features. Numerous tracks of development still exist to study all the specific features of this technique as applied to renewable energy sources and photovoltaic in particular, and thus lead to slightly more refined industrial and commercial solutions. Based on the current work, four aspects will be further developed concerning:

- **Health monitoring of defective PV panels:**
  In terms of health monitoring, apart from the operating conditions and partial shading, the faulty conditions should be further considered. Typical faults are summarized in Chapter 1. Degradation, especially, is closely related to the system's lifetime, and necessitates a long-term measurement and analysis for a proper characterization. IS spectra under more operating conditions will be measured based on the proposed methods in the next step. During this process, additional features may need to be defined to describe the specific faults.

- **Feature analysis based on intelligent algorithms:**
  This comment focuses on the extraction methods of features. Intelligent algorithms, such as machine learning, can facilitate the online fault detection and make the monitoring results faster and more accurate. In the following work, as more fault features are obtained, intelligent algorithms will be further applied to fault diagnosis.

- **Monitoring based on high voltage-ratio converter:**
  To obtain a higher bus-voltage, some novel modular DC/DC converters may be applied in MGs. They may have multiple inputs or multiple outputs. In general, their equivalent switching frequency is higher than the switching frequency of the conventional boost converter. Additionally, the transfer function of the converter changes accordingly. Therefore, the limitations of the perturbation signal will be different and need additional analysis.

  In addition, an IS spectrum with a wider frequency range may be obtained. If the maximum value of the perturbation frequency exceeds 10 kHz, it is possible to obtain the top point information of the second arc in Figure 3.9. In this condition, more features can be extracted for health monitoring.

- **Influence of the perturbation signal on the stabilization of the DC-bus voltage:**
  Injecting perturbation signals result in a certain fluctuation on the DC-bus voltage after the power converter. Based on MATLAB/Simulink, it is observed that the DC-bus voltage fluctuation induced by the perturbation signal within the selected frequency range in our work can be maintained within the engineering specifications, i.e., $\leq 5\%$, by the implementation of an energy management strategy (EMS) as developed by S. Ali in the same project (ANR EREMITE-WP4). Under the control of EMS, most of the low-frequency component can be absorbed by the other energy storage system installed in MGs, e.g., batteries, supercapacitors, and so on. However, the absorption of the high-frequency part is not significant, which may result in instability in the system. The detailed analysis of the influence of the perturbation on the stability of the DC-bus voltage is essential and will be analyzed in the next step work.

- **Interconnection between health monitoring results and energy management strategy of MGs:**
  In addition to its application in PV panels, the proposed converter-based IS can also be implemented in other elements of MGs, such as batteries and supercapacitors, to perform real-time fault detection of the whole system. The monitored health information can be fed back to the EMS to achieve a better maintenance of the operating points/constraints of each component of MGs. This work will be combined with the other part of the ANR EREMITE project in the future, which has been focused on the EMS aspect of MGs.

Bibliography

[1] IRENA. World energy transitions outlook 2023 - 1.5°C Pathway - Preview. *International Renewable Energy Agency*, pages 1–54, 2023.

[2] Brent L Iverson and Peter B Dervan. *Comprehensive Guide on Organic and Inorganic Solar Cells*. Elsevier, 2022.

[3] Zuyu Wu, Yihua Hu, Jennifer X. Wen, Fubao Zhou, and Xianming Ye. A Review for Solar Panel Fire Accident Prevention in Large-Scale PV Applications. *IEEE Access*, 8:132466–132480, 2020.

[4] Zhixue Zheng, Xiaoyu Wang, and Yongdong Li. A control method for grid-friendly photovoltaic systems with hybrid energy storage units. *DRPT 2011 - 2011 4th International Conference on Electric Utility Deregulation and Restructuring and Power Technologies*, (51007044):1437–1440, 2011.

[5] Alexandros Ch Lazanas and Mamas I. Prodromidis. Electrochemical Impedance Spectroscopy: A Tutorial. *ACS Measurement Science Au*, 3(3):162–193, 2023.

[6] Raffaele PETRONE. Electrochemical Impedance Spectroscopy for the on-board diagnosis of PEMFC via on-line identification of Equivalent Circuit Model parameters. page 197, 2014.

[7] Travis Yeow, Jing Sun, Zheng Yao, Jean-nicolas Jaubert, and Kevin P Musselman. Evaluation of impedance spectroscopy as a tool to characterize degradation mechanisms in silicon photovoltaics. *Solar Energy*, 184(March):52–58, 2019.

[8] Osbel Almora, Yicheng Zhao, Xiaoyan Du, Thomas Heumueller, Gebhard J. Matt, Germà Garcia-Belmonte, and Christoph J. Brabec. Light intensity modulated impedance spectroscopy (LIMIS) in all-solid-state solar cells at open-circuit. *Nano Energy*, 75(November 2019), 2020.

[9] J. E. Garland, D. J. Crain, J. P. Zheng, C. M. Sulyma, and D. Roy. Electro-analytical characterization of photovoltaic cells by combining voltammetry and impedance spectroscopy: Voltage dependent param-

eters of a silicon solar cell under controlled illumination and temperature. *Energy and Environmental Science*, 4(2):485–498, 2010.

[10] Elizabeth Von Hauff. Impedance Spectroscopy for Emerging Photovoltaics. *Journal of Physical Chemistry C*, 123(18):11329–11346, 2019.

[11] Jagannath Panigrahi, Ashutosh Pandey, Shrestha Bhattacharya, Alok Pal, Sourav Mandal, and Vamsi Krishna Komarala. Impedance spectroscopy of amorphous/crystalline silicon heterojunction solar cells under dark and illumination. *Solar Energy*, 259(May):165–173, 2023.

[12] Alireza Bahadori and Chikezie Nwaoha. A review on solar energy utilisation in Australia. *Renewable and Sustainable Energy Reviews*, 18:1–5, 2013.

[13] Jiaxin Ni, Li Zhao, Zhengtao Zhang, Ying Zhang, Jianyuan Zhang, Shuai Deng, and Minglu Ma. Dynamic performance investigation of organic Rankine cycle driven by solar energy under cloudy condition. *Energy*, 147:122–141, 2018.

[14] IRENA. Renewables 2023 Analysis and forecast to 2028. *International Renewable Energy Agency*, 2023.

[15] SolarPower Europe. EU solar reaches record heights of 56 GW in 2023 but warns of clouds on the horizon. Technical report.

[16] Enrique Romero-Cadaval, Giovanni Spagnuolo, Leopoldo Garcia Franquelo, Carlos Andres Ramos-Paja, Teuvo Suntio, and Weidong Michael Xiao. Grid-connected photovoltaic generation plants: Components and operation. *IEEE Industrial Electronics Magazine*, 7(3):6–20, 2013.

[17] Gaëlle Faure, Mathieu Vallée, Cédric Paulus, and Tuan Quoc Tran. Fault detection and diagnosis for large solar thermal systems: A review of fault types and applicable methods. *Solar Energy*, 197(February 2019):472–484, 2020.

[18] R.H.Lasseter. Basic Control of Real and Reactive Power. *2002 IEEE Power Engineering Society Winter Meeting. Conference Proceedings (Cat. No.02CH37309)*, pages 305–308, 2002.

[19] Luiz Antonio De Souza Ribeiro, Osvaldo Ronald Saavedra, Shigeaki Leite De Lima, and Jos Gomes De Matos. Isolated micro-grids with renewable hybrid generation: The case of Lençóis island. *IEEE Transactions on Sustainable Energy*, 2(1):1–11, 2011.

[20] Mohammad E. Khodayar, Masoud Barati, and Mohammad Shahidehpour. Integration of high reliability distribution system in microgrid operation. *IEEE Transactions on Smart Grid*, 3(4):1997–2006, 2012.

[21] Wenlong Jing, Chean Hung Lai, Shung Hui Wallace Wong, and Mou Ling Dennis Wong. Battery-supercapacitor hybrid energy storage system in standalone DC microgrids: Areview. *IET Renewable Power Generation*, 11(4):461–469, 2017.

[22] Ataul Bari, Jin Jiang, Walid Saad, and Arunita Jaekel. Challenges in the smart grid applications: An overview. *International Journal of Distributed Sensor Networks*, 2014, 2014.

[23] Qing Wang, Seigo Ito, Michael Grätzel, Francisco Fabregat-Santiago, Iván Mora-Seró, Juan Bisquert, Takeru Bessho, and Hachiro Imai. Characteristics of high efficiency dye-sensitized solar cells. *Journal of Physical Chemistry B*, 110(50):25210–25221, 2006.

[24] Anthony Lewis, Joel R. Troughton, Benjamin Smith, James McGettrick, Tom Dunlop, Francesca De Rossi, Adam Pockett, Michael Spence, Matthew J. Carnie, Trystan M. Watson, and Cécile Charbonneau. In-depth analysis of defects in TiO2 compact electron transport layers and impact on performance and hysteresis of planar perovskite devices at low light. *Solar Energy Materials and Solar Cells*, 209(November 2019), 2020.

[25] Linfeng Shi, Chengyue Sun, Yong Liu, Ke Liu, Weinan Zhang, Yiyong Wu, Hongliang Guo, and Qiang Sun. A novel method of determining bias lights for spectral response measurement of GaAs multi-junction laser power converters and its applications. *Solar Energy Materials and Solar Cells*, 266(November 2023):112661, 2024.

[26] Siyi Liu, Yong Qian, Yinyue Lin, Lijie Sun, Yongxin Zhu, and Dongdong Li. Multilayer anti-reflective coating with ultra-low refractive index SiO2 nanopillars for high efficiency multi-junction GaAs solar cells. *Solar Energy Materials and Solar Cells*, 266(September 2023):112679, 2024.

[27] National Renewable Energy Laboratory. Best Research-Cell Efficiencies, 2024.

[28] Gianluca Acciari, Davide Graci, and Amedeo La Scala. Higher PV module efficiency by a novel CBS bypass. *IEEE Transactions on Power Electronics*, 26(5):1333–1336, 2011.

[29] Katherine A. Kim, Chenyang Xu, Lei Jin, and Philip T. Krein. A dynamic photovoltaic model incorporating capacitive and reverse-bias characteristics. *IEEE Journal of Photovoltaics*, 3(4):1334–1341, 2013.

[30] Vun Jack Chin, Zainal Salam, and Kashif Ishaque. Cell modelling and model parameters estimation techniques for photovoltaic simulator application: A review. *Applied Energy*, 154:500–519, 2015.

[31] Ratnakar Babu Bollipo, Suresh Mikkili, and Praveen Kumar Bonthagorla. Hybrid, optimal, intelligent and classical PV MPPT techniques: A review. *CSEE Journal of Power and Energy Systems*, 7(1):9–33, 2021.

[32] M. Köntges, S. Kurtz, C.E. Packard, U. Jahn, K. Berger, K. Kato, T. Friesen, H. Liu, and M. Van Iseghem. *Performance and reliability of photovoltaic systems subtask 3.2: Review of failures of photovoltaic modules: IEA PVPS task 13: external final report IEA-PVPS*. 2014.

[33] Patrizio Manganiello, Marco Balato, and Massimo Vitelli. A Survey on Mismatching and Aging of PV Modules: The Closed Loop. *IEEE Transactions on Industrial Electronics*, 62(11):7276–7286, 2015.

[34] Kais Abdulmawjood, Shady S. Refaat, and Walid G. Morsi. Detection and prediction of faults in photovoltaic arrays: A review. *Proceedings - 2018 IEEE 12th International Conference on Compatibility, Power Electronics and Power Engineering, CPE-POWERENG 2018*, pages 1–8, 2018.

[35] Asma Triki-Lahiani, Afef Bennani-Ben Abdelghani, and Ilhem Slama-Belkhodja. Fault detection and monitoring systems for photovoltaic installations: A review. *Renewable and Sustainable Energy Reviews*, 82(September 2017):2680–2692, 2018.

[36] Dhanup S. Pillai and N. Rajasekar. A comprehensive review on protection challenges and fault diagnosis in PV systems. *Renewable and Sustainable Energy Reviews*, 91(April):18–40, 2018.

[37] Baojie Li. electrical measurements Health monitoring of photovoltaic modules using electrical measurements. 2021.

[38] Mingyao Ma, Zhixiang Zhang, Zhen Xie, Ping Yun, Xing Zhang, and Fei Li. Fault diagnosis of cracks in crystalline silicon photovoltaic modules through I-V curve. *Microelectronics Reliability*, 114(October):113848, 2020.

[39] Baloji Adothu, Parth Bhatt, Shashwata Chattopadhyay, Sarita Zele, Jeroen Oderkerk, H. P. Sagar, Francis Reny Costa, and Sudhanshu Mallick. Newly developed thermoplastic polyolefin encapsulant–A potential candidate for crystalline silicon photovoltaic modules encapsulation. *Solar Energy*, 194(November):581–588, 2019.

[40] Siva Ramakrishna Madeti and S. N. Singh. A comprehensive study on different types of faults and detection techniques for solar photovoltaic system. *Solar Energy*, 158(June):161–185, 2017.

[41] Mahmoud Dhimish and Zhicong Chen. Novel Open-Circuit Photovoltaic Bypass Diode Fault Detection Algorithm. *IEEE Journal of Photovoltaics*, 9(6):1819–1827, 2019.

[42] Mohammad Amin Ghasemi, Hossein Mohammadian Forushani, and Mostafa Parniani. Partial shading detection and smooth maximum power point tracking of PV arrays under PSC. *arXiv*, 31(9):6281–6292, 2018.

[43] R. Hariharan, M. Chakkarapani, G. Saravana Ilango, and C. Nagamani. A Method to Detect Photovoltaic Array Faults and Partial Shading in PV Systems. *IEEE Journal of Photovoltaics*, 6(5):1278–1285, 2016.

[44] Mahmoud Dhimish and Ghadeer Badran. Photovoltaic Hot-Spots Fault Detection Algorithm Using Fuzzy Systems. *IEEE Transactions on Device and Materials Reliability*, 19(4):671–679, 2019.

[45] John H. Wohlgemuth and Sarah R. Kurtz. How can we make PV modules safer? *Conference Record of the IEEE Photovoltaic Specialists Conference*, (June):3162–3165, 2012.

[46] Shashwata Chattopadhyay, Rajiv Dubey, Sonali Bhaduri, Sachin Zachariah, Hemant Kumar Singh, Chetan Singh Solanki, Anil Kottantharayil, Narendra Shiradkar, Brij M. Arora, K. L. Narasimhan, and Juzer Vasi. Correlating infrared thermography with electrical degradation of PV modules inspected in all-india survey of photovoltaic module reliability 2016. *IEEE Journal of Photovoltaics*, 8(6):1800–1808, 2018.

[47] D Aaron R Barkhouse, Oki Gunawan, Tayfun Gokmen, Teodor K Todorov, and David B Mitzi. On the detection of shunts in silicon solar cells by photo and electroluminescence imaging. *Progress in Photovoltaics: Research and Applications*, 20(1):6–11, 2015.

[48] Ghada M. El-Banby, Nada M. Moawad, Belal A. Abouzalm, Wessam F. Abouzaid, and E. A. Ramadan. Photovoltaic system fault detection techniques: a review. *Neural Computing and Applications*, 35(35):24829–24842, 2023.

[49] Romain Duru, Delphine Le Cunff, Maxime Cannac, Isabella Mica, Jose Baruchel, Thu Nhi Tran-Thi, and Georges Bremond. Photoluminescence Imaging for Buried Defects Detection in Silicon: Assessment and Use-Cases. *IEEE Transactions on Semiconductor Manufacturing*, 32(1):23–30, 2019.

[50] Karl Bedrich, Matevz Bokalic, Martin Bliss, Marko Topic, Thomas R. Betts, and Ralph Gottschalg. Electroluminescence Imaging of PV Devices: Advanced Vignetting Calibration. *IEEE Journal of Photovoltaics*, 8(5):1297–1304, 2018.

[51] Karl G. Bedrich, Wei Luo, Mauro Pravettoni, Daming Chen, Yifeng Chen, Zigang Wang, Pierre J. Verlinden, Peter Hacke, Zhiqiang Feng, Jing Chai, Yan Wang, Armin G. Aberle, and Yong Sheng Khoo.

Quantitative Electroluminescence Imaging Analysis for Performance Estimation of PID-Influenced PV Modules. *IEEE Journal of Photovoltaics*, 8(5):1281–1288, 2018.

[52] Ulrike Jahn, Magnus Herz, Marc Köntges, David Parlevliet, Marco Paggi, and Ioannis Tsanakas. *Review on infrared and electroluminescence imaging for PV field applications: International Energy Agency Photovoltaic Power Systems Programme: IEA PVPS Task 13, Subtask 3.3: report IEA-PVPS T13-12: 2018*. 2018.

[53] Ula Hijjawi, Subhash Lakshminarayana, Tianhua Xu, Gian Piero Malfense Fierro, and Mostafizur Rahman. A review of automated solar photovoltaic defect detection systems: Approaches, challenges, and future orientations. *Solar Energy*, 266(August):112186, 2023.

[54] Hayder Yousif and Zahraa Al-Milaji. Fault detection from PV images using hybrid deep learning model. *Solar Energy*, 267(April 2023):112207, 2024.

[55] Wenguan Wang, Alex Chun For Liu, Henry Shu Hung Chung, Ricky Wing Hong Lau, Jun Zhang, and Alan Wai Lun Lo. Fault Diagnosis of Photovoltaic Panels Using Dynamic Current-Voltage Characteristics. *IEEE Transactions on Power Electronics*, 31(2):1588–1599, 2016.

[56] Zhixiang Zhang, Mingyao Ma, Hai Wang, Haisong Wang, Wenting Ma, and Xing Zhang. A fault diagnosis method for photovoltaic module current mismatch based on numerical analysis and statistics. *Solar Energy*, 225(July):221–236, 2021.

[57] S. Fadhel, C. Delpha, D. Diallo, I. Bahri, A. Migan, M. Trabelsi, and M. F. Mimouni. PV shading fault detection and classification based on I-V curve using principal component analysis: Application to isolated PV system. *Solar Energy*, 179:1–10, 2019.

[58] Batoul Zbib and Hiba Al Sheikh. Fault Detection and Diagnosis of Photovoltaic Systems through I-V Curve Analysis. *2nd International Conference on Electrical, Communication and Computer Engineering, ICECCE 2020*, (June):12–13, 2020.

[59] Baojie Li, Claude Delpha, Anne Migan-Dubois, and Demba Diallo. Fault diagnosis of photovoltaic panels using full I–V characteristics and machine learning techniques. *Energy Conversion and Management*, 248:114785, 2021.

[60] Y. Stauffer, D. Ferrario, E. Onillon, and A. Hutter. Power monitoring based photovoltaic installation fault detection. *2015 International Conference on Renewable Energy Research and Applications, ICRERA 2015*, 5:199–202, 2015.

[61] Suguru Osawa, Takuma Nakano, Shunya Matsumoto, Noboru Katayama, Yusuke Saka, and Hiroki Sato. Fault diagnosis of photovoltaic modules using AC impedance spectroscopy. *2016 IEEE International Conference on Renewable Energy Research and Applications, ICRERA 2016*, 5:210–215, 2017.

[62] Xiao-Zi Yuan, Chaojie Song, Haijiang Wang, and Jiujun Zhang. *Electrochemical Impedance Spectroscopy in PEM Fuel Cells*. Springer, 2014.

[63] Matthew W. Losey and James J. Kelly. *Electrochemical Impedance Spectroscopy and its Applications*, volume 1. Springer Science+Business Media New York, New York, USA, 2014.

[64] Xiaozi Yuan, Jian Colin Sun, Mauricio Blanco, Haijiang Wang, Jiujun Zhang, and David P. Wilkinson. AC impedance diagnosis of a 500 W PEM fuel cell stack. Part I: Stack impedance. *Journal of Power Sources*, 161(2):920–928, 2006.

[65] E. Bradley Easton and Peter G. Pickup. An electrochemical impedance spectroscopy study of fuel cell electrodes. *Electrochimica Acta*, 50(12):2469–2474, 2005.

[66] Mina Abedi Varnosfaderani and Dani Strickland. Online Electrochemical Impedance Spectroscopy (EIS) estimation of a solar panel. *Vacuum*, 139:185–195, 2017.

[67] Hao Yuan, Runben Du, Xueyuan Wang, Xuezhe Wei, and Haifeng Dai. Advanced Online Broadband Impedance Spectrum Acquisition of Fuel Cells by S-Transform. *IEEE Transactions on Industrial Electronics*, 70(4):3740–3750, 2023.

[68] J Ross Macdonald and a John Wiley. *Impedance Spectroscopy Theory, Experiment, and Applications*. 2005.

[69] Made-in-Chine. CS310 Electrochemical Workstation Potentiostat Galvanostat with EIS.

[70] Xueyuan Wang, Xuezhe Wei, Qijun Chen, Jiangong Zhu, and Haifeng Dai. Lithium-ion battery temperature on-line estimation based on fast impedance calculation. *Journal of Energy Storage*, 26(September), 2019.

[71] Wangxin Huang and Jaber A. Qahouq. An online battery impedance measurement method using DC-DC power converter control. *IEEE Transactions on Industrial Electronics*, 61(11):5987–5995, 2014.

[72] O. Bethoux, M. Hilairet, and T. Azib. A new on-line state-of-health monitoring technique dedicated to PEM fuel cell. *IECON Proceedings (Industrial Electronics Conference)*, (December):2745–2750, 2009.

[73] Sean Moore and Paul Barendse. Online condition monitoring of lithium-ion batteries using impedance spectroscopy. *2017 IEEE Energy Conversion Congress and Exposition, ECCE 2017*, 2017-Janua:5617–5624, 2017.

[74] Olufemi I. Olayiwola and Paul S. Barendse. Power Electronic Implementation of Electrochemical Impedance Spectroscopy on Photovoltaic Modules. *ECCE 2020 - IEEE Energy Conversion Congress and Exposition*, pages 3654–3661, 2020.

[75] Taha Nurettin Gücin and Levent Ovacik. Online Impedance Measurement of Batteries Using the Cross-Correlation Technique. *IEEE Transactions on Power Electronics*, 35(4):4365–4375, 2020.

[76] Noboru Katayama and Sumio Kogoshi. Real-Time Electrochemical Impedance Diagnosis for Fuel Cells Using a DC-DC Converter. *IEEE Transactions on Energy Conversion*, 30(2):707–713, 2015.

[77] Hossein Haji Abbasali and Shahin Jafarabadi Ashtiani. Online Broadband Battery Impedance Spectroscopy Using Current-Mode Boost Converter. *IEEE Transactions on Instrumentation and Measurement*, 71:1–8, 2022.

[78] Jaber A.Abu Qahouq and Zhiyong Xia. Single-Perturbation-Cycle Online Battery Impedance Spectrum Measurement Method with Closed-Loop Control of Power Converter. *IEEE Transactions on Industrial Electronics*, 64(9):7019–7029, 2017.

[79] Jiabin Shen, Hooman Homayouni, and Jiacheng Wang. Converter-Based Electrochemical Impedance Spectroscopy for High-Power Fuel Cell Stacks with Resonant Controllers. *IEEE Transactions on Industrial Electronics*, 68(9):8819–8828, 2021.

[80] D. T. Cotfas, P. A. Cotfas, and S. Kaplanis. Methods and techniques to determine the dynamic parameters of solar cells: Review. *Renewable and Sustainable Energy Reviews*, 61:213–221, 2016.

[81] Pierre-alexis Gril, Julian Vernier, Daniel Depernet, Pierre-alexis Gril, Julian Vernier, Daniel Depernet, Caractérisation De, Pierre-alexis Gril, Julian Vernier, and Daniel Depernet. Caractérisation de panneaux photovoltaïques par mesure d ' impédance. *Symposium de Genie Electrique*, 2019.

[82] Zahra Moradi-shahrbabak, Student Member, and Ahmadreza Tabesh. Effects of Front-End Converter and DC-Link of a Utility-Scale PV Energy System on Dynamic Stability of a Power System. *IEEE Transactions on Industrial Electronics*, 65(1):403–411, 2018.

[83] Linda Shelembe and Paul Barendse. An Adaptive Amplitude-Modulated Pseudo-Random Binary Sequence Excitation for Converter-Based Impedance Spectroscopy Characterization of Photovoltaic Modules. *IEEE Transactions on Industry Applications*, 59(2):2007–2018, 2023.

[84] Z. Zheng, R. Petrone, M. C. Pera, D. Hissel, M. Becherif, and C. Pianese. Diagnosis of a commercial PEM fuel cell stack via incomplete spectra and fuzzy clustering. *IECON 2013 - 39th Annual Conference of the IEEE Industrial Electronics Society*, pages 1595–1600, 2013.

[85] Rudy Alexis Guejia-Burbano, Giovanni Petrone, and Michel Piliougine. Impedance Spectroscopy for Diagnosis of Photovoltaic Modules Under Outdoor Conditions. *IEEE Journal of Photovoltaics*, 12(6):1503–1512, 2022.

[86] Matei I. Oprea, Sergiu V. Spataru, Dezso Sera, Peter B. Poulsen, Sune Thorsteinsson, Ronni Basu, Anders R. Andersen, and Kenn H.B. Frederiksen. Detection of potential induced degradation in c-Si PV panels using electrical impedance spectroscopy. *Conference Record of the IEEE Photovoltaic Specialists Conference*, 2016-Novem(2):1575–1579, 2016.

[87] Noboru Katayama, Suguru Osawa, Shunya Matsumoto, Takuma Nakano, and Mutsumi Sugiyama. Degradation and fault diagnosis of photovoltaic cells using impedance spectroscopy. *Solar Energy Materials and Solar Cells*, 194(February):130–136, 2019.

[88] D. Chenvidhya, K. Kirtikara, and C. Jivacate. A new characterization method for solar cell dynamic impedance. *Solar Energy Materials and Solar Cells*, 80(4):459–464, 2003.

[89] Katherine A Kim, Gab Su Seo, Bo Hyung Cho, and Philip T Krein. Photovoltaic Hot-Spot Detection for Solar Panel Substrings Using AC Parameter Characterization. *IEEE Transactions on Power Electronics*, 31(2):1121–1130, 2016.

[90] Katherine A Kim, Chenyang Xu, Lei Jin, and Philip T Krein. A dynamic photovoltaic model incorporating capacitive and reverse-bias characteristics. *IEEE Journal of Photovoltaics*, 3(4):1334–1341, 2013.

[91] Jay Johnson, David Schoenwald, Scott Kuszmaul, Jason Strauch, and Ward Bower. Creating Dynamic Equivalent PV Circuit Models With Impedance. *37th IEEE Photovoltaic Specialists Conference*, pages 2328–2333, 2011.

[92] Petru Adrian Cotfas, Daniel Tudor Cotfas, Paul Nicolae Borza, Dezso Sera, and Remus Teodorescu. Solar cell capacitance determination based on an RLC resonant circuit. *Energies*, 11(3), 2018.

[93] R. Anil Kumar, M. S. Suresh, and J. Nagaraju. Silicon (BSFR) solar cell AC parameters at different temperatures. *Solar Energy Materials and Solar Cells*, 85(3):397–406, 2005.

[94] Pankaj Yadav, Brijesh Tripathi, Kavita Pandey, and Manoj Kumar. Investigating the charge transport kinetics in poly-crystalline silicon solar cells for low-concentration illumination by impedance spectroscopy. *Solar Energy Materials and Solar Cells*, 133:105–112, 2015.

[95] Pankaj Yadav, Kavita Pandey, Brijesh Tripathi, and Manoj Kumar. Investigation of interface limited charge extraction and recombination in polycrystalline silicon solar cell: Using DC and AC characterization techniques. *Solar Energy*, 116:293–302, 2015.

[96] Sanjai Kumar, P K Singh, and G S Chilana. Study of silicon solar cell at different intensities of illumination and wavelengths using impedance spectroscopy. *Solar Energy Materials and Solar Cells*, 93(10):1881–1884, 2009.

[97] Olufemi Olayiwola and Paul Barendse. Characterization of Photovoltaic Cells Using Time Domain Voltage Decay Analysis. *IEEE AFRICON Conference*, 2019-Septe:1–8, 2019.

[98] D. J. Crain, J. E. Garland, S. E. Rock, and D. Roy. Quantitative characterization of silicon solar cells in the electro-analytical approach: Combined measurements of temperature and voltage dependent electrical parameters. *Analytical Methods*, 4(1):106–117, 2012.

[99] Ivan Mora-Seró, Yan Luo, Germà Garcia-Belmonte, Juan Bisquert, Delfina Muñoz, Cristóbal Voz, Joaquim Puigdollers, and Ramon Alcubilla. Recombination rates in heterojunction silicon solar cells analyzed by impedance spectroscopy at forward bias and under illumination. *Solar Energy Materials and Solar Cells*, 92(4):505–509, 2008.

[100] Pankaj Yadav, Brijesh Tripathi, Kavita Pandey, and Manoj Kumar. Recombination kinetics in a silicon solar cell at low concentration: Electro-analytical characterization of space-charge and quasi-neutral regions. *Physical Chemistry Chemical Physics*, 16(29):15469–15476, 2014.

[101] Olufemi Isaac Olayiwola and Paul S Barendse. Characterization of Silicon-Based Photovoltaic Cells Using Broadband Impedance Spectroscopy. *IEEE Transactions on Industry Applications*, 54(6):6309–6319, 2018.

[102] Olufemi Issac Olayiwola and Paul S. Barendse. Photovoltaic Cell/Module Equivalent Electric Circuit Modeling Using Impedance Spectroscopy. *IEEE Transactions on Industry Applications*, 56(2):1190–1701, 2020.

[103] Olufemi I Olayiwola and Paul S Barendse. Dynamic Equivalent Circuit Modelling of Polycrystalline Silicon Photovoltaic Cells. 2017.

[104] Mohamed M. Shehata, Thien N. Truong, Rabin Basnet, Hieu T. Nguyen, Daniel H. Macdonald, and Lachlan E. Black. Impedance spectroscopy characterization of c-Si solar cells with SiOx/ Poly-Si rear passivating contacts. *Solar Energy Materials and Solar Cells*, 251(December 2022):112167, 2023.

[105] David A. van Nijen, Mirco Muttillo, Rik Van Dyck, Jef Poortmans, Miro Zeman, Olindo Isabella, and Patrizio Manganiello. Revealing capacitive and inductive effects in modern industrial c-Si photovoltaic cells through impedance spectroscopy. *Solar Energy Materials and Solar Cells*, 260(April):112486, 2023.

[106] Tadanori Tanahashi, Norihiko Sakamoto, Hajime Shibata, and Atsushi Masuda. Localization and characterization of a degraded site in crystalline silicon photovoltaic cells exposed to acetic acid vapor. *IEEE Journal of Photovoltaics*, 8(4):997–1004, 2018.

[107] Pankaj Yadav, Kavita Pandey, Vishwa Bhatt, Manoj Kumar, and Joondong Kim. Critical aspects of impedance spectroscopy in silicon solar cell characterization: A review. *Renewable and Sustainable Energy Reviews*, 76(November 2016):1562–1578, 2017.

[108] Francisco Fabregat-Santiago, Germà Garcia-Belmonte, Iván Mora-Seró, and Juan Bisquert. Characterization of nanostructured hybrid and organic solar cells by impedance spectroscopy. *Physical Chemistry Chemical Physics*, 13(20):9083–9118, 2011.

[109] Azimah Omar, Mohd Syukri Ali, and Nasrudin Abd Rahim. Electron transport properties analysis of titanium dioxide dye-sensitized solar cells (TiO2-DSSCs) based natural dyes using electrochemical impedance spectroscopy concept: A review, 2020.

[110] Cedric Gonzales, Antonio Guerrero, and Juan Bisquert. Transition from Capacitive to Inductive Hysteresis: A Neuron-Style Model to Correlate I- V Curves to Impedances of Metal Halide Perovskites. *Journal of Physical Chemistry C*, 126(32):13560–13578, 2022.

[111] Jenny Nelson. *The Physics of Solar Cells*. Imperial College Press, Singapore, 2003.

[112] Ferdaous Masmoudi, Fatma Ben Salem, and Nabil Derbel. Single and double diode models for conventional mono-crystalline solar cell with extraction of internal parameters. *13th International Multi-Conference on Systems, Signals and Devices, SSD 2016*, pages 720–728, 2016.

[113] W. Shockley. The theory of p-n junctions in semiconductors and p-n junction transistors. *The Bell System Technical Journal*, pages 435–489, 1949.

[114] B.G. Streetman Banerjee. and S. Solid State Electronic Devices. In *5th Edi- tion, Prentice Hall (2000) Chapter 5.6.2 Recombination and generation in the transition region, 214*. 2000.

[115] O. Almora and Germà Garcia-Belmonte. Light capacitances in silicon and perovskite solar cells. *Solar Energy*, 189(July):103–110, 2019.

[116] C. Yunmei L. hui and L. Xiangwei. Study of bypass diodes configuration on PV modules with partial shaded. In *2019 Chinese Control And Decision Conference (CCDC)*, pages 511–515, Nanchang, China, 2019.

[117] T. Hamada, K. Nakamoto, I. Nanno, N. Ishikura, S. Oke, and M. Fujii. Fault Characteristics of Schottky Barrier Diode used as Bypass Diode in Photovoltaic Module against Repetitive Surges. In *2020 47th IEEE Photovoltaic Specialists Conference (PVSC)*, Calgary, AB, Canada, 2020.

[118] Qihao Guo, Imen Bahri, Demba Diallo, and Eric Berthelot. Model predictive control and linear control of DC–DC boost converter in low voltage DC microgrid: An experimental comparative study. *Control Engineering Practice*, 131(October 2022):105387, 2023.

[119] Thanh Tuan Nguyen, Van Tuan Doan, and Woojin Choi. Design of a fuel cell power conditioning system for online diagnosis and load leveling. *Journal of Power Electronics*, 16(2):695–703, 2016.

[120] Edison R.C. da Silva and Malik E. Elbuluk. *Fundamentals of Power Electronics*, volume 59. 2013.

[121] Tao Ye, Ning Yi Dai, Chi Seng Lam, Man Chung Wong, and Josep M. Guerrero. Analysis, design, and implementation of a quasi-proportional-resonant controller for a multifunctional capacitive-coupling grid-connected inverter. *IEEE Transactions on Industry Applications*, 52(5):4269–4280, 2016.

[122] SiC module PEB 8024.

[123] Aliaksandr Bandarenka and Genagy Ragoisha. EIS Spectrum Analyser, 2008.